APPLIED COMPUTATIONAL ELECTROMAGNETICS SOCIETY JOURNAL

March 2026
Vol. 41 No. 03
ISSN 1054-4887

The ACES Journal is abstracted in INSPEC, in Engineering Index, DTIC, Science Citation Index Expanded, the Research Alert, and to Current Contents/Engineering, Computing & Technology.

The illustrations on the front cover have been obtained from the ARC research group at the Department of Electrical Engineering, Colorado School of Mines

Published, sold and distributed by: River Publishers, Broagervej 10, 9260 Gistrup, Denmark

THE APPLIED COMPUTATIONAL ELECTROMAGNETICS SOCIETY
http://aces-society.org

EDITORS-IN-CHIEF

Sami Barmada
University of Pisa, ESE Dept.
56122 Pisa, Italy

Atef Elsherbeni
Colorado School of Mines, EE Dept.
Golden, CO 80401, USA

ASSOCIATE EDITORS

Giulio Antonini
Università degli Studi dell'Aquila
Italy

Marco Arjona
La Laguna Institute of Technology
Coahuila 27266, Mexico

Abd A. Arkadan
Colorado School of Mines, Golden
CO 80401, USA

Alireza Baghai-Wadji
University of Cape Town
Cape Town, 7701, South Africa

Santanu Behera
National Institute of Technology
Rourkela-769008, India

Rui Chen
Nanjing University of Science
and Technology
China

Vinh Dang
Sandia National Laboratories
USA

Sounik Kiran Kumar Dash
SRM Institute of Science and Technology
Chennai, India

Alessandro Formisano
Seconda Universita di Napoli
81031 CE, Italy

Nunzia Fontana
University of Pisa
56122 Pisa, Italy

Fatih Kaburcuk
Sivas Cumhuriyet University
Sivas, Turkey

Piotr Gas
AGH University of Kraków
30-059 Krakow, Poland

Mona El Helbawy
University of Colorado
Boulder, CO 80302, USA

Zhixiang Huang
Anhui University
China

Qiuhua Huang
Colorado School of Mines
USA

Long Li
Xidian University
Shaanxi 710071, China

Yingsong Li
Harbin Engineering University
Harbin 150001, China

Wenxing Li
Harbin Engineering University
Harbin 150001, China

Ibrahim Mahariq
Gulf University for Science and Technology
Kuwait

Riyadh Mansoor
Al-Muthanna University
Samawa, Al-Muthanna, Iraq

Maria Evelina Mognaschi
University of Pavia
Italy

Antonino Musolino
University of Pisa
56123 Pisa, Italy

Sima Noghanian
Wafer LLC
Beverly, MA 01915, USA

Mauro Parise
University Campus Bio-Medico of Rome
00128 Rome, Italy

Luca Di Rienzo
Politecnico di Milano
20133 Milano, Italy

Daniele Romano
Università degli Studi dell'Aquila
Italy

Huseyin Savci
Istanbul Medipol University
Turkey

Stefano Selleri
DINFO – University of Florence
0139 Florence, Italy

Sihua Shao
Colorado School of Mines
USA

Jiming Song
Iowa State University
IA 50011, USA

Sheng Sun
University of Electronic Science
and Technology of China
China

Francesca Venneri
DIMES, Università della Calabria
Italy

Steven Weiss
US Army Research Laboratory
USA

Wei-Chung Weng
National Chi Nan University
Puli, Nantou 54561, Taiwan

Kaikai Xu
University of Electronic Science
and Technology of China
China

Lei Zhao
China University of Mining
and Technology, Jiangsu 221116
China

EDITORIAL ASSISTANTS

Matthew J. Inman
University of Mississippi, EE Dept.
University, MS 38677, USA

Shanell Lopez
Colorado School of Mines, EE Dept.
Golden, CO 80401, USA

EMERITUS EDITORS-IN-CHIEF

Duncan C. Baker
EE Dept. U. of Pretoria
0002 Pretoria, South Africa

Allen Glisson
University of Mississippi, EE Dept.
University, MS 38677, USA

Ahmed Kishk
Concordia University, ECS Dept.
Montreal, QC H3G 1M8, Canada

Robert M. Bevensee
Box 812
Alamo, CA 94507-0516

Ozlem Kilic
Catholic University of America
Washington, DC 20064, USA

David E. Stein
USAF Scientific Advisory Board
Washington, DC 20330, USA

EMERITUS ASSOCIATE EDITORS

Yasushi Kanai
Niigata Inst. of Technology
Kashiwazaki, Japan

Mohamed Abouzahra
MIT Lincoln Laboratory
Lexington, MA, USA

Alexander Yakovlev
University of Mississippi, EE Dept.
University, MS 38677, USA

Levent Gurel
Bilkent University
Ankara, Turkey

Sami Barmada
University of Pisa, ESE Dept.
56122 Pisa, Italy

Ozlem Kilic
Catholic University of America
Washington, DC 20064, USA

Erdem Topsakal
Mississippi State University, EE Dept.
Mississippi State, MS 39762, USA

Alistair Duffy
De Montfort University
Leicester, UK

Fan Yang
Tsinghua University, EE Dept.
Beijing 100084, China

Rocco Rizzo
University of Pisa
56123 Pisa, Italy

Atif Shamim
King Abdullah University of Science and
Technology (KAUST)
Thuwal 23955, Saudi Arabia

William O'Keefe Coburn
US Army Research Laboratory
Adelphi, MD 20783, USA

Mohammed Hadi
Kuwait University, EE Dept.
Safat, Kuwait

Amedeo Capozzoli
Univerita di Naoli Federico II, DIETI
I-80125 Napoli, Italy

Maokun Li
Tsinghua University
Beijing 100084, China

Lijun Jiang
University of Hong Kong, EEE Dept.
Hong, Kong

Shinishiro Ohnuki
Nihon University
Tokyo, Japan

Kubilay Sertel
The Ohio State University
Columbus, OH 43210, USA

Salvatore Campione
Sandia National Laboratories
Albuquerque, NM 87185, USA

Toni Bjorninen
Tampere University
Tampere, 33100, Finland

Paolo Mezzanotte
University of Perugia
I-06125 Perugia, Italy

Yu Mao Wu
Fudan University
Shanghai 200433, China

Amin Kargar Behbahani
Florida International University
Miami, FL 33174, USA

Laila Marzall
University of Colorado, Boulder
Boulder, CO 80309, USA

Qiang Ren
Beihang University
Beijing 100191, China

EMERITUS EDITORIAL ASSISTANTS

Khaleb ElMaghoub
Trimble Navigation/MIT
Boston, MA 02125, USA

Kyle Patel
Colorado School of Mines, EE Dept.
Golden, CO 80401, USA

Christina Bonnigton
University of Mississippi, EE Dept.
University, MS 38677, USA

Anne Graham
University of Mississippi, EE Dept.
University, MS 38677, USA

Madison Lee
Colorado School of Mines, EE Dept.
Golen, CO 80401, USA

Allison Tanner
Colorado School of Mines, EE Dept.
Golden, CO 80401, USA

Mohamed Al Sharkawy
Arab Academby for Science and Technology, ECE Dept.
Alexandria, Egypt

MARCH 2026 REVIEWERS

Jogesh Chandra Dash
Ping Du
Junbing Duan
Giacomo Giannetti
Lu Guo
Mikko Kokkonen
BEHIH Mohamed
Beulah Jabaseeli N
Michel M. Ney
Mahdi Oliaei
Ananya Parameswaran
Andrew Peterson
Giuseppe Pettanice
Shi Pu
Natarajamani S
Ehsan Akbari Sekehravani
Partha Shome
Marsellas Waller
Yi Wang

THE APPLIED COMPUTATIONAL ELECTROMAGNETICS SOCIETY JOURNAL

Vol. 41 No. 03 March 2026

TABLE OF CONTENTS

Women's History Month Special Article: Interview with Professor Natalia Nikolova
Sima Noghanian 203

A Full-Wave Method for Radar Cross-Section Analysis with Locally Generated Structured Electromagnetic Waves
Matthew J. Dodd, Kobe Prior, Joseph E. Diener, Veysel Demir, and Atef Z. Elsherbeni . . 207

A PEC Conformal FDTD Algorithm with Distorted Grid Face Filtering for Enhanced Efficiency
Chenshu Liu, Kaihang Fan, and Juan Chen 216

Modeling of Thin Shielding Layer Based on Unstructured Grid Vector Finite Element Method and Analysis of its Effect on SQUID TEM Observation Signal
Binyuan Ma, Nansong Chang, Yanju Ji, Xuejiao Zhao, and Hui Luan 225

A High-Precision Beamforming Reflectarray Using an Improved Hybrid PSO-GA Algorithm and Low-Coupling Element
Ren Jiawei and Li Zuowen 238

Electromagnetic Exposure to Child Passengers of Positioning Antennas for Autonomous Driving Electric Vehicles
Xuwei Dong, Yufei Ren, and Mai Lu 244

Inversion Method Based on CNN-BiLSTM-Attention for SQUID TEM Data with IP Effect
Yanju Ji, Jinxiu Yuan, Hui Luan, Yuan Wang, and Qiong Wu 258

Numerical Analysis on the Equivalent Physical Temperature Estimation for Pyramidal Microwave Calibration Targets Based on Infrared Imagery
Ming Jin, Jiacheng Qian, and Miaomiao Peng 271

An Endfire Array Antenna for Simultaneous Operation in C- and X-Bands
Z. N. Jiang, W. X. Gao, and C. Peng 281

Enhanced Compressive Sensing Method of Moments via Physics-Aware Characteristic Modes and LSQR Solver
Yang Liu, Zhonggen Wang, Wenyan Nie, and Longhui Sun 288

Women's History Month Special Article: Interview with Professor Natalia Nikolova

Sima Noghanian

Ruckus Networks
Sunnyvale, CA, USA
Sima_noghanian@ieee.org

Abstract – In recent years, *Applied Computational Electromagnetics Society (ACES) Journal* has highlighted the work of women in applied and computational electromagnetics. These articles aim not only to showcase the contributions of outstanding female researchers and educators but also to inspire young students and professionals as they pursue their careers in the field. This year, we were fortunate to learn from Professor Natalia Nikolova, who shared her insights about her professional journey, as well as her advice and guidance for the next generation of scientists and engineers.

Index Terms – Women in STEM, women in applied and computational electromagnetics, women in microwave and antennas.

I. INTRODUCTION

This year, I had the opportunity to interview Professor Natalia Nikolova, a highly respected educator, mentor, leader, and researcher. I have followed her work for many years and have learned tremendously from her lectures and scientific publications. Her contributions to the field and dedication to education have been a constant source of inspiration. Beyond her impressive expertise, Professor Nikolova stands out for her humility and approachability. Despite her accomplishments, she remains down-to-earth, friendly, and genuinely supportive of others, making her not only an outstanding scholar but also a remarkable role model.

Professor Nikolova (Fig. 1) is a professor in the Department of Electrical and Computer Engineering at McMaster University and has received numerous recognitions for her contributions to microwave imaging and computational electromagnetics [1]. She is a Fellow of the IEEE and the Canadian Academy of Engineering (Fig. 2), and she held the prestigious Canada Research Chair in High-Frequency Electromagnetics. Her work and leadership have been widely recognized through professional honors, invited lectures, and service to the international electromagnetics community. Professor Nikolova has built a strong record of teaching, mentorship, and research leadership.

Fig. 1. Professor Natalia K. Nikolova.

At McMaster University, she founded and leads the Electromagnetic Vision (EMVi) Laboratory, where her group develops advanced methods for microwave and millimeter-wave imaging, inverse scattering, and radar sensing. Her research includes pioneering contributions to microwave imaging and sensitivity analysis, developing computational techniques that reconstruct images from electromagnetic measurements and evaluate how variations in material properties or geometry affect system performance. These advances have important applications in medical diagnostics, security screening, and non-destructive evaluation. Prof. Nikolova has authored more than 310 refereed manuscripts, 7 book chapters, and 2 books, including the monograph "Introduction to Microwave Imaging" [2]. She has delivered 58 invited lectures, webinars, and short courses internationally on the subjects of microwave imaging and computer-aided electromagnetic analysis and design, including an inspiring lecture delivered at ACES EM School in February 2026.

Submitted On: November 17, 2026
Accepted On: November 18, 2026

https://doi.org/10.13052/2026.ACES.J.410301

Fig. 2. Professor Nikolova receiving her official certificate as a fellow of the Canadian Academy of Engineering.

II. QUESTIONS AND ANSWERS (Q & A)

Q1: Can you share a bit about your journey to becoming a professor? What was your motivation in your career path?

A1**:** As a student, I aspired to be a researcher and make discoveries, but being a professor was not my goal. As a post-doctoral fellow, however, I appreciated the academic freedom in research choices, the daily interaction with bright researchers and students in the university, and the feeling of accomplishment brought by teaching. The first exposure to teaching revealed that it requires as much focus, innovation, and creativity as research. I really enjoyed it, especially when I saw the spark of understanding and excitement in the eyes of the students. So, when an opportunity presented itself at McMaster University, I took it.

Q2: What initially sparked your interest in engineering, and how did you decide to specialize in electromagnetics (EM)?

A2**:** My career path was strongly influenced by my years as an undergraduate student in the Radio Engineering Department at the Technical University of Varna, Bulgaria, which, at the time, boasted the best antenna and microwave labs in the country. Seeing the antennas and the test instrumentation in action, along with a design project on a low-noise amplifier using the first microwave circuit simulator PUFF, made me an EM enthusiast. During my Ph.D. studies at the University of Electro-Communications, Tokyo, Japan (Fig. 3), I focused on time-domain full-wave simulations under the guidance of Prof. Eikichi Yamashita, one of Japan's renowned pioneers in computational electromagnetics. On a more fundamental level, my career path has been driven by curiosity about how electromagnetism shapes nature and how we harness it.

Fig. 3. Professor Nikolova receiving her Ph.D. degree certificate at the graduation ceremony in 1997.

Q3: Could you describe your experience going from B.Sc. degree to a graduate degree and then a post-doctoral fellowship? I understand you did your B.Sc. in Bulgaria, your graduate degree in Japan, and your post-doctoral fellowship in Canada. How did the study and research in different countries and cultures influence you, your approach to solving difficult problems, and your points of view?

A3: I had the exceptional opportunity to pursue my Ph.D. studies in Japan thanks to a scholarship from the Japanese government (the Monbusho scholarship). I remember well my first days in Tokyo, when I was dazzled by the highly technological and orderly society that made the crowded multi-million city function like a clockwork. The Japanese people and culture had a marked influence on me. In their reserved but kind and calm ways, they taught me patience, persistence, time management, and punctuality, and the importance of paying attention to detail (Fig. 4). To this day, it is these qualities that I find essential in solving difficult problems.

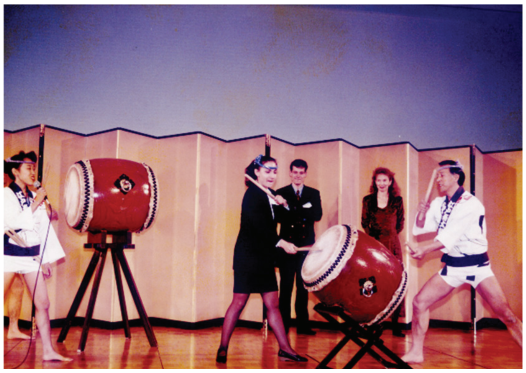

Fig. 4. Professor Nikolov called on stage to perform at the Taiko Ceremony, held during the IEEE APMC 1996 conference.

On to Canada, where I met the kindest people and where I found my final career destination. In Canada, innovation and creativity are strongly encouraged, which directed my research into topics such as high-frequency electromagnetic sensitivity analysis and microwave imaging, which, at the time, were emerging and not well-understood topics.

Q4: Did you have a mentor who influenced your career path? How do you think mentorship impacts students' and young professionals' success?

A4: Both my Ph.D. and post-doctoral supervisors influenced my career path. They have influenced my choices of research topics as well as activities within professional societies such as the IEEE and ACES. The mentorship of my post-doctoral supervisor, Prof. John Bandler, was the most long-lasting as he was also a collaborator for over a decade in the research for efficient sensitivity analysis methods. Prof. Bandler (Fig. 5) was a strong proponent of women in the engineering profession. His encouragement and support helped me and numerous other female professionals pursue successful academic and industrial R&D careers. I think that mentorship is one of the most effective ways of setting young professionals on a path to success.

Fig. 5. Professor Nikolova with the late Prof. John Bandler and her students, celebrating the new year.

Q5: Why do you believe it is crucial to have female role models in electromagnetics and engineering in general?

A5: Of course, female role models show that a successful career is possible in these demanding, male-dominated fields. Importantly, female senior researchers and academics also enable networking, mentorship, and support of female junior researchers in their career advancement. This latter role is crucial for expanding the presence of young female professionals in our fields (Fig. 5).

Q6: What are some of the biggest challenges women face in this field, and how can academia and/or industry better support diversity?

A6: The challenges that women in this field face likely depend on the region and the institution where they practice their profession. Discrimination and prejudice against female engineers seem to be on the decline worldwide, but the problem still exists. The technical qualifications and capabilities of female engineers may be unreasonably scrutinized, whereas those of their male counterparts are not. This puts much pressure on female engineers to prove themselves over and beyond the norm. In my experience, this is less of a problem in academia compared to industry. But another major challenge comes from balancing work and family. It is this challenge, in my opinion, that inhibits gender diversity in the demanding engineering professions. How can academia and industry address this? This is a difficult and long-standing question. In my opinion, there must be accommodation across all genders, to allow for work-life balance, as well as on-site facilities for childcare and health care in the case of larger organizations. But society and governments must also recognize the importance of such accommodations and give incentives to employers to implement them.

Q7: Can you share a particularly memorable moment from your teaching or research that reinforced your passion for academia?

A7: There are two "eureka" moments in my research that are indeed memorable. One is the derivation of the analytical response-sensitivity formula for scattering parameters. The second is the discovery of a new inverse-scattering formula, which led to a significant improvement of our microwave imaging reconstruction with the scattered-power mapping method. But my passion for academia is most strongly reinforced by the enthusiastic feedback from my undergraduate students in the electromagnetics courses and the antenna/microwave course. I feel that my biggest career accomplishment is getting my students excited about electromagnetics, microwave, and antenna engineering, and seeing them continue to graduate school to pursue advancement in this field.

Q8: What excites you the most about research in applied and computational EM? Are there any emerging trends that you find particularly promising? What do you see as the short- and long-term future for the applied or computational electromagnetics?

A8: Applied and computational EM is an intersection of engineering, mathematical physics, and applied mathematics. It is this interdisciplinarity that is exciting.

One interesting trend for me is the rise of fast radar simulators that can emulate a true real-time imaging scenario, such as the imaging of a walking person, or that of an imaging radar mounted on a UAV. Another exciting trend is the development of novel fast image-reconstruction algorithms along with the fully electronic microwave and millimeter-wave imagers.

Q9: You are renowned for your work in microwave imaging, including cancer imaging. What motivated you to advance the research in this field?

A9: I am a believer in microwave technology as an alternative medical imaging modality, despite the numerous challenges it still faces. My microwave-imaging research was originally in the general field of inverse scattering and real-time image reconstruction with synthetic aperture radar. I took on the challenge of breast-cancer diagnostics because current screening methods are less effective than what is needed for early-stage treatment. I also believe that the success of this technology hinges on innovation in hardware, which is a very interesting and engaging engineering research.

Q10: How can one person be better at leadership in her field?

A10: Leadership begins with compassion, commitment to help others, and listening to your team and colleagues. Then comes the vision, the judgment of methods and opportunities, and the hard work.

Q11: What advice would you give to students and young professionals who are interested in pursuing careers in applied and computational electromagnetics?

A11: Think out of the box! There are always emerging new technologies (THz, sensing and imaging) and new materials (organics, semiconductors and plasmas), and so there is always a need for new EM and multi-physics analytical models and simulation tools.

REFERENCES

[1] Research Spotlight |Dr. Natalia Nikolova - Electrical & Computer Engineering, available online: https://www.youtube.com/watch?v=dq_lxAEbd28.

[2] N. K. Nikolova, *Introduction to Microwave Imaging*. Cambridge, U.K.: Cambridge University Press, 2017. doi:10.1017/9781316084267.

Sima Noghanian is the chair of the ACES Communication and Membership Committee and serves as the vice president of ACES in 2026. She received a B.Sc. degree in electrical engineering from the Sharif University of Technology, Tehran, Iran, and an M.Sc. and Ph.D. degrees, both in electrical engineering, from the University of Manitoba, Winnipeg, Canada. She is currently a Distinguished Hardware Engineer at Ruckus Networks. Her research interests include MIMO antennas for wireless communications, wearable and implanted antennas, 3D printed antennas, wireless power transfer, microwave imaging, and wireless channel modeling.

A Full-Wave Method for Radar Cross-Section Analysis with Locally Generated Structured Electromagnetic Waves

Matthew J. Dodd[1], Kobe Prior[1], Joseph E. Diener[1],
Veysel Demir[2], and Atef Z. Elsherbeni[1]

[1]Department of Electrical Engineering
Colorado School of Mines, Golden, CO 80401, USA
mdodd@mines.edu, kdprior@mines.edu, jdiener@mines.edu,
aelsherb@mines.edu

[2]Department of Electrical Engineering
Northern Illinois University, DeKalb, IL 60115, USA
vdemir@niu.edu

Abstract – This work presents a full-wave numerical method for simulating the radar cross-section (RCS) of targets illuminated by structured electromagnetic waves generated by physically realizable sources embedded within the simulation domain. The proposed framework enables RCS prediction using practical excitation mechanisms, such as antenna arrays, rather than idealized incident fields. To demonstrate the approach, we compute the RCS of several canonical targets under illumination by an orbital angular momentum (OAM) vortex wave produced by a uniform circular array (UCA) of dipole antennas. The simulated results reveal distinctive scattering behaviors and increased RCS diversity associated with OAM-based structured wave excitation. The methodology establishes a foundation for future studies of target scattering under a broad range of structured electromagnetic fields and source configurations.

Index Terms – Radar cross-sections, microwave orbital angular momentum, finite difference time domain (FDTD), method of moments (MoM).

I. INTRODUCTION

Structured electromagnetic waves constitute a class of field distributions characterized by spatially varying phase and amplitude profiles in the far field. Common examples include Laguerre-Gaussian (LG) and Hermite-Gaussian (HG) modes, which exhibit nontrivial wavefront structures and unique propagation characteristics. In this work, we focus on structured waves carrying orbital angular momentum (OAM), often referred to as vortex beams. The electric field of an OAM mode can be expressed as

$$E(x,y,z) = E_0(x,y,z)e^{-jkz}e^{j\ell \tan^{-1}(y/x)}, \qquad (1)$$

where $\ell \in \mathbb{Z}$ is the azimuthal mode index and $k = \frac{2\pi}{\lambda}$ is the wavenumber.

A number of prior studies have investigated the radar cross-section (RCS) diversity associated with OAM-wave illumination. Physical optics (PO)-based techniques have been widely used to model scattering from electrically large objects under OAM excitation [1–6], and several experimental measurements of OAMinduced RCS variations have been reported for canonical and complex targets [1, 7–9]. Additional studies have examined reflection and refraction of OAM waves from dielectric and perfectly conducting slabs [10]. While PO methods offer computational efficiency for large scatterers, they inherently neglect important mechanisms such as edge diffraction, creeping waves, and higher-order interactions

Full-wave electromagnetic techniques-including the method of moments (MoM) and the finitedifference time-domain (FDTD) method-provide a more rigorous alternative, yielding accurate scattered fields for objects of arbitrary size and geometry. Prior full-wave studies involving OAM illumination have typically injected vortex beams using analytical field expressions prescribed at a domain boundary or source plane [11, 12]. Mie theory has also been used to analyze LG-mode scattering from spherical objects [13]. In [14], OAM excitation generated by idealized Hertzian dipoles was examined within a PO framework for PEC targets.

In contrast to these approaches, this work develops a full-wave simulation methodology in which the structured wave is generated by a physical source located inside the simulation domain. Specifically, we model an OAM beam produced by a uniform circular array (UCA) of dipole antennas, where each element is excited with a phase proportional to its azimuthal position

Submitted On: December 23, 2025
Accepted On: April 01, 2026

https://doi.org/10.13052/2026.ACES.J.410302

$\phi = \tan^{-1}\frac{y}{x}$ of the array elements consistent with (1). This approach enables realistic modeling of structured-wave illumination from practical antenna architecture. Because the UCA radiates directly into the far field, the total computed fields contain contributions from both the source and the target scatterer. To analyze the RCS, we therefore introduce a systematic procedure for separating the scattered field from the directly radiated field. Another challenge arises in defining RCS for structured waves. Traditional RCS definitions assume plane-wave illumination with uniform incident power density (S_{inc}). Structured waves violate this assumption due to their inherently nonuniform spatial distributions. Accordingly, we adopt the generalized RCS definition

$$RCS(\theta,\phi) = \lim_{R\to\infty} \frac{4\pi A R^2 S_{scat}}{P_{inc}}, \tag{2}$$

where $\frac{P_{inc}}{A}$ is the average incident power density computed over a designated capture plane of area A. This formulation enables consistent comparison between scattering under OAM illumination and traditional plane-wave excitation, similar to the normalization approach in [12]. It is important to note that the RCS is, in general, a function of the transmit and received polarization. The received polarization components are referred to by spherical coordinate unit vectors RCS_θ and RCS_ϕ, or the total $RCS_{tot} = RCS_\theta + RCS_\phi$. The results m presented are for an incident polarization in the +y direction (ϕ-component in YZ plane).

The remainder of this paper is organized as follows. Section II presents the methodology for generating OAM excitation using an embedded antenna array and for isolating the scattered field in full-wave simulations. Section III provides numerical results illustrating the RCS of canonical PEC objects under OAM illumination. Conclusions and potential extensions to other structured-wave sources are discussed in section IV.

II. METHOD

In full-wave electromagnetic simulations, the radiated far fields are computed from the currents induced by the excitation sources. In FDTD simulations, these far fields are obtained from the simulated near fields via the surface equivalence theorem [15]. A fictitious closed surface is placed around the radiating and scattering structures, and equivalent electric and magnetic surface currents representing the radiated fields are given by

$$\vec{J}_s = \hat{n} \times \vec{H}, \tag{3}$$

$$\vec{M}_s = -\hat{n} \times \vec{E}, \tag{4}$$

where $\vec{H}$ are the magnetic fields on the surface, $\vec{E}$ are the electric fields, and $\hat{n}$ is the unit normal vector to the surface.

When both antennas and scatterers are present inside the same computational domain, the equivalent surface currents naturally contain contributions from both the antenna radiation and the object's scattered response. To isolate the scattered fields, we introduce a two-step simulation procedure, illustrated in Fig. 1.

1. **Step 1:** Simulate the full configuration containing the antenna array and the scatterer. Extract the total fictitious currents $(J_{s,total}, M_{s,total})$.
2. **Step 2:** Remove the scatterer and repeat the simulation using the same excitation. The resulting fictitious currents $(J_{s,incident}, M_{s,incident})$ represent the incident fields due solely to the antenna. A fluxcapture plane of area A, aligned with the projected area of the scatterer, is used to compute the average incident power density $\frac{P_{inc}}{A}$ which is required to normalize the RCS.

The scattered-field equivalent currents are then obtained by subtraction:

$$J_{s,scattered} = J_{s,total} - J_{s,incident}, \tag{5}$$

$$M_{s,scattered} = M_{s,total} - M_{s,incident}. \tag{6}$$

The scattered far fields are computed using the standard radiation integrals with vector potentials [15]:

$$\vec{N} = \int_S \vec{J}_S e^{-jkr'\cos\psi} dS', \tag{7}$$

$$\vec{L} = \int_S \vec{M}_S e^{-jkr'\cos\psi} dS'. \tag{8}$$

Substituting the resulting scattered fields into the generalized RCS definition in (2) yields the desired bistatic RCS. The two RCS polarization components are

$$RCS_\theta(\theta,\phi) = \frac{Ak^2}{8\pi\eta_0 P_{inc}} \left|\vec{L}_\theta + \eta_0 \vec{N}_\theta\right|^2, \tag{9}$$

$$RCS_\phi(\theta,\phi) = \frac{Ak^2}{8\pi\eta_0 P_{inc}} \left|\vec{L}_\phi + \eta_0 \vec{N}_\phi\right|^2, \tag{10}$$

where $k = \frac{2\pi}{\lambda}$ is the wavenumber and η_0 is the free space impedance.

Throughout this work, we report the bistatic RCS for the case where the incident beam propagates along the +z direction with back and forward scattering directions correspond to $\theta = 180^\circ$ and $\theta = 0^\circ$, respectively. This coordinate convention is the spherical coordinate system for antenna far field patterns. The observation direction $\vec{r}$, has an elevation angle θ that is measured from the +z axis and an azimuth angle ϕ that is measured from the +x axis as shown in Fig. 2.

Both the MoM framework of [16] and the FDTD solver of [17] are used. In MoM, the equivalent twostep subtraction process is applied in the far field rather than

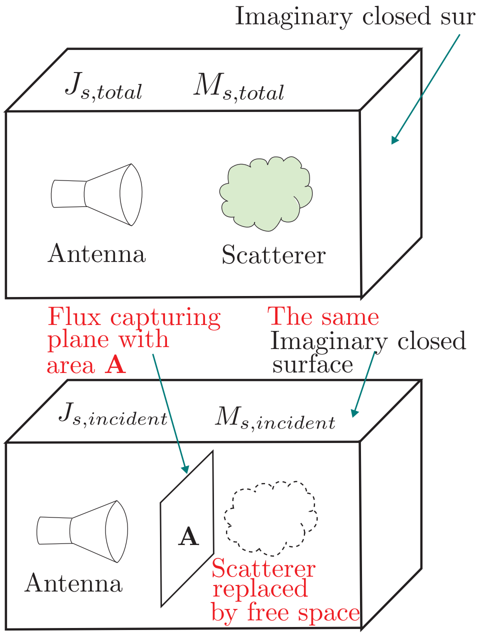

Fig. 1. (Top) The first simulation step in the process contains both the local sources and the scatterer inside an imaginary closed surface. (Bottom) The second step removes the scatterer from the domain and includes a flux capture plane for incident power on the scatterer.

at the equivalent surface, i.e. $E_{scattered} = E_{total} - E_{incident}$ which requires twice the number of far-field evaluations but is otherwise equivalent.

III. RESULTS

To validate the local-source RCS methodology, we first analyze a configuration where the scatterer is placed in the far field of a half-wavelength dipole antenna. At sufficiently large distance, the dipole radiation approximates a plane wave, enabling comparison with standard plane-wave RCS results obtained from full-wave simulations. Simulations are performed for both a PEC sphere and a PEC square plate at 8.75 GHz.

The far-field distance is computed as

$$z_{ff} = \frac{2D^2}{\lambda}, \tag{11}$$

where D is the diameter of the radiating structure. For the validation study, the PEC sphere with diameter equal to λ is placed at a distance 60 times z_{ff} to ensure an excellent plane-wave approximation (Fig. 2). The RCS results appear in Fig. 3 and show excellent agreement between the local-source method and the conventional plane-wave RCS.

A similar comparison is made for the PEC plate shown in Fig. 4. Again, the RCS computed using the proposed two-step method matches the plane-wave RCS exactly as seen in Fig. 5, confirming the correctness of the field-separation procedure.

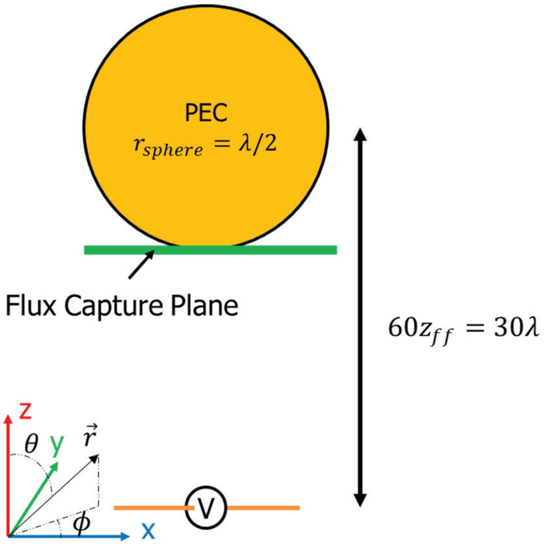

Fig. 2. Simulation scenario to approximate a linearly polarized plane wave incident on a PEC sphere. The diameter of the sphere is one wavelength. The coordinate axis shows the spherical coordinate convention used to define the observation angles θ and ϕ for an observation direction towards the vector $\vec{r}$. The origin of the coordinates system is physically located at the center of the dipole source; however, it is offset in the figure for clarity.

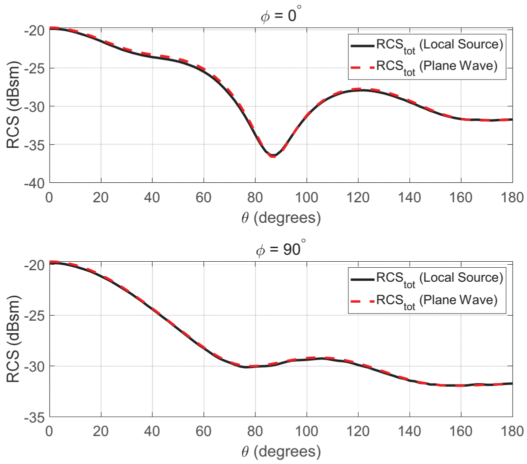

Fig. 3. RCS computed by the local source method for a PEC sphere compared to the traditional plane wave RCS.

A. PEC sphere RCS under OAM modes

We next examine RCS under OAM illumination. Structured waves are generated by a UCA of eight halfwavelength dipoles arranged with radius 17 mm

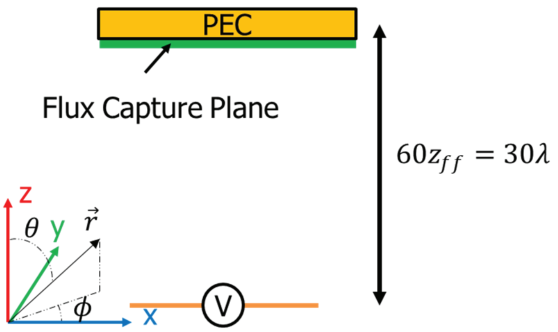

Fig. 4. Simulation scenario to approximate a linearly polarized plane wave incident on a PEC plate. The width and length of the plate in the x–y plane are one wavelength. The origin of the coordinates system is physically located at the center of the dipole source; however, it is offset in the figure for clarity.

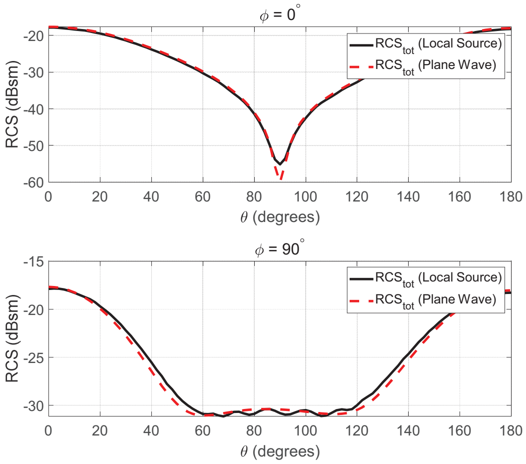

Fig. 5. RCS computed by the local source method for a PEC plate compared to the traditional plane wave RCS.

(approximately $\lambda/2$ at 8.75 GHz). The UCA is mounted 9 mm above a circular PEC reflector (radius 58.5 mm) to achieve unidirectional radiation (Fig. 6). Each OAM mode with index ℓ is synthesized by assigning element phases proportional to azimuthal angle as in (1).

Because OAM beams exhibit mode-dependent angular radiation maxima, the scatterer is repositioned for each mode so that it lies along the direction of maximum radiated power of the mode, ensuring consistent illumination across modes and accurate comparison with the plane wave RCS, as well as comparison between modes. Sample radiation patterns for modes $\ell = 0, 1$, and 2 are shown in Fig. 7.

Far field bistatic RCS patterns for the PEC sphere are shown in Fig. 8 for the elevation plane where $\phi = 90^\circ$ and compared with the other modes as well as a plane wave on the same axis. For all results in this section, both the θ - and ϕ-polarized components of the RCS are presented separately. These polarization components are aligned with the spherical coordinate unit vectors. In the cartesian YZ plane, where $\phi = 90^\circ$ or $\phi = 270^\circ$, the ϕ-polarization vector is pointing towards $-$x or $+$x direction respectively. The θ polarization vector is pointing towards $+$y when $\theta = 0^\circ$, is pointing towards $-$z when $\theta = 90^\circ$, and is pointing towards $-$y when $\theta = 180^\circ$. This description applies to all polarized RCS calculations presented here. In the $\ell = 0$ mode, the ϕ-polarized component is a very close approximation of a plane wave. It is notable that the ϕ polarized scattering component is higher magnitude for $\theta \approx 50^\circ$ and $\theta \approx 150^\circ$ for $\ell = 2$ and at $\theta \approx 180^\circ$ for $\ell = 3$ modes, indicating an RCS diversity for the higher order

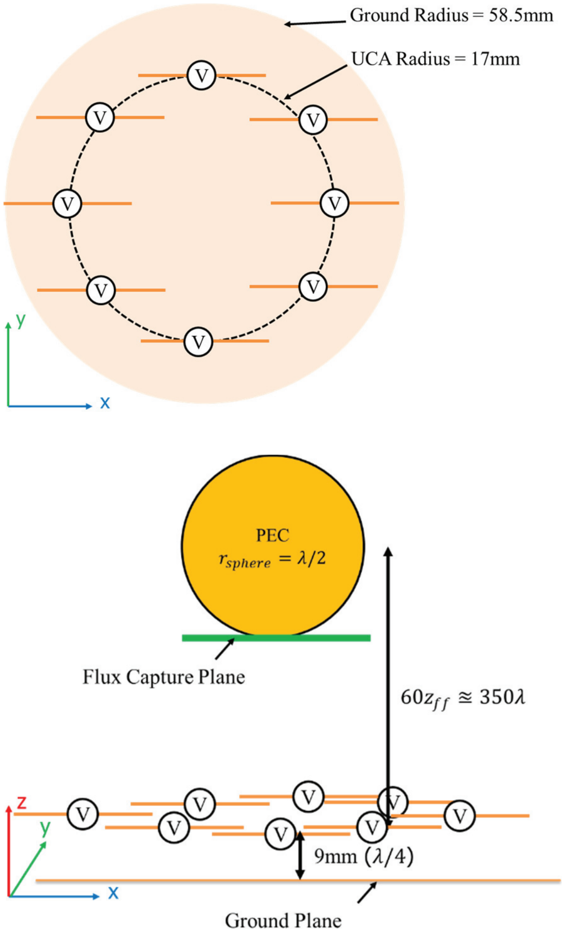

Fig. 6. Geometry of the UCA shown from a top-down view (top) and from a side on view (bottom). The UCA consists of eight half wavelength dipole elements arranged in a circle above a PEC ground plane acting as a reflector. All dipole antennas are at the same height from the ground reflector but shown here at different heights for clarity. The origin of the coordinates system is physically located at the center of the ground plane; however, it is offset in the figure for clarity.

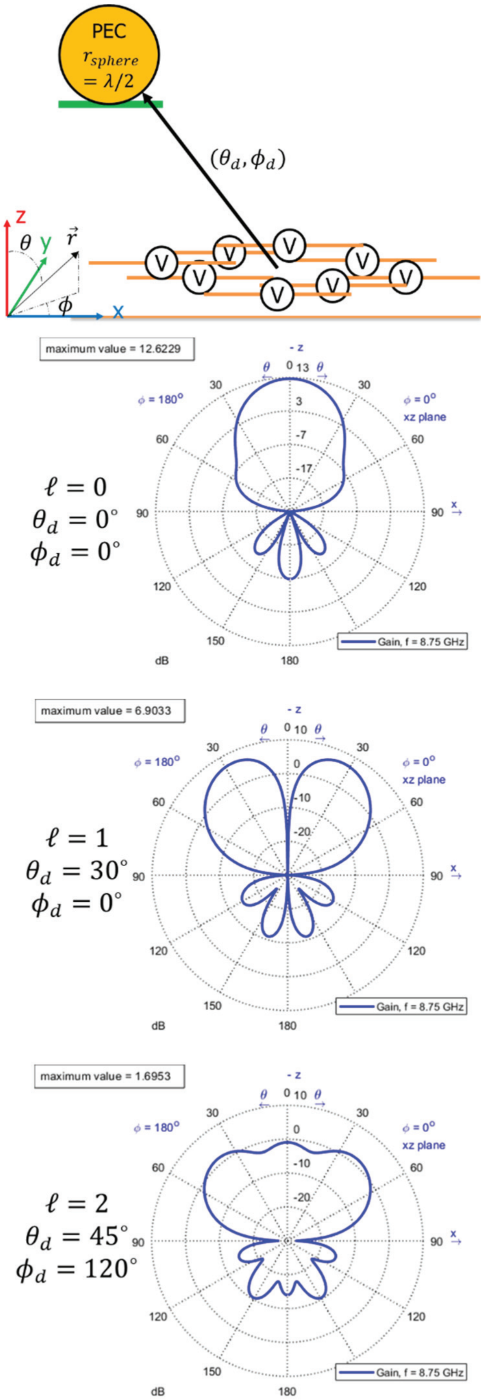

Fig. 7. Geometry of the scattering simulations, with the target object located in the direction of maximum radiation, (θ_d, ϕ_d) as shown (top). The far field radiation patterns of the UCA for modes $\ell = 0, 1,$ and 2 with annotations for the direction of maximum radiation identified. All dipole antennas are at the same height from the ground reflector but shown here at different heights for clarity. The origin of the coordinates system is physically located at the center of the ground plane; however, it is offset in the figure for clarity.

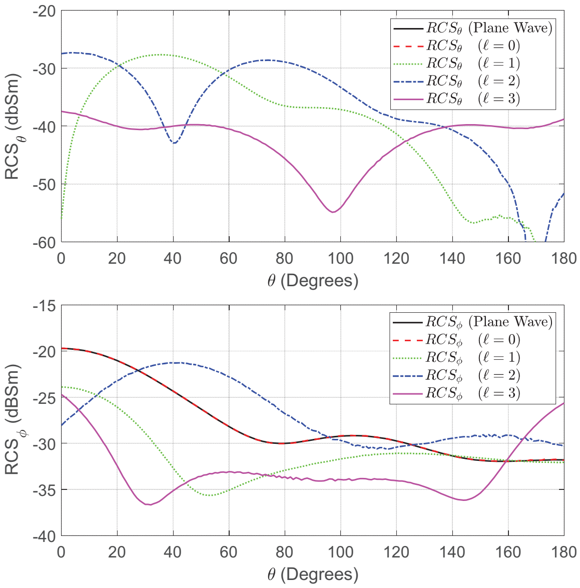

Fig. 8. The bistatic RCS of the PEC sphere for modes $\ell = 0, 1, 2, 3$ in the $\phi = 90°$ plane for the θ-polarized component (top) and ϕ-polarized component (bottom).

OAM mode illuminating beams even in the co-polarized scattered fields.

Another significant characteristic of the sphere scattering results is the significant increase in the cross polarized θ-component of the scattered fields for all modes $\ell > 0$. The cross polarized component is nonexistent in the plane wave and $\ell = 0$ modes, indicating a strong diversity induced by the OAM wave even for a rotationally symmetric scattering target such as the PEC sphere.

To further validate the method, scattered fields (not RCS) computed using MoM and FDTD are compared with the sphere moved to a distance of $z_{ff} \approx 210$ mm. The FDTD domain contains 64 million cells and is run for 15,000 steps; MoM requires only discretization of the sphere and antenna (2362 edges). The normalized scattered fields for $\ell = 1, 2$ are shown in Fig. 9 and exhibit good agreement. Small deviations occur primarily in cross-polarized components where field magnitudes are low and numerical precision is limited. When computing simulations for a single frequency with only PEC objects in the domain, the MoM is typically more efficient. However, many applications will require dielectric objects and wideband frequency simulation which reduces the efficiency of the MoM solution. In these applications, the FDTD computation is more efficient.

B. PEC plate RCS under OAM modes

The next canonical object used as a scattering target is the PEC plate. The PEC plate has a square

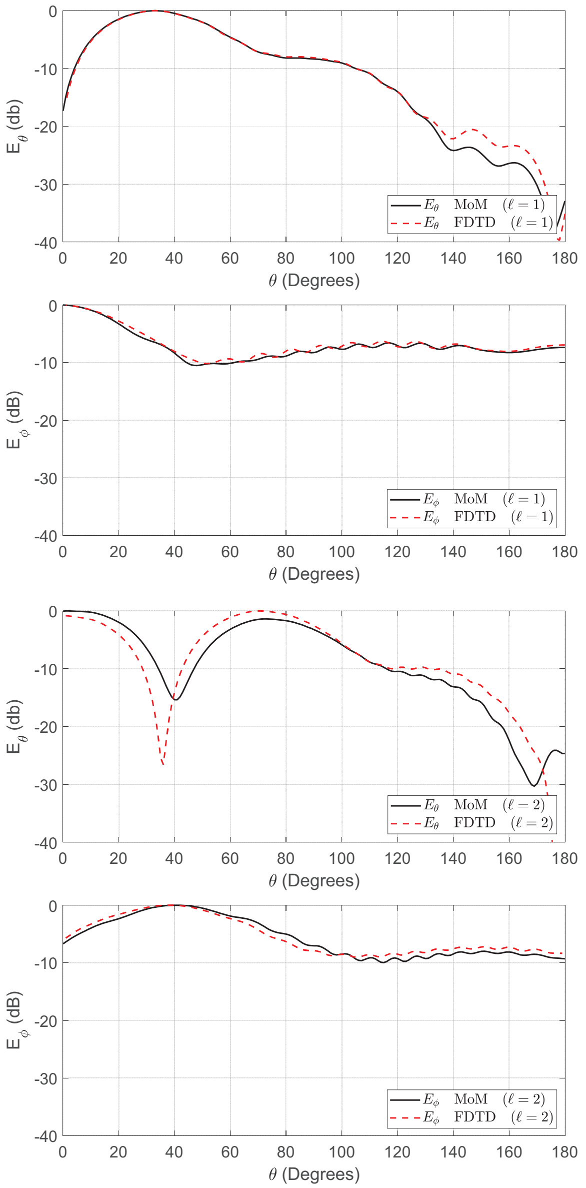

Fig. 9. Normalized scattered field comparison for a PEC sphere between MoM and FDTD simulation methods. The results for $\ell = 1$ are shown for the θ polarized (top) and ϕ-polarized (second from top) components of the scattered electric field. The same results for $\ell = 2$ are shown for the θ-polarized (third from top) and ϕ-polarized (bottom) components.

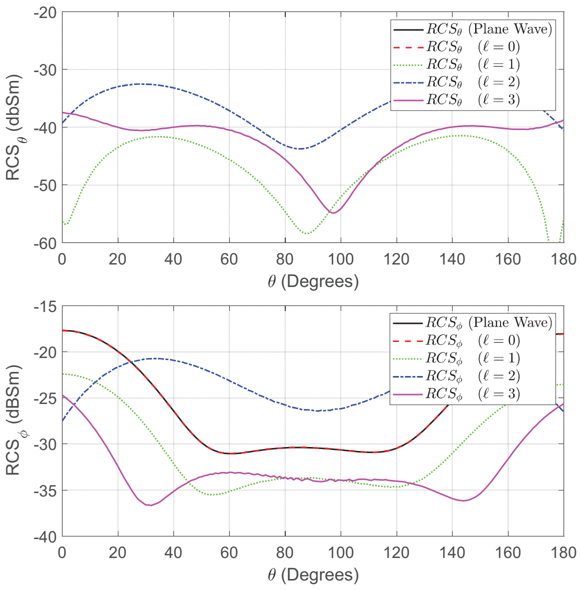

Fig. 10. The bistatic RCS of the PEC plate for modes $\ell = 0, 1, 2, 3$ in the $\phi = 90°$ plane. The θ-polarized component (top) and the ϕ-polarized component (bottom).

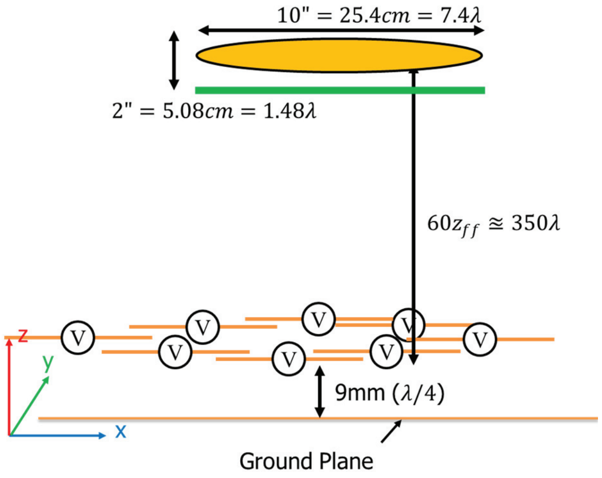

Fig. 11. The PEC ogive is placed at 60 times the farfield distance above the UCA. The dimensions of the ogive are defined according to the standardized model used in RCS literature [18]. The origin of the coordinates system is physically located at the center of the ground plane; however, it is offset in the figure for clarity.

cross-section with length and width equal to one wavelength at 8.75 GHz. The same simulation configurations that were used for the PEC sphere are repeated for the PEC plate. The RCS results are presented in Fig. 10 in the $\phi = 90°$ plane. The PEC plate RCS values are improved for the $\ell = 2$ mode for the co-polarized ϕ-component while other modes follow a similar pattern to the plane wave but are lower in magnitude. As with the sphere, significant increases appear in the cross-polarized θ-component for all $\ell > 0$, again demonstrating OAM-induced polarization conversion.

C. PEC ogive RCS under OAM modes

The ogive is a commonly used object for RCS studies with standardized dimensions [18]. The simulation

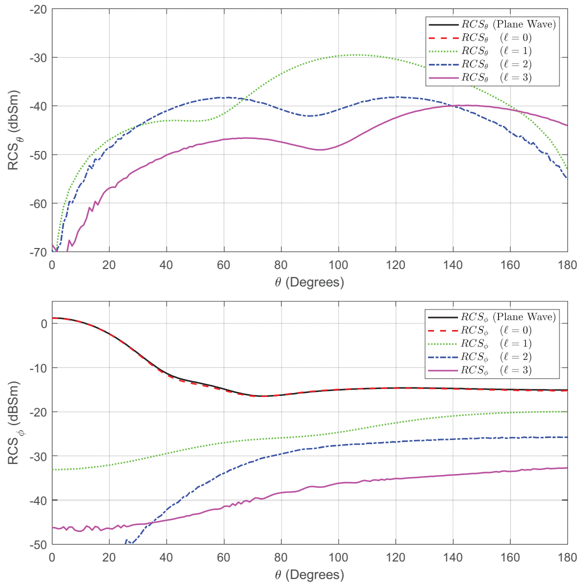

Fig. 12. The bistatic RCS of the PEC ogive is calculated for modes $\ell = 0, 1, 2, 3$. The $\phi = 90°$ plane is compared between modes and to a plane wave for the θ-polarized component (top) and ϕ-polarized component (bottom).

configuration is shown for a PEC ogive in Fig. 11. The corresponding RCS results are shown in Fig. 12 indicating that, unlike the sphere and plate, the ogive does not exhibit increased co-polarized scattering for OAM modes. However, a substantial increase in the cross-polarized component is again observed for all $\ell > 0$ modes, suggesting that OAM-induced polarization conversion persists across geometrically distinct canonical scatterers.

IV. CONCLUSION

This work presents a general method for computing the scattered fields and radar cross-section of objects illuminated by structured electromagnetic waves generated by sources embedded within the simulation domain. This method is applicable to both FDTD and MoM solvers and provides a practical two-step procedure for isolating scattered fields from direct antenna radiation.

The approach is validated by comparing localsource RCS results with traditional plane-wave RCS for canonical PEC targets, showing excellent agreement. We then apply the method to OAM illumination produced by a realistic uniform circular dipole array. Across a range of canonical objects including a sphere, plate, and ogive we observe significant increases in cross-polarized scattering for OAM modes $\ell > 0$ relative to plane waves. In some cases, increases in copolarized side-scattering are also observed.

These results demonstrate the RCS diversity achievable through structured-wave excitation and illustrate the capability of the proposed method to simulate realistic OAM sources. The framework provides a foundation for future work involving more general structured-wave excitations, complex scatterers, and advanced antenna architectures.

ACKNOWLEDGMENT

This work is sponsored by the Defense Advanced Research Projects Agency (DARPA) under Agreement No. HR00112590137.

REFERENCES

[1] Z. Wu, T. Qu, J. Wu, Z. Wu, L. Yang, and X. Li, “Scattering of electromagnetic waves with orbital angular momentum on metallic sphere,” *IEEE Antennas Wirel. Propag. Lett.*, vol. 19, no. 8, pp. 1365–1369, Aug. 2020.

[2] M. Sun, S. Liu, L. Guo, and W. Pan, “Scattering of arbitrarily incident Laguerre–Gaussian vortex electromagnetic beams by electrically large-scaled complex targets,” *JOSA A*, vol. 40, no. 3, pp. 502–509, Mar. 2023.

[3] K. Liu, Y. Gao, X. Li, and Y. Cheng, “Target scattering characteristics for OAM-based radar,” *AIP Adv.*, vol. 8, no. 2, p. 025002, Feb. 2018.

[4] Z. Wu, J. Wu, H. Li, T. Qu, X. Meng, Q. Xu, Z. Wu, J. Bai, L. Yang, L. Gong, and Y. Yun, “Integrated physical optics for calculating electric-large metallic sphere scattering irradiated by vortex wave in microwave frequency band,” *IEEE Antennas Wirel. Propag. Lett.*, vol. 21, no. 6, pp. 1288-1292, June 2022.

[5] M. Arfan, A. Ghaffar, M. A. S. Alkanhal, M. Y. Naz, A. H. Alqahtani, and Y. Khan, “Orbital angular momentum wave scattering from perfect electromagnetic conductor (PEMC) sphere,” *Optik*, vol. 253, p. 168562, Mar. 2022.

[6] Z. Wu, J. Wu, T. Qu, Z. Wu, Q. Xu, H. Li, L. Yang, X. Meng, and J. Bai, “Scattering characteristics of an electrically-large aircraft object illuminated by Bessel vortex beams,” *IEEE Access*, vol. 10, pp. 126023–126029, 2022.

[7] X. Bu, X. Liang, Z. Zhang, L. Chen, H. Tang, and Z. Zeng, “Scattering characteristics of vortex electromagnetic waves for a wedge,” in *2018 Progress in Electromagnetics Research Symposium (PIERS-Toyama)*, pp. 801–804, Aug. 2018.

[8] C. Zhang, D. Chen, and X. Jiang, “RCS diversity of electromagnetic wave carrying orbital angular momentum,” *Sci. Rep.*, vol. 7, no. 1, p. 15412, Nov. 2017.

[9] X. Bu, Z. Zhang, X. Liang, Z. Zeng, L. Chen, and H. Tang, “Scattering characteristics of vortex electromagnetic waves for typical targets,” in

2018 Asia-Pacific Microwave Conference (APMC), pp. 648–650, Nov. 2018.

[10] Y. Yao, X. Liang, M. Zhu, W. Zhu, J. Geng, and R. Jin, “Analysis and experiments on reflection and refraction of orbital angular momentum waves,” *IEEE Trans. Antennas Propag.*, vol. 67, no. 4, pp. 2085–2094, Apr. 2019.

[11] W. Hanfei, Y. Xiaoli, Z. Zhaoyuan, and W. Xinhong, “Study on single particle scattering characteristics of OAM light based on finite-difference time-domain method,” in *2023 IEEE 6th International Conference on Electronics and Communication Engineering (ICECE)*, pp. 44–48, Dec. 2023.

[12] W. Sun, Y. Hu, C. Weimer, K. Ayers, R. R. Baize, and T. Lee, “A FDTD solution of scattering of laser beam with orbital angular momentum by dielectric particles: Far-field characteristics,” *J. Quant. Spectrosc. Radiat. Transf.*, vol. 188, pp. 200–213, Feb. 2017.

[13] X. Zambrana-Puyalto and G. Molina-Terriza, “The role of the angular momentum of light in Mie scattering. Excitation of dielectric spheres with Laguerre–Gaussian modes,” *J. Quant. Spectrosc. Radiat. Transf.*, vol. 126, pp. 50–55, Sep. 2013.

[14] K. Liu, H. Liu, W. E. I. Sha, Y. Cheng, and H. Wang, “Backward scattering of electrically large standard objects illuminated by OAM beams,” *IEEE Antennas Wirel. Propag. Lett.*, vol. 19, no. 7, pp. 1167–1171, July 2020.

[15] A. Z. Elsherbeni and V. Demir, *The Finite-Difference Time-Domain Method for Electromagnetics with Matlab Simulations*, 3rd ed. Edison, NJ: SciTech Publishing Inc. an Imprint of the IET, 2016.

[16] FEKO. Altair Engineering, Inc. Available: www.altair.com/feko.

[17] V. Demir and A. Z. Elsherbeni. (Aug. 2022). Computational Electromagnetics Simulator (CEMS) [Online]. Available: veysdemir@gmail.com.

[18] A. C. Woo, H. T. G. Wang, M. J. Schuh, and M. L. Sanders, “EM programmer’s notebook-benchmark radar targets for the validation of computational electromagnetics programs,” *IEEE Antennas Propag. Mag.*, vol. 35, no. 1, pp. 84–89, Feb. 1993.

Matthew J. Dodd received his B.S. degree in Materials Science and Engineering from UWMadison, Madison, WI, USA, in 2018. He received his M.S. degree in Electrical Engineering from Colorado School of Mines, Golden, CO, in 2024 and is currently pursuing the Ph.D. in Electrical Engineering under Atef Elsherbeni. His research interests include optimization methods for electromagnetics, metamaterials, and phased array antennas.

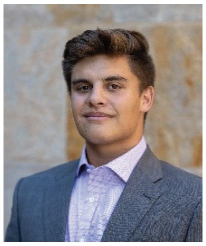

Kobe Prior is pursuing the combined B.S. and M.S. degrees from Colorado School of Mines, Golden, CO, USA. His main research interests are antenna design, computational electromagnetics, structured electromagnetic waves, including orbital angular momentum (OAM) modes, phased array synthesis, and experimental characterization of scattering phenomena.

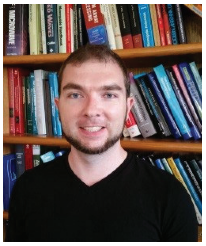

Joseph E. Diener obtained his M.S. degree in Electrical Engineering at Colorado School of Mines, Golden, CO, USA, and is currently pursuing his Ph.D. in Electrical Engineering under Atef Elsherbeni. His research interests include FDTD methods, GPU acceleration, genetic algorithms, antennas, active and passive circuits, and phased array systems.

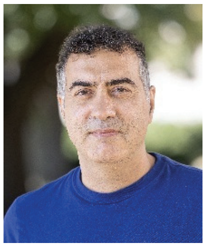

Veysel Demir is an Associate Professor at the Department of Electrical Engineering at Northern Illinois University, USA. He received his Bachelor of Science degree in Electrical Engineering from Middle East Technical University, Ankara, Turkey, in 1997. He studied at Syracuse University, New York, where he received both a Master of Science and Doctor of Philosophy degrees in Electrical Engineering in 2002 and 2004, respectively. During his graduate studies, he worked as a Research Assistant for Sonnet Software, Inc., Liverpool, New York. He worked as a visiting Research Scholar in the Department of Electrical Engineering at the University of Mississippi from 2004 to 2007. He joined Northern Illinois University in August 2007 and served as an Assistant Professor until August 2014. He has been serving as an Associate Professor since then.

Atef Z. Elsherbeni received his Ph.D. degree in Electrical Engineering from Manitoba University, Winnipeg, Manitoba, Canada, in 1987. He started his engineering career as a part time Software and System Design Engineer from March 1980 to December 1982 at the Automated Data System Center, Cairo, Egypt. From January to August 1987, he was a Post-Doctoral Fellow at Manitoba University. Elsherbeni joined the faculty at the University of Mississippi in August 1987 as an Assistant Professor of Electrical Engineering and progressed to the full professor and the Associate Dean of the College of Engineering for Research and Graduate Programs. He then joined the Electrical Engineering and Computer Science (EECS) Department at Colorado School of Mines in August 2013. Elsherbeni is an IEEE Life Fellow and ACES Fellow. He is the Editor-in-Chief for Applied Computational Electromagnetics Society (ACES) Journal, and a past Associate Editor to the Radio Science Journal. He was the Chair of the Engineering and Physics Division of the Mississippi Academy of Science, the Chair of the Educational Activity Committee for IEEE Region 3 Section, and the past President of ACES Society. He received the 2023 IEEE APS Harington-Mittra Award for his contribution to computational electromagnetics with hardware acceleration and the ACES 2025 Computational Electromagnetics Award.

A PEC Conformal FDTD Algorithm with Distorted Grid Face Filtering for Enhanced Efficiency

Chenshu Liu, Kaihang Fan, and Juan Chen

School of Information and Communications Engineering
Xi'an Jiaotong University, Xi'an 710049, China
Shelleylcs@stu.xjtu.edu.cn, khfan@xjtu.edu.cn, chen.juan.0201@xjtu.edu.cn

Abstract – The finite-difference time-domain (FDTD) method suffers from accuracy loss when applied to curved targets due to the staircase approximation. To improve the surface fitting accuracy of curved perfect electric conductor (PEC) objects, the conformal finite-difference time-domain (CFDTD) has been introduced. However, when high-precision conformal cell fitting is performed, the time step in CFDTD is significantly reduced by the presence of distorted small cells, leading to much lower computational efficiency. In this paper, a novel PEC CFDTD algorithm with distorted grid face filtering is proposed, which allows a larger time step. By deriving the stability condition of CFDTD, a Conformal Distortion Index (*CDI*) is defined and used as a filtering criterion. The conformal cells are retained in regions with low *CDI*, while areas with high *CDI* are reverted to the staircase mesh. A sensitivity study on a PEC sphere is used to determine an optimal filtering ratio of 5%, under which the proposed method greatly improves computational efficiency while incurring only a minimal loss in accuracy. Numerical examples are presented to validate the effectiveness of the proposed method.

Index Terms – Conformal finite-difference time-domain (CFDTD), curved targets, grid face filtering, time step reduction.

I. INTRODUCTION

The finite-difference time-domain (FDTD) is widely used in computational electromagnetics due to its explicit time-stepping scheme, inherent parallelism, and time-domain broadband response in a single simulation [1–4]. However, significant staircase errors are introduced in FDTD when discretizing curved perfect electric conductor (PEC) surfaces with Yee cells, which restricts its accuracy in curved target analysis [5–7]. Conformal FDTD (CFDTD) addresses this issue by employing conformal meshes to fit the curved surfaces for improving modeling accuracy [8]. Nevertheless, high-precision conformal fitting inevitably produces numerous small and highly distorted cells in PEC objects. Because the time step is limited by the smallest cell, the computational efficiency of CFDTD decreases significantly with increasing mesh distortion [9].

To improve the balance between accuracy and efficiency of the CFDTD methods for PEC structures, several schemes have been proposed. Yu and Mittra approximated the area of conformal cells to those of Yee cells, which eases the stability constraint but reduces accuracy [10]. Other methods, such as global mesh adjustment and enlarged cell technique, seek to control distortion or enlarge small cells. This often involves manual intervention or complex field update equations [11–14]. Mesh modification strategies, such as adjusting edge lengths or shifting intersection points, are used to regularize cell shapes for relaxing the stability constraint [15, 16]. Alternatively, local or multi-rate time stepping schemes have been introduced. This typically requires additional interpolation, thus increasing complexity and computational cost [17, 18]. In these methods, all conformal cells are still preserved, and the restriction imposed by the smallest cells is handled by making the time-stepping scheme or the mesh structure more complicated.

In addition, recent work has extended CFDTD to higher-order and advanced algorithms to further improve stability and enable larger time steps in complex PEC models [19–26]. Implicit or weakly conditionally stable schemes, such as conformal alternating direction implicit (C-ADI)-FDTD and conformal locally one-dimensional (C-LOD)-FDTD, can formally relax the limit but require solving linear systems at each time step. In practice, C-ADI-FDTD may still suffer from stability degradation on highly distorted conformal meshes. In contrast, C-LOD-FDTD, though unconditionally stable, exhibits relatively large numerical dispersion and may need finer meshes to match the accuracy of explicit CFDTD.

With these advances, CFDTD has continued to mature in recent years, demonstrating improved accuracy, broader applicability, and greater reliability. It has

Submitted On: August 20, 2025
Accepted On: March 03, 2026

https://doi.org/10.13052/2026.ACES.J.410303

been successfully applied to waveguide ports [9, 27, 28], periodic and anisotropic structures [29], and advanced boundary conditions [30]. These applications underscore the significance of these algorithms and the need for further improvements in computational efficiency and stability, especially for severely distorted meshes.

In this paper, a novel PEC CFDTD algorithm with distorted grid face filtering is proposed. Instead of updating all the highly distorted conformal cells, the proposed method operates directly on the mesh by filtering out a portion of the most problematic cells. By quantitatively relating a Conformal Distortion Index (*CDI*) to the global time step stability constraint, a filtering criterion is established to replace a preset proportion of highly distorted conformal cells with staircase cells. Thus, a small sacrifice of geometric accuracy for a limited number of cells leads to a much larger allowable time step and a substantial improvement in computational efficiency. A sensitivity study on a PEC sphere identifies 5% as the optimal filtering ratio. Under this setting, the proposed method achieves significant improvement in computational efficiency while introducing only a minor accuracy loss compared to the conventional CFDTD, as verified by numerical results.

II. STABILITY ANALYSIS OF CFDTD

When applying the CFDTD method to PEC, conformal meshes truncate the boundary Yee cells. Therefore, the electromagnetic field calculation for the mesh in the boundary region needs to be corrected using Faraday's law as

$$\oint_{\partial S} \vec{E} \cdot d\vec{l} = -\frac{\partial}{\partial t} \iint_{S} \mu \vec{H} \cdot d\vec{S}, \tag{1}$$

where S represents the area of the region, ∂S denotes its boundary, l is the length of the grid cell along the boundary of the region, t is the time, and μ is the magnetic permeability.

According to equation (1), the explicit magnetic field calculation must be modified to account for changes in the integration path and regions outside the PEC. As shown in Fig. 1, the equation for the z-component of the magnetic field is given as [8]

$$\begin{aligned} & H_z^{n+1/2}(i,j,k) \\ & \quad = H_z^{n-1/2}(i,j,k) + \frac{\Delta t}{\mu S_z(i,j,k)} \\ & \qquad \cdot \begin{bmatrix} E_x^n(i,j+1,k) l_x(i,j+1,k) \\ -E_x^n(i,j,k) l_x(i,j,k) \\ -E_y^n(i+1,j,k) l_y(i+1,j,k) \\ +E_y^n(i,j,k) l_y(i,j,k) \end{bmatrix}, \end{aligned} \tag{2}$$

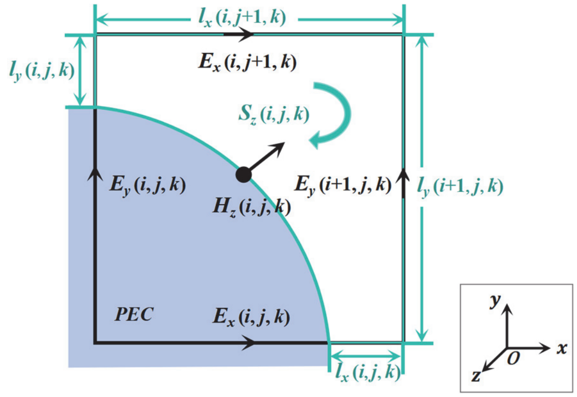

Fig. 1. Illustration of changes in conformal mesh integration path and area.

where Δt denotes the time step size. At the grid point with three-dimensional coordinates (i,j,k), $S_z(i,j,k)$ represents the area of the H_z-associated grid cell outside the PEC, l_x, l_y denote the lengths of the grid edges along the x and y directions at the boundary of $S_z(i,j,k)$ outside the PEC, and n is the time step index.

To preserve the finite-difference formulation of the magnetic field components along different coordinate directions in CFDTD, equivalent edge lengths l_v' and equivalent areas $S_v'(v = x,y,z)$ are introduced. Using the magnetic field component in the z-direction, illustrated in Fig. 1 as an example, we define

$$l_x' = l_x/\Delta x, \quad l_y' = l_y/\Delta y, \quad S_z' = S/\Delta x \Delta y, \tag{3}$$

where $\Delta v(v = x,y,z)$ denotes the full sizes of the Yee cells in the x, y, and z directions, respectively, representing the differential discretization intervals along each axis.

Thus, the equivalent edge lengths of the conformal cell are $l_x'(i,j+1,k)$ and $l_y'(i+1,j,k)$, and the equivalent area is $S_z(i,j,k)$. Consequently, the magnetic field update equation in CFDTD is modified as

$$\begin{aligned} & H_z^{n+1/2}(i,j,k) \\ & \quad = H_z^{n-1/2}(i,j,k) + \frac{\Delta t}{\mu S_z'(i,j,k)} \\ & \qquad \cdot \begin{bmatrix} \dfrac{E_x^n(i,j+1,k) l_x'(i,j+1,k) - E_x^n(i,j,k) l_x'(i,j,k)}{\Delta y} \\ \dfrac{E_y^n(i,j,k) l_y'(i,j,k) - E_y^n(i+1,j,k) l_y'(i+1,j,k)}{\Delta x} \end{bmatrix}. \end{aligned} \tag{4}$$

While the magnetic field is adjusted in the CFDTD method, the electric field calculation still follows the conventional FDTD formulation.

The stability proof of the CFDTD method in this work is based on a simplified form of equation (4).

By incorporating all coefficients of the electric field terms in equation (4) into a new definition $E_{v*}^{n}(i,j,k) = E_{v}^{n}(i,j,k) \cdot l_{v}'(i,j,k), (v = x,y,z)$, the equation can be rewritten as

$$\begin{aligned} & H_z^{n+1/2}(i,j,k) \\ & \quad = H_z^{n-1/2}(i,j,k) \\ & \quad\quad + \frac{\Delta t}{\mu S_z'(i,j,k)} \begin{bmatrix} \dfrac{E_{x*}^{n}(i,j+1,k) - E_{x*}^{n}(i,j,k)}{\Delta y} \\ -\dfrac{E_{y*}^{n}(i+1,j,k) + E_{y*}^{n}(i,j,k)}{\Delta x} \end{bmatrix}. \end{aligned} \tag{5}$$

Considering a linear, isotropic, lossy medium, the fundamental computation equations of CFDTD can be written in matrix form as

$$\begin{aligned} & \begin{bmatrix} 1 & 0 & 0 & 0 & 0 & 0 \\ 0 & 1 & 0 & 0 & 0 & 0 \\ 0 & 0 & 1 & 0 & 0 & 0 \\ 0 & -\mathrm{C}_q \cdot \dfrac{\partial}{\partial z}\dfrac{1}{S_x} & \mathrm{C}_q \cdot \dfrac{\partial}{\partial y}\dfrac{1}{S_x} & 1 & 0 & 0 \\ \mathrm{C}_q \cdot \dfrac{\partial}{\partial z}\dfrac{1}{S_y} & 0 & -\mathrm{C}_q \cdot \dfrac{\partial}{\partial x}\dfrac{1}{S_y} & 0 & 1 & 0 \\ -\mathrm{C}_q \cdot \dfrac{\partial}{\partial y}\dfrac{1}{S_z} & \mathrm{C}_q \cdot \dfrac{\partial}{\partial x}\dfrac{1}{S_z} & 0 & 0 & 0 & 1 \end{bmatrix} \\ & \times \begin{bmatrix} E_{x*}^{n+1} \\ E_{y*}^{n+1} \\ E_{z*}^{n+1} \\ H_x^{n+1} \\ H_y^{n+1} \\ H_z^{n+1} \end{bmatrix} \\ & = \begin{bmatrix} 1 & 0 & 0 & 0 & -\mathrm{C}_b \cdot \dfrac{\partial}{\partial z} & \mathrm{C}_b \cdot \dfrac{\partial}{\partial y} \\ 0 & 1 & 0 & \mathrm{C}_b \cdot \dfrac{\partial}{\partial z} & 0 & -\mathrm{C}_b \cdot \dfrac{\partial}{\partial x} \\ 0 & 0 & 1 & -\mathrm{C}_b \cdot \dfrac{\partial}{\partial y} & \mathrm{C}_b \cdot \dfrac{\partial}{\partial x} & 0 \\ 0 & 0 & 0 & 1 & 0 & 0 \\ 0 & 0 & 0 & 0 & 1 & 0 \\ 0 & 0 & 0 & 0 & 0 & 1 \end{bmatrix} \\ & \times \begin{bmatrix} E_{x*}^{n} \\ E_{y*}^{n} \\ E_{z*}^{n} \\ H_x^{n} \\ H_y^{n} \\ H_z^{n} \end{bmatrix}, \end{aligned} \tag{6}$$

where $C_b = \frac{\Delta t}{\varepsilon}, C_q = \frac{\Delta t}{\mu}$, and ε is the dielectric constant.

The field components E^n and H^n in equation (2) can be represented as three-dimensional plane waves at time step n

$$\begin{cases} E^n = \phi_E \zeta^n \exp[j(k_x x + k_y y + k_z z)] \\ H^n = \phi_H \zeta^n \exp[j(k_x x + k_y y + k_z z)] \end{cases}, \tag{7}$$

where ϕ is the amplitude of the field components, ζ is the amplification factor, and k_x, k_y, k_z are the wavenumbers in the x, y, z directions, respectively.

Substituting equation (7) into equation (6) and discretizing the spatial components $\exp[j(k_x x + k_y y + k_z z)$ gives

$$\begin{aligned} & \begin{bmatrix} \zeta - 1 & 0 & 0 & 0 & C_{bx}'\sigma_z & -C_{bx}'\sigma_y \\ 0 & \zeta - 1 & 0 & -C_{by}'\sigma_z & 0 & C_{by}'\sigma_x \\ 0 & 0 & \zeta - 1 & C_{bz}'\sigma_y & -C_{bz}'\sigma_x & 0 \\ 0 & -\zeta C_{qx}' \cdot \sigma_z & \zeta C_{qx}'\sigma_y & \zeta - 1 & 0 & 0 \\ \zeta C_{qy}'\sigma_z & 0 & -\zeta C_{qy}'\sigma_x & 0 & \zeta - 1 & 0 \\ -\zeta C_{qz}'\sigma_y & \zeta C_{qz}'\sigma_x & 0 & 0 & 0 & \zeta - 1 \end{bmatrix} \\ & \cdot \begin{bmatrix} \phi_{E_x}\zeta_n \\ \phi_{E_y}\zeta_n \\ \phi_{E_z}\zeta_n \\ \phi_{H_x}\zeta_n \\ \phi_{H_y}\zeta_n \\ \phi_{H_z}\zeta_n \end{bmatrix} = 0, \end{aligned} \tag{8}$$

where $\sigma_x = 2j\sin\left(\frac{k_x \Delta x}{2}\right)/\Delta x$, $\sigma_y = 2j\sin\left(\frac{k_y \Delta y}{2}\right)/\Delta y$, $\sigma_z = 2j\sin\left(\frac{k_z \Delta z}{2}\right)/\Delta z$, $C_{bv}' = \frac{\Delta t \cdot l_v'}{\varepsilon}$, $C_{qv}' = \frac{\Delta t}{\mu \cdot S_v'}$, $(v = x,y,z)$.

For equation (8) to have non-trivial solutions, the determinant of the coefficient matrix must be zero, that is

$$(\zeta - 1)^2 \begin{bmatrix} \zeta(C_{bx}'C_{qx}'\sigma_x^2 + C_{by}'C_{qy}'\sigma_y^2 + C_{bz}'C_{qz}'\sigma_z^2) \\ -(\zeta - 1)(\zeta - 1) \end{bmatrix}^2 = 0. \tag{9}$$

To ensure numerical stability during iterative computation, the amplitude of the amplification factor must satisfy $|\zeta| = 1$, thus, equation (9) is equivalent to

$$\zeta - 1 = 0, \tag{10}$$

$$\zeta(C_{bx}'C_{qx}'\sigma_x^2 + C_{by}'C_{qy}'\sigma_y^2 + C_{bz}'C_{qz}'\sigma_z^2) - (\zeta - 1)^2 = 0. \tag{11}$$

By solving equation (10), we obtain $|\zeta| = |1| \leq 1$, indicating that this stability condition is always satisfied. Equation (11) can then be rearranged as

$$\zeta^2 - [2 + C_{bx}'C_{qx}'\sigma_x^2 + C_{by}'C_{qy}'\sigma_y^2 + C_{bz}'C_{qz}'\sigma_z^2]\zeta + 1 = 0. \tag{12}$$

For the convenience of calculation, a linear transformation defined by $\zeta = \frac{r+1}{r-1}$ is applied to equation (12) as

$$[-C'_{bx}C'_{qx}\sigma_x^2 + C'_{by}C'_{qy}\sigma_y^2 + C'_{bz}C'_{qz}\sigma_z^2]r^2 + [4 + C'_bC'_q(\sigma_x^2 + \sigma_y^2 + \sigma_z^2)] = 0. \tag{13}$$

Using the Routh-Hurwitz criterion [31], the necessary and sufficient condition for numerical stability in equation (13) is that all coefficients are positive. The first-order terms are always positive, so only the constant term requires further analysis, which is simplified as

$$\begin{aligned}&\left[\frac{l'_x}{S'_x}\cdot\left(\frac{\sin\left(\frac{k_x\Delta x}{2}\right)}{\Delta x}\right)^2 + \frac{l'_y}{S'_y}\cdot\left(\frac{\sin\left(\frac{k_y\Delta y}{2}\right)}{\Delta y}\right)^2 + \frac{l'_z}{S'_z}\cdot\left(\frac{\sin\left(\frac{k_z\Delta z}{2}\right)}{\Delta z}\right)^2\right] \\ &\le \left[\frac{l'_x}{S'_x}\left(\frac{1}{\Delta x}\right)^2 + \frac{l'_y}{S'_y}\left(\frac{1}{\Delta y}\right)^2 + \frac{l'_z}{S'_z}\left(\frac{1}{\Delta z}\right)^2\right] \le \frac{\varepsilon\mu}{(\Delta t)^2}.\end{aligned} \tag{14}$$

Accordingly, the time step Δt in CFDTD should meet the following criterion

$$\begin{aligned}\Delta t_{CFDTD} &\le \sqrt{\frac{\varepsilon\mu}{\frac{l'_x}{S'_x}\left(\frac{1}{\Delta x}\right)^2 + \frac{l'_y}{S'_y}\left(\frac{1}{\Delta y}\right)^2 + \frac{l'_z}{S'_z}\left(\frac{1}{\Delta z}\right)^2}} \\ &\le \sqrt{\frac{\varepsilon\mu}{\left(\frac{l'}{S'}\right)_{\max(x,y,z)}\left[\left(\frac{1}{\Delta x}\right)^2 + \left(\frac{1}{\Delta y}\right)^2 + \left(\frac{1}{\Delta z}\right)^2\right]}} \\ &= \Delta t_{FDTD} / \left(\sqrt{\frac{l'}{S'}}\right)_{\max(x,y,z)}.\end{aligned} \tag{15}$$

In summary, the stability condition for the CFDTD method is $\Delta t_{CFDTD} \le \Delta t_{FDTD}/(\sqrt{\frac{l'}{S'}})_{\max}$.

III. IMPLEMENTATION OF CFDTD BASED ON DISTORTED MESH SURFACES FILTERING

A. Conformal Distortion Index

As discussed in Section II, the conformal treatment of PEC boundaries modifies the effective edge lengths and areas of the truncated Yee cells, and these equivalent geometric parameters enter the stability condition in (15). In this paper, we introduce the *CDI* to characterize the distortion of conformal mesh surfaces in a way that is directly linked to this stability constraint.

The *CDI* of a conformal mesh surface is calculated as shown in Fig. 2. Here, l'_a, l'_b, l'_c, and l'_d are the equivalent lengths of the mesh surface's four edges, respectively, and S represents the equivalent area.

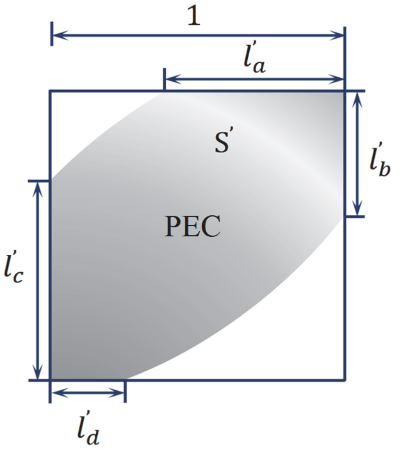

Fig. 2. Illustration of *CDI* parameter analysis for the conformal mesh surface.

Hence, the defined *CDI* in a conformal mesh surface can be expressed as

$$CDI = (\sqrt{l'/S'})_{\max} = \sqrt{\max(l'_a, l'_b, l'_c, l'_d)/S'} = \sqrt{l'_c/S'}. \tag{16}$$

Substituting (16) into (15), the numerical stability condition for CFDTD can be expressed as

$$\Delta t_{CFDTD} \le \Delta t_{FDTD}/CDI_{\max}, \tag{17}$$

where CDI_{max} refers to the maximum *CDI* among all conformal mesh surfaces. For a given conformal cell surface, the time step is limited by CDI_{max}. According to [11], it can be seen that $CDI_{max} \ge 1$. As the CDI_{max} of the conformal cell increases, the time step will be smaller and, consequently, the computational efficiency in CFDTD is also reduced.

Unlike conventional mesh-quality metrics, *CDI* is constructed directly from the equivalent edge lengths and equivalent area so that it appears explicitly in the CFDTD stability constraint in (17), and therefore quantitatively describes how strongly the most distorted conformal surfaces restrict the global time step. To alleviate this limitation, a novel CFDTD method with distorted grid surface filtering is proposed to remove highly distorted conformal cell surfaces, thereby reducing the overall CDI_{max}.

B. Specific implementation

The proposed PEC CFDTD with distorted grid surface filtering proceeds as follows.

(a) Calculate the *CDI* for all conformal cell surfaces using (16) and rank them in descending order to create a priority list for filtering.

(b) Set the removal ratio η and remove the top η fraction of the distorted surfaces from the list. Removed mesh cells are converted back to regular grid cells based on the dielectric properties at their centers, aiming to preserve the geometric integrity as much as possible.

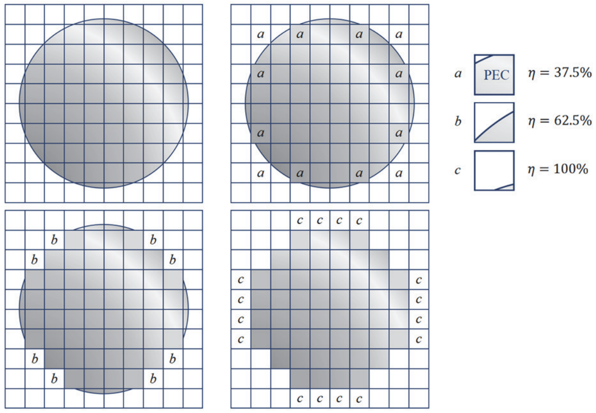

Fig. 3. Illustration of the proposed CFDTD method incorporating distorted grid surface filtering.

To clarify the proposed approach, a two-dimensional circular PEC surface, shown in Fig. 3, was constructed and discretized using conformal meshing. For this model, the filtering procedure was applied to conformal meshes, which are divided into filtering regions *a*, *b*, and *c* according to descending *CDI* values. At a removal ratio η of 37.5%, cells in region *a* are reverted to the conventional Yee cell; increasing η to 62.5% includes region *b* as well, thereby filtering out meshes with moderate *CDI* values. When η reaches 100%, region *c* is also converted back to the base mesh, so that subsequent calculations are performed entirely on the standard FDTD grid.

After applying a certain proportion of filtering to the mesh using this method, the maximum time step for the proposed method is then given by

$$\begin{aligned}\Delta t_{filtered} &= \Delta t_{FDTD}/CDI'_{\max} \\ &= \Delta t_{FDTD}/(CDI_{\max})_{the\ remaining\ grids}. \end{aligned} \tag{18}$$

A larger time step is allowed by increasing the removal ratio, but this may reduce the accuracy of the proposed method. In specific engineering problems, an appropriate ratio can improve computational efficiency significantly within an acceptable range of accuracy loss.

In practical simulations, it is necessary to determine an optimal filtering ratio at which the time step is maximally relaxed while the loss of computational accuracy remains negligible. To identify the optimal filtering ratio, we will perform a detailed parameter sensitivity analysis on typical examples in section IV, thereby establishing a selection criterion for η and verifying the effectiveness of the chosen filtering ratio.

IV. NUMERICAL EXAMPLES AND RESULT ANALYSIS

To verify the effectiveness of the proposed PEC CFDTD algorithm based on distorted mesh surface filtering, the radar cross-section (RCS) of two typical curved metal surfaces is analyzed. All simulations are performed on a Windows 10 operating system equipped with an Intel(R) Xeon(R) 8360Y CPU @ 2.40 GHz (up to 3.50 GHz) and 1.0 TB RAM.

A. PEC sphere

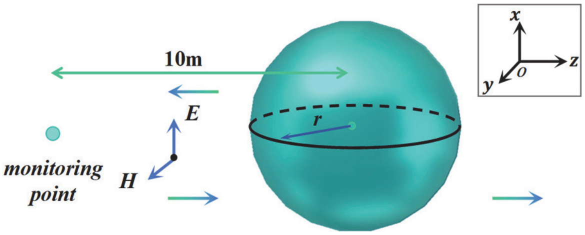

Fig. 4. Model for PEC sphere backscattering RCS calculation.

In the first example, a PEC sphere with a radius of 0.36 m is analyzed. An *x*-polarized plane wave is incident along the positive *z*-direction, with a Gaussian pulse $f(t) = \exp[-4\pi(t-t_0)^2/\tau^2]$, where $\tau = 2 \times 10^{-9}$ s, $t_0 = 0.8\ \tau$. A monitoring point is set at 10 m along the negative *z*-axis to record the backscattering RCS characteristics of the metal sphere, as shown in Fig. 4.

For an accurate reference solution, the FDTD method uses a uniform small grid of 0.01 m to discretize the metal sphere, while both conventional and proposed CFDTD allow a coarser grid of 0.03 m. The air region adopts a uniform grid of 0.03 m.

The variation of CDI_{max} and the average RCS error with respect to the removal ratio η is investigated in Fig. 5. When η increases from 0% to 5%, CDI_{max} drops sharply. Since the time step is inversely proportional to CDI_{max}, this corresponds to a substantial relaxation of the time step constraint and thus several improvements in computational efficiency. Meanwhile, the RCS curve remains almost unchanged, and the increase in the average error does not exceed 0.1 dB·m^2. When η exceeds 5%, the decrease of CDI_{max} gradually saturates, so further increasing η brings marginal gains in the allowable time step, while the RCS error grows more noticeably. Therefore, $\eta = 5\%$ is identified as an effective compromise. The algorithm removes the highly distorted cells that dominate the time step constraint, while keeping the loss of accuracy at a low level.

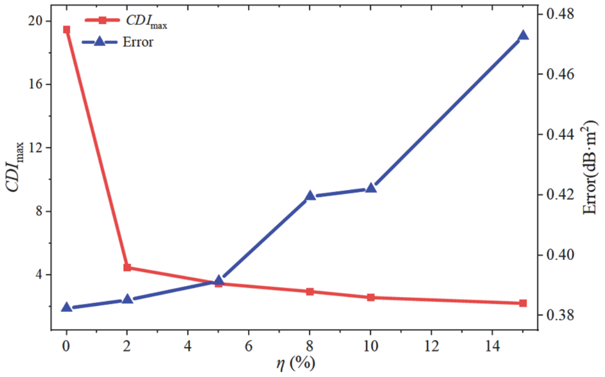

Fig. 5. Variations of CDI_{max} and average RCS error with respect to removal ratio η for the PEC sphere.

To visually verify that this choice is appropriate, Fig. 6 compares the RCS curves for different η values. The curve for $\eta = 5\%$ almost coincides with CFDTD and the Mie analytical solution, indicating that the proposed method preserves the high accuracy of CFDTD while improving efficiency. In contrast, the RCS curve for $\eta = 15\%$ shows clear deviations, implying that excessive filtering destroys the geometric features of the curved surface and deteriorates the scattering response.

Figure 7 further presents the time-domain results of the observation point located 0.03 m from the center of the incident plane wave. The results indicate that for $\eta = 15\%$, the time-domain response exhibits noticeable deviations. In contrast, for $\eta = 5\%$, it is in good agreement with that of CFDTD throughout the entire simulation time. This confirms both the numerical stability and the accuracy of the proposed method in the time domain.

The detailed simulation parameters and relative errors of the four methods are summarized in Table 1, with the analytical Mie series solution employed as the exact reference. For the conventional CFDTD, the presence of small distorted cells imposes a strict constraint on the time step, leading to an overall runtime even longer than that of the fine mesh FDTD. In contrast, when the proposed filtering strategy with $\eta = 5\%$ is applied, the computation time is reduced from 943 s to 151 s, a decrease of about 84.0%. At the same time, the relative error of the backscattering RCS remains around 2.40%, which is essentially comparable to that of the conventional CFDTD. When η reaches 15%, the error grows significantly, whereas the gain in computation time becomes negligible.

In summary, for the PEC sphere example, a removal ratio of $\eta = 5\%$ provides an almost optimal balance between computational efficiency and accuracy.

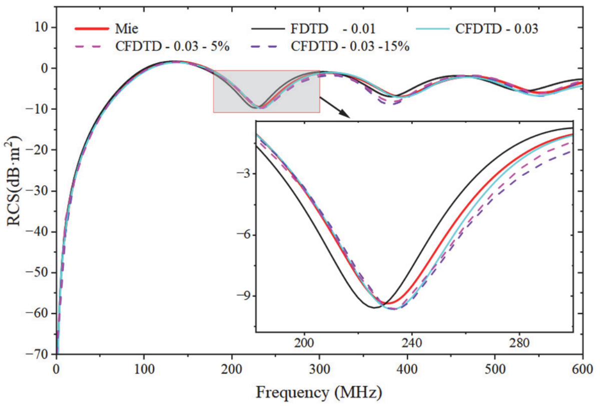

Fig. 6. Frequency response of RCS of the PEC sphere.

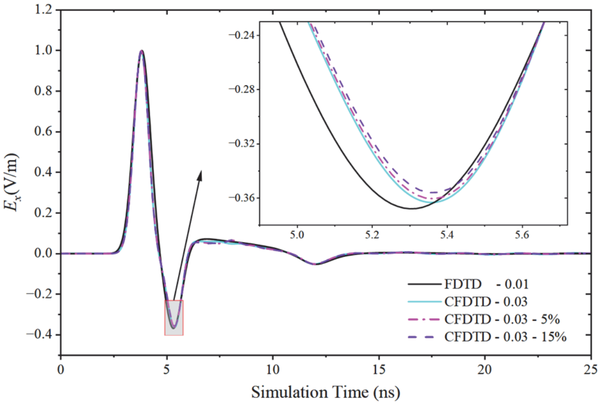

Fig. 7. Time-domain results of the PEC sphere.

Table 1: Comparison of computation parameters for FDTD and proposed methods of the sphere

η (%)	Time (s)	Grid Number	Relative Error (%)	Memory (MB)
FDTD	1050	438,976	3.99	1400
0	1179	21,952	2.39	549
5	189	21,952	2.40	365
15	133	21,952	2.58	364

B. F117 aircraft model

To further verify the generality of the optimal removal ratio $\eta = 5\%$ in complex targets, the F117 aircraft is analyzed. In this example, the aircraft has an overall length of 20.08 m, a height of 3.78 m, and a wingspan of 13.20 m. An x-polarized plane wave at 500 MHz is incident along the positive z-axis, as shown in Fig. 8. The background FDTD domain uses a uniform fine mesh of 0.03 m, while both the conventional CFDTD and the proposed method adopt a grid size of 0.06 m in the conformal region.

Figure 9 compares the forward RCS frequency responses obtained by different methods. The results of

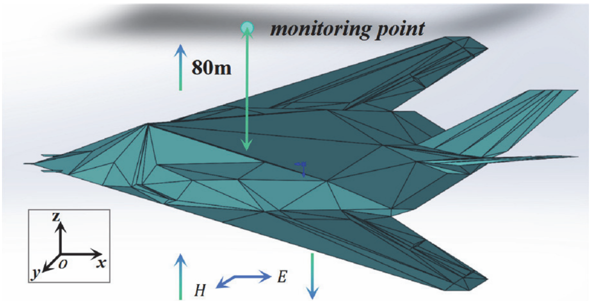

Fig. 8. F117 forward RCS computation model.

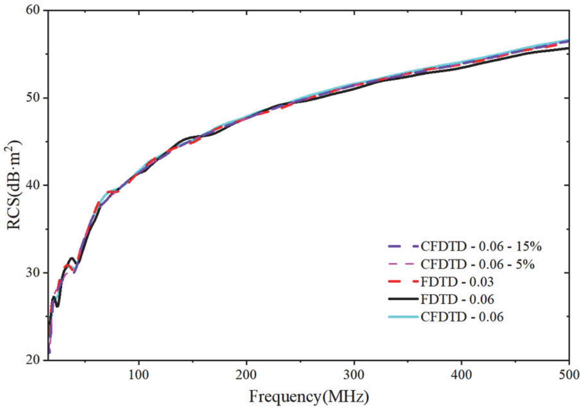

Fig. 9. Frequency response of forward RCS for F117.

the proposed filtering method agree very well with those of the conventional CFDTD, while achieving a clear improvement in computational efficiency compared with the fine-mesh FDTD.

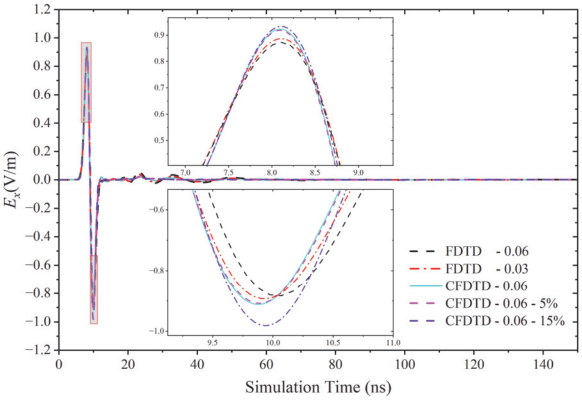

Fig. 10. Time-domain results of F117.

The detailed simulation parameters and errors for the five methods applied to the F117 are summarized in Table 2, where the result of the conventional CFDTD is used as the reference. When the recommended removal ratio of 5% is used, the computation time is reduced from 3234 minutes to 651 minutes, corresponding to a 79.9% reduction, while the RCS relative error with respect to the conventional CFDTD is only 1.778%. When the removal ratio is increased to 15%, the computation time is further reduced. However, the additional gain is much less significant than that obtained when increasing the removal ratio from 0% to 5%, while the error continues to increase. This trend is particularly evident in the time-domain results shown in Fig. 10. For a 15% removal ratio, the time-domain result deviates noticeably from CFDTD, while the 5% case still matches it well.

Therefore, choosing a 5% removal ratio for distorted grid faces filtering provides a robust trade-off between accuracy and efficiency, which strongly demonstrates the applicability of the proposed method to electromagnetic simulations of complex targets.

Table 2: Comparison of computation parameters for FDTD and proposed methods of F117

η (%)	**Time (min)**	**Grid Number**	**Relative Error (%)**	**Memory (GB)**
FDTD-0.03	1417	22,368,060	1.886	26.25
FDTD-0.06	135	3,025,848	2.582	6.90
0	3234	3,025,848	-	6.95
5	651	3,025,848	1.778	6.93
15	302	3,025,848	2.211	6.91

As shown in the two examples, the proposed CFDTD improves efficiency by filtering part of the distorted grids while keeping the accuracy loss small. As the removal ratio η increases, the decrease of the maximum CDI becomes slower. In practice, a removal ratio of about 5% already gives a large gain in the allowable time step and computational efficiency, with only minor error. Therefore, users can choose η according to their accuracy and runtime requirements, with $\eta = 5\%$ as a recommended optimal choice.

V. CONCLUSION

To improve the computational efficiency of traditional conformal FDTD, this paper proposes a conformal PEC FDTD method with distorted grid-face filtering. A *CDI* is defined to measure the grid distortion, and a simple statistical filtering scheme is used. Only a small number of conformal cells that impose the most restrictive global time step limit are filtered, which directly relaxes the constraint. Numerical examples for a PEC sphere and an F117 aircraft show that, when the filtering ratio is set to 5%, the proposed method is generally applicable and greatly improves computational efficiency with only a small loss of accuracy. This method provides a simple, robust, and efficient approach for electromagnetic simulation of large and complex targets, allowing users to flexibly balance computational efficiency and geometric modeling accuracy according to practical engineering needs.

ACKNOWLEDGMENT

This work was supported by the National Natural Science Foundation of China Youth Science Fund Project (Category A) under No. 62525114, the National Natural Science Foundation of China Youth Science Fund Project (Category C) under No. 62401455, the Shaanxi Province Innovation Capability Support Plan under No. 2024RS-CXTD-07, and the Key R&D Program of Shaanxi Province under No. 2024GX-ZDCYL-05-04.

REFERENCES

[1] K. S. Yee, "Numerical solution of initial boundary value problems involving Maxwell's equations," *IEEE Trans. Antennas Propag.*, vol. 14, no. 3, pp. 302–207, May 1966.

[2] K. S. Kunz and R. J. Luebbers, *The Finite-Difference Time-Domain Method for Electromagnetics*. Boca Raton, FL, USA: CRC Press, 1993.

[3] A. Taflove and S. C. Hagness, *Computational Electrodynamics: The Finite-Difference Time-Domain Method*. Norwood, MA, USA: Artech House, 2005.

[4] A. V. Boriskin, A. Rolland, R. Sauleau, and A. I. Nosich, "Assessment of FDTD accuracy in the compact hemielliptic dielectric lens antenna analysis," *IEEE Trans. Antennas Propag.*, vol. 56, no. 3, pp. 758–764, Mar. 2008.

[5] T. G. Jurgens, A. Taflove, K. Umashankar, and T. G. Moore, "Finite-difference time-domain modeling of curved surfaces," *IEEE Trans. Antennas Propag.*, vol. 40, no. 4, pp. 357–366, Apr. 1992.

[6] Y. Hao and C. J. Railton, "Analyzing electromagnetic structures with curved boundaries on Cartesian FDTD meshes," *IEEE Trans. Microw. Theory Techn.*, vol. 46, no. 1, pp. 82–88, Jan. 1998.

[7] A. C. Cangellaris and D. B. Wright, "Analysis of the numerical error caused by the stair-stepped approximation of a conducting boundary in FDTD simulations of electromagnetic phenomena," *IEEE Trans. Antennas Propag.*, vol. 39, no. 10, pp. 1518–1525, Oct. 1991.

[8] S. Dey and R. Mittra, "A locally conformal finite-difference time-domain (CFDTD) algorithm for modeling three-dimensional perfectly conducting objects," *IEEE Microw. Guided Wave Lett.*, vol. 17, no. 9, pp. 273–275, Sep. 1997.

[9] G. Chen, J. Stang, and M. Moghaddam, "A conformal FDTD method with accurate waveport excitation and S-parameter extraction," *IEEE Trans. Antennas Propag.*, vol. 64, no. 10, pp. 4504–4509, Oct. 2016.

[10] W. Yu and R. Mittra, "A conformal FDTD algorithm for modeling perfectly conducting objects with curve-shaped surfaces and edges," *Microw. Opt. Technol. Lett.*, vol. 27, no. 2, pp. 136–138, Aug. 2000.

[11] S. Benkler, N. Chavannes, and N. Kuster, "A new 3-D conformal PEC FDTD scheme with user-defined geometric precision and derived stability criterion," *IEEE Trans. Antennas Propag.*, vol. 54, no. 6, pp. 1843–1849, June 2006.

[12] T. Xiao and Q. H. Liu, "Enlarged cells for the conformal FDTD method to avoid the time step reduction," *IEEE Microw. Wireless Compon. Lett.*, vol. 14, no. 12, pp. 551–553, Dec. 2004.

[13] R. Schuhmann, I. A. Zagorodnov, and T. Weiland, "Comment on 'Enlarged cells for the conformal FDTD method to avoid the time step reduction,'" *IEEE Microw. Wireless Compon. Lett.*, vol. 16, no. 1, p. 55, Jan. 2006.

[14] T. Xiao and Q. H. Liu, "A 3-D enlarged cell technique (ECT) for the conformal FDTD method," *IEEE Trans. Antennas Propag.*, vol. 56, no. 3, pp. 765–773, Mar. 2008.

[15] I. A. Zagorodnov, R. Schuhmann, and T. Weiland, "Conformal FDTD method to avoid time step reduction with and without cell enlargement," *J. Computational Phys.*, vol. 225, pp. 1493–1507, Aug. 2007.

[16] M. R. Cabello, L. D. Angulo, J. Alvarez, A. R. Bretones, G. G. Gutierrez, and S. G. Garcia, "A new efficient and stable 3D conformal FDTD," *IEEE Microw. Wireless Compon. Lett.*, vol. 26, no. 8, pp. 553–555, Aug. 2016.

[17] C. M. Kuo and C. W. Kuo, "A new scheme for the conformal FDTD method to calculate the radar cross-section of perfect conducting curved objects," *IEEE Antennas Wireless Propag. Lett.*, vol. 9, pp. 16–19, 2010.

[18] C.-M. Kuo and C.-W. Kuo, "A novel FDTD time-stepping scheme to calculate RCS of curved conducting objects using adaptively adjusted time steps," *IEEE Trans. Antennas Propag.*, vol. 61, no. 10, pp. 5127–5134, Oct. 2013.

[19] M. Chai, T. Xiao, and Q. H. Liu, "Conformal method to eliminate the ADI-FDTD staircasing errors," *IEEE Trans. Electromagn. Compat.*, vol. 48, no. 2, pp. 273–281, May 2006.

[20] J. Dai, Z. Chen, D. Su, and X. Zhao, "Stability analysis and improvement of the conformal ADI-FDTD methods," *IEEE Trans. Antennas Propag.*, vol. 59, no. 6, pp. 2248–2258, June 2011.

[21] J. Wang and W. Y. Yin, "Development of a novel FDTD (2, 4)-compatible conformal scheme for electromagnetic computations of complex curved PEC objects," *IEEE Trans. Antennas Propag.*, vol. 61, no. 1, pp. 299–309, Jan. 2013.

[22] W. Shi, J. Wang, Q.-F. Liu, W.-J. Wu, and W.-Y. Yin, "A conformal scheme for modeling curved dispersive medium objects compatible with ADE-FDTD (2, 4) method," *IEEE Antennas Wireless*

Propag. Lett., vol. 24, no. 1, pp. 177–181, Jan. 2025.

[23] X. Wei, W. Shao, S. Shi, Y. Zhang, and B. Wang, “An efficient locally one-dimensional finite-difference time-domain method based on the conformal scheme,” *Chin. Phys. B*, vol. 24, no. 7, pp. 76–84, May 2015.

[24] H. Liu, X. Zhao, X.-H. Wang, S. Yang, and Z. Chen, “An unconditionally stable conformal LOD-FDTD method for curved PEC objects and its application to EMC problems,” *IEEE Trans. Electromagn. Compat.*, vol. 64, no. 3, pp. 827–839, June 2022.

[25] M. Zhu, Q. Cao, L. Zhao, and X. Li, “Analysis of three-dimensional curved objects by Runge-Kutta high-order time-domain method,” *Appl. Comput. Electromagn.*, vol. 30, no. 1, pp. 86–92, 2015.

[26] M. A. Kourah, M. F. Hadi, and A. S. Al-Zayed, “Extending the enlarged cell and uniformly stable conformal techniques to modeling curved conductors in two-dimensional high-order finite-difference time-domain algorithms,” *Int. J. Numer. Model. Electron. Netw. Devices Fields*, vol. 26, no. 3, pp. 205–306, May 2013.

[27] K. Wang, S. Zuo, Q. Wu, Z. Lin, Y. Zhang, and X. Zhao, “A novel compact conformal 2-D FDFD method for modeling waveports in 3-D FDTD,” *IEEE Antennas Wireless Propag. Lett.*, vol. 23, no. 7, pp. 2091–2095, July 2024.

[28] G. Lin, T. Huang, W. Cai, D. Gong, and X. Jin, “An efficient scheme of waveguide port modeling based on conformal and nonuniform mesh for time-domain finite integration technique,” *IEEE Trans. Antennas Propag.*, vol. 73, no. 2, pp. 1047–1058, Feb. 2025.

[29] K. Wang, Q. Wu, F. Yu, S. Zuo, Z. Lin, X. Zhao, and Y. Zhang, “Conformal anisotropic periodic boundary condition for FDTD method,” *IEEE Antennas Wireless Propag. Lett.*, vol. 24, no. 1, Jan. 2025.

[30] S. Gaucher, C. Guiffaut, N. Bui, A. Reineix, and O. Cessenat, “Angle-dependent face-centered SIBC model of metamaterial in conformal FDTD methods,” *IEEE Trans. Antennas Propag.*, vol. 71, no. 9, pp. 7438–7446, Sep. 2023.

[31] A. Pereda, L. A. Vielva, A. Vegas, and A. Prieto, “Analyzing the stability of the FDTD technique by combining the von Neumann method with the Routh-Hurwitz criterion,” *IEEE Trans. Microw. Theory Tech.*, vol. 49, no. 2, pp. 377–381, Feb. 2001.

Chenshu Liu was born in Hubei, China, in 2002. She received her B.S. degree in Electronic and Information Engineering from Xi’an Jiaotong University, Xi’an, in 2024, where she is currently working toward an M.S. degree in Electromagnetic Field and Microwave Technology. Her current research interests include computational electromagnetics.

Kaihang Fan received the B.S. degree in electronic information science and technology from Xidian University, Xi’an, China, in 2014, and the Ph.D. degree in radio physics, Xidian University, Xi’an, in 2021. She is currently an Assistant Professor with the School of Information and Communications Engineering, Xi’an Jiaotong University, Xi’an. Her current research interests include computational electromagnetics numerical methods and multi-physics field simulation.

Juan Chen was born in Chongqing, China. She received the Ph.D. degree from Xi’an Jiaotong University, Xi’an, in 2008, in electromagnetic field and microwave technology. She is currently working in Xi’an Jiaotong University, Xi’an, as a professor. Her research interests include computational electromagnetics and microwave device design.

Modeling of Thin Shielding Layer Based on Unstructured Grid Vector Finite Element Method and Analysis of its Effect on SQUID TEM Observation Signal

Binyuan Ma[1], Nansong Chang[1], Yanju Ji[1,2], Xuejiao Zhao[1,2], and Hui Luan[1,2]

[1]College of Instrumentation and Electrical Engineering
Jilin University, Changchun 130000, China
maby20@mails.jlu.edu.cn, changns24@mails.jlu.edu.cn,
jiyj@jlu.edu.cn, zhaoxuejiao@jlu.edu.cn, luanhui@jlu.edu.cn

[2]Key Laboratory of Geophysical Exploration Equipment Ministry of Education
Jilin University, Changchun 130000, China

Abstract – Superconducting Quantum Interference Devices Time-Domain Electromagnetic Method (SQUID TEM) is currently the most accurate electromagnetic detection technology used in geophysics. However, SQUID is highly susceptible to electromagnetic interference in outdoor spaces, so it needs to work continuously and stably in a Dewar bucket wrapped with a metal shielding material. Therefore, the influence of the metal shielding thin layer on the observation signal cannot be ignored. We propose a vector finite element method based on unstructured grids to spatially model the sleeve formed by the metal shielding thin layer wrapped around the SQUID and analyze the influence of the metal shielding sleeve on the SQUID TEM observation signal. Firstly, we derive the governing equations from Maxwell's equations. Secondly, the Galerkin method is used for finite element discretization of the control equations, and unstructured mesh discretization is applied to the metal shielding sleeve and other computational areas. By solving the interpolation basis functions of tetrahedral vector elements, the local equations of each element are obtained and combined into a global large sparse matrix. Finally, the direct solution method is used to calculate the electromagnetic response at the observation points inside the metal shielding sleeve. The effectiveness and universality of the proposed method are verified through numerical simulations. Furthermore, through field experiments in the Da Hinggan Ling area, the necessity of metal shielding sleeves in field experiments and the reliability of the calculation results proposed have been demonstrated.

Index Terms – SQUID TEM, thin shielding layer modeling, unstructured tetrahedral mesh, vector finite element method.

I. INTRODUCTION

Superconducting Quantum Interference Devices Time-Domain Electromagnetic Method (SQUID TEM) is currently the most accurate electromagnetic detection method used for geophysical field surveys, with unique advantages in weak magnetic signal observation and polymetallic mineral exploration [1–6]. Due to the complex physical properties and parameter information of polymetallic ores in nature, most of them exhibit low resistivity or polarization characteristics in time-domain electromagnetic detection [7–10]. The physical properties of these ores are reflected in the sign reversal in the magnetic field signals observed by SQUID TEM systems [11, 12]. In actual field exploration, the SQUID sensor placed in a Dewar vessel containing liquid nitrogen must be wrapped with a certain thickness of metal material as a shielding sleeve outside the Dewar vessel to achieve spatial electromagnetic interference shielding, so as to achieve long-term stable operation of the system [13–15]. The effective signals observed by SQUID sensors, especially the polarized signals containing deep mineral layer information, are usually on the order of pT $(10^{-12}\mathrm{T})$ or even fT $(10^{-15}\mathrm{T})$, and the weak electromagnetic signals that characterize deep information are usually in the late low-frequency range. Therefore, it is very necessary to study the influence of

Submitted On: October 13, 2025
Accepted On: March 24, 2026

https://doi.org/10.13052/2026.ACES.J.410304

metal shielding sleeves on the observation signal in the SQUID TEM detection.

In order to achieve mesh modeling of curved surfaces and numerical simulation of spatial electromagnetic response in geophysical methods, scholars have conducted extensive research on mesh partitioning methods and numerical simulation methods. He et al. proposed a method that combines curved hexahedral mesh and regular hexahedral mesh to solve the problem of the influence of the surface topography and gradient approximation on inversion results [16]. Cao et al. used unstructured tetrahedral mesh to simulate complex underground structures and rugged terrain and successfully achieved forward modeling and inversion calculation of the Z-axis tipper electromagnetic (ZTEM) using the finite element method [17]. Zhu et al. achieved numerical simulation of the electromagnetic response of complex underground structures in electromagnetic (EM) detection by introducing a spectral element method based on unstructured tetrahedral grids [18]. Key used unstructured triangular or quadrilateral grids to simulate geometric shapes that conform to actual measurements, and then accurately calculated electromagnetic responses through adaptive finite element method [19]. Li et al. simulated the geometric shapes of complex models based on unstructured tetrahedral grids and solved the marine controlledsource electromagnetic (CSEM) response using adaptive finite element method [20]. Zhou et al. used an unstructured tetrahedral mesh to accurately discretize the true complex shape of unexploded bombs and combined it with the finite element method to accurately simulate the time-domain electromagnetic response of unexploded bombs in TEM measurements [21]. Rong et al. proposed an arbitrary anisotropic inversion method based on unstructured tetrahedral mesh discretization, which can adapt well to complex structures such as Earth's terrain and coastline, and ultimately produce inversion results that conform to actual geological data [22]. In summary, whether obtaining accurate numerical simulation results through forward modeling or achieving outcomes more consistent with actual geological data via inverse modelling, it is necessary to take into account the geometric modeling of the actual survey situation. Furthermore, realistic geometric modeling and appropriate numerical simulation methods are key to accurately obtaining electromagnetic responses. Therefore, it is very important to accurately calculate the electromagnetic response at the observation point of the SQUID TEM system under the condition of a thin shielding sleeve.

At present, scholars have a certain theoretical research basis for the numerical calculation of spatial electromagnetic field distribution with thin layers. Liu et al. used the finite difference method and nonuniform mesh partitioning technique to study the influence of metal thin layers on the detection of effective anomalous signals in TEM detection. The results showed that metal thin layers would reduce the detection sensitivity of TEM and weak the electromagnetic response of low resistivity anomalous targets [23]. Zhou et al. proposed an enriched finite element method to numerically simulate the electromagnetic response of magneto electro elastic composite materials excited by external electric or magnetic fields and improved the solution accuracy through grid refinement [24]. Etse et al. proposed a method that combined homogenization of multi-layer shielding layers with the second-order AMSL method to accurately model thin layers of metal composite materials and applied it to magnetic shielding [25]. Gao et al. used the finite element method to model and calculate multi-layer metal thin shell structures for magnetic shielding, quantitatively analyze their electromagnetic characteristics, and provided a theoretical basis for precision measurement research of low-noise magnetic shielding [26]. Korkotadze et al. calculated the near-field shielding effect of two-layer and three-layer thin plates based on vector wave equations and boundary conditions, which can predict the shielding effect of multi-layer plates under known material properties and help determine the optimal thickness of the shielding layer [27]. In addition, some scholars used commercial software based on finite element method for numerical simulation and calculation and made significant progress in various fields such as simulating electromagnetic interference of shielded cables [28], simulating the effects of return stroke parameters and soil water content on EMF characteristics [29], and simulating the influence of augmented rail geometry on rail gun design parameters [30]. The availability of finite element commercial software is only for the problems that are suitable for the software to solve, and there may be issues with low computing efficiency [31]. It can be seen that the finite element method and its extensions are one of the flexible and efficient important techniques among many methods in different fields of studying electromagnetic field related problems [24, 26, 32–34]. However, most scholars' research is limited to the physical modeling of shielding thin-layer materials and the analysis of shielding performance, and the computational research area is mostly within the calculation area near the thin layer, which has not yet involved the problem of low computational efficiency or even non-convergence that may occur due to a large calculation area. Due to the fact that SQUID TEM long wire sources are usually several kilometers long, and the distribution of underground ore bodies detected is often tens of meters or even thousands of meters, it is necessary to study how to calculate the influence of small-sized metal shielding sleeves on weak signals observed inside the cylinder in large-scale space.

We propose a vector finite element method based on unstructured grids for modeling thin metal shielding sleeves and analyze their impact on SQUID TEM observation signals. In the first place, the thin metal shielding sleeve is finely modeled using the unstructured tetrahedral mesh, and the entire calculation area is discretized reasonably. The control equations are derived from the Maxwell equations, and the Galerkin method is used for finite element discretization of the control equations. Then, the metal shielding sleeve and other calculation areas are discretized using the unstructured mesh. Secondly, by solving the interpolation basis functions of tetrahedral vector elements, the local equations of each element are obtained, and the local equations are combined into a global large sparse matrix. Finally, the direct solution method is used to calculate the electromagnetic response at the observation point with a metal shielding sleeve. To demonstrate the effectiveness of our proposed method, we have designed three typical models and have calculated the effects of metal shielding sleeves on the SQUID TEM observation signals under different models. In addition, we have also verified the correctness of the proposed method's calculation conclusions through field experiments in the Da Hinggan Ling area.

II. THEORY

A. Vector finite element method

The first and second equations of Maxwell's system of equations:

$$\nabla \times \boldsymbol{E} = -i\omega\mu\boldsymbol{H}, \tag{1}$$

$$\nabla \times \boldsymbol{H} = \sigma\boldsymbol{E} + \boldsymbol{J}. \tag{2}$$

The dual curl equation of the electric field can be derived:

$$\nabla \times \nabla \times \boldsymbol{E} + i\omega\mu\sigma(\omega)\boldsymbol{E} = i\omega\mu\boldsymbol{J}. \tag{3}$$

In order to avoid the problem of non-singularity caused by the source term during the solving process, the total field is written in the form of the superposition of the background field and the quadratic field, that is

$$\boldsymbol{E} = \boldsymbol{E}_b + \boldsymbol{E}_s. \tag{4}$$

Therefore, the control equation can be written as:

$$\nabla \times \nabla \times \boldsymbol{E}_s + i\omega\mu_0\sigma(\omega)\boldsymbol{E}_s = -i\omega\mu_0\sigma_a(\omega)\boldsymbol{E}_p. \tag{5}$$

For the convenience of subsequent solving

$$\kappa^2 = i\omega\mu_0\sigma, \tag{6}$$

$$\kappa_s^2 = -i\omega\mu_0\sigma_a. \tag{7}$$

Substituting equations (6) and (7) into equation (5) and organizing them, we can obtain:

$$\nabla \times \nabla \times \boldsymbol{E}_s + \kappa^2\boldsymbol{E}_s = \kappa_s^2\boldsymbol{E}_p. \tag{8}$$

The Galerkin method [35] is used to discretize equation (8), and the residual expression of the control equation is:

$$\boldsymbol{R} = \nabla \times \nabla \times \boldsymbol{E}_s^0 + \kappa^2\boldsymbol{E}_s^0 - \kappa_s^2\boldsymbol{E}_p, \tag{9}$$

where $\boldsymbol{E}_s^0$ is the approximate solution of the quadratic field to be solved.

Let the weight function be $\boldsymbol{W}$, and let the residual $\boldsymbol{R}$ of all units in the calculation area and the inner product of the weight function $\boldsymbol{W}$ be zero to seek the optimal solution, that is:

$$\iiint_\Omega \boldsymbol{R}\cdot\boldsymbol{W}dv = 0. \tag{10}$$

By substituting the residual equation into equation (10), we can obtain:

$$\iiint_\Omega \boldsymbol{W}\cdot\nabla\times\nabla\times\boldsymbol{E}_s^0 d\Omega + \iiint_\Omega \boldsymbol{W}\cdot(\kappa^2\boldsymbol{E}_s^0 - \kappa_s^2\boldsymbol{E}_p)d\Omega = 0. \tag{11}$$

By using Green's formula to expand the first term of equation (11), we can obtain:

$$\begin{aligned}\iiint_\Omega \boldsymbol{W}\cdot\nabla\times\nabla\times\boldsymbol{E}_s^0 d\Omega &= \iiint_\Omega (\nabla\times\boldsymbol{W})\cdot(\nabla\times\boldsymbol{E}_s^0)d\Omega \\ &\quad - \iint_\Gamma \boldsymbol{W}\times\left(\nabla\times\boldsymbol{E}_s^0\right)\cdot\boldsymbol{n}d\Gamma.\end{aligned} \tag{12}$$

That is:

$$\begin{aligned}\iiint_\Omega \boldsymbol{W}\cdot\nabla\times\nabla\times\boldsymbol{E}_s^0 d\Omega &= \iiint_\Omega (\nabla\times\boldsymbol{W})\cdot\left(\nabla\times\boldsymbol{E}_s^0\right)d\Omega \\ &\quad - \iint_\Gamma \boldsymbol{W}\times\left(\nabla\times\boldsymbol{E}_s^0\times\boldsymbol{n}\right)d\Gamma,\end{aligned} \tag{13}$$

$$\begin{aligned}\iiint_\Omega \boldsymbol{W}\cdot\nabla\times\nabla\times\boldsymbol{E}_s^0 d\Omega &= \iiint_\Omega (\nabla\times\boldsymbol{W})\cdot\left(\nabla\times\boldsymbol{E}_s^0\right)d\Omega \\ &\quad + \iint_\Gamma \boldsymbol{W}\times\left(\boldsymbol{n}\times\nabla\times\boldsymbol{E}_s^0\right)d\Gamma,\end{aligned} \tag{14}$$

where $\boldsymbol{n}$ is the unit normal vector on the surface Γ. The electric field within each unit can be written as:

$$\boldsymbol{E}^0 = \sum_{i=1}^{6}\boldsymbol{E}_i\boldsymbol{N}_i, \tag{15}$$

where $\boldsymbol{N}_i$ is the vector basis function and i is the number of each edge of the tetrahedral element.

Based on the Galerkin method, the weight function is taken as the vector basis function and further integrated within the vector finite element calculation area:

$$\iiint_{\Omega}[(\nabla\times\boldsymbol{E}_s^0)\cdot(\nabla\times\boldsymbol{N})+\kappa^2\boldsymbol{E}_s^0\cdot\boldsymbol{N}]d\Omega$$
$$=\kappa^2\iiint_{\Omega}\boldsymbol{E}_p\cdot\boldsymbol{N}d\Omega. \tag{16}$$

Discretize each tetrahedral element to obtain the equation in the discrete form of each tetrahedron:

$$[\boldsymbol{A}_{mn}][\boldsymbol{E}_n]=[\boldsymbol{T}_n], \tag{17}$$

where m and n represent the labels of rows and columns, $\boldsymbol{A}$ is the left-hand term matrix of the equation, and $\boldsymbol{T}$ is the right-hand term matrix of the equation.

Combine all equations in equation (17) into a global equation and represent it as a sparse matrix:

$$[\boldsymbol{A}][\boldsymbol{E}]=[\boldsymbol{T}]. \tag{18}$$

By using the direct solution method to solve equation (18), the electric field matrix can be obtained, and then the magnetic field matrix can be solved from equation (1). Finally, the time-domain magnetic field response can be obtained through frequency-time transformation [36].

B. Unstructured tetrahedral mesh and vector interpolation basis function solution

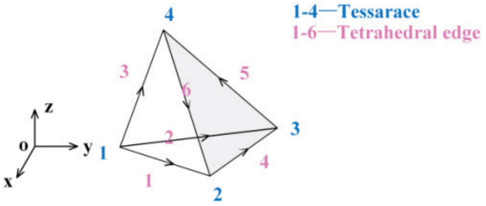

Fig. 1. Schematic diagram of the unstructured tetrahedral unit.

In any tetrahedral element, as shown in Fig. 1, the expression of the basis function to be solved can be set as:

$$\Phi^e(x,y,z)=a^e+b^ex+c^ey+d^ez, \tag{19}$$

where e is tetrahedral unit numbers and a^e, b^e, c^e, and d^e are undetermined coefficients.

By substituting equation (19) into each vertex, we can obtain:

$$\Phi_1^e(x,y,z)=a^e+b^ex_1+c^ey_1+d^ez_1, \tag{20}$$
$$\Phi_2^e(x,y,z)=a^e+b^ex_2+c^ey_2+d^ez_2, \tag{21}$$
$$\Phi_3^e(x,y,z)=a^e+b^ex_3+c^ey_3+d^ez_3, \tag{22}$$
$$\Phi_4^e(x,y,z)=a^e+b^ex_4+c^ey_4+d^ez_4, \tag{23}$$

where $(x_1,y_1,z_1),(x_2,y_2,z_2),(x_3,y_3,z_3)$, and (x_4,y_4,z_4) correspond to the coordinates of vertices $1,2,3$, and 4, respectively.

By solving equations (20)–(23) simultaneously, we can obtain:

$$a^e=\frac{1}{6}\begin{vmatrix}1&1&1&1\\x_1&x_2&x_3&x_4\\y_1&y_2&y_3&y_4\\z_1&z_2&z_3&z_4\end{vmatrix}$$
$$=\frac{1}{6V^e}(a_1^e\Phi_1^e+a_2^e\Phi_2^e+a_3^e\Phi_3^e+a_4^e\Phi_4^e), \tag{24}$$

$$b^e=\frac{1}{6V^e}\begin{vmatrix}1&1&1&1\\\Phi_1^e&\Phi_2^e&\Phi_3^e&\Phi_4^e\\y_1&y_2&y_3&y_4\\z_1&z_2&z_3&z_4\end{vmatrix}$$
$$=\frac{1}{6V^e}(b_1^e\Phi_1^e+b_2^e\Phi_2^e+b_3^e\Phi_3^e+b_4^e\Phi_4^e), \tag{25}$$

$$c^e=\frac{1}{6V^e}\begin{vmatrix}1&1&1&1\\x_1&x_2&x_3&x_4\\\Phi_1^e&\Phi_2^e&\Phi_3^e&\Phi_4^e\\z_1&z_2&z_3&z_4\end{vmatrix}$$
$$=\frac{1}{6V^e}(c_1^e\Phi_1^e+c_2^e\Phi_2^e+c_3^e\Phi_3^e+c_4^e\Phi_4^e), \tag{26}$$

$$d^e=\frac{1}{6V^e}\begin{vmatrix}1&1&1&1\\x_1&x_2&x_3&x_4\\y_1&y_2&y_3&y_4\\\Phi_1^e&\Phi_2^e&\Phi_3^e&\Phi_4^e\end{vmatrix}$$
$$=\frac{1}{6V^e}(d_1^e\Phi_1^e+d_2^e\Phi_2^e+d_3^e\Phi_3^e+d_4^e\Phi_4^e), \tag{27}$$

where V^e represents the volume of tetrahedral units:

$$V^e=\frac{1}{6}\begin{vmatrix}1&1&1&1\\x_1&x_2&x_3&x_4\\y_1&y_2&y_3&y_4\\z_1&z_2&z_3&z_4\end{vmatrix}. \tag{28}$$

According to the coordinates of the four vertices of the tetrahedral element, each undetermined coefficient in the basis function equation (19) to be solved can be calculated separately, that is:

$$a_1^e = \begin{vmatrix} x_2 & y_2 & z_2 \\ x_3 & y_3 & z_3 \\ x_4 & y_4 & z_4 \end{vmatrix}, \quad a_2^e = -\begin{vmatrix} x_1 & y_1 & z_1 \\ x_3 & y_3 & z_3 \\ x_4 & y_4 & z_4 \end{vmatrix},$$

$$a_3^e = \begin{vmatrix} x_1 & y_1 & z_1 \\ x_2 & y_2 & z_2 \\ x_4 & y_4 & z_4 \end{vmatrix}, \quad a_4^e = -\begin{vmatrix} x_1 & y_1 & z_1 \\ x_2 & y_2 & z_2 \\ x_3 & y_3 & z_3 \end{vmatrix},$$

$$b_1^e = -\begin{vmatrix} 1 & y_2 & z_2 \\ 1 & y_3 & z_3 \\ 1 & y_4 & z_4 \end{vmatrix}, \quad b_2^e = \begin{vmatrix} 1 & y_1 & z_1 \\ 1 & y_3 & z_3 \\ 1 & y_4 & z_4 \end{vmatrix},$$

$$b_3^e = -\begin{vmatrix} 1 & y_1 & z_1 \\ 1 & y_2 & z_2 \\ 1 & y_4 & z_4 \end{vmatrix}, \quad b_4^e = \begin{vmatrix} 1 & y_1 & z_1 \\ 1 & y_2 & z_2 \\ 1 & y_3 & z_3 \end{vmatrix},$$

$$c_1^e = -\begin{vmatrix} x_2 & 1 & z_2 \\ x_3 & 1 & z_3 \\ x_4 & 1 & z_4 \end{vmatrix}, \quad c_2^e = \begin{vmatrix} x_1 & 1 & z_1 \\ x_3 & 1 & z_3 \\ x_4 & 1 & z_4 \end{vmatrix},$$

$$c_3^e = -\begin{vmatrix} x_1 & 1 & z_1 \\ x_2 & 1 & z_2 \\ x_4 & 1 & z_4 \end{vmatrix}, \quad c_4^e = \begin{vmatrix} x_1 & 1 & z_1 \\ x_2 & 1 & z_2 \\ x_3 & 1 & z_3 \end{vmatrix},$$

$$d_1^e = -\begin{vmatrix} x_2 & y_2 & 1 \\ x_3 & y_3 & 1 \\ x_4 & y_4 & 1 \end{vmatrix}, \quad d_2^e = \begin{vmatrix} x_1 & y_1 & 1 \\ x_3 & y_3 & 1 \\ x_4 & y_4 & 1 \end{vmatrix},$$

$$d_3^e = -\begin{vmatrix} x_1 & y_1 & 1 \\ x_2 & y_2 & 1 \\ x_4 & y_4 & 1 \end{vmatrix}, \quad d_4^e = \begin{vmatrix} x_1 & y_1 & 1 \\ x_2 & y_2 & 1 \\ x_3 & y_3 & 1 \end{vmatrix}.$$

Substituting the above coefficients into the expression of the basis function to be solved, the basis function can be written as:

$$\Phi^e(x,y,z) = \sum_{i=1}^{4} L_i^e(x,y,z)\Phi_i^e, \tag{29}$$

where $L_i^e(x,y,z)$ is the interpolation basis function, whose expression is:

$$L_i^e(x,y,z) = \frac{1}{6V^e}(a_i^e + b_i^e x + c_i^e y + d_i^e z). \tag{30}$$

Therefore, the tetrahedral vector basis function can be expressed as:

$$\boldsymbol{N}_i^e = (L_{i_1}^e \nabla L_{i_2}^e - L_{i_2}^e \nabla L_{i_1}^e) l_i^e. \tag{31}$$

It satisfies the condition of zero divergence, and the curl expression is:

$$\nabla \times \boldsymbol{N}_i^e = 2(\nabla L_{i_1}^e \times \nabla L_{i_2}^e) \cdot l_i^e. \tag{32}$$

That is:

$$\nabla \times N_i^e = \frac{2l_i^e}{(6V^e)^2} \begin{bmatrix} (c_{i1}^e d_{i2}^e - d_{i1}^e c_{i2}^e)\boldsymbol{x} \\ +(d_{i1}^e b_{i2}^e - b_{i1}^e d_{i2}^e)\boldsymbol{y} \\ +(b_{i1}^e c_{i2}^e - c_{i1}^e b_{i2}^e)\boldsymbol{z} \end{bmatrix}, \tag{33}$$

where $\boldsymbol{x}, \boldsymbol{y}$, and $\boldsymbol{z}$ are the unit vectors of direction x, y, and z, respectively.

III. NUMERICAL RESULTS

In order to investigate the effect of the metal shielding layer wrapped around the Dewar vessel with SQUID on the measurement of secondary field signals in the SQUID TEM observation experiments, we have first modeled and meshed the SQUID TEM experimental system based on the actual situation. Then, we have studied the influence of the shielding layer on the observed signals when the measurement background is a uniform ground. In this section, we compare the proposed method with the calculation results of the traditional finite element method to verify the accuracy and correctness of our proposed method.

Subsequently, we introduce the low resistivity anomalous body into the uniform ground model and study the impact of the shielding layer on the observation signal by calculating the electromagnetic response curve with and without the shielding layer. In this section, we study and discuss the influence of the thickness of the metal shielding layer on the magnetic field signal.

Finally, to demonstrate the universality of our proposed method, we introduce the polarized anomalous body into the uniform ground model and analyze the influence of the shielding layer on the electromagnetic response of the SQUID TEM system for detecting polarized anomalies. In addition, we discuss and compare the effect of the shielding layer on the electromagnetic response of SQUID TEM system detecting polarization anomalies under different polarization parameters.

We have constructed a calculation area of 10 km × 5 km × 2 km, as shown in Fig. 2, with an air layer and a uniform ground, respectively. The length of the long wire source is 1 km, and the current is 20 A. The long wire source is placed in the large geological formation along the x-axis direction, with a horizontal distance of 300 m from the center point of the source to the center point of the metal shielding cylinder. Considering that the commonly used shielding material for SQUID TEM systems in actual field measurements is aluminum foil [6, 12, 37, 38], we have constructed a cylindrical shielding sleeve with an outer diameter of 30 cm and an

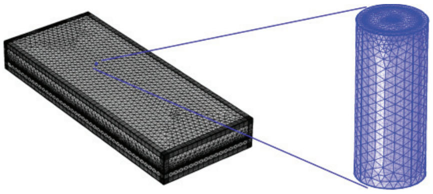

Fig. 2. SQUID TEM observation system and modeling of thin shielding layer.

inner diameter of 24 cm. The outer shielding material is aluminum and the conductivity is 3×10^7 S/m. In field experiments, the aluminum foil usually wrapped around the cylinder is more than ten layers, so the thickness of the aluminum metal shielding layer is designed to be 60 μm.

A. Influence of a thin shielding layer on the SQUID TEM signal under a uniform half space model

On the basis of the above modeling, the conductivity of a uniform ground is set to 0.01 S/m, and the horizontal distance between the center of the shielding bucket and the long wire source is 300 m. The electromagnetic response of the observation point at a distance of 10 cm from the ground surface inside the shielding bucket and the electromagnetic response at the same observation point without the shielding bucket are calculated separately. The calculation results are shown in Fig. 3.

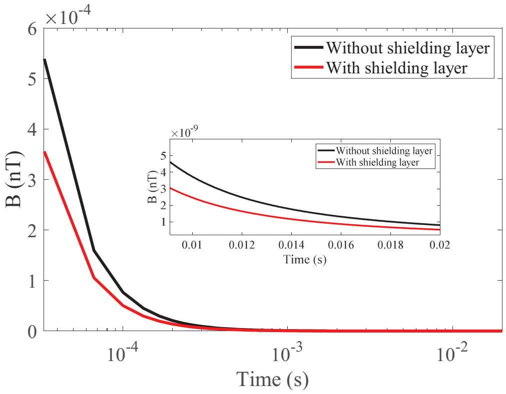

Fig. 3. Influence of a thin shielding layer on the SQUID TEM signal under a uniform half-space model.

The calculation results in Fig. 3 indicate that when a shielding bucket is present, the magnetic field response inside the shielding bucket is always smaller than that without the shielding bucket, indicating that the shielding bucket has a certain weakening effect on the magnetic field signal observed in the SQUID TEM system. It can be clearly seen that the presence of the shielding bucket has a stronger weakening effect on early signals.

In order to verify the correctness and effectiveness of the proposed method, taking the uniform geodetic model as an example, we have set the same model parameters and compared the calculation results of the traditional finite element method with those of the method proposed in Fig. 3. The comparison results are shown in Fig. 4.

From the calculation results in Fig. 4, it can be seen that the proposed method is consistent with the traditional finite element method. Therefore, the correctness and effectiveness of the numerical simulation method proposed have been verified.

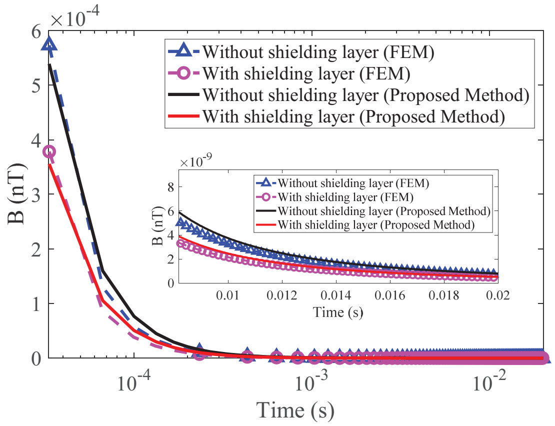

Fig. 4. Comparison of calculation results between the unstructured grid vector finite element method and the finite element method.

B. Influence of a thin shielding layer on the SQUID TEM signal under a low resistivity anomalous body model

On the basis of the above modeling, a uniform earth conductivity of 0.01 S/m is set, and a low resistivity anomalous body of 500 m × 500 m × 200 m is set at 500 m below the surface with a conductivity of 0.05 S/m. The center of the shielding cylinder with a thin layer of metal aluminum is set to coincide with the center of the anomalous body in the vertical direction. The electromagnetic response at the observation point 10 cm away from the surface inside the shielding cylinder and the electromagnetic response at the same observation point without a shielding cylinder are calculated separately. The calculation results are shown in Fig. 5.

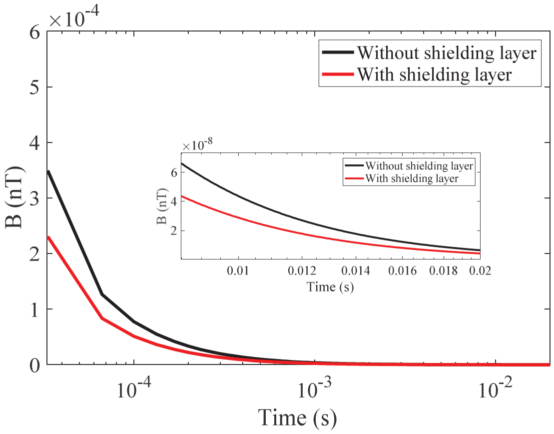

Fig. 5. Influence of a thin shielding layer on the SQUID TEM signal under a low resistivity anomaly model.

The calculation results in Fig. 5 indicate that, in addition to the attenuation effect on the SQUID TEM observation signal when the shielding bucket is present, compared with the magnetic field response curve calculated for the uniform half-space model in Fig. 3, the magnetic field amplitude of the corresponding curve in Fig. 5 is significantly smaller due to the presence of the low resistivity anomalous body. Therefore, the introduction of shielding bucket modeling will not affect the basic characteristics of TEM observation signals under low resistivity anomaly models, that is, the magnetic field signal inside the shielding bucket can still be used to display the relative magnitude of the resistivity of the anomalous body.

Compared with the magnetic field response without the shielding bucket (black curve in Fig. 5), the TEM magnetic field response curve observed inside the shielding bucket will first decay to the resolution threshold of the SQUID sensor, especially for late time channels. Due to the deeper geological exploration depth corresponding to the late time channel in TEM detection, the signal attenuation caused by the presence of the shielding bucket would ideally result in a shallower maximum effective depth for future data interpretation and inversion.

In order to further study and analyze the influence of the thickness of the metal shielding thin layer on the magnetic field signal observed by SQUID TEM, based on the low resistivity anomalous body model mentioned above, we assume that the thickness of a single layer of aluminum foil is 1 μm, and calculate the electromagnetic response of the observation point position 10 cm away from the ground surface in the cylinder under shielding layers $1, 5, 10, 20$, and 50, respectively. That is, the corresponding shielding layer thickness $\mathrm{D} = 1\ \mu\mathrm{m}, 5\ \mu\mathrm{m}, 10\ \mu\mathrm{m}, 20\ \mu\mathrm{m}$ and 50 μm, and the calculation results are shown in Fig. 6.

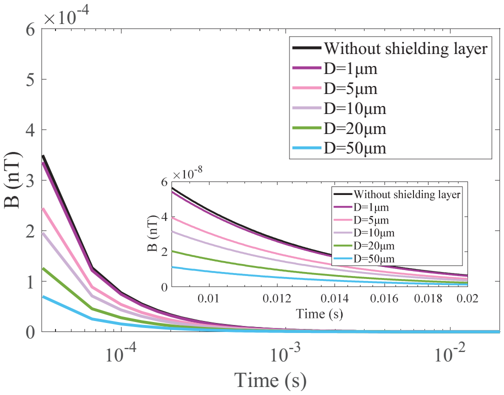

Fig. 6. Influence of a thin shielding layer thickness on the SQUID TEM signal under a low resistivity anomaly model.

From the calculation results in Fig. 6, it can be seen that compared with the magnetic field curve of the unshielded thin layer, when the shielding layer is 1 μm, both curves almost overlap in both the early and late stages, and the shielding layer has little effect on the magnetic field response. As the thickness of the shielding layer increases, the early magnetic field values significantly decrease, indicating that the thicker the shielding layer, the better the shielding effect. However, if the shielding layer is too thick, the attenuation curve will become flatter (blue curve in Fig. 6), and it will no longer be able to effectively distinguish whether low resistivity anomalies exist. Therefore, the thickness of the shielding thin layer is not necessarily the thicker the better. There is a suitable thickness that could shield the SQUID from external electromagnetic interference while still allowing the abnormal body information carried by the attenuation curve to be clearly distinguished.

C. The influence of a thin shielding layer on the SQUID TEM signal under a polarized anomalous body model

On the basis of the above modeling, the conductivity of a uniform ground is set to 0.01 S/m. Based on typical parameters of common polymetallic ores, a 500 m × 500 m × 200 m polarization anomaly body is set 500 m below the surface. The Cole-Cole model parameters of the anomaly body are zero frequency conductivity of 0.1 S/m, polarization rate of 0.5, time constant of 2×10^{-3} s, and dispersion coefficient of 0.5. We set the center of the shielding cylinder with a thin layer of metal aluminum to coincide with the center of the anomalous body in the vertical direction. Then, We calculate the electromagnetic response at the observation point 10 cm away from the ground surface inside the shielding cylinder and the electromagnetic response at the same observation point without the shielding cylinder. The calculation results are shown in Fig. 7.

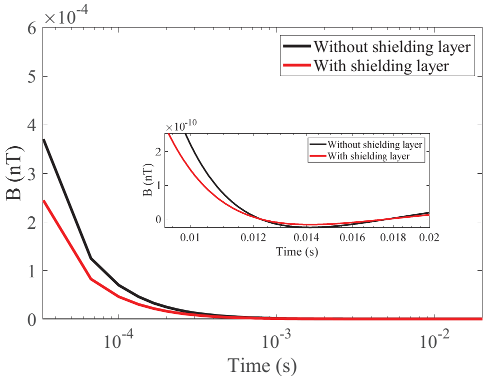

Fig. 7. Influence of a thin shielding layer on the SQUID TEM signal under a polarized anomaly model.

The calculation results in Fig. 7 indicate that, in addition to the attenuation effect on the SQUID TEM observation signal when the shielding bucket is present, there are two intersection points in the magnetic field response curves of Fig. 7 with and without the shielding bucket compared to Fig. 3. From the perspective of the electromagnetic field, this indicates that both positive and negative response parts are attenuated by the shielding bucket, rather than the polarization signal being larger when the shielding bucket is present than when it is absent. Therefore, in actual detection, the presence of a shielding bucket has a significant impact on the polarization information of rock and ore carried by the polarization signal, so the influence of a metal thin layer shielding bucket cannot be ignored.

In order to further analyze the influence of the presence of metal shielding thin layers on the electromagnetic response of polarized anomalous bodies, we have calculated the magnetic field curves of the anomalous body with different polarizations at the shielding layer thickness of $D = 60\ \mu$m, and we also have studied the differences between them. We have set polarizations of $\eta = 0.2, \eta = 0.6$, and $\eta = 0.8$, respectively, and have studied the influence of metal shielding thin layers on the electromagnetic response of anomalous bodies with different degrees of polarization. The calculation results are shown in Figs. 8 and 9, where Fig. 9 is a locally enlarged view of the polarization response characteristic segment of the curve in Fig. 8.

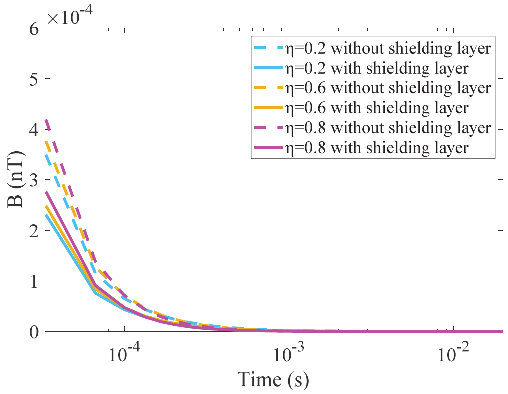

Fig. 8. Magnetic field response curves of anomalous bodies with different polarizations under the same shielding thin layer condition.

From Fig. 8, it can be seen that the higher the polarizability of the anomalous body, the greater the attenuation effect of the shielding thin layer on the early signals observed by SQUID TEM. Furthermore, Fig. 9 is a partial enlargement of the polarization response characteristic segments of the curve in Fig. 8. From Fig. 9 (a), we can see that the weak polarization signal will no longer exhibit negative response in the late stage, and the introduction of the shielding layer will not cause false amplitude response in the curve that originally had no negative response. The phenomenon consistent with Fig. 7 is observed in Figs. 9 (b) and (c). Comparing Figs. 9 (b) and (c), it can be seen that the introduction of a shielding thin layer only reduces the absolute value of the maximum negative value representing the polarization response characteristic and does not completely eliminate the polarization response that should have existed. Therefore, the method proposed in this paper can be used to accurately model the shielding thin layer and analyze its impact on the SQUID TEM observation signal, providing reliable theoretical guidance for practical detection.

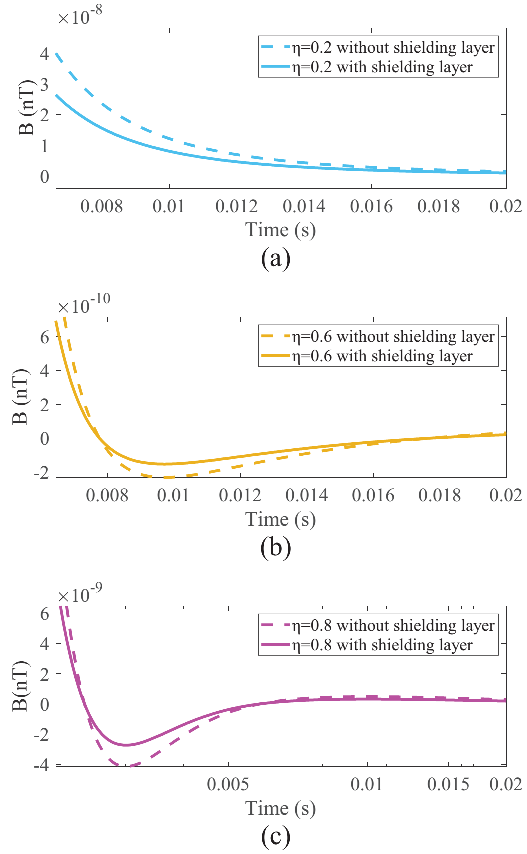

Fig. 9. Magnetic field curves of polarization response amplification segments of anomalous bodies with different polarizations under the same shielding thin layer conditions: (a) $\eta = 0.2$, (b) $\eta = 0.6$, (c) $\eta = 0.8$.

In the above three typical geoelectric models, the introduction of the shielding layer has a certain degree of impact on the magnetic field signal observed by SQUID TEM, which is reflected in the characteristics of the electromagnetic response curve. Table 1 summarizes the magnetic field characteristics with and without the shielding bucket.

The summary in Table 1 indicates that the presence of the shielding bucket has different effects on the SQUID TEM observation signal depending on the geological model. The more parameters in the geoelectric model, the more complex it becomes, and the more diverse the impact of the shielding bucket on the SQUID TEM observation signal. This highlights the necessity of precise calculation and analysis of the influence of the thin shielding layer on SQUID TEM observation signal. Furthermore, the method proposed also lays a theoretical foundation for future research on how to accurately interpret and invert data based on the impact of the shielding bucket.

Table 1: Summary of the magnetic field characteristics with and without the shielding layer

Model	Characterization	Result
Uniform Half Space	① The magnetic field inside the shielding bucket is always smaller than that without the shielding bucket. ② The shielding bucket has a certain weakening effect on the magnetic field signal.	Fig. 3
Low Resistivity Anomalous Body Model	① The magnetic field signal inside the shielding bucket could still display the relative magnitude of the resistivity of the anomalous body. ② The signal attenuation caused by the shielding bucket would result in a shallower maximum effective depth for later data interpretation	Fig. 5
Polarized Anomalous Body Model	① The higher the polarizability of the anomalous body, the greater the attenuation effect of the shielding thin layer on the early signal. ② The shielding thin layer only reduces the absolute value of the maximum negative value representing the polarization response characteristic.	Fig. 7 Fig. 8 Fig. 9

IV. FIELD SURVEY EXPERIMENT AND RESULTS

To further verify the effectiveness of the proposed method and the reliability of the calculation conclusions, a long wire source SQUID TEM field experiment has been conducted in the Da Hinggan Ling area of Heilongjiang Province, China. The detection area is located on the east side of the main peak basin in the northern section of the Da Hinggan Ling, with an average elevation of 1300 m and a relative elevation difference of 300–450 m. The main metallic minerals present are lead zinc polymetallic deposits with polarization effects. The surrounding rocks mainly include marble and skarn, and the shallow surface mainly consists of gravel and clay.

The instruments used in the experiment are shown in Fig. 10. The metal material wrapped around the acrylic cylinder is aluminum foil. The transmitter generates bipolar trapezoidal waves with a period of 80 ms to excite the underground target ore body and generate electromagnetic response. The SQUID TEM system has a resolution of 100 fT and a sampling rate of 30 kHz for the receiver.

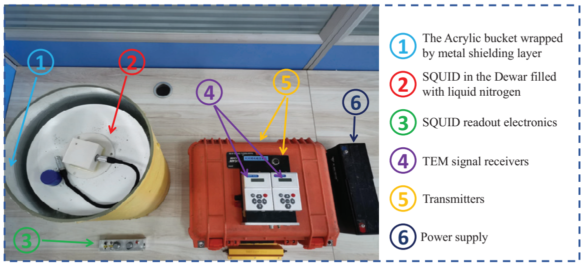

Fig. 10. SQUID TEM experimental instruments.

The actual location and layout of the measuring points in the survey area are shown in Fig. 11. The emission source is 1.7 km long and emits a current of 18 A. A total of 12 measurement points are measured from the near source to the far source, with a distance of 50 m between each point. Due to the serious influence of high-power power supply vehicles and spatial electromagnetic interference, the SQUID sensor without the shielding bucket could only work intermittently at the two furthest points from the emission source, but there is still a problem of frequent loss of lock and unstable measurement [39]. Therefore, very little effective data can be collected, which also indicates the necessity and importance of metal shielding layer. Moreover, we have taken the measurement results of the observation point furthest from the emission source as the example to verify the reliability of the method proposed in this paper and its conclusions. The measurement results of the furthest point and the typical measurement curves caused by SQUID unlocking due to electromagnetic interference are shown in Fig. 12.

As shown in Fig. 12 (a), the influence of the shielding bucket on the experimental measurement results is almost identical to the trend obtained from the numerical simulation method proposed. Due to the fact that the actual earth is not uniform and the actual parameters of the geological environment are very complex, the

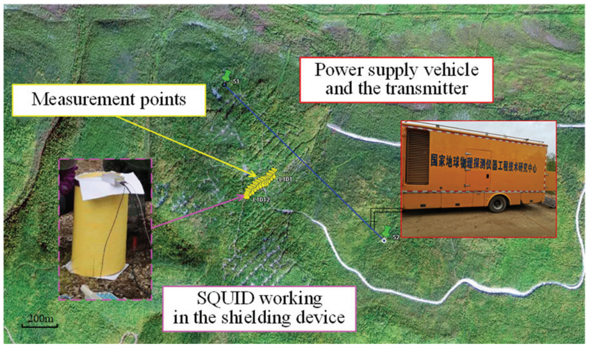

Fig. 11. Layout of SQUID TEM field experiment site in the Da Hinggan Ling area.

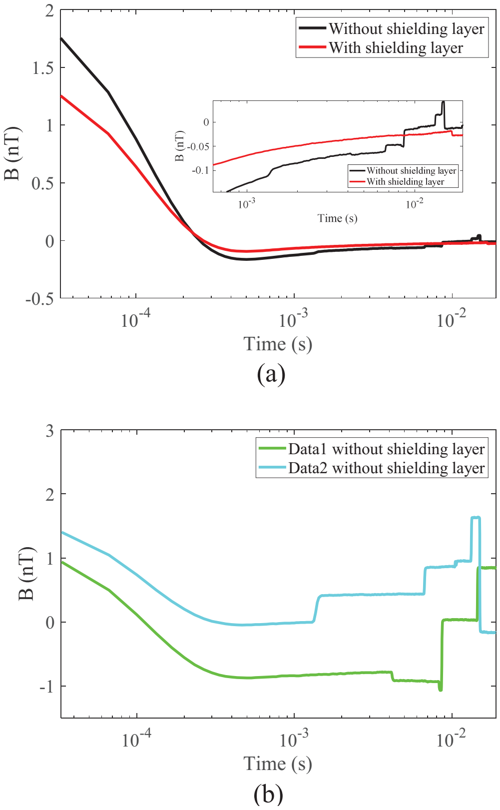

(a)

(b)

Fig. 12. Measured SQUID TEM magnetic field signals: (a) comparison of electromagnetic response with and without the shielding cylinder at the furthest point and (b) typical unlocked magnetic field curves.

amplitude and attenuation rate of the magnetic field response curves obtained from experimental measurements are not exactly the same as those obtained from numerical simulations. However, the trend of the shielding bucket's influence on the SQUID TEM measurement results reflected by the two is almost alike.

Furthermore, due to the significant impact of external electromagnetic interference on the SQUID sensor when measuring without the shielding bucket, the interference on the later measurement curve is extremely severe, as shown in the enlarged part of Fig. 12 (a). Although we have conducted multiple measurements in the field, the SQUID sensor itself is still severely affected by surrounding electromagnetic interference in the unshielded environment, which leads to irregular jumps in the late-stage signal, resulting in a small segment of the signal intersecting with the signal measured in a shielded environment that should not have occurred. Therefore, the rock mineral resistivity information carried by the later signal is unreliable, which once again confirms the importance of measurement inside the shielding bucket.

Figure 12 (b) shows the magnetic field curves that can be measured without the shielding cylinder, however, most of the time in the experiment, the system cannot be locked for normal measurements. This also indicates that it is necessary to study the influence of metal shielding thin layers on SQUID TEM observation signals through the method proposed in this manuscript, which lays a theoretical foundation for further research on how to eliminate the influence of shielding thin layers on magnetic field response and improve detection resolution in the future.

V. CONCLUSION

We propose a vector finite element method based on unstructured grids. The Galerkin method is used to solve the vector basis functions, and the unstructured grids are discretized for the shielding thin layer and other calculation areas. Finally, the electromagnetic response calculation of the area with shielding thin layer is achieved. By calculating the effect of shielding thin layers on the SQUID TEM observation signals under different models, the influence of the presence of metal thin layer shielding sleeves on the SQUID TEM signals under three common model conditions has been summarized. Furthermore, the field detection experiments have been designed and conducted to verify the effectiveness and reliability of the proposed method in this paper. The method proposed can accurately calculate and analyze the impact of thin shielding layers on the SQUID TEM observation signals, providing theoretical basis and research foundation for the subsequent research on how to eliminate the influence of shielding thin layers and accurately invert observation data.

ACKNOWLEDGMENT

This work was supported by National Science and Technology Project of China No. 2024ZD1002605 and Key Laboratory of Geophysical Exploration Equipment, Ministry of Education (Jilin University) under Grant 20240104.

REFERENCES

[1] R. Stolz, M. Schiffler, M. Becken, A. Thiede, M. Schneider, G. Chubak, P. Marsden, A. B. Bergshjorth, M. Schaefer, and O. Terblanche, "SQUIDs for magnetic and electromagnetic methods in mineral exploration," *Mineral Economics*, vol. 35, pp. 467–494, 2022.

[2] R. Stolz, M. Schmelz, V. Zakosarenko, C. Foley, K. Tanabe, X. Xie, and R. L. Fagaly, "Superconducting sensors and methods in geophysical applications," *Superconductor Science and Technology*, vol. 34, pp. 1–33, 2021.

[3] E. Arai, "State-of-the-art geophysics for metal exploration," *Resource Geology*, vol. 71, pp. 470–491, 2021.

[4] H. Ren, Y. Wang, C. Chen, G. Fu, L. Qiu, L. Guo, C. Xie, Y. He, H. Sun, and J. Teng, "Underground laboratories · Deep underground observation · Scientific questions—Insights from observations of multi-physic fields in deep underground labs," *Science China Earth Sciences*, vol. 68, pp. 343–362, 2025.

[5] J. Wu, Q. Zhi, X. Deng, X. Wang, X. Chen, Y. Zhao, and Y. Huang, "Deep gold exploration with SQUID TEM in the Qingchengzi Orefield, Eastern Liaoning, Northeast China," *Minerals*, vol. 12, p. 102, 2022.

[6] I. Mohanty, R. Nagendran, L. Bisht, A. V. T. Arasu, R. Baskaran, B. V. L. Kumar, and M. B. Verma, "Development of SQUID based TDEM system and its utilization for field survey at Tumallapalle, Andhra Pradesh, India," *Journal of Applied Geophysics*, vol. 204, p. 104746, 2022.

[7] A. Revil, D. Mao, Z. Shao, M. F. Sleevi, and D. Wang, "Induced polarization response of porous media with metallic particles—Part 6: The case of metals and semimetals," *Geophysics*, vol. 82, pp. E97–E110, 2017.

[8] D. J. Marshall and T. R. Madden, "Induced polarization, a study of its causes," *Geophysics*, vol. 24, pp. 790–816, 1959.

[9] G. Xue, N. Zhou, B. Su, A. Zhang, Y. Yang, J. Mo, and X. Wu, "Geophysical exploration strategy for Cu-Ni-Co deposits in China: A review," *Geophysics*, vol. 89, pp. WB25–WB34, 2024.

[10] Z. Guo, G. Xue, J. Liu, and X. Wu, "Electromagnetic methods for mineral exploration in China: A review," *Ore Geology Reviews*, vol. 118, p. 103357, 2020.

[11] S. Du, Y. Zhang, Y. Pei, K. Jiang, L. Rong, C. Yin, Y. Ji, and X. Xie, "Study of transient electromagnetic method measurements using a superconducting quantum interference device as B sensor receiver in polarizable survey area," *Geophysics*, vol. 83, pp. E111–E116, 2018.

[12] B. Ma, Y. Ji, Y. Ma, Q. Wu, X. Zhao, D. Li, M. Teng, and Y. Yu, "Research on parameters extraction of resistivity and polarizability from SQUID TEM data based on adaptive differential optimization algorithm," *Chinese Journal of Geophysics*, vol. 67, pp. 4468–4481, 2024.

[13] J. R. Claycomb and J. H. Miller, "Superconducting magnetic shields for SQUID applications," *Review of Scientific Instruments*, vol. 70, pp. 4562–4568, 1999.

[14] R. L. Fagaly, "Superconducting quantum interference device instruments and applications," *Review of Scientific Instruments*, vol. 77, pp. 1–45, 2006.

[15] L. Wei, G. Wang, J. Li, S. Zhang, and G. Hong, "Multilayer magnetic shielding for testing a superconducting single-flux-quantum circuit chip in liquid helium Dewar," *Journal of Instrumentation*, vol. 16, p. 04007, 2021.

[16] H. He, T. Li, and R. Zhang, "Joint inversion of 3D gravity and magnetic data under undulating terrain based on combined hexahedral grid," *Remote Sensing*, vol. 14, pp. 4651–4673, 2022.

[17] X. Cao, X. Huang, C. Yin, L. Yan, and Y. Han, "3-D inversion of Z-axis tipper electromagnetic data using finite-element method with unstructured tetrahedral grids," *IEEE Transactions on Geoscience and Remote Sensing*, vol. 60, pp. 1–11, 2021.

[18] J. Zhu, C. Yin, L. Gao, Z. Hui, Y. Liu, X. Ren, B. Zhang, J. Wang, and B. Xiong, "3D unstructured spectral element method for frequency-domain airborne EM forward modeling based on Coulomb gauge," *IEEE Transactions on Geoscience and Remote Sensing*, vol. 60, pp. 1–13, 2022.

[19] K. Key, "MARE2DEM: A 2-D inversion code for controlled-source electromagnetic and magnetotelluric data," *Geophysical Journal International*, vol. 207, pp. 571–588, 2016.

[20] J. Li, Y. Li, Y. Liu, K. Spitzer, and B. Han, "3-D marine CSEM forward modeling with general anisotropy using an adaptive finite-element method," *IEEE Geoscience and Remote Sensing Letters*, vol. 18, pp. 1936–1940, 2021.

[21] Y. Zhou, Y. Yi, J. Li, and X. Hu, "Response characteristics of transient electromagnetic methods for unexploded ordnances considering metal shell thickness and shell fragments," *IEEE Transactions on Geoscience and Remote Sensing*, vol. 62, pp. 1–13, 2020.

[22] Z. Rong, Y. Liu, C. Yin, L. Wang, X. Ma, C. Qiu, B. Zhang, X. Ren, Y. Su, and A. Weng, "Three-dimensional magnetotelluric inversion for arbitrarily anisotropic earth using unstructured tetrahedral discretization," *Journal of Geophysical Research: Solid Earth*, vol. 127, pp. 1–26, 2022.

[23] Y. Liu, S. Liu, M. Li, X. Liu, and W. Guo, "Influence of metal roadway supports on transient electromagnetic detection in mines," *Earth Sciences Research Journal*, vol. 25, pp. 109–114, 2021.

[24] L. Zhou and Y. Gao, "Mechanical-electromagnetic coupling enriched finite element method for static

analysis of magneto-electroelastic composites," *Mechanics of Advanced Materials and Structures*, vol. 31, pp. 4374–4386, 2024.

[25] K. Etse, P. Clerico, L. Prevond, A. L. Helbert, T. Baudin, and X. Mininger, "Comparative study of thin layers modeling in electromagnetism: Application to multilayer magnetic shielding," *IEEE Transactions on Electromagnetic Compatibility*, vol. 65, pp. 1351–1359, 2023.

[26] Y. Gao, D. Ma, K. Wang, X. Xu, S. Li, Y. Dou, and J. Li, "A low-noise multilayer Mu-metal thin shell magnetic shield for ultra-highly sensitive atomic sensors," *Sensors and Actuators A: Physical*, vol. 352, p. 114207, 2023.

[27] G. Korkotadze, G. Chiqovani, and R. Jobava, "Analytical prediction of magnetic field shielding for multilayer thin sheets excited by loop sources," in *2024 IEEE 29th International Seminar/Workshop on Direct and Inverse Problems of Electromagnetic and Acoustic Wave Theory (DIPED)*, Tbilisi, Georgia, pp. 12–17, 2024.

[28] Y. Yang, F. Zhu, N. Lu, and Y. Xiao, "Study on the electromagnetic interference of shielded cable in rail weighbridge," *Applied Computational Electromagnetics Society (ACES) Journal*, vol. 37, pp. 215–221, 2022.

[29] M. I. Mousa, Z. Abdul-Malek, and M. R. M. Esa, "Effects of return stroke parameters and soil water content on EMF characteristics," *Applied Computational Electromagnetics Society (ACES) Journal*, vol. 34, pp. 1219–1225, 2019.

[30] M. N. S. Kumar, R. Murugan, J. Lydia, and S. L. S. Vimalraj, "Investigations on the influence of augmented rail geometry on rail gun design parameters using finite element method," *Applied Computational Electromagnetics Society (ACES) Journal*, vol. 40, pp. 564–570, 2025.

[31] X. Zhang, R. Chen, and A. Zhan, "A difference subgridding method for solving multiscale electro-thermal problems," *Applied Computational Electromagnetics Society (ACES) Journal*, vol. 37, pp. 168–175, 2022.

[32] M. Xue and J. Jin, "Finite-element domain decomposition methods for analysis of large-scale electromagnetic problems," *Applied Computational Electromagnetics Society (ACES) Journal*, vol. 29, pp. 990–1002, 2014.

[33] S. Zuo, Y. Zhang, D. G. Doñoro, X. Zhao, and Q. Liu, "A novel finite element mesh truncation technology accelerated by parallel multilevel fast multipole algorithm and its applications," *Applied Computational Electromagnetics Society (ACES) Journal*, vol. 34, pp. 1671–1678, 2019.

[34] S. Zuo, Z. Lin, Z. Yue, D. G. Doñoro, Y. Zhang, and X. Zhao, "An efficient parallel hybrid method of FEM-MLFMA for electromagnetic radiation and scattering analysis of separated objects," *Applied Computational Electromagnetics Society (ACES) Journal*, vol. 35, pp. 1127–1136, 2020.

[35] J. M. Jin, The Finite Element Method in Electromagnetics. Hoboken, NJ: John Wiley & Sons, 2015.

[36] J. H. Knight and A. P. Raiche, "Transient electromagnetic calculations using the GaverStehfest inverse Laplace transform method," *Geophysics*, vol. 47, pp. 47–50, 1982.

[37] M. Bick, G. Panaitov, N. Wolters, Y. Zhang, H. Bousack, A. I. Braginski, U. Kalberkamp, H. Burkhardt, and U. Matzander, "A HTS rf SQUID vector magnetometer for geophysical exploration," *IEEE Transactions on Applied Superconductivity*, vol. 9, pp. 3780–3785, 1999.

[38] T. Nagaishi, H. Ota, E. Arai, T. Hayashi, and H. Itozaki, "High Tc SQUID system for transient electromagnetic geophysical exploration," *IEEE Transactions on Applied Superconductivity*, vol. 15, pp. 749–752, 2005.

[39] A. Chwala, R. Stolz, M. Schmelz, V. Zakosarenko, M. Meyer, and H. G. Meyer, "SQUID systems for geophysical time domain electromagnetics (TEM) at IPHT Jena," *IEICE Transactions on Electronics*, vol. 98, pp. 167–173, 2015.

Binyuan Ma received the B.S. degree in measurement and control technology and instrumentation from the College of Instrumentation and Electrical Engineering, Jilin University, Changchun, China, in 2018, where he is currently pursuing the Ph.D. degree in detection technology and automatic equipment. His research interests include artificial intelligence algorithms, electromagnetic signal correction & processing, parameters extraction and their applications in SQUID TEM detection.

Nansong Chang received the B.S. degree in electrical engineering and automation from the College of Instrumentation and Electrical Engineering, Jilin University, Changchun, China, in 2020, where she is currently pursuing the Ph.D. degree in detection technology and automatic equipment. Her research interests include electromagnetic signal data processing and parameter extraction, deep learning algorithms and applications of electromagnetic signals in superconductivity.

Yanju Ji received the M.S. degree in measurement technology and instrument and the Ph.D. degree in Earth exploration and information techniques from Jilin University, Changchun, China, in 1998 and 2004, respectively. From 2004 to 2009, she was an Associate Professor with Jilin University. Since 2010, she has been with Jilin University where she is currently a Professor of instrument science and technology. She has authored or coauthored more than 200 articles. Her current research interests include computational electromagnetics, inverse problems, and electromagnetic detecting instrument.

Xuejiao Zhao received the B.S. degree in electrical engineering and automation, and the Ph.D. degree in detection technology and automatic equipment from Jilin University, Changchun, China, in 2013 and 2019, respectively. She is currently a Post-Doctoral Fellow in instrument science and technology with Jilin University. She has authored or coauthored more than 20 papers in journals and conference proceedings. Her research interests include electromagnetic anomalous diffusion and time-space fractional differential solution in the time domain.

Hui Luan received the Ph.D. degree in microwave remote sensing from the Chinese Academy of Science, Beijing, China, in 2007. Since 2007, she has been with the College of Instrumentation and Electrical Engineering, Jilin University, Changchun, where she is currently a Professor. Her research interests include the development of transient electromagnetic instruments and electromagnetic numerical simulation.

A High-Precision Beamforming Reflectarray Using an Improved Hybrid PSO-GA Algorithm and Low-Coupling Element

Ren Jiawei and Li Zuowen

Artificial Intelligence and Human Language Lab
Beijing Foreign Studies University, Beijing 100089, China
22053@bfsu.edu.cn, lizuowen@bfsu.edu.cn

***Abstract* –** This paper proposes a high-precision cosecant square beamforming reflectarray using an improved hybrid Particle Swarm Optimization and Genetic Algorithm (PSO-GA) and low-coupling square ring element. Firstly, a novel hybrid PSO-GA algorithm is carried out to optimize the phase distribution of the high-precision beamforming reflectarray. Then, an element is presented whose reflection phase is insensitive to different incident angles and reflection amplitude stable with variations of element size. By using the above-mentioned methods, a high-precision beamforming reflectarray is designed and analyzed. The experimental results show well-defined cosecant squared beams in the predefined direction are achieved in the frequency range from 13.1 to 14.3 GHz and have low loss.

***Index Terms* –** Beamforming reflectarray, optimization, reflectarray antenna.

I. INTRODUCTION

Reflectarray antennas combine many of the favorable traits of both reflectors and phased arrays while minimizing many of the drawbacks of the two. Reflectarray antennas are a low-profile, lightweight, and planar high-gain alternative to the conventional large and bulky parabolic reflectors and phased array antennas [1–4]. Reflectarrays can perform beamforming while remaining planar. Due to the lack of feed network, it also ensures a much greater efficiency for the reflectarrays compared with the phased array antennas.

A shaped-beam reflectarray with a cosecantsquared pattern was first presented in [5]. A narrowband reflectarray making use of a single layer of varying-sized patches is shown in [6], providing a European coverage. Reflectarray antennas have also been used to provide accurate shaped beams by using a flat sandwich with printed patches appropriately optimized [7, 8]. In [9], Particle Swarm Optimization (PSO) and Genetic Algorithm (GA) are compared and it is inferred that the convergence of PSO is faster than that of GA to the desired radiation pattern.

Evolutionary Algorithms (EAs) such as GA and PSO are effective and flexible techniques able to optimize multi-modal and non-convex cost functions like those modelling in general many engineering problems, and more specifically antennas ones [10–13]. For less complex problems, it demonstrates some advantages over the Back Propagation (BP) Neural Network algorithm [14]. Although the heuristic mentioned algorithms have been widely utilized as optimization tools, there are also some demerits, such as trapping of the local optimum [15], low accuracy, and early-maturing problems.

In reflectarrays, the array elements are designed with varying sizes [16] or rotation angles [17] to provide the desired phase distribution. Therefore, each element exhibits different mutual coupling levels and works at different resonance states, which leads to difficulties in the designing of high-precision beamforming reflectarrays.

This paper presents a high-precision beamforming reflectarray based on an improved hybrid PSO-GA algorithm and a low-coupling square ring element. First, an improved PSO-GA algorithm and a robust element design are proposed, featuring incident-angleinsensitive phase stability and minimal reflection amplitude fluctuation across size variations, which collectively reduce phase errors and enhance reflectarray performance. Next, a high-precision reflectarray antenna using these methods is designed, measured, and analyzed. Finally, key conclusions are summarized.

II. PROPOSED APPROACH

A. An improved hybrid PSO-GA algorithm for calculation of phase distribution of the reflectarray

In order to obtain phase distribution of the shaped beam reflectarray, an improved hybrid PSO-GA algorithm is proposed. It combines the advantages of PSO and GA. It is a heuristic optimization technique that is robust and efficient in solving antenna problems.

Submitted On: May 28, 2025
Accepted On: March 12, 2026

https://doi.org/10.13052/2026.ACES.J.410305

The flow chart of the improved hybrid PSO-GA algorithm is shown in Fig. 1.

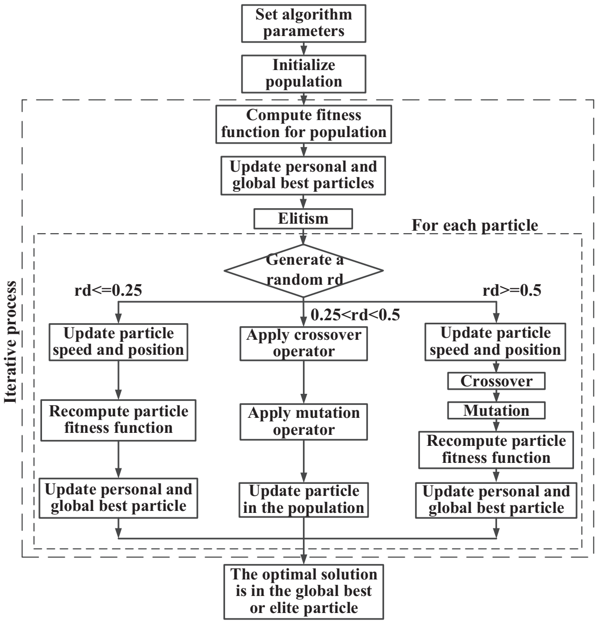

Fig. 1. Flow chart of the improved hybrid PSO-GA algorithm.

The specific procedure of the hybrid PSO-GA algorithm is as follows:

Step 1: Set algorithm parameters and initialize particle swarm. Set the node number of particle swarm as n. Let $X_i = (X_{i1}, X_{i2}, \ldots X_{in})$ be the position vector of i th particle, $v_i = (v_{i1}, v_{i2}, \ldots v_{in})$ be the velocity vector, $p_i = (p_{i1}, p_{i2}, \ldots p_{in})$ be the best position that particle has gone through, which can also be denoted as p_{ibest}, g be the index numbers of best position that all particles has gone through, so $p_g = (p_{g1}, p_{g2}, \ldots p_{gn})$, i.e. g_{best}. Set the maximum velocity V_{max}, learning factors C_1 and C_2, inertia weight w, maximum iteration times m_{max}, solution precision value E, crossing probability P_c and mutation probability P_v.

Step 2: Calculate the fitness function value of each particle. Select the particle with the optimal fitness value. Store and update the position of the particle in the optimal position of the particle P_{best}. Compare all the values P_{best}. Store and update the optimal adaptation value and the position of the particle in the optimal position of the group g_{best}.

Step 3: In each iteration, when an individual is selected for update, a random number rd is generated, ranging from 0 to 1.

Step 4.1: If $rd \leq 0.25$, the original PSO algorithm is used. Update the velocity and position of the particles by (1) and (2), then update the adaption value of particle:

$$v_i(k+1) = wv_i(k) + c_1 r_1 \left[p_i - x_i(k)\right] + c_2 r_2 [p_g - x_i(k)], \tag{1}$$

$$x_i(k+1) = x_i(k) + v_i(k+1), \tag{2}$$

where k represents evolution times, r_1 and r_2 are quasi-random numbers generated within $[0,1]$. To prevent the velocity of the particle becoming too quick in the iteration, the velocity of the particle should be restricted in interval $[-V_{\max}, V_{\max}]$.

Step 4.2: If $0.25 < rd < 0.5$, then pure GA is used. Firstly, the crossing operation: choosing a set of particles with better adaption, which are matched by pairs in random. Crossing operation is carried out according to the certain probability P_c. For those matched particles X_i and X_j, the crossing process is shown as follows:

$$x_i(k+1) = \alpha^* x_i(k) + (1-\alpha) x_j(k), \tag{3}$$

$$x_j(k+1) = (1-\alpha)^* x_i(k) + \alpha x_j(k), \tag{4}$$

where α is random number in interval $[0,1]$. Detecting the adaption value of every particle, the particles of weaker adaption value are made mutation operation by a certain probability P_v:

$$x_i(k+1) = x_i(k) + randn \times \sigma, \tag{5}$$

where $randn$ is a normal random integer and σ is a constant value $\sigma = (maximum\ domain - minimum\ domain)/10$. Then update the adaption value of the particle.

Step 4.3: If $rd \geq 0.5$, the hybrid PSO-GA algorithm is used to obtain the phase distribution of beamforming reflectarray. The operations of selecting and crossing GA are introduced into PSO such that the information among the particles can be shared and convergence rate of particle swarm can be quickened. Using (1) and (2), update the position and velocity information of the particle. Using (3), (4) and (5), compare the adaption value of son-particle and that of father-particle. The particle with better adaption value should be left for the next iteration.

Step 5: Judge whether the maximum number of iterations has been reached or whether the best fitness value of the particle swarm has achieved the given accuracy. If so, the iteration process terminates and the result is output. Otherwise, return to **Step 2** until the final result is obtained.

The proposed improved hybrid PSO-GA systems can find a better solution without trapping in local optimum solutions and achieve a faster convergence rate. When the PSO particles stagnate, GA diversifies the particle position even though the solution is worse. In PSO-GA, particle movement uses randomness in its search. Hence, it is a kind of stochastic optimization algorithm that can search a complicated and uncertain area.

B. Optimization of the phase distribution of the cosecant square beamforming reflectarray

To generate a cosecant beam with requirements on the pattern at levels 2 dB below the maximum, the phase distribution of a square cosecant beamforming reflectarray antenna at center frequency of $f = 13.88$ GHz is proposed in this section. The reflecting surface consists of 22×22 unit cells, and the period of the element is chosen to be $p = 8.6$ mm. Classically, lossless elementary antennas have a reflection magnitude $|\rho|$ of 0 dB and the phase distribution of planar reflectarray antennas by adjusting only the phase.

The radiation pattern obtained by the proposed algorithm is shown in Fig. 2 (a). Traditional PSO and GA are also used to obtain the phase distribution of the shaped beam reflectarray. Comparison of the cost function values of all three algorithms against the number of iterations is shown in Fig. 2 (b). As can be seen, both PSO and the improved hybrid PSO-GA algorithm exhibit faster convergence than GA. This is because PSO updates the evolutionary direction based on current optimal particles, which provides enhanced directional guidance. However, PSO tends to trap in local optima in the later stages. GA has a better global optimization capability and high-precision because it can effectively escape local optima through operations such as crossover and mutation, but it has a low convergence speed compared with PSO. Compared with PSO and GA, the results obtained using the improved hybrid PSO-GA algorithm is able to reach global optima of the phase distribution of the reflectarray, and this hybrid method improves the precision and efficiency of the model.

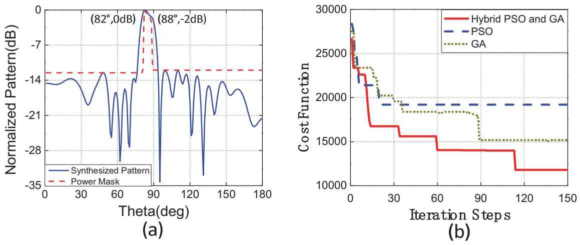

(a) (b)

Fig. 2. (a) Radiation pattern obtained by the proposed algorithm and (b) comparison of convergence speed of three algorithms.

Phase distribution obtained by the improved hybrid PSO-GA algorithm is shown in Table 1.

Table 1: Phase distribution obtained by the improved hybrid PSO-GA algorithm

No.	**Phase**	**No.**	**Phase**
1	184.8935	12	184.6788
2	259.3447	13	220.9182
3	59.6594	14	208.4418
4	266.4084	15	239.4929
5	27.57922	16	250.0374
6	251.1031	17	287.8221
7	65.75094	18	265.2022
8	193.9426	19	303.5217
9	117.6788	20	254.5281
10	163.933	21	356.9709
11	146.8121	22	299.101

C. Design and analysis of a low-coupling square ring element

To design a high-precision beamforming reflectarray, an element which has a low loss and the phase shift produced by the cell is nearly insensitive to the angle of incidence variations for angles up to 45° is presented in this section. The geometry of the unit cell is shown in Fig. 3.

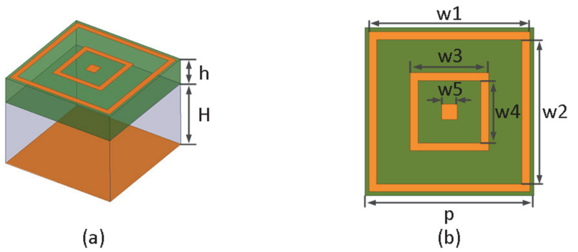

(a) (b)

Fig. 3. Geometry of the element.

The proposed element consists of two square rings and a square patch printed on the same side of a RT 5880 substrate with thickness of h mm which is separated from a ground plane by an air layer with thickness of H mm. The period of the element is chosen of $\boldsymbol{p} = \mathbf{8.6}$ mm. The length of outer side of the outer ring is w_1, and the inner side is $\boldsymbol{w2} = \mathbf{7.4}$ mm. The length of outer side and inner side of the middle ring are $\boldsymbol{w3} = \mathbf{2} \times \boldsymbol{l}$ mm and $\boldsymbol{w4} = \mathbf{2} \times \boldsymbol{l} - \mathbf{0.8}$ mm, respectively, and the length of the inner square patch is $\boldsymbol{w5} = \mathbf{0.8}$ mm. The phase of the reflected field is adjusted by changing the length of the variable $l(\mathbf{0.4}\ \mathrm{mm} \leq \boldsymbol{l} \leq \mathbf{4.1}\ \mathrm{mm})$. The lengths of w_1, h and H in the unit cell are adjusted to improve the bandwidth of the reflectarray.

Figures 4 (a) and (b) show the phase-shift and amplitude versus the variable length $\boldsymbol{I}$ for different

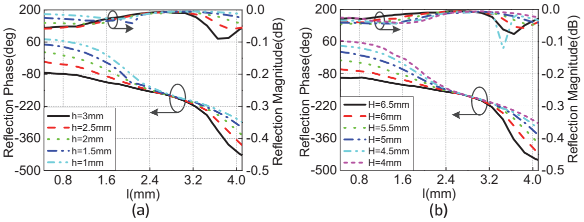

Fig. 4. Simulated reflection phase and amplitude versus length l for (a) different thickness h of dielectric layer and (b) different air thickness $\boldsymbol{H}$.

thickness h of the dielectric layer and different air thickness H at 13.88 GHz when one parameter is changed and another parameter is unchanged. It can be seen from Figs. 4 (a) and (b) that both h and H have some effects on the reflection phase and amplitude. Based on the linearity of the reflection phase curve and the smoothness of the reflection amplitude, the thicknesses of the medium and air layer have been chosen as $h = \mathbf{2}$ mm and $\boldsymbol{H} = \mathbf{5}$ mm, respectively.

Next, the effect of the length of $w1$ over the reflection phase and amplitude versus the length l for different incident angle $\boldsymbol{\theta}$ is studied as shown in Fig. 5 (a). It can be seen that, as $w1$ increases, the phase response variation for different incident angles ($\boldsymbol{\theta} = 0°, 25°, 45°$) also increases, primarily due to the coupling between adjacent elements and the resonance of the element. The lower the coupling between adjacent elements, the less influence on the phase shift for different incident angles. It can also be observed that $w1$ has little effect on the reflection amplitude. Considering the phase shift and amplitude variations under different incident angles, the value of $w1$ has been set to $\boldsymbol{w_1} = \mathbf{8.2}$ mm.

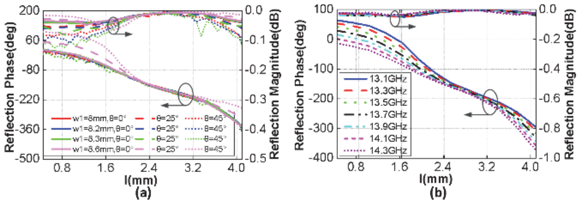

Fig. 5. (a) Simulated phase shift and amplitude versus length l for different lengths $w1$ and incident angles $\boldsymbol{\theta}$ and (b) simulated phase shift and amplitude versus length l for normal incidence at different frequencies.

Figure 5 (b) plots the phase and magnitude of the reflection as functions of l for normal incidence at different frequencies. As shown in Fig. 5 (b), the reflection phases versus l plots are linear at different frequencies, and the amount of delayed phase increases as the frequency rises from 13.1 to 14.3 GHz. The losses of the reflection magnitude are lower than 0.05 dB within this frequency band. The final parameter values of the reflectarray antenna element are summarized in Table 2.

Table 2: Detailed parameters of the unit cell

Parameter	Value	Parameter	Value
p	8.6 mm	$w4$	$2 \times l - 0.8$
$w1$	8.2 mm	$w5$	0.8 mm
$w2$	7.4 mm	h	2 mm
$w3$	2×1	H	5 mm
l	$0.4 - 4.1$ mm		

III. DESIGN AND PERFORMANCE OF A SQUARE COSECANT BEAMFORMING REFLECTARRAY ANTENNA

A center-fed high-precision beamforming reflectarray consisted of elements based on the analysis above is designed as shown in Fig. 6. The antenna is designed for the operating frequency of 13.88 GHz and the square aperture of the reflectarray is 189.2 mm. The phase distribution in Table 1 is used for the design of the reflectarray to provide the required shaped beam: pencil in azimuth and squared cosecant in elevation. In order to reduce the variation of the phase shift of the element for different incident angles, a larger focal length $F = 227.04$ mm is used, which indicates a ratio of 1.2.

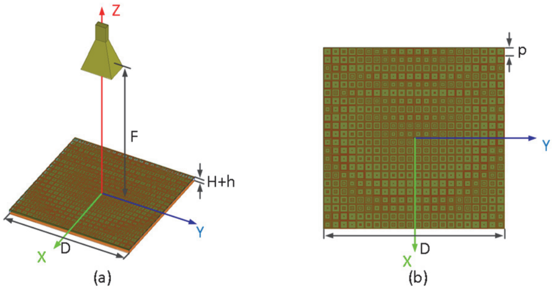

Fig. 6. Prototype of beamforming reflectarray.

A prototype of the feed and the reflectarray is shown in Fig. 7 (a). The reflectarray was simulated in a full wave EM simulation and was measured by the NSI planar near-field system as shown in Fig. 7 (b).

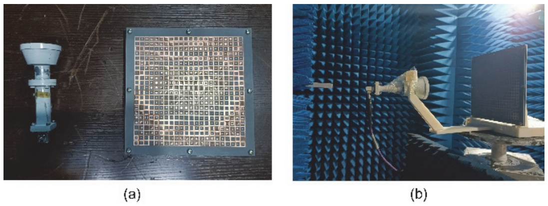

Fig. 7. (a) Photograph of feed antenna and reflectarray and (b) near-field measurement.

The simulated and measured radiation patterns of the reflectarray at different frequencies are shown in Fig. 8. And the simulated polar radiation patterns of the reflectarray at 13.88 GHz is shown in Fig. 9. In all of the cosecant square regions, well-defined cosecant squared beams in the predefined direction are achieved and good agreement between the simulated and measured results is achieved in the frequency range from 13.1 to 14.3 GHz. However, discrepancies in sidelobe levels exist, primarily due to the scattered field on the reflectarray edges.

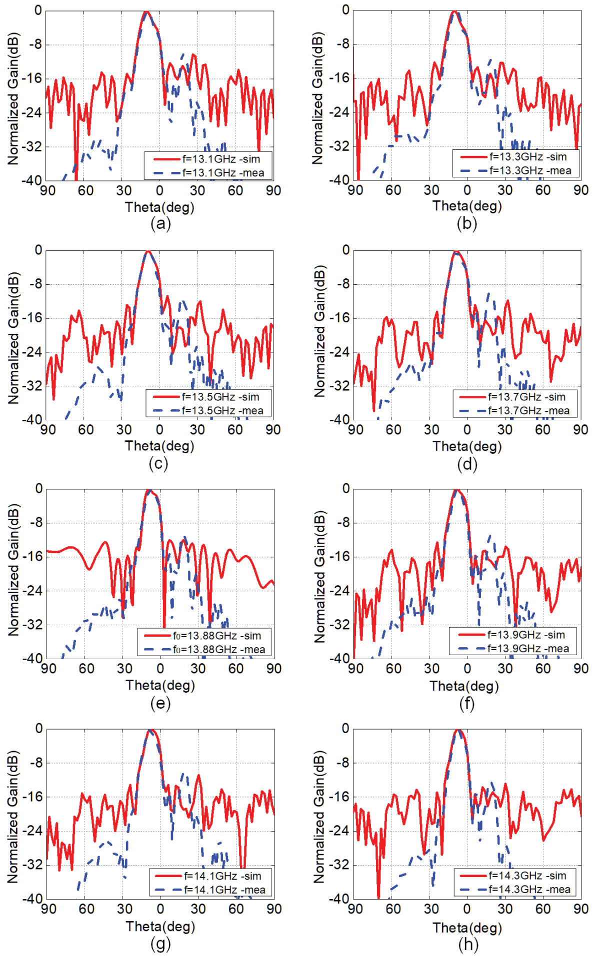

(a) (b) (c) (d) (e) (f) (g) (h)

Fig. 8. Simulated and measured radiation patterns of the reflectarray at (a) 13.1 GHz, (b) 13.3 GHz, (c) 13.5 GHz, (d) 13.7 GHz, (e) 13.88 GHz, (f) 13.9 GHz, (g) 14.1 GHz and (h) 14.3 GHz.

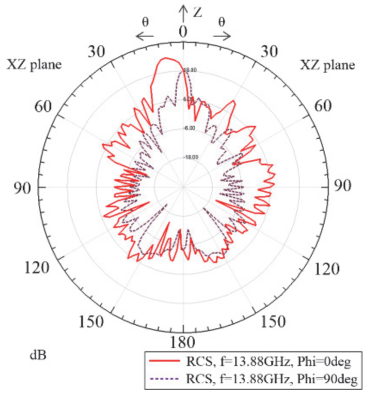

Fig. 9. Simulated polar radiation patterns of the reflectarray at 13.88 GHz.

The simulated and measured gains and aperture efficiencies of the proposed reflectarray are shown in Fig. 10. It can be observed that the measured gain is consistently lower than the simulated gain. The simulated gain is increased from 21.2 to 23.7 dB as the working frequency increases from 12.5 to 14.5 GHz with a 1 – dB bandwidth of 8.6% (13.3–14.5 GHz) and the measured gain is from 18.3 to 22.6 dB with 1-dB bandwidth of 8.6% (13.3–14.5 GHz). The difference between the simulated and measured gains is attributed to the fabrication and measurement errors. The substrate of the element may distort during fabrication, causing errors in the phase compensation of the element. Other errors are introduced by blockage and misalignment of the feed. The aperture efficiencies of the reflectarray are also plotted in Fig. 10. The simulated and measured efficiencies vary from 36.6–39.2% and 31.7–37.4%, respectively. Although the 1 dB gain bandwidth of the reflectarray is 8.6%, some discrepancies exist between the simulated and measured radiation patterns and gains, which can be attributed to fabrication and measurement tolerances. Nevertheless, well-defined cosecant-squared beams in the predefined direction are maintained across the entire operating band, as shown in Fig. 8. This result demonstrates the strong robustness of the phase distribution optimized by our proposed algorithm against phase errors. Such bandwidth performance is highly competitive for a high-gain, shaped-beam reflectarray.

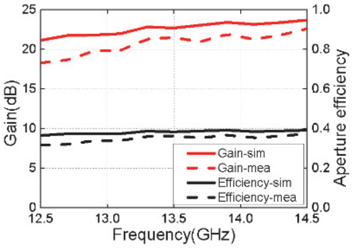

Fig. 10. Simulated and measured gains and aperture efficiencies.

IV. CONCLUSION

This paper designs a high-precision shaped beam reflectarray using phase only control to achieve a cosecant squared beam. First, an improved hybrid PSOGA algorithm is proposed. Simulation results show that the hybrid algorithm outperforms PSO and GA in convergence speed and global optimization. The second part of this paper proposes an element whose reflection phase is insensitive to different incident angles and reflection amplitude keep stable with variation of element size. Finally, a high-precision beamforming reflectarray is designed using these methods. The simulation and measured results show that well-defined cosecant squared beams in the predefined direction are achieved in the frequency range from 13.1 to 14.3 GHz, which validates the effectiveness of the proposed approach.

ACKNOWLEDGMENT

This work was sponsored by the Central Universities Basic Research Operating Expenses Project of China under Grant 2023JJ008; in part by the Young Academic Innovation Team Project of Beijing Foreign Studies University under Grant 2023TD001.

REFERENCES

[1] J. Huang and J. A. Encinar, *Reflectarray Antenna*. Hoboken, NJ, USA: Wiley, 2007.

[2] Y. H. Cho, W. J. Byun, and M. S. Song, "High gain metal-only reflectarray antenna composed of multiple rectangular grooves," *IEEE Trans. Antennas Propag.*, vol. 59, no. 12, pp. 4559–4568, 2011.

[3] R. S. Malfajani and Z. Atlasbaf, "Design and implementation of a broadband single layer circularly polarized reflectarray antenna," *Antennas Wireless Propag. Lett.*, vol. 11, pp. 973–976, 2012.

[4] J. Ruze, "Aperture tolerance theory: A review," in *1965 Antennas and Propagation Society International Symposium*, pp. 210–210, 1965.

[5] D. C. Chang and M. C. Huang, "Feasibility study of erecting cosecant pattern by planar microstrip reflectarray antenna," in *Proc. AMPC'93*, vol. 2, pp. 19.20–19.24, 1993.

[6] D. M. Pozar, S. D. Targonski, and R. Pokuls, "A shaped-beam microstrip patch reflectarray," *IEEE Trans. Antennas Propag.*, vol. 47, pp. 1167–1173, 1999.

[7] M. Arrebola, J. A. Encinar, and M. Barba, "Multifed printed reflectarray with three simultaneous shaped beams for LMDS central station antenna," *IEEE Trans. Antennas Propag.*, vol. 56, pp. 1518–1527, 2008.

[8] J. A. Encinar, M. Arrebola, L. F. de la Fuente, and G. Toso, "A transmit-receive reflectarray antenna for direct broadcast satellite applications," *IEEE Trans. Antennas Propag.*, vol. 59, no. 9, pp. 3255–3264, 2011.

[9] D. W. Boeringer and D. H. Werner, "Particle swarm optimization versus genetic algorithms for phased array synthesis," *IEEE Trans. Antennas Propag.*, vol. 25, no. 3, pp. 771–779, 2004.

[10] J. M. Johnson and Y. Rahmat-Samii, "Genetic algorithm optimization and its application to antenna design," *IEEE Xplore*, vol. 1, pp. 326–329, 1994.

[11] D. Olcan, R. Golubovic, and B. Kolundzija, "On the efficiency of particle swarm optimizer when applied to antenna optimization," *IEEE Int. Antennas and Propag. Symposium*, pp. 3297–3300, 2006.

[12] F. Grimaccia, M. Mussetta, P. Pirinoli, and R. E. Zich, "Optimization of a reflectarray antenna via hybrid evolutionary algorithms," in *2006 17th International Zurich Symposium on Electromagnetic Compatibility*, Singapore, pp. 254–257, 2006.

[13] A. Sheikholeslami and Z. Atlasbaf, "Novel phase distributions for large electronically beamscanning reflectarrays," *Scientific Reports*, vol. 11, no. 1, p. 21877, 2021.

[14] S. Du, W. Li, and K. Cao, "A learning algorithm of artificial neural network based on GA-PSO," in *2006 6th World Congress on Intelligent Control and Automation*, vol. 1, 2006.

[15] S. Mesloub and A. Mansour, "Hybrid PSO and GA for global maximization," *Int. J. Open Problems Compt. Math.*, vol. 2, no. 4, pp. 597–608, 2009.

[16] L. Chang and S. V. Hum, "An electronically tunable single-layer reflectarray antenna element with improved bandwidth," *Antennas Wireless Propag. Lett.*, vol. 9, pp. 1241–1244, 2010.

[17] J. Huang and R. J. Pogorzelski, "A Ka-band microstrip reflectarray with elements having variable rotation angles," *IEEE Trans. Antennas Propag.*, vol. 46, pp. 650–656, 1998.

Ren Jiawei was born in Hebei, China, in 1992. He received the B.S. degree from the Hebei University, Hebei, and the M.S. and Ph.D. degrees from the University of Chinese Academy of Sciences, Beijing, and Nation Space Science Center, Chinese Academy of Sciences, Beijing. His current research interests include reflectarray, microstrip antennas, lowloss antenna, and wideband antenna.

Li Zuowen is a professor and doctoral supervisor, currently serving as director of the Key Laboratory of Artificial Intelligence and Human Language at Beijing Foreign Studies University, China. He received his doctoral degree from Shanghai International Studies University and conducted postdoctoral research at Peking University. His current research interests include artificial intelligence and natural language processing.

Electromagnetic Exposure to Child Passengers of Positioning Antennas for Autonomous Driving Electric Vehicles

Xuwei Dong, Yufei Ren, and Mai Lu

Key Laboratory of Opto-Electronic Technology and Intelligent Control Ministry of Education
Lanzhou Jiaotong University, Lanzhou 730070, China
dxw007@lzjtu.edu.com, 12232052@stu.lzjtu.edu.com, mai.lu@hotmail.com

Abstract – With the rapid development of electric vehicles (EVs) and autonomous driving (AD) technologies, the issue of electromagnetic exposure of passengers, especially children, to the electromagnetic radiation generated by the positioning antennas of AD has received increasing attention. In this study, COMSOL Multiphysics is used to construct the models of an EV, a positioning antenna and a child human body, and the levels of electromagnetic exposure of a child passenger to the positioning antenna in AD are calculated. Results indicate that the maximum value of induced electric field in a child's body is 23 V/m, and the maximum value of the SAR_{1g} of the child's body is 0.19 W/kg. Additionally, the maximum temperature rise in the child body is 0.55°C. The electromagnetic exposure levels of the child passenger calculated in this study are all lower than the safety limits defined by international authoritative institutions. Therefore, the electromagnetic radiation levels from the positioning antenna comply with international safety standards. Based on the analysis of this study, no significant health effects on child passengers have been observed. The results of this study can supplement studies on the electromagnetic environment of AD in EVs and can provide guidance for ensuring the travel safety of child passengers.

Index Terms – Autonomous driving, child passenger, electric vehicles, electromagnetic radiation, positioning antenna.

I. INTRODUCTION

In recent years, the global new energy vehicle market has experienced remarkable growth [1]. In contrast to traditional internal combustion engine vehicles, electric vehicles (EVs) produce no exhaust emissions during driving, eliminating the source of harmful gases and contributing to the improvement of the global ecological environment and the protection of public health [2]. As an interdisciplinary field between artificial intelligence and the automotive industry, autonomous driving (AD) EVs have achieved rapid development in recent years [3]. High-precision positioning antennas are critical components for ensuring the safe operation of AD vehicles [4]. The positioning antenna provides centimeter-level or even millimeter-level positioning accuracy for AD vehicles by sending out precise position signals, ensuring that the vehicles can drive safely and stably under complex road conditions.

High-voltage electrical equipment installed in EVs, such as inverters, power cables, and wireless charging systems, generates spatial electromagnetic fields (EMFs) of a certain intensity during operation, exposing passengers to this electromagnetic environment [5–7]. Meanwhile, with the rapid development of intelligent connected technologies, modern EVs are also integrated with various wireless communication devices, including 4/5G, C-V2X, GPS, Bluetooth, and Wi-Fi antennas. During their operation, these wireless devices also create a high-frequency electromagnetic environment inside the vehicle, rendering the in-vehicle electromagnetic environment more complex. Whilst people are enjoying the convenience of AD vehicles, passengers are inevitably exposed to the electromagnetic environment, and an induction field is formed in the human body [8]. As a special group, children have not yet fully developed physically and may be more sensitive to electromagnetic radiation [9]. Therefore, in the study of electromagnetic exposure to automobile antennas, special attention should be paid to the physical health needs of children to ensure that the electromagnetic exposure level of children meets the safety standards. In view of the physical characteristics and special electromagnetic sensitivity of children, studying the effect of electromagnetic radiation generated by the positioning antenna of AD vehicles on child passengers is crucial and meaningful.

With the vigorous development of a new round of global scientific and technological revolution and industrial transformation, the automotive industry has entered an era of transformation unseen in a century, and EVs have ushered in new development opportunities [10].

Submitted On: March 22, 2025
Accepted On: March 03, 2026

https://doi.org/10.13052/2026.ACES.J.410306

Relevant studies have shown that human exposure to the electromagnetic environment generated by the power system of EVs causes certain biological reactions and physiological effects [11, 12]. The safety of human metal medical implants exposed to the wireless power transfer system of EVs was studied, and the results showed that the specific absorption rate (SAR) of human tissues around the metal medical implants would be greater [13]. The induced electric field in different parts of the human body for infants and adults under different driving conditions was analyzed to compare the differences in the induced electric field in the body between children and adults due to physical differences [14]. The electromagnetic exposure of passengers in different positions in the carriage to the radiation of the wireless power transfer system was studied, and the results were all lower than the safety limits specified by International Commission on Non-ionizing Radiation Protection (ICNIRP) [15]. The SAR in adults and children at different locations in the EV under the combined radiation of rod antennas, wire harnesses and DC–DC converters was studied, and the results showed that the amount of electromagnetic radiation suffered by adults and children varied [16] The electromagnetic exposure of adults and children in different postures and positions of the wireless charging system in the EV was evaluated, and the results showed that the induced electric fields of the cardiopulmonary system in lying children and the heart in lying adults exceeded the safety limits specified by ICNIRP [17].

In addition, the explosive development of electronic information technology has filled the human living environment with radiofrequency (RF) EMFs. As early as the mid-20th century, with the emergence of RF applications such as radar technology, scientists began to explore initially the potential effects of radio frequency EMFs on organisms [18]. Although no studies have conclusively shown that RF EMFs would pose adverse effects on human health [19], public concern is increasing, and the study on the radiation characteristics of RF EMFs is also deepening. The effect of the distance and angle between the mobile phone antenna and the human head on the SAR in the human head was studied [20]. Also studied was the influence of vehicle glass antennas placed in different positions in the vehicle on the electromagnetic exposure of passengers [21]. SAR distribution in the human body at different ages and positions for V2V antennas at a frequency of 5.9 GHz was calculated [22, 23]. SAR distributions in a human body for mobile phone users inside a vehicle was evaluated under different scenarios, and the results showed that the SAR value of passengers using mobile phones in the vehicle was 5% higher than that of people using mobile phones in free space [24].

In this paper, the high-precision positioning antenna in AD-EVs is selected as the exposure source. COMSOL Multiphysics software is used to construct the vehicle body model, antenna model and child model. By analyzing the radiation characteristics of the antenna, the distributions of the induced electric field, SAR and temperature in the child passenger's body are calculated, and the results are compared with the electromagnetic exposure limits stipulated by the international authoritative institutions to evaluate the electromagnetic exposure level in the child's body. This study aims to provide reference for optimizing positioning antenna design and taking effective protective measures by evaluating the electromagnetic exposure level of child passengers to ensure the safety of children in AD-EVs and promote the rapid development of AD technology.

II. MATERIALS AND METHODS

A. Numerical calculation method

As an interdisciplinary field, bioelectromagnetics reveals the underlying mechanisms of interactions between EMFs and organisms. The Maxwell equations are the foundation of EMF theory and the key to solving EMF problems [25]. In this study, the RF module of COMSOL Multiphysics software based on the finite element method was employed to solve EMF problems by solving the Maxwell equations.

When the positioning antenna of an AD vehicle is operational, it radiates electromagnetic waves into the surrounding space and forms an induction field in the human body when interacting with the human body in the vehicle. SAR, a critical metric for quantifying the amount of electromagnetic radiation energy absorbed by the human body, is defined as [26]:

$$SAR = \frac{\sigma}{2\rho}|E|^2, \tag{1}$$

where σ is electrical conductivity of the tissue (S/m), ρ is tissue density (kg/m^3), and E is electric field strength in biological tissue (V/m).

Human tissues are lossy media. When exposed to an electromagnetic environment, electromagnetic energy is continuously absorbed by human tissues and gradually dissipated in the form of heat [27]. Consequently, the temperature of human tissues rises, resulting in a thermal effect. The Pennes bioheat transfer equation is derived from Maxwell's equations [28]:

$$\rho C\frac{\partial T}{\partial t} = \nabla \cdot (K\nabla T) + \rho_b C_b \omega_b (T_b - T) + Q_{met} + Q_{ext}, \tag{2}$$

where C is tissue specific heat capacity (J/[kg·°C]), T is temperature of the tissue (°C), K is thermal conductivity (W/[m·°C]), ρ_b is density of blood (kg/m^3), C_b is specific heat capacity of blood (J/[kg·°C]), ω_b is blood perfusion rate (1/s), T_b is temperature of the blood (°C), Q_{met} is heat generated by metabolism, Q_{ext} is external heat source (W/m^3). In this paper, the initial temperature of the human body is 36.5°C, and the external boundary condition of the human body is set to the thermal insulation boundary condition.

B. Dielectric parameters of human tissue

In 1996, on the basis of previous work, Gabriel proposed a four-order Cole–Cole model to calculate the dielectric properties of biological tissues [29]:

$$\widehat{\varepsilon}_r = \varepsilon_r' - j\varepsilon_r'' = \varepsilon_{r\infty} + \sum_{n=1}^{4} \frac{\Delta\varepsilon_n}{1+(j\omega\tau_n)^{1-\alpha}} + \frac{\sigma_i}{j\omega\varepsilon_0}, \quad (3)$$

where $\widehat{\varepsilon}_r$ is complex relative dielectric constant, ε_r'' is loss factor, $\varepsilon_{r\infty}$ is relative dielectric constant at optical frequency, $\Delta\varepsilon_n$ is relative dielectric constant increment, τ_n is central relaxation time (s), ε_0 is dielectric constant of a vacuum (F/m), α is relaxation distribution time $(0 \leq \alpha \leq 1)$, σ_i is ionic conductivity (S/m).

During human growth and development, the water content in tissues gradually decreases with age. The water content of biological tissues considerably influences the dielectric properties of tissues [30]. As age increases, the downward trends of the dielectric constant and electrical conductivity of most biological tissues are consistent with the downward trend of the water content in the tissues [31]. Compared to adults, children are not fully developed, and their higher water content and smaller body size result in higher electromagnetic sensitivity. Given the lack of measured data on the dielectric properties of children's tissues, mathematical relationships are often employed to estimate the dielectric properties of children based on adult tissue data [32]. The study has found that the dielectric parameters of 7-year-old children are 26–30% higher than those of adults [33]. Therefore, in this study, values that are 30% higher than the dielectric parameters of adult tissues are used as the dielectric parameters of children's tissues. As shown in Table 1, the parameters for the trunk are derived from the average values of five tissue types: skin, muscle, fat, blood and bone [34]. Additionally, the density, specific heat capacity and thermal conductivity of different organ and tissue are obtained from the "Tissue Characteristics Database' provided by the Virtual Population Project [35].

C. Antenna model

In the field of AD vehicles, the Global Navigation Satellite System (GNSS) antenna is a key component for vehicle positioning. A circularly polarized microstrip antenna takes the microstrip as the basic structure and is composed of a dielectric substrate, a metal patch and a ground plane [36]. The metal patch is printed on one side of the dielectric substrate, whilst the ground plane is located on the opposite side. This configuration endows microstrip antennas with advantages, such as compact size, light weight and easy integration [37], making them well-suited for GNSS antenna application.

The general microstrip antennas typically produce linear polarization, but the circular polarization radiation can be realized by cutting the patch radiator and adjusting the actual size of the microstrip antenna to excite two orthogonal modes with equal amplitude and 90° phase difference [38]. GNSS antennas usually rely on circular polarization to improve the reliability of signal reception, and this adjustment enables the antennas to meet the requirements of the GNSS system.

As shown in Figure 1, this study designs a coaxial single-feed square microstrip antenna based on the positioning antenna of an AD-EV (GPS320, Harxon, China). Circular polarization is achieved by truncating two diagonal corners of the patch. The antenna is excited by a voltage source with a center frequency of 1.575 GHz, impedance of 50 Ω, and input power of 0.25 W. The structure of the antenna is shown in Fig. 2.

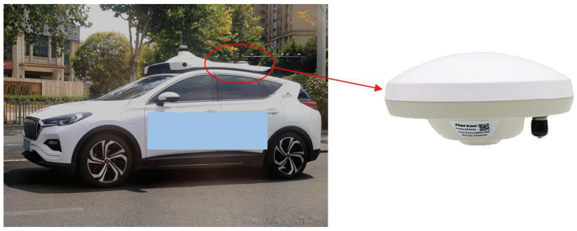

Fig. 1. Schematic of AD-EV positioning system.

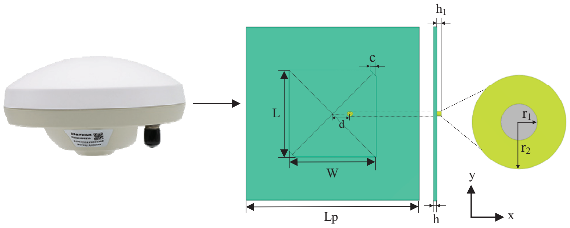

Fig. 2. Structure of positioning antenna.

Width and length of the antenna substrate are 100 mm, and relative permittivity ε_r is 3.38. The width of the square patch is determined by:

$$W = \frac{c_0}{2f_0\sqrt{\varepsilon_r}} = \frac{\lambda_0}{2\sqrt{\varepsilon_r}}, \quad (4)$$

where c_0 is speed of light, λ_0 is antenna wavelength, f_0 is operating frequency of the antenna.

Table 1: Dielectric parameters of human tissue at 1.575 GHz

Tissue	ε_r	σ **(S/m)**	ρ **(kg/m^3)**	**C (J/kg·°C)**	**k (W/m·°C)**
Grey matter	65.732	1.645	1044.5	3696	0.55
White matter	48.565	1.072	1041	3583	0.48
Cerebellum	60.692	2.060	1045	3653	0.51
Skull	25.544	0.676	1908	1313	0.32
Heart	77.952	2.109	1065.4	3651.5	0.54
Liver	58.104	1.519	1078.75	3540	0.52
Lung	64.714	1.507	394	3886	0.39
Kidney	71.712	2.340	1066.25	3763	0.53
Stomach	82.703	2.012	1088	3690	0.53
Small intestine	73.497	3.315	1030	3595	0.49
Trunk	46.264	1.251	1213	2818	0.38

In this study, the length (L) of the square patch is set equal to its width (W). Through calculation and according to the expected frequency, it is obtained that $L = W = 50.28$ mm. Once the width of the substrate is established, the position of the feed point must be determined on the basis of the width, which affects the input impedance of the antenna. The feed point is located along the edge of the rectangular patch in the x-direction, the input impedance at $x = \pm L/2$ is the highest, approximately ranging from 100 Ω to 500 Ω. On this basis, the position of the feeding point when the input impedance is 50 Ω can be calculated. As shown in (5), X_l is the position of the feed point in the x-direction when $y = 0$:

$$X_l = \frac{L}{2}\left(1 - \frac{1}{\varepsilon_e}\right), \tag{5}$$

where ε_e is effective permittivity, which can be calculated by:

$$\varepsilon_e = \frac{\varepsilon_r + 1}{2} + \frac{\varepsilon_r - 1}{2}\left(1 + 12\frac{h}{L}\right)^{-\frac{1}{2}}. \tag{6}$$

When the area S of the patch changes, the condition for the square microstrip antenna to obtain circularly polarized waves can be determined by:

$$S = L \times W, \tag{7}$$

$$\Delta S = \Delta S_1 + \Delta S_2 = c^2, \tag{8}$$

$$\left|\frac{\Delta S}{S}\right| = \frac{1}{2Q_0}, \tag{9}$$

where L is length of patch, W is width of patch, c is length of chamfer.

Based on the above, the antenna's ground plane, radiating patch, inner conductor, and outer conductor of the coaxial cable are set as perfect electric conductors (PEC), and the relative permittivity of the isolator between the inner and exterior conductors is 2.1. Additionally, a perfectly matched layer (PML) is constructed outside the spatial computational domain as an absorbing boundary condition, simulating the propagation of electromagnetic waves radiated by the 1.575 GHz positioning antenna to infinity.

Table 2: Parameters of positioning antenna

Description	**Parameter**	**Value (mm)**
Substrate width	L_p	100
Substrate thickness	h	1.524
Patch length	L	50.28
Patch width	W	50.28
Chamfer	c	3.5
Inner conductor radius	r_1	0.6
Coaxial cable radius	r_2	1.63
Position	d	10
Coaxial cable height	h_1	2

Table 2 presents the main geometric parameters of the antenna. By simulating the antenna model in COMSOL Multiphysics, the radiation characteristics of the antenna can be obtained. Figure 3 shows the curve of the $|S_{11}|$ parameter of the antenna. The optimal operating frequency of the antenna is 1.575 GHz, and the return loss is -17.95 dB, which meets the design requirements of the antenna.

Figure 4 shows the radiation pattern of the axial ratio of the designed antenna. Circularly polarized antennas emit circularly polarized waves during operation, and the axial ratio radiation pattern reflects the purity of these waves in different spatial directions. Figure 5 shows the three-dimensional far-field gain of the antenna, with a maximum gain of 6.8 dBi. All these meet the design requirements of a GNSS antenna. As

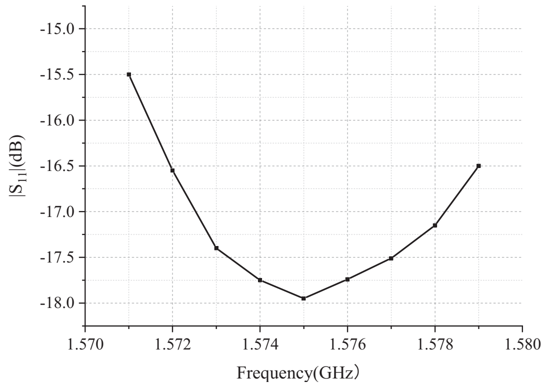

Fig. 3. $|S_{11}|$ parameters of antenna.

shown in Table 3, a comparison between the antenna designed in this paper with those reported in other literatures demonstrates that the proposed antenna has excellent comprehensive performance and meets the design requirements for GNSS antennas. The positioning antenna shell of the roof of AD vehicles is generally a circular plastic shell structure, which has minimal impact on the radiation performance of the antenna, and can also protect the internal components from the external environment (such as rain, dust), waterproof, anti-ultraviolet and extend the service life of the antenna.

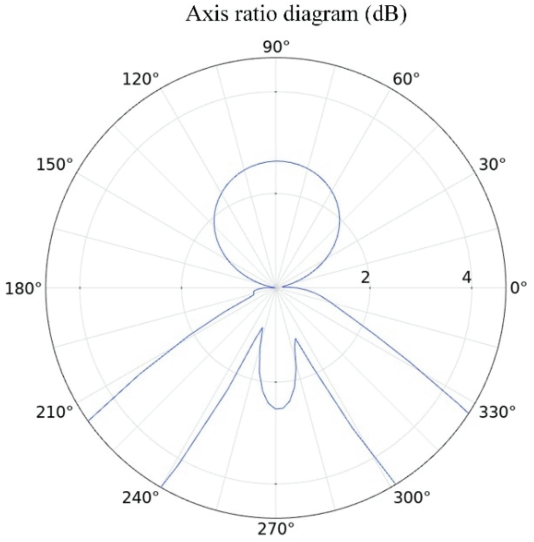

Fig. 4. Axis ratio radiation pattern.

D. Finite element model

In this study, the child human body model is an 11-year-old girl from the Virtual Population models [44]. She has a height of 1.49 m and a weight of 34.0 kg. As shown in Fig. 6, three-dimensional modelling software is used to obtain the seated child human body model for calculation. This child human body model contains 10 major tissues, such as white matter, cerebellum, skull, lung and heart.

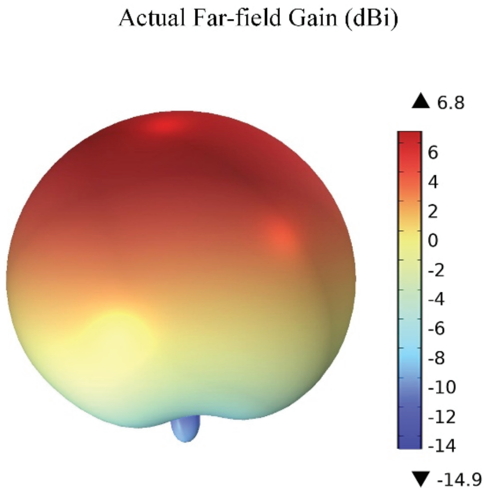

Fig. 5. Antenna gain pattern.

Table 3: Comparison of antenna parameters in this work with other literatures

Reference	Gain	$\|S_{11}\|$	Axial Ratio
This Work	6.8 dBi	-17.95 dB	<3 dB
[39]	4.12 dBiC	—	<3 dB
[40]	5.94 dBi	<-30 dB	2.5 dB
[41]	4 dBi	<-15 dB	<2 dB
[42]	3.24 dBiC	<-10 dB	<3 dB
[43]	>3.8 dBiC	<-15 dB	<3 dB

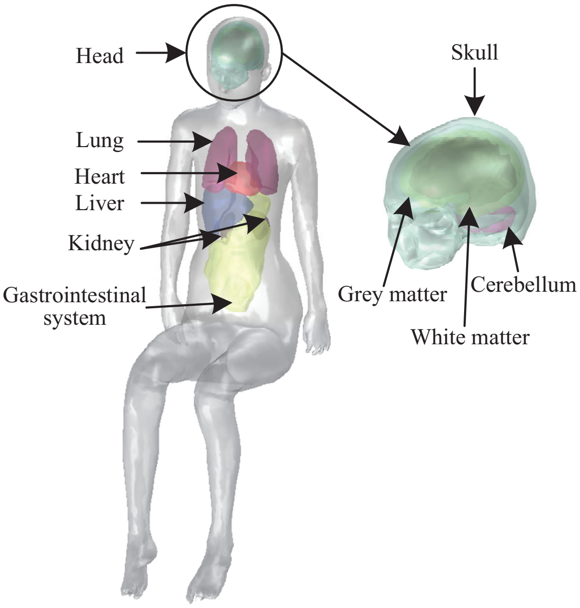

Fig. 6. Child human body model.

Table 4: Main electrical parameters for the electric vehicle

Material	**(Relative ε_r)**	**Relative Permeability (μ_r)**	**Electrical Conductivity (σ, S/m)**
Aluminum alloy	1	1	2.326×10^7
Glass	4	1	10^{-14}
Rubber	2	1	10^{-9}

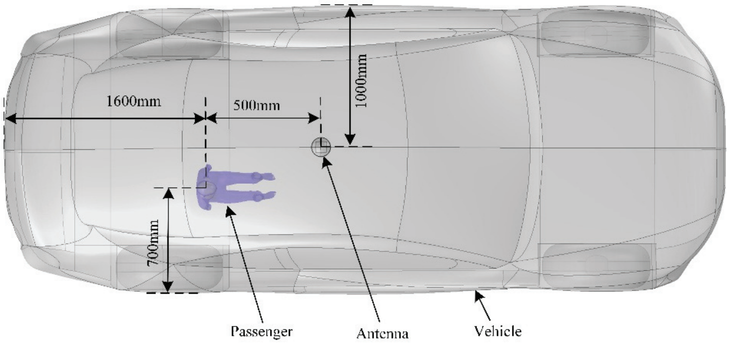

Fig. 7. Relative position of human body and antenna.

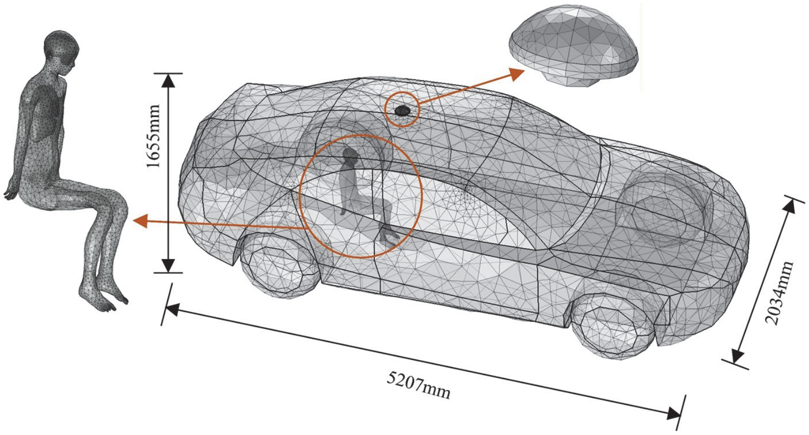

Fig. 8. Finite element model.

In reference to a real AD vehicle, a proportional vehicle body model with the dimensions of 5207 mm × 2034 mm × 1655 mm is established in this study. When constructing the vehicle body model, some details that are irrelevant to electromagnetic calculations, such as license plates and internal components, are ignored to facilitate the division of finite element meshes and reduce the finite element calculation time [45]. The simplified model of the EV is composed of the body, windows and tires. Specifically, the body is made of aluminum alloy, the windows are made of glass, and the tires are made of rubber. The main electrical parameters of the different material are listed in Table 4 [46].

The vehicle body model, antenna model and child human body model are imported into COMSOL Multiphysics, and their spatial positions are shown in Fig. 7. As shown in Fig. 8, the finite element mesh division [47, 48] of the model is performed in COMSOL Multiphysics. A relatively fine mesh division is performed on the child human body model and the antenna model, resulting in a total of approximately 380,000 mesh grids. Moreover, the simulations conducted in this chapter involve large-scale computational. All calculations are performed on a computer equipped with an Intel Core Ultra 5 processor and 128 GB of RAM, with each simulation taking approximately 90 minutes to complete. Ultimately, all computational tasks are successfully finished.

E. Verification of the calculation methodology

COMSOL Multiphysics is based on the finite element method and can perform coupling analysis of multiple physical fields. In this study, the radio frequency module and temperature field module are used to couple the electromagnetic and thermal fields. The induced electric field, SAR and temperature rise in different tissues and organs of the child's body are calculated for the electromagnetic exposure of positioning antenna.

To verify the accuracy of the research methods in this paper, a comparative validation was conducted with the results from [49]. This reference focuses on the electromagnetic exposure effects on the human body induced by a 400 MHz dipole antenna. Following the parameter configuration in this reference, a dipole antenna with a diameter of 1.0 millimeter and a length of 36.0 centimeters as the radiation source, with the output power set to 1 W, was placed at a distance of 8 centimeters from the human neck. Finally, the SAR of the human body was calculated. The comparative results are shown in Fig. 9 and Table 5.

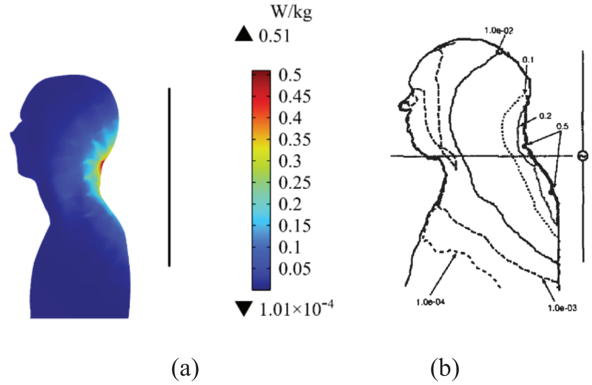

Fig. 9. Comparison of SAR distribution in (a) this paper and (b) reference [49].

Table 5: SAR comparison and error analysis

Results	Maximum SAR	Minimum SAR
This Work	0.52 W/kg	1.01×10^{-4} W/kg
Reference [49]	0.51 W/kg	1.00×10^{-4} W/kg
Error	1.96%	1.00%

Numerical calculations show that the maximum SAR of the human body derived from COMSOL is 0.52 W/kg, with a relative error of approximately 1.96% compared with the result of 0.51 W/kg in [49]. Meanwhile, the calculated minimum SAR is 1.01×10^{-4} W/kg, corresponding to a relative error of 1.00% compared to the result of 1.00×10^{-4} W/kg in [49]. Since the calculated results are in good agreement with the reference, the application of COMSOL for calculating and analyzing human electromagnetic exposure levels in this study is reliable.

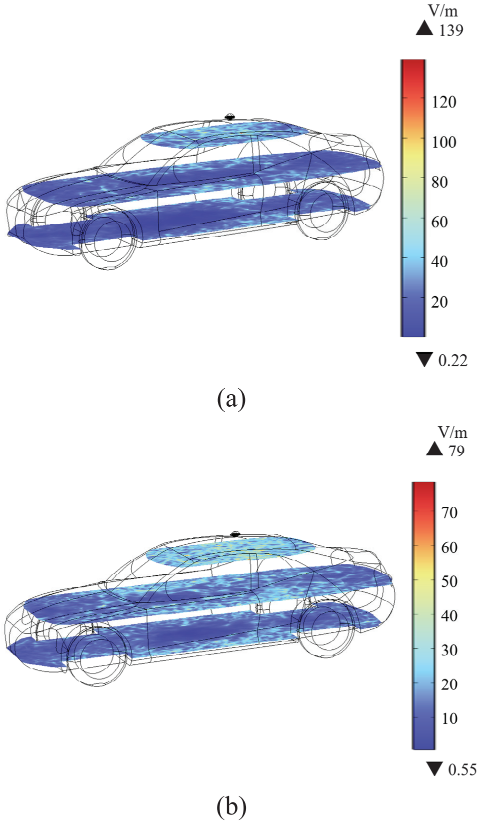

Fig. 10. Electric field distribution on different cross-sections inside the vehicle: (a) vehicle body material set as air and (b) vehicle body material set as aluminum alloy.

III. RESULTS

A. Electric field distribution inside the EV body

Figure 10 (a) shows electric field distribution on different cross-sections inside the vehicle when the body area is equivalent to the air (i.e., free space). Figure 10 (b) shows electric field distribution at the same position when the body material is aluminum alloy. From Fig. 10 (a), it can be seen that electric field intensity shows a trend of gradual decrease from the antenna position to the surrounding area. Electric field distribution on different cross-sections inside the vehicle is relatively uniform, with a relatively high field intensity, and the maximum value is approximately 139 V/m. In contrast, when the vehicle body is aluminum alloy, the maximum field intensity at the corresponding positions decreases significantly to approximately 79 V/m. Therefore, it can be seen that the aluminum alloy vehicle body has a shielding effect on electromagnetic waves, enabling the rapid attenuation of the electric field inside the vehicle. This result fully demonstrates the significant value of metal materials in automotive electromagnetic protection.

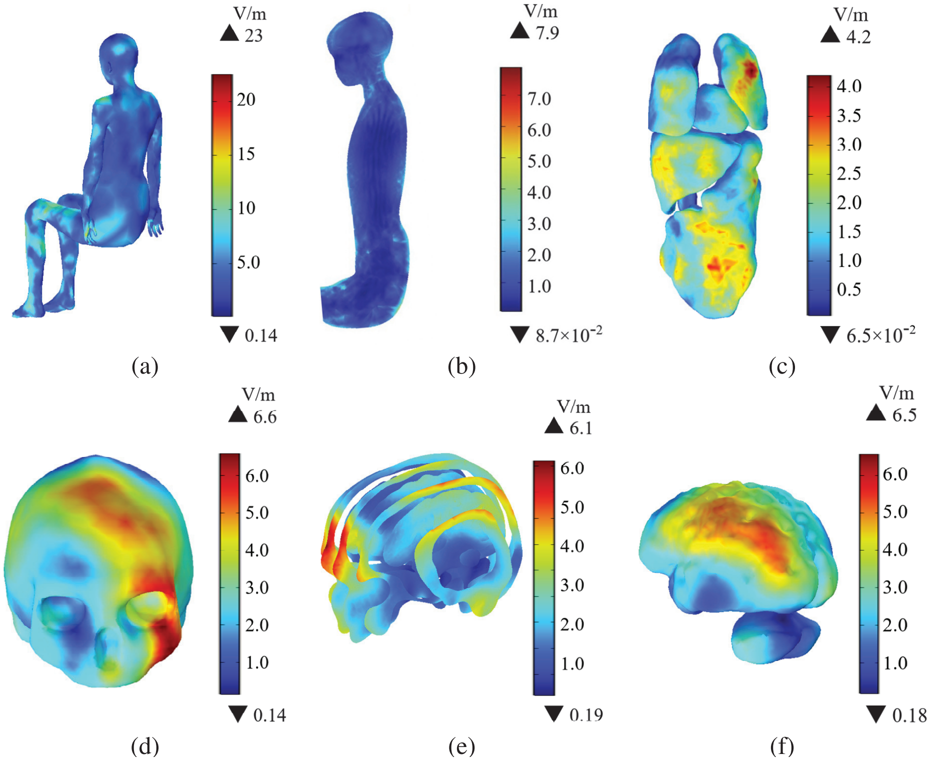

Fig. 11. Induced electric field (|E|) distributions in the child passenger's body: (a) |E| of the trunk, (b) |E| of the longitudinal cross-section of the body, (c) |E| of the different organs, (d) |E| of the skull, (e) |E| of the longitudinal cross-sections of the head, (f) |E| of the brain tissue.

B. Distribution of induced electric field in a child's body

Figure 11 shows distribution of the induced electric field (|E|) in a child's body. Figures 11 (a)–(b) are the distribution of |E| in the child passenger's trunk and central cross-section, respectively. The |E| in the trunk is relatively uniform, with a maximum value of 23 V/m. The maximum value of induced electric field ($|E|_{max}$) on the central cross-section of the child's body is 7.9 V/m. Figure 11 (c) shows the |E| in different major organs of the body. The |E| is highest in the lungs, followed by the gastrointestinal system and the liver, while the |E| in the kidneys is the smallest. The larger values of |E| are distributed on the surfaces of the organs, with a maximum value of 4.2 V/m. Given the importance of the central nervous system, Figs. 11 (d)–(f) show the distribution of |E| in the skull, and different longitudinal sections of the head and brain tissue, respectively. Brain tissue comprises grey matter, white matter, and the cerebellum, all of which are enclosed by the skull. The |E| in the skull is slightly higher, with a maximum of 6.6 V/m. Given the protective effect of the skull, the |E| in the brain tissue is relatively low, with a maximum of 6.5 V/m, and the higher values are mainly in the left-sided region of grey matter.

Figure 12 is the $|E|_{max}$ in different organs and tissues of the child passenger under the radiation of the positioning antenna. Given differences in dielectric properties and positions of various organs, the |E| in different organs also varies. The $|E|_{max}$ in the head tissue is slightly higher than in other tissues, which can be attributed to the dielectric parameters of the tissue and the proximity to the exposure source. Among other organs, the $|E|_{max}$ of the lungs is slightly higher, slightly lower in the gastrointestinal system, followed by that of the liver and heart, while the kidneys have the smallest value.

C. Distribution of SAR in the child's body

When a RF EMF interacts with the human body, electromagnetic energy is absorbed by biological tissues. SAR is used to quantify the amount of electromagnetic energy absorbed by biological tissues. The power of the radiation source is a critical parameter for regulating SAR values. When the radiation frequency of the source and the electromagnetic property parameters of human tissue are fixed, the SAR values show a significant positive correlation with the input power: increased input power enhances the electromagnetic energy absorbed by human tissue, and SAR value rises

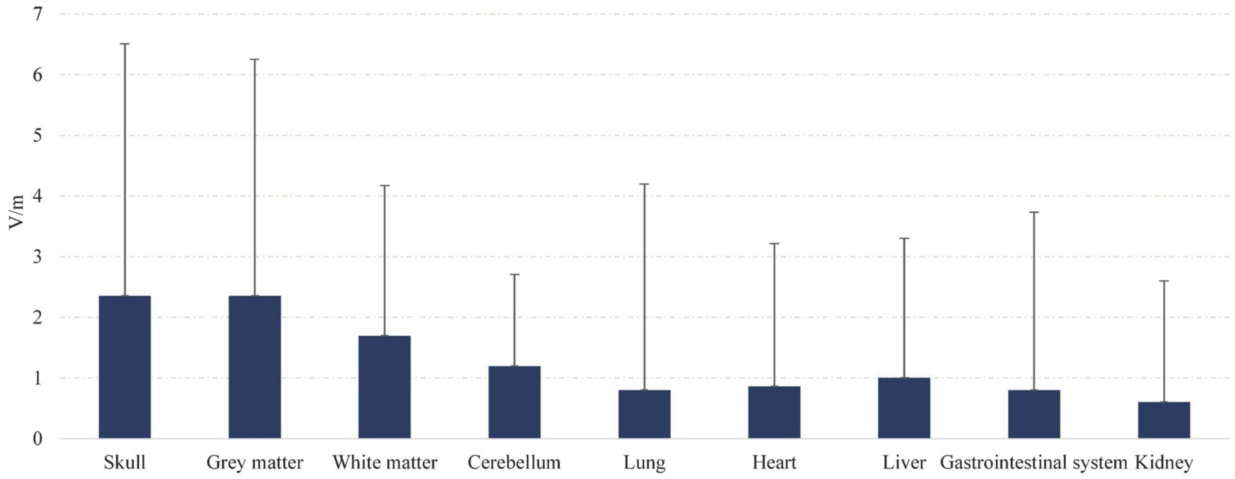

Fig. 12. $|E|_{max}$ in different organs and tissues of the child passenger.

accordingly. Conversely, reduced input power induces a decrease in SAR value. In this study, the SAR in different tissues of a child's body is calculated to evaluate the exposure of child passengers to the RF electromagnetic environment generated by the positioning antenna.

Figures 13 (a)–(b) are SAR_{1g} distribution in the child passenger's trunk and central cross-section, respectively. SAR_{1g} in the child passenger's trunk is relatively uniform. The maximum values of SAR_{1g} in the trunk and central cross-section are 0.19 W/kg and 2.4×10^{-2} W/kg, which remain below the safe limit for public exposure defined by the Federal Communications Commission's (FCC) requirements [50]. Figure 13 (c) shows SAR_{1g} in various organs of the child's body, which demonstrates that the maximum values of SAR_{1g} is primarily concentrated in the lungs with a maximum of 2.2×10^{-2} W/kg. Figures 13 (d)–(f) are SAR_{1g} in the skull, and different longitudinal sections of the head and brain tissue, respectively. The left frontal area of the head is close to the antenna, and SAR is higher, with a maximum value of 3.0×10^{-2} W/kg. From the skull to the brain tissue, the SAR_{1g} value decreases gradually, and the maximum values of SAR_{1g} in the brain tissue is 2.7×10^{-2} W/kg. SAR_{1g} is well below the safe limit of 1.6 W/kg for general exposure limit defined by the FCC's requirements.

Figure 14 is the maximum values of SAR_{1g} in the different organs and tissues of the child passenger. The maximum value of SAR_{1g} in the brain tissue is approximately 2.7×10^{-2} W/kg, which is smaller than that in the skull. In other organs, SAR_{1g} is the highest in the lungs, with a maximum of 2.2×10^{-2} W/kg, whereas SAR_{1g} in the kidneys is lowest. The differences of SAR_{1g} in different organs are due to electrical conductivity, tissue density and distance from the radiation source. Thus, the SAR_{1g} for all organs and tissues in the child's body remain below the general exposure limit of 1.6 W/kg defined by the FCC's requirements [50]. By calculation, the average whole-body SAR for the child passenger is 0.0054 W/kg, below the general exposure limit of 0.08 W/kg defined by the FCC's requirements.

D. Temperature rise in the child's body

When exposed to RF EMFs, the electromagnetic energy absorbed by the human body causes the temperature to rise. To ensure that temperature increases remain within safe limits, the ICNIRP has defined the threshold of 1°C as the limit for adverse health effects due to tissue temperature rise [51].

In this study, the initial temperature of the child's body is set to 36.5°C, and the temperature change is calculated within 30 minutes of exposure to the radiation from the positioning antenna. As shown in Figs. 15 (a)–(b), the maximum temperature rise in the child passenger's trunk and central cross-section is 0.47°C and 0.38°C, respectively. Figure 15 (c) shows the temperature rise in different major organs. The temperature rise in the lungs is the biggest, with a maximum value of 0.55°C, probably due to their lower density than other organs. Figures 15 (d)–(f) are the temperature rise in the skull, and different longitudinal sections of the head and brain tissue, respectively. The temperature rise of the skull is greater than that of the brain tissue, and the maximum temperature rise in the skull is 0.38°C. The maximum temperature rise in the brain tissues is 0.27°C.

Figure 16 is a comparison of temperature rise in different organs and tissues within 60 minutes under the radiation of the positioning antenna. The temperature of each organ increases rapidly in the early stage and then gradually stabilizes. In brain tissue, the temperature rise

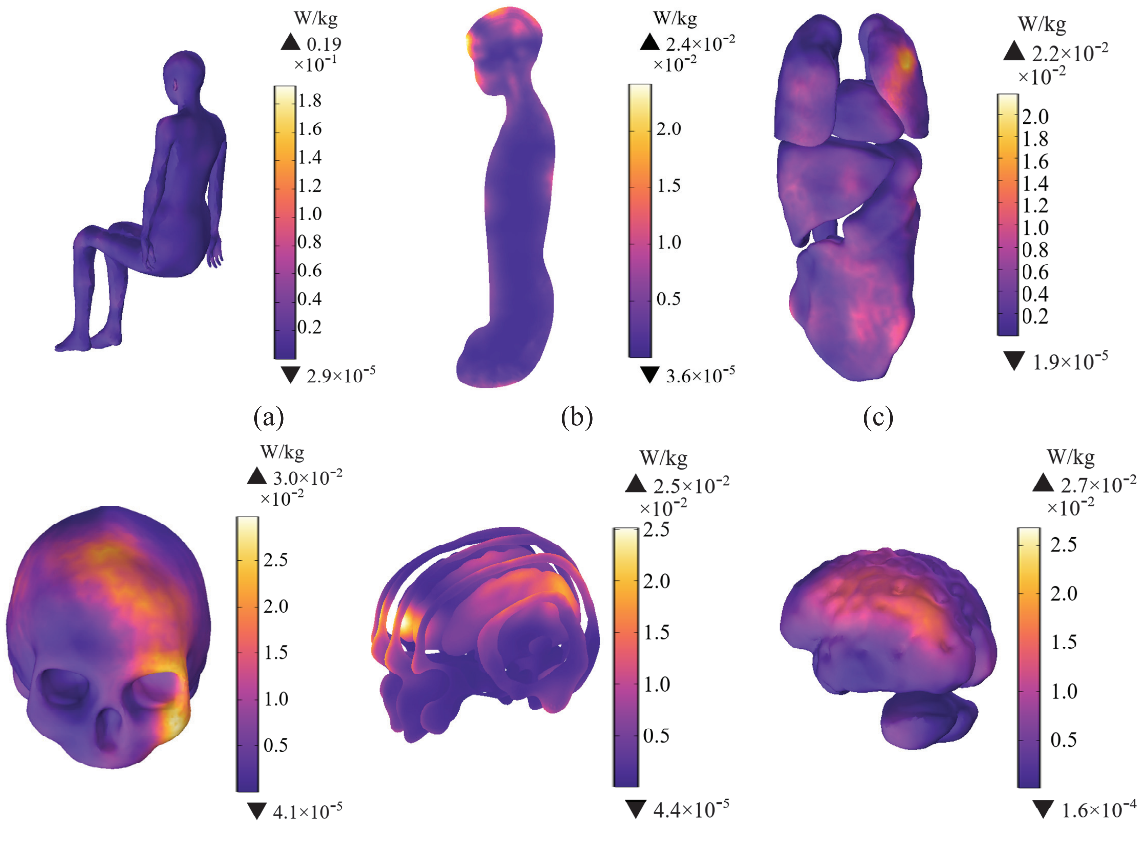

(a) (b) (c)

(d) (e) (f)

Fig. 13. SAR_{1g} distributions in the child passenger's body: (a) SAR_{1g} of the trunk, (b) SAR_{1g} of the longitudinal cross-section of the body, (c) SAR_{1g} of the different organs, (d) SAR_{1g} of the skull, (e) SAR_{1g} of the longitudinal cross-sections of the head, (f) SAR_{1g} of the brain tissue.

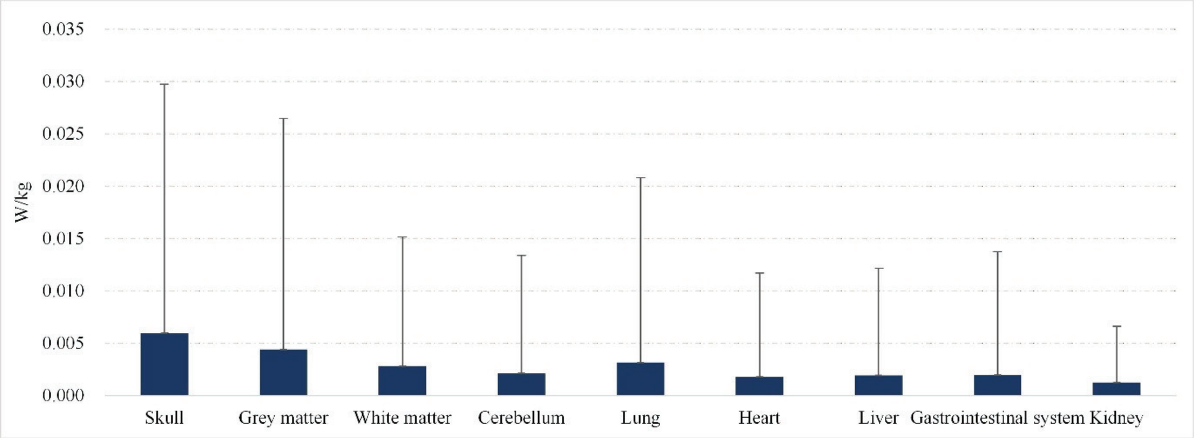

Fig. 14. Maximum values of SAR_{1g} in different organs and tissues of the child passenger.

trends of grey matter, white matter, and the cerebellum are similar. The increase is fastest within the first 0-5 minutes, then gradually slows down. Over a 60-minute period, their temperature increase is also the smallest, all at approximately 0.3°C. The temperature rise of the skull increases gradually within 60 minutes, reaching a maximum rise of 0.55°C. Compared with other organs and tissues, the temperature rise in the lungs is the largest with a maximum of 0.64°C. The rate of temperature rise of other organs within 60 minutes is relatively moderate,

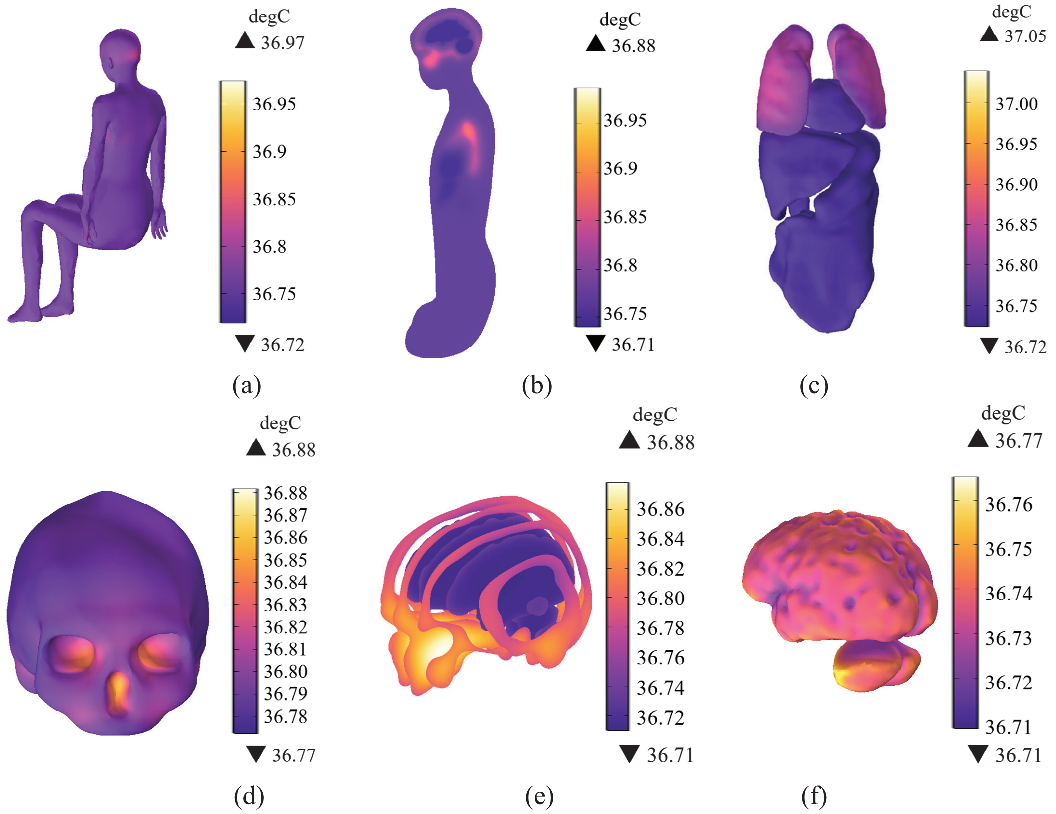

Fig. 15. Temperature rise in the child passenger's body: (a) temperature rise of the trunk, (b) temperature rise of the longitudinal cross-section of the body, (c) temperature rise of the different organs, (d) temperature rise of the skull, (e) temperature rise of the longitudinal cross-sections of the head, (f) temperature rise of the brain tissue.

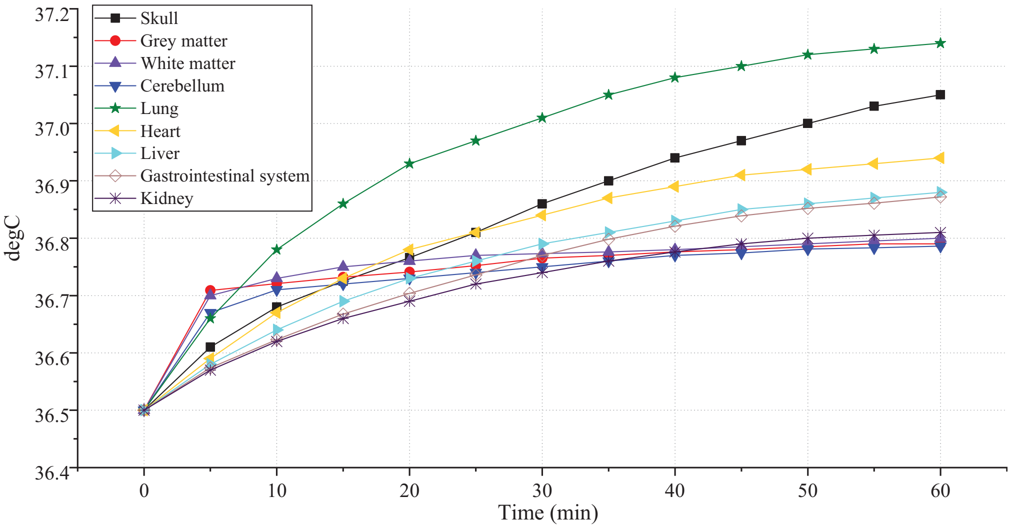

Fig. 16. Temperature rise of different organs and tissues of the child passenger within 60 minutes.

between 0.3°C and 0.4°C. In summary, the temperature rise in all tissues and organs of the child's body remains below the ICNIRP limit of 1°C [51].

IV. DISCUSSION

With the rapid development of EVs and AD technology, positioning antennas have been widely installed on AD vehicles. The body of a child passenger may be more sensitive to electromagnetic radiation because it is still growing and developing; thus, the electromagnetic radiation level of child passengers in EVs must be studied. Taking the positioning antenna of EV as the exposure source, this study constructed an electromagnetic environment model including the vehicle body, the positioning antenna and the child passenger model. COMSOL Multiphysics was used to calculate the electromagnetic environment of the positioning antenna with a frequency of 1.575 GHz and to quantify the exposure levels in different tissues and organs of the child passenger. The results show that $|E|_{\max}$ in the child's body is 23 V/m, and $|E|_{\max}$ in the child's brain is 6.6 V/m. Moreover, the maximum of SAR_{1g} in the child's body is 0.19 W/kg, the maximum of SAR_{1g} in the child's brain is 2.7×10^{-2} W/kg. The SAR_{1g} levels calculated for the child models in this study are all below the safety limit of 1.6 W/kg defined by the FCC's requirements. Within 30 minutes, the region of the child's body with the maximum temperature rise is the lungs, with a maximum rise of 0.55°C, while the maximum temperature rise in the head is 0.38°C. The temperature rises calculated for the child models in this study are all below the safety limit of 1°C defined by ICNIRP 2020. The distribution of induced field is slightly different due to different dielectric parameters of tissues and different positions with the exposure source. Therefore, the electromagnetic radiation generated by the positioning antenna does not pose a threat to the health of the child passenger. The calculation results of this study effectively supplement research on the electromagnetic environment of EVs and improve public cognition of the electromagnetic environment of EVs. In addition, it can provide reference for the revision of electromagnetic radiation standards and the optimization of positioning antenna design.

ACKNOWLEDGMENT

This work was supported by the National Natural Science Foundation of China (Grant No.52467026), the Natural Science Foundation of Gansu Province, China (Grant No. 23JRRA889), the Innovation Fund Project of Colleges and Universities in Gansu Province (Grant No. 2024B-057) and the Key Research Platform Construction Project of Gansu Province (Grant No. 2024CXPT-11).

REFERENCES

[1] R. Wu, "Research on the development trend of new energy electric vehicles in China based on mathematical model," *SJEMR*, vol. 6, no. 10, pp. 26–33, Oct. 2024.

[2] J. N. Barkenbus, "Prospects for electric vehicles," *Sustainability*, vol. 12, no. 14, pp. 5813, July 2020.

[3] K. Kaur and G. Rampersad, "Trust in driverless cars: Investigating key factors influencing the adoption of driverless cars," *J. Eng. Technol. Manage.*, vol. 48, pp. 87–96, Apr. 2018.

[4] J. L. Volakis, A. J. O'Brien, and C.-C. Chen, "Small and adaptive antennas and arrays for GNSS applications," *Proc. IEEE*, vol. 104, no. 6, pp. 1221–1232, June 2016.

[5] X. Dong, Y. Ren, and M. Lu, "Electromagnetic exposure level of pure electric vehicle inverter to human body in different seating positions," *Radiat. Prot. Dosim.*, vol. 201, no. 4, pp. 270–283, Mar. 2025.

[6] Y. Hakuta, T. Watanabe, T. Takenaka, T. Ito, and A. Hirata, "Safety standard compliance of human exposure from vehicle cables using coupling factors in the frequency range of 0.3-400 kHz," *IEEE Trans. Electromagn. Compat.*, vol. 63, no. 1, pp. 313–318, Feb. 2021.

[7] T. Tan, T. Jiang, Y. Wu, Y. Zhu, and Y. Chi, "Safety assessment of gender-specific human electromagnetic exposure with aortic valve stents for EV-WPT," *Applied Computational Electromagnetics Society (ACES) Journal*, pp. 742–753, Aug. 2024.

[8] T. Wang, B. Li, K. Zhao, and Q. Yu, "Evaluation of electromagnetic exposure of the human with a coronary stent implant from an electric vehicle wireless power transfer device," *Electronics*, vol. 12, no. 20, p. 4231, Oct. 2023.

[9] V. Anderson, "Comparisons of peak SAR levels in concentric sphere head models of children and adults for irradiation by a dipole at 900 MHz," *Phys. Med. Biol.*, vol. 48, no. 20, pp. 3263–3275, Oct. 2003.

[10] T. Mo, Y. Li, K. Lau, C. K. Poon, Y. Wu, and Y. Luo, "Trends and emerging technologies for the development of electric vehicles," *Energies*, vol. 15, no. 17, p. 6271, Aug. 2022.

[11] P. Moreno-Torres Concha, P. Velez, M. Lafoz, and J. R. Arribas, "Passenger exposure to magnetic fields due to the batteries of an electric vehicle," *IEEE Trans. Veh. Technol.*, vol. 65, no. 6, pp. 4564–4571, June 2016.

[12] N. Haussmann, R. Mease, M. Zang, S. Stroka, H. Hensel, and M. Clemens, "Efficient high-resolution electric and magnetic field simulations inside the human body in the vicinity of wireless power transfer systems with varying models," *COMPEL*, vol. 42, no. 4, pp. 903–913, June 2023.

[13] I. A. Shah, Y. Cho, and H. Yoo, "Safety evaluation of medical implants in the human body for a wireless power transfer system in an electric vehicle," *IEEE Trans. Electromagn. Compat.*, vol. 63, no. 3, pp. 681–691, June 2021.

[14] J. Lin, M. Lu, T. Wu, L. Yang, and T. Wu, "Evaluating extremely low frequency magnetic fields in the rear seats of the electric vehicles," *Radiat. Prot. Dosim.,* vol. 182, no. 2, pp. 190–199, Dec. 2018.

[15] W. Yang, Y. L. Xu, C.Q. Wang, F.H. Lin, and L. Dong, "Research on the safety of human electromagnetic environment of wireless energy transfer locomotive," *Transactions of China Electrotechnical Society*, vol. 37, no. 11, pp. 2665–2672, 2023.

[16] J. Wang, S. Mu, and Z. Hai, "Research on the influence of electromagnetic radiation in the automobile on the SAR value of human body," *J. Phys.: Conf. Ser.*, vol. 1684, no. 1, p. 012153, Nov. 2020.

[17] M. Y. Li and X. Zhang, "Modeling and electromagnetic safety assessment of wireless power transfer systems for electric vehicles," *J. Power Supply*, vol. 21, no. 04, pp. 177–185, 2023.

[18] B. Pophof, B. Henschenmacher, D. R. Kattnig, J. Kuhne, A. Vian, and G. Ziegelberger, "Biological effects of radiofrequency electromagnetic fields above 100 MHz on fauna and flora: Workshop report," *Health Phys.*, vol. 124, no. 1, pp. 31–38, Jan. 2023.

[19] A. Bortkiewicz, "Health effects of radiofrequency electromagnetic fields (RF EMF)," *Ind. Health*, vol. 57, no. 4, pp. 403–405, 2019.

[20] M. I. Hossain, M. R. I. Faruque, and M. T. Islam, "Analysis on the effect of the distances and inclination angles between human head and mobile phone on SAR," *Prog. Biophys. Mol. Biol.*, vol. 119, no. 2, pp. 103–110, Nov. 2015.

[21] E. Baramili, R. Sarkis, and M. B. Saleh, "Investigation of driver EMF exposure from 4G/5G automotive glass mounted antennas," in *IEEE International Symposium on Antennas and Propagation and North American Radio Science Meeting*, Montreal, QC, Canada, pp. 1451–1452, July 2020.

[22] G. Tognola, B. Masini, S. Gallucci, and M. Bonato, "Numerical assessment of RF human exposure in smart mobility communications," *IEEE J. Electromagn. RF Microw. Med. Biol.*, vol. 5, no. 2, pp. 100–107, June 2021.

[23] G. Tognola, M. Benini, M. Bonato, S. Gallucci, and M. Parazzini, "Assessment of the variability of human exposure to radiofrequency electromagnetic fields arising from 5.9 GHz vehicular communication in urban environments," *Sensors*, vol. 23, no. 15, p. 6802, July 2023.

[24] S.-W. Leung, Y. Diao, K.-H. Chan, Y.-M. Siu, and Y. Wu, "Specific absorption rate evaluation for passengers using wireless communication devices inside vehicles with different handedness, passenger counts, and seating locations," *IEEE Trans. Biomed. Eng.,* vol. 59, no. 10, pp. 2905–2912, Oct. 2012.

[25] J. Malmivuo and R. Plonsey, *Bioelectromagnetism Principles and Applications of Bioelectric and Biomagnetic Fields*. Oxford: Oxford University Press, 1995.

[26] H. Sun, S. Hou, Y. Zhao, W. Yan, and Y. Wu, "Investigation of electromagnetic exposure of WPT coil to human body based on biological electromagnetic safety assessment," *Applied Computational Electromagnetics Society (ACES) Journal*, vol. 36, no. 10, pp. 1355–1366, Nov. 2021.

[27] I. Liorni, C. Myles, W. Luuk, W. Joe, J. Wout, C. Elisabeth, G. Mònica, V. Roel, and T. Arno, "Evaluation of specific absorption rate in the far-field, near-to-far field and near-field regions for integrative radiofrequency exposure assessment," *Radiat. Prot. Dosim.*, vol. 190, no. 4, pp. 459–472, Oct. 2020.

[28] H. H. Pennes, "Analysis of tissue and arterial blood temperatures in the resting human forearm," *Journal of Applied Physiology*, vol. 1, no. 2, pp. 93–122, Aug. 1948.

[29] S. Gabriel, R. W. Lau, and C. Gabriel, "The dielectric properties of biological tissues: III. Parametric models for the dielectric spectrum of tissues," *Phys. Med. Biol.*, vol. 41, no. 11, pp. 2271–2293, Nov. 1996.

[30] M. Thurai, V. D. Goodridge, R. J. Sheppard, and E. H. Grant, "Variation with age of the dielectric properties of mouse brain cerebrum," *Phys. Med. Biol.*, vol. 29, no. 9, pp. 1133–1136, Sep. 1984.

[31] A. Peyman and C. Gabriel, "Cole–Cole parameters for the dielectric properties of porcine tissues as a function of age at microwave frequencies," *Phys. Med. Biol.*, vol. 55, no. 15, pp. N413-N419, Aug. 2010.

[32] A. Peyman, A. A. Rezazadeh, and C. Gabriel, "Changes in the dielectric properties of rat tissue as a function of age at microwave frequencies," *Phys. Med. Biol.*, vol. 46, pp. 1617–1629, 2001.

[33] A. K. Lee, H. D. Choi, and J. I. Choi, "Study on SARs in head models with different shapes by age using SAM model for mobile phone exposure at 835 MHz," *IEEE Trans. Electromagn. Compat.*, vol. 49, no. 2, pp. 302–312, May 2007.

[34] X. Dong, Y. Qian, and M. Lu, "Electromagnetic exposure levels of electric vehicle drive motors to passenger wearing cardiac pacemakers," *Sensors*, vol. 24, no. 13, p. 4395, July 2024.

[35] P. A. Hasgall, F. Di Gennaro, C. Baumgartner, and E. Neufeld, "IT'IS Database for thermal and electromagnetic parameters of biological tissues," *Version 3.0*, Sep. 2015.

[36] Y. Fan, Z. Jin, Z. Fu, X. Cai, and Q. Lin, "Low-profile, broadband, and high-gain circularly polarized meta surface antenna using characteristic mode analysis," *Applied Computational Electromagnetics Society (ACES) Journal*, vol. 40, no. 05, pp. 401–408, May 2025.

[37] S. S. Hao, Q. Q. Chen, J. Y. Li, and J. Xie, "A high-gain circularly polarized slotted patch antenna," *Antennas Wirel. Propag. Lett.*, vol. 19, no. 6, pp. 1022–1026, June 2020.

[38] C. L. Lin, *Antenna Engineering Manual*. Beijing: Publishing House of Electronics Industry, 2002.

[39] C. Sun, H. Zheng, and Y. Liu, "Analysis and design of a low-cost dual-band compact circularly polarized antenna for GPS application," *IEEE Trans. Antennas Propagat.*, vol. 64, no. 1, pp. 365–370, Jan. 2016.

[40] S. Mishra, S. Das, S. S. Pattnaik, S. Kumar, and B. K. Kanaujia, "Low-profile circularly polarized planar antenna for GPS L1, L2, and L5 bands," *Microw. Opt. Techn. Let.*, vol. 62, no. 2, pp. 806–815, Mar. 2020.

[41] L. Garcia-Gamez, L. Bernard, S. Collardey, H. Covic, R. Sauleau, K. Mahdjoubi, P. Potier, and P. Pouliguen, "Compact GNSS metasurface-inspired cavity antennas," *Antennas Wirel. Propag. Lett.,* vol. 18, no. 12, pp. 265–2656, Dec. 2019.

[42] H. Aliakbari, X. Li, C. Lötbäck, and B. K. Lau, "Roof-glass integrated antenna for vehicular GNSS applications," in *18th European Conference on Antennas and Propagation*, Glasgow, pp. 1–5, Mar. 2024.

[43] Q. H. Dang, N. Nguyen-Trong, T. Kaufmann, T. Saarnimo, C. Hide, and C. Fumeaux, "Dual-band circularly-polarized transparent GNSS antenna for vehicular applications," *IEEE Open J. Antennas Propag.*, vol. 6, no. 1, pp. 201–211, Feb. 2025.

[44] M. C. Gosselin, E. Neufeld, H. Moser, and E. Huber, "Development of a new generation of high-resolution anatomical models for medical device evaluation: The Virtual Population 3.0," *Phys. Med. Biol.*, vol. 59, no. 18, pp. 5287–5303, 2014.

[45] V. De Santis, L. Giaccone, and F. Freschi, "Influence of posture and coil position on the safety of a WPT system while recharging a compact EV," *Energies*, vol. 14, no. 21, p. 7248, Nov. 2021.

[46] J. Grosinger, L. W. Mayer, C. F. Mecklenbrauker, and A. L. Scholtz, "Determining the dielectric properties of a car tire for an advanced tire monitoring system," in *IEEE 70th Vehicular Technology Conference Fall.*, Anchorage, AK, pp. 1–5, Sep. 2009.

[47] H.-Y. Kim and H.-G. Kim, "A hexahedral-dominant FE meshing technique using trimmed hexahedral elements preserving sharp edges and corners," *Eng. Comput.*, vol. 38, no. 5, pp. 4307–4322, Oct. 2022.

[48] A. Conchin Gubernati, F. Freschi, L. Giaccone, and R. Scorretti, "Analysis of numerical artifacts using tetrahedral meshes in low frequency numerical dosimetry," *Appl. Sci.,* vol. 12, no. 13, p. 6526, June 2022.

[49] A. Hirata, T. Fujino, and T. Shiozawa, "SAR in the human body due to EM waves emitted from a dipole antenna at 400 MHz band," in *IEEE International Symposium on Electromagnetic Compatibility*, Istanbul, vol. 1, pp. 17–20, 2003.

[50] X. Hu, S. Yan, J. Zhang, V. Volski, and G. A. E. Vandenbosch, "Omni-directional circularly polarized button antenna for 5 GHz WBAN applications," *IEEE Trans. Antennas Propagat.,* vol. 69, no. 8, pp. 5054–5059, Aug. 2021.

[51] ICNIRP, "Guidelines for limiting exposure to electromagnetic fields (100 kHz to 300 GHz)," *Health Phys.*, vol. 118, no. 5, pp. 483–524, May 2020.

Xuwei Dong received the Ph.D. degree from Lanzhou Jiaotong University, Lanzhou, China, in 2019. He is an associate professor at Lanzhou Jiaotong University. He has successively undertaken or participated in the National Natural Science Foundation project of China. His main research fields are biomedical electromagnetism and electromagnetic exposure safety assessment.

Yufei Ren received the B.S. degree in communication engineering from Henan University, Zhengzhou, China, in 2023. She is currently pursuing the master's degree at Lanzhou Jiaotong University. Her work centers on evaluating the safety of RF-EMF exposure and biomedical electromagnetism.

Mai Lu received the Ph.D. degree from Lanzhou University, Lanzhou, China in 1999. He is a professor at Lanzhou Jiaotong University, Lanzhou. He has successively undertaken or participated in the UK EPSRC project, the seventh EU framework agreement project, and the National Natural Science Foundation project. His main research fields are biomedical electromagnetism and electromagnetic exposure safety assessment.

Inversion Method Based on CNN-BiLSTM-Attention for SQUID TEM Data with IP Effect

Yanju Ji[1,2], Jinxiu Yuan[1], Hui Luan[1,2], Yuan Wang[1,2], and Qiong Wu[1,2]*

[1]College of Instrumentation and Electrical Engineering
Jilin University, Changchun 130026, China
jiyj@jlu.edu.cn, yuanjx6522@mails.jlu.edu.cn, luanhui@jlu.edu.cn,
wangyuan_ciee@jlu.edu.cn, wuqiong_515@sina.cn*

[2]State Key Laboratory of Deep Earth Exploration and Imaging
Jilin University, Changchun 130026, China

Abstract – The superconducting quantum interference device time-domain electromagnetic (SQUID TEM) method has been widely used for the exploration of geological and mineral resources. Extracting resistivity and polarizability from TEM data aids in delineating subsurface metallic mineralization. However, traditional inversion methods are computationally intensive and slow. We propose an inversion method based on a convolutional neural network and bidirectional long short-term memory with attention (CNN-BiLSTM-Attention) to extract resistivity and polarizability of polarizable media from SQUID TEM data acquired with a magnetic source. The method combines the advantages of CNN for automatic feature extraction with the capabilities of BiLSTM for processing temporal data. Additionally, it incorporates an attention mechanism that emphasizes the extraction of key polarization features, thereby optimizing the parameters extraction process. The method can effectively extract resistivity and polarizability from SQUID TEM data. It is validated by the TEM data of theoretical models, and the errors of CNN-BiLSTM-Attention inversion results are smaller than that of the BiLSTM and CNN-LSTM methods.

Index Terms – Attention mechanism, BiLSTM, CNN, inversion method, polarizable medium, SQUID TEM.

I. INTRODUCTION

The lack of mineral resources resulting from socioeconomic development may adversely affect global economic stability. To guarantee resource security and sustainable economic development, it is essential to advance deep earth exploration technologies for the precise identification of mineral resources [1]. These minerals typically exist in the form of sulfide or disseminated ores, which may cause an induced polarization (IP) effect. Resistivity and polarizability are two essential characteristics that affect the electromagnetic effect, and they indicate the positions of the ore bodies which are vital for the identification of metallic ores [2, 3]. Advancing inversion techniques can improve both accuracy and speed, which will in turn support secure and efficient mineral resource exploration through TEM inversion.

To detect exceedingly weak electromagnetic field signals, numerous researchers have studied superconducting quantum interference devices (SQUID), which are highly sensitive magnetic sensors capable of detecting magnetic field variations on the order of 10^{-15} T [4]. Superconducting quantum interference devices time domain electromagnetic (SQUID TEM) detection method has been extensively utilized in the investigation of geological and mineral resources. In practical exploration, TEM responses may exhibit sign reversal, a phenomenon commonly attributed to the polarization effect of the subsurface medium [5–7]. Consequently, it is essential to investigate the inversion method for electromagnetic induction-polarization (EM-IP) effect. In recent years, there have been numerous investigations into the extraction of the relevant polarization parameters. Viezzoli et al. inverted time-domain airborne electromagnetic IP parameters using a 1D lateral constraint method, showing that when the time constant is within a certain range, the method provides good solutions for both resistivity and polarizability [8]. Man et al. proposed an inversion method for airborne TEM data with IP effect based on Pearson correlation constraints, improving the accuracy and stability of

Submitted On: April 29, 2025
Accepted On: December 23, 2025

https://doi.org/10.13052/2026.ACES.J.410307

the inverted resistivity and polarizability, and reducing inversion non-uniqueness [9]. Lu et al. presented a quasi-2-D inversion scheme for extracting resistivity and IP parameters from semi-airborne TEM data, improving inversion stability and recovering underground property distributions [10]. Wang et al. introduced a modified quasi-2D regularized Newton inversion scheme for extracting IP parameters of ColeCole model [11].

Conventional parameter-extraction methods often rely on an initial model and iterative solvers, making them computationally intensive and time-consuming. This poses a significant challenge in achieving a balance between efficiency and accuracy, especially when handling large-scale geophysical data. The neural networks have become a promising solution of geophysical problems, such as exploration geophysics, Earth system analysis [12, 13]. Ji et al. presented a neural network method using Rademacher complexity to accurately invert ground-source airborne TEM data for resistivity and roughness in rough geological media [14]. Alyousuf and Li presented a physics-based neural network inversion method that combines deterministic and neural network approaches [15]. Li et al. developed a probabilistic seismic petrophysical inversion method using a physics-informed neural network (PINN), improving accuracy and quantifying model uncertainty in predicting petrophysical properties from seismic data [16]. Neural networks, through extensive learning from vast amounts of training data, are capable of performing inversion without explicitly calculating the forward model, significantly reducing the computational complexity inherent in traditional methods. At the same time, the powerful learning capability and excellent generalization ability of neural networks enable them to provide higher parameter extraction accuracy and faster computational speeds when addressing various types of geophysical problems. This method enhances parameter extraction efficiency and expands its potential application in intricate geological settings.

We propose an attention-based CNN-BiLSTM inversion method to extract polarization parameters from SQUID TEM data acquired with a magnetic source. This method can leverage the benefits of convolutional neural network (CNN) in automatic feature extraction, combined with the capacity of bidirectional long short-term memory networks (BiLSTM) to capture temporal data and geographical context. Moreover, by integrating the attention mechanism, the model may autonomously concentrate on essential aspects within the input data. This method streamlines the parameter extraction process, dramatically improving both accuracy and speed. The method shows improved generalization and broader application potential compared with existing approaches.

II. NUMERICAL SIMULATION METHOD OF THE TIME-DOMAIN EM-IP RESPONSE

A. Numerical simulation method

Several physical models describe the polarization behavior of rocks. Notable instances encompass the Debye model, the Dias model, and the GEMTIP model, among others. The Cole-Cole complex resistivity model [17], introduced by Pelton et al. in 1978, is a typical approach and is articulated as follows:

$$\rho(\omega) = \rho_0 \left(1 - \eta \left(1 - \frac{1}{1 + (\mathrm{i}\omega\tau)^C}\right)\right), \qquad (1)$$

where ρ_0 is dc resistivity, η is polarizability, τ is time constant, c is frequency-dependent coefficient, i is imaginary unit, and ω is angular frequency.

This study assumes a layered medium model, and the magnetic source with a radius of a positioned at the horizontal surface. The formula for the vertical magnetic field in the frequency domain H_Z is expressed as [18, 19]:

$$H_z = \frac{Ia}{2} \int_0^\infty [e^{-u_0(z+h)} + r_{TE} e^{u_0(z-h)}] \frac{\lambda^2}{u_0} J_1(\lambda a) d\lambda, \quad (2)$$

where I is source-current amplitude, J_1 is first-order Bessel function, r_{TE} is reflection coefficient determined by the geoelectric parameters, $u_0 = (\lambda^2 - k^2)^{1/2}$, k is wave number of the polarization medium, especially $k = (-i\omega\mu/\rho(\omega))^{1/2}$, μ is permeability of the medium, and λ represents integrable variable quantity of the Hankel transform. The frequency-domain electromagnetic response is derived using the Hankel transform. The vertical component of the induced voltage $V_z(s)$ is calculated by the equation: $V_z(s) = -s\mu H_z$. The frequency-domain results are subsequently converted to the time-domain using Guptasarma's numerical linear filtering approach.

B. Validation of numerical simulation methods

Figure 1 presents the schematic diagram of the SQUID TEM system, which intuitively illustrates the geometric configuration and parameter settings of the system. The transmitter loop with a radius of 100 m is placed on the ground surface, and the SQUID receiver (Rx) is located at the center of the loop to measure the TEM response. The subsurface is represented by a horizontally layered geoelectric model, where each layer is characterized by its resistivity ρ and polarizability η parameters based on the Cole-Cole model. In SQUID TEM system, the transmitter emits a bipolar square wave current, and the SQUID receiver collects TEM responses containing underground information. Figure 2 displays the electromagnetic response of half-space model with the resistivity at 100 Ωm, and the numerical simulation results nearly coincide with the analytical solution. The relative error is below 1.2%, and the accuracy of the numerical simulation method is verified.

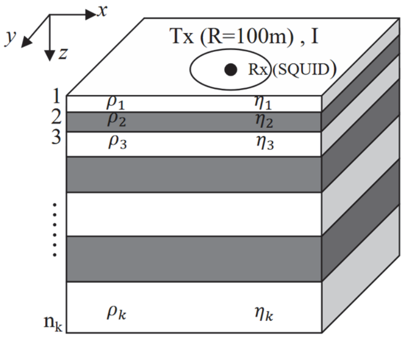

Fig. 1. Configuration of SQUID TEM system.

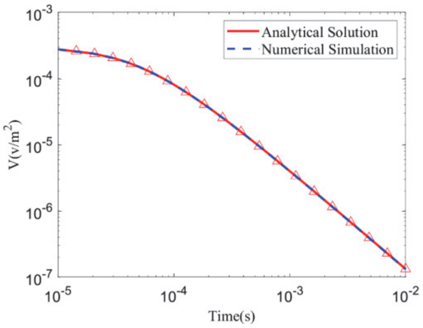

Fig. 2. Numerical simulation results of electromagnetic response of half-space model.

C. Polarizable medium parameters characteristics

The Cole-Cole model of a polarizable medium comprises four parameters: resistivity ρ, polarizability η, time constant τ, and frequency-dependent coefficient c. The time-domain EM-IP effect may be significantly affected by the resistivity and polarizability. The time-domain EM-IP effect of magnetic source of varying resistivities and polarizabilities is calculated. The TEM response curves presented in this paper represent the results after taking the absolute values. Figure 3 illustrates the TEM responses for resistivities ρ of 10,100, and 1000 Ω m, with a polarizability $\eta = 0.5$. In Fig. 3, it can be seen that the effect of different resistivities on the electromagnetic response exhibits a clear difference in the time and amplitude characteristics [20]. When resistivity is low (e.g., blue curve, $\rho = 10$ Ω m), the decay of the response curve is slower, the negative response appears later, and the amplitude of the negative response is larger; conversely, as resistivity increases (e.g., the red curve, $\rho = 100$ Ω m and the yellow curve, $\rho = 1000$ Ω m), the decay of the electromagnetic response is markedly expedited, the negative response emerges sooner, and the amplitude progressively diminishes. Figure 4 shows the electromagnetic response corresponding to resistivity $\rho = 100$ Ω m and polarizability $\eta = 0.3, 0.5, 0.7$. The differences in polarizability η significantly affect electromagnetic responses, particularly in the timing and amplitude features of negative responses. When the polarizability is low (e.g., blue curve, $\eta = 0.3$), the negative response occurs at a later stage, and its magnitude is relatively reduced. Conversely, as the polarizability escalates (e.g., red curve, $\eta = 0.5$ and yellow curve, $\eta = 0.7$), the negative response manifests sooner, while the magnitude progressively intensifies.

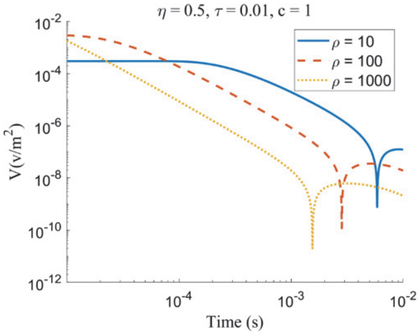

Fig. 3. Electromagnetic response curves for different resistivities.

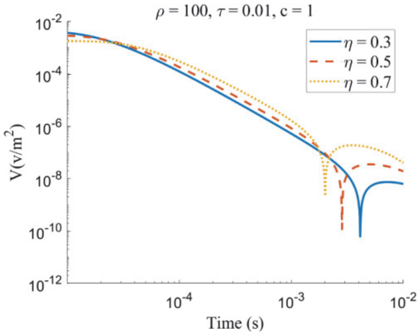

Fig. 4. Electromagnetic response curves for different polarizabilities.

III. CNN-BILSTM-ATTENTION INVERSION METHOD FOR EM-IP EFFECT

A. Convolutional neural network

The basic architecture of CNN comprises a convolutional layer, a pooling layer, and a fully connected layer, as illustrated in Fig. 5. The convolutional layer enables the extraction of local features from the input data via convolutional operations, thereby efficiently collecting essential patterns and structural information in the time series data of the EM-IP effect [21]. The pooling layer utilizes maximum pooling to reduce computing requirements and improve feature stability. The ReLU activation function is utilized to exclude insignificant data and improve the network's nonlinear representation. The precise formulation of the ReLU activation function is $\mathrm{ReLU}(x) = \max(0, x)$.

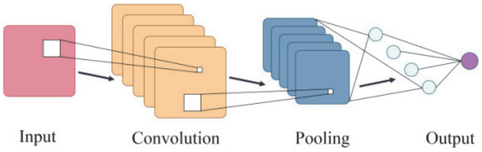

Fig. 5. Convolutional neural network architecture diagram.

B. Bidirectional long short-term memory network

Long short-term memory (LSTM) networks effectively handle time series data by integrating longterm and short-term memories via a gating mechanism [22]. Figure 6 illustrates the cellular architecture of LSTM.

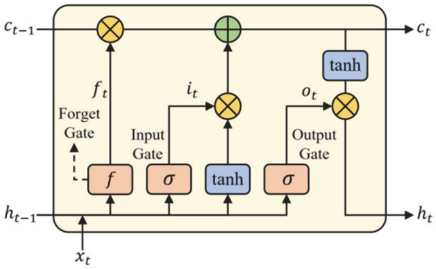

Fig. 6. Diagram of the internal structure of the long short-term memory.

In Fig. 6, c_{t-1} represents the previous cell state, h_{t-1} is the prior hidden state, and x_t is the current input. The forget gate f determines which information from c_{t-1} is discarded, while the relevant information is passed to c_t. The input gate σ controls how much of the current input x_t is retained, and the output gate o regulates the transfer of information from the current cell state to the output h_t.

BiLSTM enhances the conventional unidirectional LSTM. A conventional LSTM analyzes historical data in a single direction and cannot leverage future information. The BiLSTM, through its unique gating mechanisms and bidirectional processing capability, can simultaneously learn the temporal dependencies of this feature sequence from both the forward and reverse directions [23]. This capability is particularly advantageous for analyzing the temporal data of the EM-IP effect, as it comprehensively captures temporal relationships, amalgamates historical and future information, optimizes the training process, and enhances the accuracy of parameters extraction. The structure is illustrated in Fig. 7.

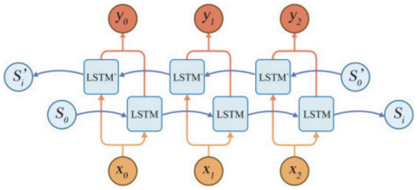

Fig. 7. Diagram of the structure of Bi-LSTM.

C. Attention mechanism

The attention mechanism is a bio-inspired selective processing method that emulates the human visual system's ability to focus on critical information. In the context of sequence modeling, it facilitates a weighted aggregation of features across all time steps by learning a set of normalized weights, thereby enabling the network to automatically emphasize the most task-relevant segments [24]. To enhance the efficiency of parameter extraction from EM-IP data, this study employs a soft attention mechanism. This allows the model to concentrate its computational resources on the most information-rich temporal segments while suppressing diffuse background signals. Let the matrix $Y = [y_1, \ldots, y_T] \in R^{d\times \mathrm{T}}$ represent the hidden state sequence from the BiLSTM, where $R^{d\times \mathrm{T}}$ is the matrix space of real-valued elements with d rows and T columns. Consequently, the state at the t-th time step, y_t is a dimensional column vector, and the total sequence length is T. The attention is computed as follows:

$$M = tanh(Y), \tag{3}$$

$$\alpha = softmax(w_a^T M), \tag{4}$$

$$A = Y\alpha^T, \tag{5}$$

where w_a is trainable weight matrix, α is normalized attention weight vector, and A is resulting context vector which aggregates the sequence information. The soft attention mechanism adaptively emphasizes the late-time windows that are most sensitive to polarizability by assigning higher weights to the corresponding time steps. The SoftMax normalization effectively suppresses noise and early-time transmitter interference by assigning them extremely low weights, thereby reducing the prediction variance. Concurrently, the attention weight vector α provides an interpretable map of temporal importance.

D. Data preprocessing

An essential step in the successful extraction of parameters is data preparation. This procedure involves applying normalization to input and output data in order to adjust them [25]. To reduce the effect of training bias caused by differences in numerical ranges, different electromagnetic response magnitudes are normalized to a constant range in the input data. For EM-IP effect data with a time series structure, this is very important. To improve forecast accuracy, the output data of polarizability and resistivity are also normalized. In bidirectional LSTM networks, normalization takes on a special importance. It avoids the vanishing or ballooning gradients that result from data that has not been normalized. Moreover, it improves accuracy and makes model convergence easier. Figure 8 present the loss curves for unnormalized and normalized data. The loss curve for the normalized data exhibits faster convergence and a lower final loss, thereby demonstrating the significant improvement in training efficiency and convergence performance afforded by normalization.

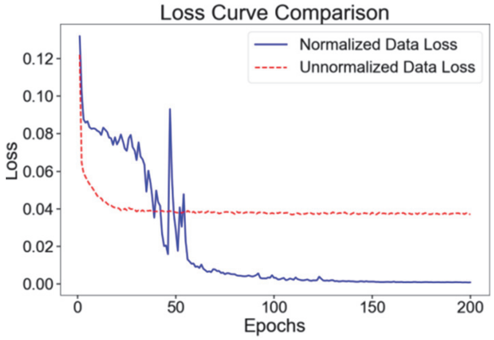

Fig. 8. Loss curve comparison.

E. CNN-BiLSTM-Attention inversion method

Figure 9 illustrates the overall architecture of the CNN-BiLSTM-Attention inversion framework proposed in this paper. Its core concept lies in a multi-stage, multi-dimensional feature extraction and focusing process, designed to achieve a deep analysis of the complex non-linear relationship between the transient electromagnetic (TEM) response data and the parameters of resistivity (ρ) and polarizability (η). It establishes a hierarchical “local-global-focus” analysis pipeline. The convolutional layers extract local patterns, the BiLSTM models bidirectional dependencies, and the attention layer re-weights the sequence according to α to generate the context vector A. Finally, the resistivity and polarizability are estimated. This method circumvents the drawbacks of traditional inversion methods, which are dependent on an initial model, computationally intensive, and may converge to local optima. The advantage of this framework stems from the functional complementarity of its components and its progressive, intelligent analysis capability.

The process commences with a one-dimensional CNN. In geophysical inversion, the local morphology of the TEM response curve across different time channels contains a wealth of geoelectric information. The CNN layers, through their convolutional kernels, can efficiently capture these local, fundamental feature patterns. This serves as an effective feature “preprocessing” and dimensionality reduction of the original high-dimensional time-series signal, laying a solid foundation for the more complex temporal analysis that follows.

The feature sequence extracted by the CNN is fed into a BiLSTM. The EM-IP effect is inherently a dynamic process that spans the entire time window, with long-range dependencies existing between signals at different time points. The BiLSTM, through its unique gating mechanisms and bidirectional processing capability, can simultaneously learn the temporal dependencies of this feature sequence from both the forward and reverse directions. Compared to a unidirectional LSTM or a traditional recurrent neural network, the BiLSTM can more comprehensively understand the contextual relationships within the signal, thereby achieving a more profound grasp of the overall dynamic evolution of the TEM response.

Finally, introduction of the Attention mechanism is a key optimization for the model and represents the core advantage of this architecture over other hybrid models. In a complex TEM response, not all temporal data points are of equal importance to the final parameter prediction. For instance, the negative-value region where the polarization effect occurs or the inflection points of the decay curve often contribute more significantly to the inversion result. The attention mechanism can, based on the hidden states output by the BiLSTM layer,

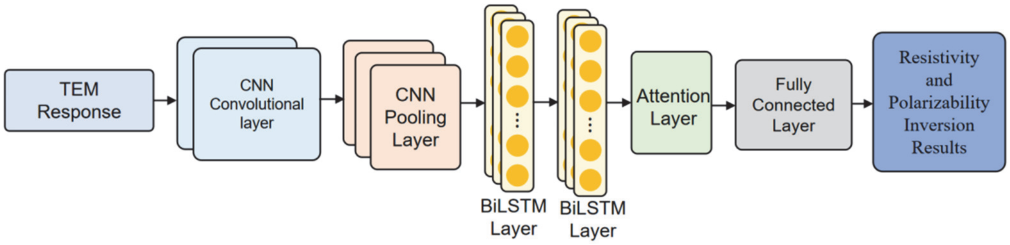

Fig. 9. Overall framework of CNN-BiLSTM-Attention.

dynamically assign different weights to the features of each time step. This allows the model to "focus" on those signal segments that are most sensitive to resistivity and polarizability and are most information-rich, while simultaneously suppressing noise and irrelevant information. This focusing capability is critical for enhancing the model's accuracy and robustness.

IV. KEY PARAMETER SETTINGS OF CNN-BILSTM-ATTENTION

In the CNN-BiLSTM-Attention framework, the selection of critical parameters, including the initial learning rate and Dropout value, significantly influences the model's performance, particularly for parameters extraction efficacy. Therefore, to guarantee that the model is trained under ideal conditions and attains high accuracy, this study systematically picks and optimizes critical hyperparameters [26].

A. Dropout value setting

During the training of deep neural networks, a small dataset combined with a complex model can lead to overfitting. This is primarily indicated by a higher loss function on the test dataset compared to the training set, along with reduced prediction accuracy relative to the training set. Dropout mitigates overfitting by randomly deactivating neurons during training [27].

The selection of the Dropout value will yield varying impacts on the training process. This paper selects Dropout values of 0.0001, 0.001, 0.01, and 0.1 for comparison. The test results, illustrated in Fig. 10, indicate that the loss function decreases most rapidly at a Dropout value of 0.001, yielding the smallest final loss function value. Consequently, the optimal Dropout value for this study is determined to be 0.001 for the CNN-BiLSTM-Attention inversion method.

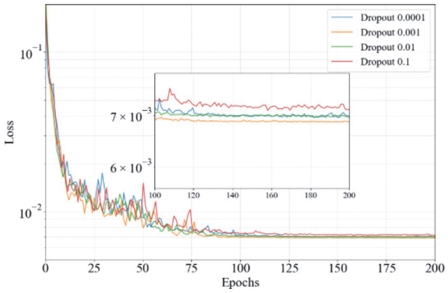

Fig. 10. Comparison of loss curves at different Dropout values.

B. Initial learning rate selection

This paper employs Adam's adaptive learning rate strategy, which adjusts the learning rate depending on current and historical gradient information [28]. A high initial learning rate can enhance training efficiency; nevertheless, an excessively high learning rate may bypass the global optimum or result in gradient explosion, preventing convergence. Figure 11 illustrates the comparison of loss curves corresponding to various beginning learning rates. With an initial learning rate of 0.1, the loss function nearly ceases to decrease after one training iteration, resulting in a gradient explosion; conversely, the final value of the loss function is minimized and most stable at a learning rate of 0.01.

Following the optimization and study of additional parameters, we established the definitive key parameter settings, with the particular values and corresponding settings detailed in Table 1. The neural network exhibited superior performance, and the model functioned effectively to obtain the most dependable inversion results.

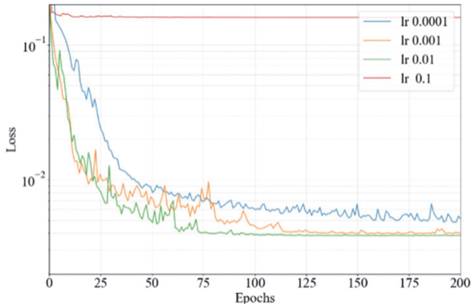

Fig. 11. Comparison of loss curves at different initial learning rates.

Table 1: Neural network key parameter settings

Neural Network Parameters	Values
CNN Convolutional Layer Kernel Size	2
CNN Convolutional Layer Count	2
BiLSTM Hidden Layer Node Count	64
BiLSTM Layer Count	2
Learning Rate Optimization Algorithm	Adam
Dropout Value	0.001
Initial Learning Rate	0.01

V. THEORETICAL MODEL VERIFICATION

To validate the efficacy of the CNN-BiLSTMAttention inversion method, theoretical models are developed for method verification.

A. Dataset, training strategy

This paper designs three models, a polarizable half-space, a three-layer polarizable model and a five-layer polarizable model. For all models, the time constant τ and the frequency-dependent coefficient c are kept consistent, with a time constant of 0.01 and a frequency-dependent coefficient of 1, to ensure the comparability of results across different geometric complexities. We generate parameter combinations centered around the baseline parameters of each theoretical model within a range of 25% to 200%. Resistivity (ρ) is sampled using logarithmic equal-ratio steps, while polarizability (η) is sampled with linear equal-distance steps. Based on this, the corresponding TEM response data are generated to form the complete sample datasets.

The sample datasets are divided into training, validation, and test sets (70%, 15%, 15%). Furthermore, all input TEM response data and output parameter labels are normalized to eliminate dimensional differences and accelerate model convergence. The optimization objective of the model training is to minimize the Mean Squared Error (MSE) between the predicted parameters and the true theoretical parameters, using the Adam adaptive moment estimation optimizer for the iterative updating of model weights. To prevent model overfitting and achieve stable convergence, we designed a combined convergence criterion. The core of this criterion consists of an Early Stopping mechanism and a dynamic learning rate decay strategy. The Early Stopping mechanism monitors the validation set loss; when it does not improve for 25 consecutive epochs, the training is automatically terminated, and the model weights that performed best on the validation set are restored. Concurrently, if the validation set loss stagnates for 15 epochs, the learning rate is automatically reduced to 0.5 times its previous value, with a minimum learning rate of 10^{-6}, then the model may perform a finer search when approaching an optimum.

B. Polarizable half-space model

We extract the parameters from TEM data for the polarizable half-space model. The polarizable halfspace model is configured with polarizability ranging from 0.1 to 0.9, resistivity from 1 to 1000 Ω m, a time constant $\tau = 0.01$, and a frequency-dependent coefficient $C = 1$. The TEM responses are calculated and the sample set is obtained.

Considering the correlation between resistivity and polarizability, the joint extraction error of the two parameters provides a more thorough indication of the correctness of the parameter extraction. In the computation of the combined relative error, resistivity and polarizability are assigned equal weight. To assess the accuracy of the extraction method, Fig. 12 displays the relative errors of the joint parameters extraction for various resistivity and polarization combinations, with their distribution illustrated through color coding. The relative error of the combined extraction results remains below 4% for all combinations of resistivity and polarizability. The effectiveness of the CNN-BiLSTMAttention inversion method is verified.

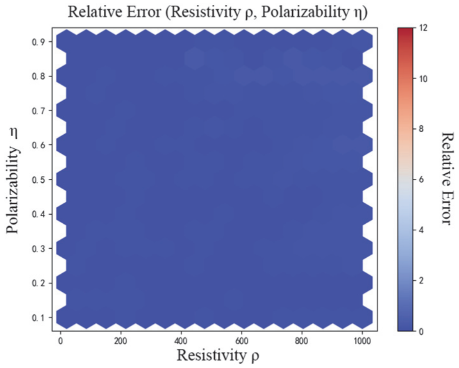

Fig. 12. Joint relative error of resistivity and polarizability extraction.

C. Three-layer polarizable model

To further validate the effectiveness of the CNN-BiLSTM-Attention inversion method, this study conducts verification on the resistivity and polarizability extraction of a three-layer polarizable model. The thickness of each layer, and the resistivity and polarizability of the theoretical model are presented in Table 4. The polarizable medium models are developed, and the TEM response is computed as the sample set, followed by the application of the neural network for parameters extraction. Furthermore, we applied BiLSTM and CNN-LSTM to invert the TEM response of the layered model, and a comparison of their inversion accuracies is presented in the tables.

To more clearly evaluate the performance of the neural network inversion at the time-series level, we quantify it from three complementary dimensions: absolute error energy, mean absolute deviation, and relative percentage deviation, using the Root Mean Square Error (RMSE), Mean Absolute Error (MAE), and Mean Absolute Percentage Error (MAPE), respectively. The following metrics are all calculated on the absolute-valued waveforms to avoid the impact of sign reversals on the evaluation.

The RMSE, as defined in equation (6), holistically measures the "energy" of the error and is more sensitive to larger deviations, which facilitates the perception of significant mismatches occurring in critical time windows:

$$\mathrm{RMSE} = \sqrt{\frac{1}{T}\sum_{t=1}^{T}(|\hat{s}_t| - |z_t|)^2}. \qquad (6)$$

MAE, as defined in equation (7), measures the overall deviation as the average of the absolute differences;

it is both intuitive and robust, which facilitates direct comparison across different datasets.

$$\mathrm{MAE} = \frac{1}{T}\sum_{t=1}^{T} |\hat{S}_t| - |s_t|||. \tag{7}$$

MAPE, as defined in equation (8), characterizes the relative amplitude deviation in percentage terms, making it well-suited for the characteristics of TEM data, which decay across several orders of magnitude.

$$\mathrm{MAPE}(\%) = \frac{1}{T}\sum_{t=1}^{T} \frac{||\hat{s}_t| - |s_t||}{|s_t|} \times 100\% \tag{8}$$

Tables 2 and 3 present a detailed comparison of these performance metrics for the inversion of resistivity and polarizability, respectively. The results show that the CNN-BiLSTM-Attention model consistently outperforms the other two models across all metrics. For both resistivity and polarizability, it achieves the lowest RMSE, MAE, and MAPE values, indicating higher prediction accuracy and stability. This quantitative analysis further confirms the superiority of the proposed model.

Table 2: Comparison of resistivity inversion accuracy using different methods

Method	**RMSE**	**MAE**	**MAPE (%)**
CNN-BiLSTM-Attention	16.23	12.15	5.57
BiLSTM	33.85	28.12	13.05
CNN-LSTM	31.43	26.35	15.24

Table 3: Comparison of polarizability inversion accuracy using different methods

Method	**RMSE**	**MAE**	**MAPE (%)**
CNN-BiLSTM-Attention	0.035	0.028	6.75
BiLSTM	0.078	0.065	15.32
CNN-LSTM	0.069	0.057	16.54

The TEM response of the inversion results is compared with the theoretical response, as illustrated in Fig. 13. This figure clearly demonstrates that the inversion results of the CNN-BiLSTM-Attention model exhibit the highest correlation between the TEM response and the theoretical response, signifying that the model adeptly captures the characteristics of the electromagnetic response and is suitable for resistivity and polarizability parameters extraction. Tables 4–6 present the inversion results for the CNN-BiLSTMAttention, BiLSTM, and CNN-LSTM methods, respectively. The CNN-BiLSTM-Attention model demonstrates a significant advantage in both the accuracy and stability of parameter extraction. It achieves a highly precise extraction of resistivity and polarizability across all layers, with the relative errors of the extracted parameters consistently below 6.5%, thereby validating the effectiveness of the CNN-BiLSTM-Attention method.

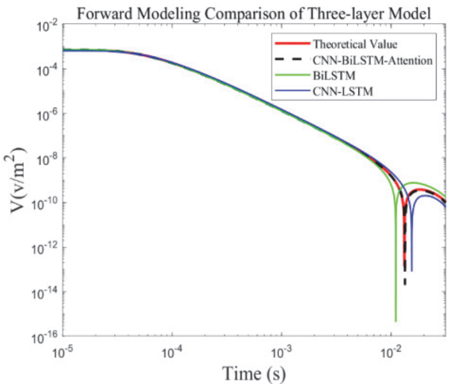

Fig. 13. Comparison of the inversion TEM response and theoretical response for the three-layer model.

D. Five-layer polarizable model

In order to further assess the feasibility of the method, we selected a typical five-layer polarizable model for parameters extraction. The thickness of each layer, along with the parameter settings for resistivity and polarizability, is presented in Table 7. The CNN-BiLSTM-Attention, BiLSTM, and CNN-LSTM inversion methods were employed to extract the parameters from the TEM responses of the five-layer polarizable medium model, respectively. Figure 14 compares the TEM responses derived from various parameters extraction methods against the theoretical response. It is evident that the TEM response from the CNN-BiLSTM-Attention method exhibits the greatest concordance with the theoretical response, signifying its

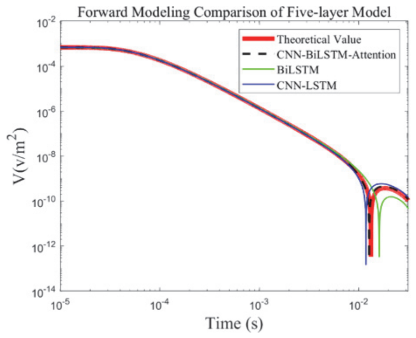

Fig. 14. Comparison of the inversion TEM response and theoretical response for the five-layer model.

Table 4: CNN-BiLSTM-Attention model

Layer	Thickness (m)	Theoretical Resistivity (Ωm)	Extracted Resistivity (Ωm)	Relative Error in Resistivity (%)	Theoretical Polarizability	Extracted Polarizability	Relative Error in Polarizability (%)
Layer1	100	100	103.97	3.97	0.1	0.0968	3.20
Layer2	100	10	10.65	6.50	0.6	0.6341	5.68
Layer3	INT	100	102.93	2.93	0.2	0.2096	4.80

Table 5: BiLSTM model

Layer	Thickness (m)	Theoretical Resistivity (Ωm)	Extracted Resistivity (Ωm)	Relative Error in Resistivity (%)	Theoretical Polarizability	Extracted Polarizability	Relative Error in Polarizability (%)
Layer1	100	100	92.18	7.82	0.1	0.0878	12.20
Layer2	100	10	11.23	12.30	0.6	0.6823	13.72
Layer3	INT	100	108.93	8.93	0.2	0.2338	16.90

Table 6: CNN-LSTM model

Layer	Thickness (m)	Theoretical Resistivity (Ωm)	Extracted Resistivity (Ωm)	Relative Error in Resistivity (%)	Theoretical Polarizability	Extracted Polarizability	Relative Error in Polarizability (%)
Layer1	100	100	106.27	6.27	0.1	0.1083	8.30
Layer2	100	10	9.13	8.70	0.6	0.5078	15.37
Layer3	INT	100	111.97	11.97	0.2	0.1738	13.10

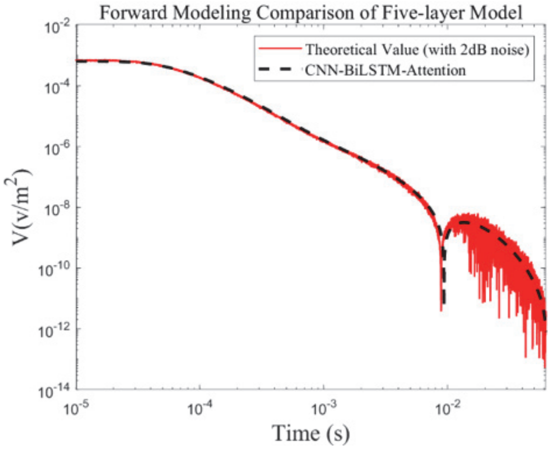

Fig. 15. Forward modeling comparison for the fivelayer model with added noise.

Table 7: CNN-BiLSTM-Attention model

Layer	Thickness (m)	Theoretical Resistivity (Ωm)	Extracted Resistivity (Ωm)	Relative Error in Resistivity (%)	Theoretical Polarizability	Extracted Polarizability	Relative Error in Polarizability (%)
Layer1	200	100	100.54	0.54	0.1	0.1047	4.7
Layer2	100	75	78.46	4.61	0.3	0.3217	7.23
Layer3	50	50	51.67	3.34	0.6	0.6118	1.96
Layer4	100	75	71.94	4.08	0.3	0.3133	4.43
Layer5	INT	500	531.27	6.25	0.1	0.1051	5.10

Table 8: BiLSTM model

Layer	**Thickness (m)**	**Theoretical Resistivity (Ωm)**	**Extracted Resistivity (Ωm)**	**Relative Error in Resistivity (%)**	**Theoretical Polarizability**	**Extracted Polarizability**	**Relative Error in Polarizability (%)**
Layer1	200	100	103.06	3.06	0.1	0.1135	13.5
Layer2	100	75	78.92	5.23	0.3	0.3299	9.96
Layer3	50	50	43.45	13.10	0.6	0.6649	10.81
Layer4	100	75	68.93	8.09	0.3	0.2567	14.43
Layer5	INT	500	598.88	19.77	0.1	0.1182	18.20

Table 9: CNN-LSTM model

Layer	**Thickness (m)**	**Theoretical Resistivity (Ωm)**	**Extracted Resistivity (Ωm)**	**Relative Error in Resistivity (%)**	**Theoretical Polarizability**	**Extracted Polarizability**	**Relative Error in Polarizability (%)**
Layer1	200	100	96.16	3.84	0.1	0.0829	17.1
Layer2	100	75	80.64	7.52	0.3	0.2771	7.63
Layer3	50	50	55.17	10.34	0.6	0.4883	18.61
Layer4	100	75	76.9	2.53	0.3	0.3253	8.43
Layer5	INT	500	546.37	9.274	0.1	0.1113	11.30

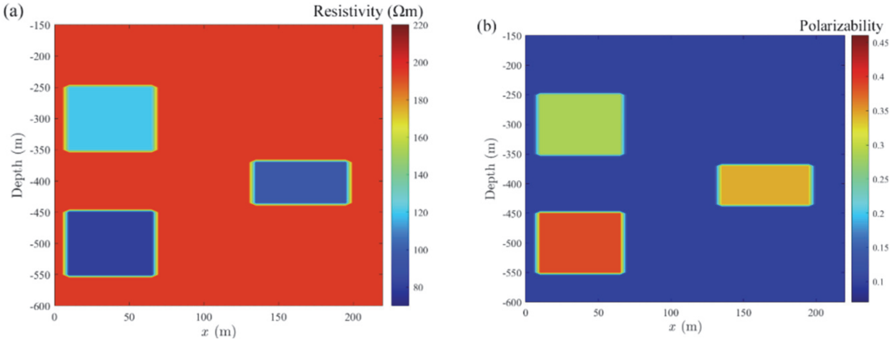

Fig. 16. Polarizable anomalies theoretical model.

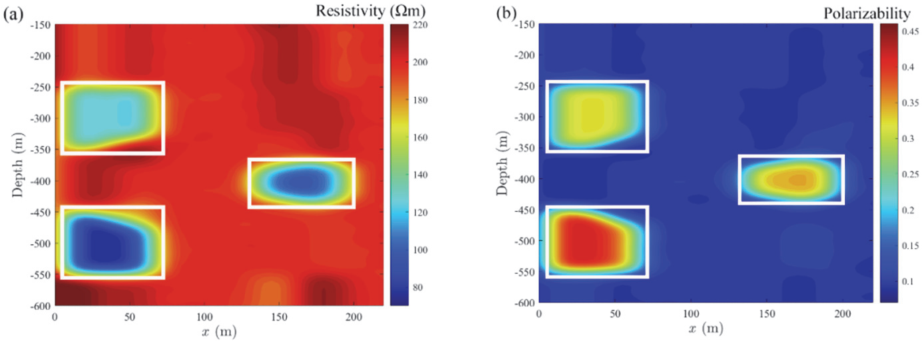

Fig. 17. Inversion result of polarizable anomalies.

superior performance in parameters extraction. The inversion results are presented in Tables 7–9, indicating that the relative errors for the CNN-BiLSTM-Attention approach are less than 7.3%, demonstrating superior accuracy and stability compared to alternative methods.

To further verify the stability of the inversion method proposed in this paper, we conducted an anti-noise test. We added Gaussian white noise to the theoretical TEM response data of the five-layer model, with the SNR of 2 dB. We used the noisy theoretical

TEM response as input to the CNN-BiLSTM-Attention model for inversion. A comparison between the forward response of the inversion results and the noisy theoretical response is shown in Fig. 15. As can be seen from this figure, although the theoretical signal is significantly disturbed by noise, the forward response derived from the CNN-BiLSTM-Attention model's inversion results still fits the noisy theoretical curve very well. This indicates that the method proposed in this paper has good stability and noise-resistance performance. The method accurately invert the resistivity and polarizability parameters for the noisy TEM data, demonstrating its potential value for processing field data.

E. Polarizable anomaly model

To verify the effectiveness of the CNN-BiLSTMAttention inversion method, a simple anomaly model can be created [29, 30]. Two polarizable anomalies model are constructed, as illustrated in Fig. 16. The model contains three low-resistivity, high-polarizability anomaly regions. One anomaly is located at $x = 10{\sim}65$ m, with a depth of -250 m ~ -350 m, resistivity $\rho = 120\Omega$ m, and polarizability $\eta = 0.3$. Another anomaly is at $x = 10 \sim 65$ m, with a depth of -450 m ~ -550 m, resistivity $\rho = 80\Omega$ m, and polarizability $\eta = 0.4$. The third anomaly is located at $x = 135 \sim 195$ m, with a depth of $-450 \sim -550$ m, resistivity $\rho = 100\Omega$ m, and polarizability $\eta = 0.35$. These three anomaly regions are highlighted by boxes in the inversion results shown in Fig. 17.

As shown in Fig. 17, the position and size of the polarizable anomalies in the inversion results are in excellent agreement with the theoretical model, indicating that the proposed inversion method is capable of accurately capturing the target features. These results further demonstrate that the CNN-BiLSTM-Attention inversion method exhibits strong adaptability and accuracy when handling polarizable anomalies model, thereby validating its practical effectiveness.

VI. CONCLUSION

We present a CNN-BiLSTM-Attention inversion method to estimate resistivity and polarizability from SQUID TEM data acquired with a magnetic source. The method can effectively extract the resistivity and polarizability parameters of the time-domain EM-IP effect for polarizable half-space, three-layer, and fivelayer polarizable medium models. It can also effectively extract the resistivity and polarizability parameters from the polarizable anomalies model. The effectiveness of the CNN-BiLSTM-Attention inversion method is verified. It can offer technical support for the practical application of the SQUID TEM method.

ACKNOWLEDGMENTS

This study was performed under the Science and Technology Talent Development – Young and Middleaged Scientific and Technological Talent (Team) Project (High-level Talent Development Project) of Jilin Province under Grant 20250601004RC. We thank all members of the TEM group of Jilin University (China) for their support of this study.

REFERENCES

[1] M. Radulescu, S. Dalal, U. K. Lilhore, and S. Saimiya, "Optimizing mineral identification for sustainable resource extraction through hybrid deep learning enabled FinTech model," *Resources Policy*, vol. 89, Feb. 2024.

[2] G. W. Hohmann, P. R. Kintzinger, G. D. Van Voorhis, and S. H. Ward, "Evaluation of the measurement of induced electrical polarization with an inductive system," *Geophysics*, vol. 35, no. 5, pp. 901–915, Oct. 1970.

[3] C. A. Moreira, K. Borssatto, L. M. Ilha, S. F. D. Santos, and F. T. G. Rosa, "Geophysical modeling in gold deposit through DC resistivity and induced polarization methods," *REM-International Engineering Journal*, vol. 69, no. 3, pp. 293–299, Sep. 2016.

[4] J. Clarke and A. I. Braginski, *The SQUID Handbook: Applications of SQUIDs and SQUID Systems*. Hoboken, NJ: John Wiley & Sons, 2006.

[5] C. Flores and S. A. Peralta-Ortega, "Induced polarization with in-loop transient electromagnetic soundings: A case study of mineral discrimination at El Arco porphyry copper, Mexico," *Journal of Applied Geophysics*, vol. 68, no. 3, pp. 423–436, July 2009.

[6] I. Kumar, B. V. L. Kumar, S. N. S. Birua, J. K. Dash, and A. K. Chaturvedi, "Inductive induced polarization effect in transient electromagnetic surveys for mapping sulphide-rich zone: A case study from Gurulpada area, Singhbhum Shear Zone, Jharkhand," *Journal of Geophysics*, vol. 38, no. 2, Apr. 2017.

[7] T. Lee, "Sign reversals in the transient method of electrical prospecting (one-loop version)," *Geophysical Prospecting*, vol. 23, no. 4, pp. 653–662, Dec. 1975.

[8] A. Viezzoli, V. Kaminski, and G. Fiandaca, "Modeling induced polarization effects in helicopter time domain electromagnetic data: Synthetic case studies," *Geophysics*, vol. 82, no. 2, pp. E31–E50, Feb. 2017.

[9] K. F. Man, C. C. Yin, Y. H. Liu, X. Y. Ren, S. Y. Sun, J. J. Miao, and B. Xiong, "Inversion of timedomain airborne EM data with IP effect based on Pearson correlation constraints," *Applied Geophysics*, vol. 17, no. 4, pp. 589–600, 2021.

[10] J. T. Lu, X. B. Wang, Z. W. Xu, M. S. Zhdanov, M. Guo, M. Q. Teng, and Z. Liu, "Quasi-2-D robust inversion of semi-airborne transient electromagnetic data with IP effects," *IEEE Trans. Geosci. Remote Sens.*, vol. 60, pp. 1–10, Nov. 2022.

[11] X. Wang, J. Lu, M. Guo, S. Zhang, Q. Hu, and H. El-Kaliouby, "Inversion of induced polarization-affected electrical-source transient electromagnetic data observed in the groundwater survey from eastern Tibet, China," *Geophysics*, vol. 90, no. 1, pp. B17–B28, Jan. 2025.

[12] S. Yu and J. Ma, "Deep learning for geophysics: Current and future trends," *Reviews of Geophysics*, vol. 59, no. 3, e2021RG000742, Sep. 2021.

[13] T. J. Zhao, S. Wang, C. J. Ouyang, M. Chen, C. Y. Liu, J. Zhang, L. Yu, F. Wang, and Z. Wang, "Artificial intelligence for geoscience: Progress, challenges, and perspectives," *The Innovation*, vol. 5, no. 5, p. 100691, Sep. 2024.

[14] Y. J. Ji, Y. Q. Wu, Y. H. Wu, and Y. Zhang, "Excitation process under the ramp-step waveform of inductive source-induced polarization method," *Geophysics*, vol. 85, no. 2, pp. E57–E65, Feb. 2020.

[15] T. Alyousuf and Y. Li, "Inversion using adaptive physics-based neural network: Application to magnetotelluric inversion," *Geophysical Prospecting*, vol. 70, no. 7, pp. 1252–1272, Aug. 2022.

[16] P. Li, M. L. Liu, M. Alfarraj, P. Tahmasebi, and D. Grana, "Probabilistic physics-informed neural network for seismic petrophysical inversion," *Geophysics*, vol. 89, no. 2, pp. M17–M32, Mar. 2024.

[17] K. S. Cole and R. H. Cole, "Dispersion and absorption in dielectrics: Alternating current characteristics," *The Journal of Chemical Physics*, vol. 9, no. 4, pp. 341–351, Apr. 1941.

[18] M. N. Nabighian, "Electromagnetic methods in applied geophysics," in *Investigations in Geophysics*, no. 3. Tulsa, OK, USA: Society of Exploration Geophysics, pp. 1-2, 1988.

[19] D. Guptasarma and B. Singh, "New digital linear filters for Hankel J0 and J1 transforms," *Geophys. Prospecting*, vol. 45, no. 5, pp. 745–762, Sep. 1997.

[20] M. Seidel and B. Tezkan, "1D Cole-Cole inversion of TEM transients influenced by induced polarization," *J. Appl. Geophys.*, vol. 138, pp. 220–232, Mar. 2017.

[21] L. Alzubaidi, J. L. Zhang, A. J. Humaidi, and L. Farhan, "Review of deep learning: Concepts, CNN architectures, challenges, applications, future directions," *J. Big Data*, vol. 8, no. 1, p. 53, Mar. 2021.

[22] W. J. Lu, J. Z. Li, Y. F. Li, A. J. Sun, and J. Y. Wang, "A CNN-LSTM-based model to forecast stock prices," *Complexity*, vol. 2020, no. 18, Nov. 2020.

[23] L. Q. Shan, Y. C. Liu, M. Tang, M. Yang, and X. Y. Bai, "CNN-BiLSTM hybrid neural networks with attention mechanism for well log prediction," *J. Pet. Sci. Eng.*, vol. 205, p. 108838, Oct. 2021.

[24] D. Soydaner, "Attention mechanism in neural networks: Where it comes and where it goes," *Neural Computing and Applications*, vol. 34, no. 16, pp. 13371–13385, May 2022.

[25] L. Huang, J. Qin, Y. Zhou, F. Zhu, L. Liu, and L. Shao, "Normalization techniques in training DNNs: Methodology, analysis and application," *IEEE Trans. Pattern Anal. Mach. Intell.*, vol. 45, no. 8, pp. 10173–10196, Feb. 2023.

[26] S. L. Zhou and W. Song, "Deep learning-based roadway crack classification using laser-scanned range images: A comparative study on hyper-parameter selection," *Autom. Constr.*, vol. 114, p. 103171, June 2020.

[27] P. Baldi and P. Sadowski, "The dropout learning algorithm," *Artificial Intelligence*, vol. 210, pp. 78–122, May 2014.

[28] M. Reyad, A. M. Sarhan, and M. Arafa, "A modified Adam algorithm for deep neural network optimization," *Neural Computing and Applications*, vol. 35, no. 23, pp. 17095–17112, Apr. 2023.

[29] H. Ren, D Lei, Q. Y. Di, and R. Wang, "Data discrepancy constraints for 3D airborne transient electromagnetic inversion for induced polarization parameters," *Geophysics*, vol. 90, no. 3, pp. E105–E116, May 2025.

[30] H. Z. Cai, M. H. Liu, J. J. Zhou, J. H. Li, and X. Y. Hu, "Effective 3D-transient electromagnetic inversion using finite-element method with a parallel direct solver," *Geophysics*, vol. 87, no. 6, pp. E377–E392, Nov. 2022.

Yanju Ji received the M.S. degree in measurement technology and instruments and the Ph.D. degree in earth exploration and information techniques from Jilin University, Changchun, China, in 1998 and 2004, respectively. From 2004 to 2009, she was an Associate Professor with Jilin University. Since 2010, she has been with Jilin University, where she is currently a Professor of instrument science and technology. She has authored or co-authored more than 200 articles. Her research interests include computational electromagnetics, inverse problems, and electromagnetic detecting instrument.

Jinxiu Yuan is an undergraduate student at Jilin University, pursuing a degree in measurement and control technology and instrumentation. His research interests include, but are not limited to, machine learning, neural network inversion methods, and related fields. As an emerging researcher, he actively explores the application of advanced computational techniques to scientific problems.

Hui Luan received the Ph.D. degree in microwave remote sensing from the Chinese Academy of Science, Beijing, China, in 2007. Since 2007, she has been with the College of Instrumentation and Electrical Engineering, Jilin University, Changchun, where she is currently a Professor. Her research interests include the development of transient electromagnetic instruments and electromagnetic numerical simulation.

Yuan Wang is a Professor with the College of Instrumentation and Electrical Engineering, Jilin University, Changchun, China. He specializes in the development of geophysical exploration instruments, EM instruments, and marine exploration instruments. His research interests include electrical signal detection.

Qiong Wu received the B.S. degree in electrical engineering and automation from Jilin University, Changchun, Jilin Province, China, in 2013, and the Ph.D. degree in detection technology and automatic equipment from Jilin University, in 2019. From 2016 to 2017, she was an Exchange Student with Sustainable Resources Engineering, Faculty of Engineering, Hokkaido University, Sapporo, Japan. From 2019 to 2022, she was a Post-Doctoral Researcher with Jilin University. Since 2023, she is currently an Associate Professor with Jilin University. Her research interest includes the modeling and inversion method for electromagnetic method.

Numerical Analysis on the Equivalent Physical Temperature Estimation for Pyramidal Microwave Calibration Targets Based on Infrared Imagery

Ming Jin[1], Jiacheng Qian[2], and Miaomiao Peng[1]

[1]College of Information Science and Technology
Beijing University of Chemical Technology, Beijing 100029, China
jinming@mail.buct.edu.cn, 3120256108@bit.edu.cn

[2] College of Mathematics and Physics
Beijing University of Chemical Technology, Beijing 100029, China
jcqian99@qq.com

***Abstract* –** Pyramidal microwave calibration targets (MCT) are widely applied in on-orbit and pre-launch radiometric calibrations due to its compact size. However, it is well known that array-shaped MCT suffers from the temperature gradient at tips that leads to radiating brightness temperature (BT) bias. Therefore, it is vital to estimate the equivalent physical temperature of the MCT given the tip temperature gradient for the BT bias correction. In this work, the authors numerically investigate the T_{MCT} estimation based on possible temperature measurement techniques, specifically considering a combination configuration of platinum resistor temperature (PRT) detector at the metal base and the infrared camera detector for the tipbottom temperature difference. By considering the possible variation of coating material parameters and thermal measurement errors, it is possible to evaluate T_{MCT} estimation accuracy. Numerical results indicate that this temperature measurement configuration can lead to accurate T_{MCT} estimation at the level of 0.1 K $(1-\sigma)$. Factors that notably impact on the estimation accuracy are discussed. This investigation can be a direct reference for MCT BT correction applications in the pre-launch calibration process.

***Index Terms* –** Brightness temperature estimation, microwave calibration target, pre-launch calibration.

I. INTRODUCTION

The microwave calibration target (MCT), specifically the array-shaped coated sharp pyramidal target, is widely applied in radiometric payloads [1–3]. The array-shaped MCT has the advantage of compactness in size and weight, which is beneficial for space-borne or air-borne applications [2–4], compared to other types of MCT such as cavity MCT [5, 6]. However, the key problem of the array-shaped MCT in calibration application is that a temperature gradient exists at the tip region, and it leads to radiated brightness temperature (BT) bias.

As the function of the MCT is to provide an accurate referencing BT, efforts has been made on estimating and determining the radiation performance of the MCT. After a lot of investigations were performed upon the emissivity issue of the MCT, such as wide-band reflectivity spectrum properties [7], wideband high-emissivity design strategy [8, 9], and emissivity measurement methodology [10–14], research focus has been altered towards the overall BT performance considering temperature gradient at tips. In [15], Schröder et al. proposed a numerical framework to calculate the radiated BT from the arrayshaped MCT for space-borne application. In [16], Virone et al. calculated the radiated BT for a cold source in the vacuum-thermal calibration scenario. It is evidenced in numerous works that the temperature gradient becomes the primary source of BT bias in general cases over the residual reflectivity from the array-shaped MCT. In [17, 18], Jin et al. proposed a BTbias suppressed unit kernel design of array-shaped MCT based on the numerical framework in [15].

In [15–17], numerical frameworks are established for numerically estimating the BT-bias, which offers rich information and deep understanding of BT-bias properties in space-borne platform deployment and prelaunch thermal-vacuum (T/V) tests. However, the key concepts of those works are estimations based on numerical simulations as a reference for practical application. For practical pre-launch tests, it is desired that the BT-bias can be obtained based on measurable values other than fully based on simulations. In the earlier studies in which the temperature gradient phenomenon of the

Submitted On: October 13, 2025
Accepted On: March 16, 2026

https://doi.org/10.13052/2026.ACES.J.410308

array-shaped MCT was presented, infrared imagery was applied, showing the ability to capture the temperature difference between the MCT unit tips and unit valley bottoms [2, 19]. Based on the recent progress of BT modeling methodology, it is highly applicable to use infrared imagery to obtain temperature gradient information and to estimate BT-bias with numerically concluded electromagnetic information.

In this work, the authors investigate such a possibility. Specifically, the accuracy of the BT-bias estimation is investigated considering the uncertainty of MCT coating material properties, as well as the measurable temperature difference between tips and valley bottoms. The results can be a direct reference for BT-bias estimation in ground radiometer tests such as pre-launch T/V tests.

II. METHODOLOGY FOR T_{MCT} ESTIMATION

Due to the typical MCT structure of 2-D array of coated sharp pyramids, the dominating factor for BTbias is the temperature gradient in the coating layers in the height dimension (along the z-axis). Therefore, the simulation study for the T_{MCT} estimation, is focused on the temperature gradient in the height dimension.

A. Theoretical description for equivalent temperature estimation

In [15, 17], it is concluded that the directional radiated BT from the MCT can be calculated by a crossintegration of temperature and electromagnetic absorption distribution:

$$BT = (1-r)\int_{CoatingLayer} T(\vec{r})\tilde{A}(\vec{r})dv + rBT_b, \tag{1}$$

where $T(\vec{r})$ is temperature distribution in the coating layer and $\tilde{A}(\vec{r})$ is normalized absorption rate distribution in the coating layer:

$$\int_{CoatingLayer} \tilde{A}(\vec{r})dv = 1. \tag{2}$$

Here, r is total reflectivity of the MCT to normal incident electromagnetic waves and BT_{b} is the background brightness temperature and is considered as uniform in this investigation.

Based on the former studies, it is known that the most important temperature gradient phenomenon is the tip-bottom gradient (along z-direction), due to the difference of the bottom temperature T_{base} of MCT and the background BT_{b}. Equation (1) can be simplified as:

$$BT = (1-r)\int_{CoatingLayer} T(z)\tilde{A}(z)dz + rBT_b. \tag{3}$$

Specifically, considering numerical investigations, $T(z)$ shall be calculated by thermal simulations, $\tilde{A}(z)$ and r shall be calculated by electromagnetic simulations. Equation (3) can be simplified as:

$$BT = eT_{MCT} + rBT_b, \tag{4}$$

where T_{MCT} can be defined as the equivalent physical temperature taking count of the temperature gradient in the coating layer:

$$T_{MCT} = \int_{CoatingLayer} T(z)\tilde{A}(z)dz. \tag{5}$$

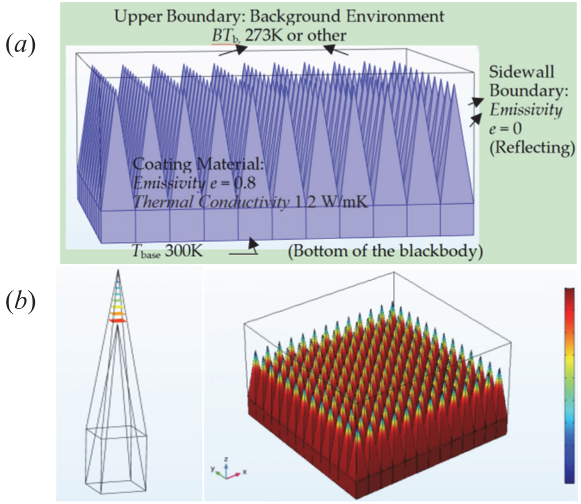

Fig. 1. Simulated temperature gradient of MCT array (in front of a colder background) showing notable temperature gradient at tips.

As the accuracy of radiated BT from the MCT is now a research focus for the microwave radiometer calibration, it was concluded that the difference between T_{MCT} and the ideal T_{base} is the key factor for the BT bias, as it generates the bias ($\triangle BT_1$ in equation 6) notably larger than that by the reflectivity factor ($\triangle BT_2$), especially at current stage that the emissivity of the MCT can be above 0.9995 even 0.9999 [4, 14]. Although T_{MCT} is a key factor for BT bias, unfortunately it cannot be directly measured based on current techniques. Therefore, it is important to develop estimation methodology according to the physical properties of impacting factors such as $T(z)$ and $\tilde{A}(z)$.

$$\Delta BT = e(T_{MCT} - T_{base}) + r(BT_b - T_{base}) = \Delta BT_1 + \Delta BT_2. \tag{6}$$

In former studies, it was found that T_{MCT} is proportional to the maximum temperature gradient at the tip ($\triangle T_{\mathrm{tip}} = T_{\mathrm{tip}} - T_{\mathrm{base}}$) [15], as expressed in equation (7), and the corresponding proportionality factor $\alpha_{\mathrm{Gradient}}$ can be numerically concluded. Also, it should be noted that, as the $\tilde{A}(z)$ is frequency-dependent, thus so as the α_{Gradient}, then the T_{MCT} shall be frequency dependent. Further, based on the above acknowledgement, the authors view the temperature measurements realizable in cases of ground radiometer calibration, as shown in Fig. 2, can be a practical path to estimate the T_{MCT} with help of numerical concluded values. It is specifically suggested to measure the T_{base} using the platinum resistor temperature (PRT) detector (T_{PRT}), which is a widely-applied contact measurement technique with excellent precision. It is suggested to use an infrared imaging camera to capture the difference between the tip temperature and the bottom temperature (ΔT_{tip}) as the maximum temperature gradient. Based on this configuration, the aim of this study is to investigate and conclude the achievable accuracy of this potential methodology.

$$T_{MCT} = T_{PRT} + \alpha_{Gradient} \Delta T_{tip}. \tag{7}$$

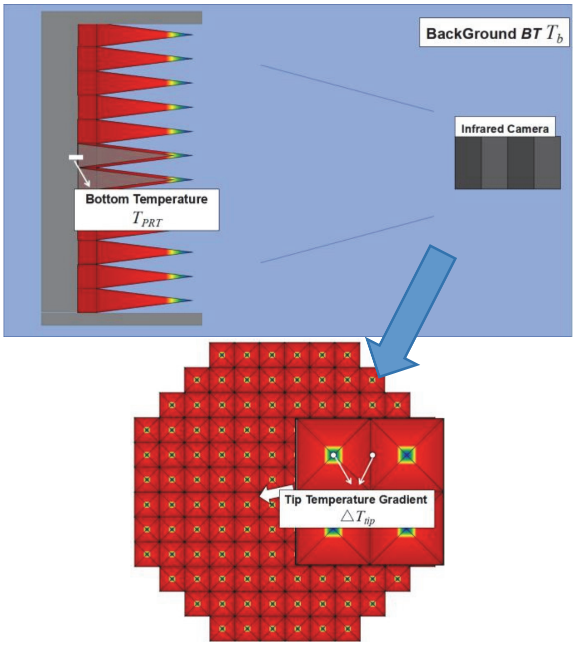

Fig. 2. Configuration for MCT temperature measurement.

It should be noted that estimating the T_{MCT} (equivalent physical temperature of the MCT) has been done in former studies based on comprehensive fullroutine numerical computations, resulting in the acknowledgement of important conclusions such as T_{MCT} is proportional (α_{Gradient}) to the maximum temperature gradient, and the proportional factor α_{Gradient} is frequency dependent. Based on that, the key aim of this work is to investigate the estimating accuracy for T_{MCT} based on measurable temperature values. This work is an update of the measurementnumerical routine from the stage of full-numerical estimation routine. The authors believe such an update is an important reference for practical applications, showing how a good estimating accuracy can be achieved.

B. Discussion of thermal simulations

Before the T_{MCT} estimating methodology is investigated, it is important to review the thermal simulation for the temperature distribution, as shown in Fig. 1 (a). The temperature gradient in the coating layers is due to difference between the base temperature and background BT, and it can be simulated based on a finite element software package (such as COMSOL). It should be noted that clearly different input thermal parameters, such as the background *BT* or the emissivity of the coating layer, will lead to different temperature distribution results. However, it was found that, after normalization, the average temperature distribution results are nearly the same [20], as shown in Fig. 3. This may be because of the structure of the MCT unit, where the coating layer with low thermal conductivity and high emissivity is located above the highly thermal conducting metal kernel, and such a combination of parts with opposite thermal properties leads to a stable normalized temperature distribution in the coating layer. Based on this important phenomenon, it can be inferred that as one can obtain the maximum temperature difference between the tip and the bottom, one gets the overall temperature distribution and will be able to calculate T_{MCT}. This is the key reason that the infrared temperature camera is used for high-accuracy T_{MCT} estimations, as the most important information is the temperature difference between the tip and bottom, as a relative value, other than the absolute temperature value at each position. The accuracy of the absolute temperature value can be counted on the PRT measurement, which is found to be promising in practical experiences.

Before further investigations, it is also interesting to check the possible temperature gradient at the tip. As shown in Fig. 4, the tip-bottom temperature difference results in cases of different background *BT* plotted. Considering the applications in ground T/V tests, where 300 K hot MCT is in front of a colder background or an 80 K cold MCT is in front of a warmer background, the range of 30–160 K base-background temperature difference will leads to the range of 3–11 K base-tip temperature difference, showing a non-linear projection relationship. The considered upper-range of the base-tip temperature difference is 12 K, which is sufficient for the reference purpose.

C. Discussion of electromagnetic simulations

Electromagnetic simulations are conducted in the unit level to obtain the local absorption rate distribution

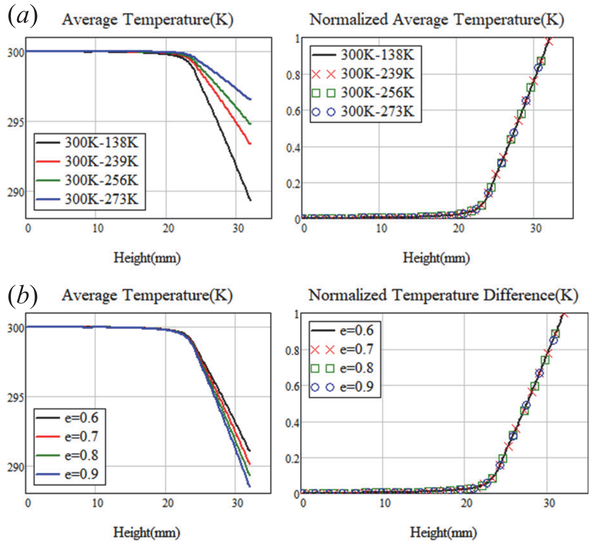

Fig. 3. Calculated $T(z)$ distributions considering different thermal parameters: (a) $e = 0.8$ and (b) temperature parameters of 300 K (MCT)-138K (Environment).

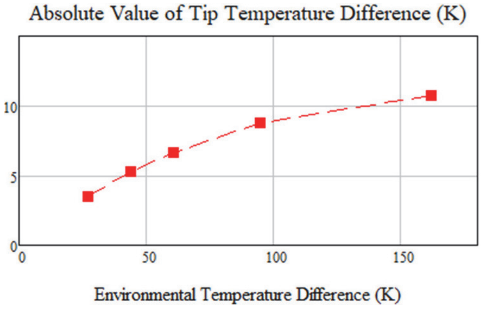

Fig. 4. Calculated tip-bottom temperature difference versus environmental temperature difference (K).

of $\tilde{A}(z)$. Specifically, based on the periodic boundary condition, one single unit is included in the computation domain of Finite Difference Time Domain (FDTD), where a plane-wave excitation is illuminating toward the unit along the z -direction and the total reflectivity r and local absorption rate $\tilde{A}(z)$ can be recorded [17, 18]. It should be noted that $\tilde{A}(z)$ is very hard to actually measure, and numerical calculation is necessary. The electromagnetic parameters of the coating layer material, such as the dielectric constant (ε), and the magnetic permeability (μ), will directly impact on the pattern of $\tilde{A}(z)$. In practical applications, the uncertainty of the (ε, μ) measurement, as well as the heterogeneity in the coating layer, will have negative impact on the accuracy of the calculated $\tilde{A}(z)$ in the process of T_{MCT} estimation. Therefore, before the overall investigation of T_{MCT} estimation accuracy can be performed, the uncertainty of $\widetilde{A}(z)$ due to the uncertainty of (ε, μ) shall be investigated.

III. ACCURACY ASSESSMENT FOR T_{MCT} ESTIMATION

In this section, the numerical results are presented and discussed for the assessment of the T_{MCT} estimation accuracy.

A. Uncertainty of $\alpha_{\mathrm{Gradient}}$ due to electromagnetic parameter variation

Uncertainty of the (ε, μ) of the coating layer material will lead to variation of the $\tilde{A}(z)$ then the counted $\alpha_{\mathrm{Gradient}}$. For this issue, the authors set up the randomly distributed (ε, μ) at different levels of standard derivation error, and performed 10 rounds of simulations to count the resulted $\alpha_{\mathrm{Gradient}}$. For each random sample, $\tilde{A}(z)$ is calculated and integrated with $T(z)$ for T_{MCT}, then c$\alpha_{\mathrm{Gradient}}$ as in equation (8). The authors considered other factors such as different frequency and different unit size, as in Tables 1 and 2. The considered frequencies, 10.65 GHz, 18.7 GHz, 36.5 GHz, 89 GHz, 183.31 GHz, are the most popular frequency channels applied in the radiometer payloads, and the performance of the MCT at those frequency points are favored by radiometer developers:

$$\alpha_{Gradient} = \frac{T_{MCT} - T_{base}}{\Delta T_{tip}}, \tag{8}$$

Table 1: Geometry parameters for MCT

Case	Period	Height to Period	Coating Thickness
Case 1	6.0 mm	□4 : 1	1.0 mm
Case 2	7.5 mm	□4 : 1	1.0 mm

Table 2: Considered coating material electromagnetic parameters at different frequencies

Frequencies	Dielectric Constant	Magnetic Permeability
10.65 GHz	10.284 – 0.185j	1.511 – 0.872j
18.7 GHz	10.253 – 0.32j	1.203 – 0.594j
36.5 GHz	10.133 – 0.588j	0.736 – 0.205j
89 GHz	9.604 – 1.06j	0.956 – 8.165e – 3j
183.31 GHz	8.752 – 1.161j	0.99 – 8.563e – 4j

Note: The parameters are from the MF114 description based on the measured data in [20].

Based on the initial parameters, the calculated results are presented in Figs. 5–7. In Figs. 5 and 6, the calculated local absorption rates $\tilde{A}(z)$ are presented in cases of different unit size and at different frequencies. It is clear that $\tilde{A}(z)$ is highly frequency dependent. A higher absorption rate in the tip region will lead to a higher $\alpha_{\mathrm{Gradient}}$. At 36.5 GHz and 89 GHz the counted

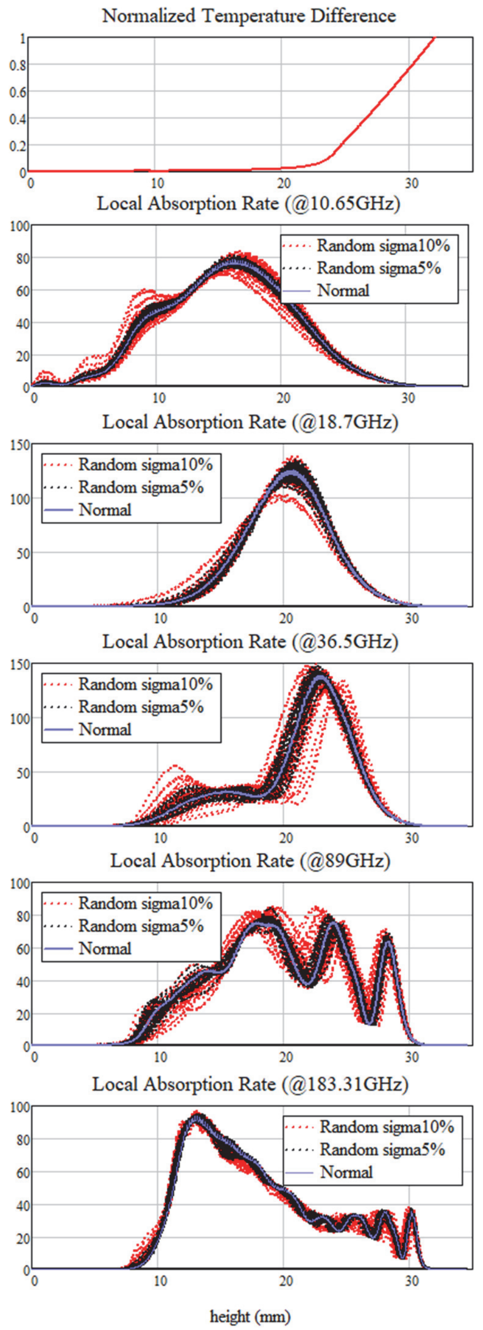

Fig. 5. Calculated local absorption distribution results in cases of different frequency, considering random samples, and referenced to the average temperature distribution in the coating layer. Unit period size $p = 6.0$ mm, considering random samples with 5% std in (ε, μ) and with 10% std in (ε, μ).

α_{Gradient} will be relatively higher. In Figs. 5 and 6, the $\tilde{A}(z)$ curves for random samples are also plotted. One can intuitively observe the influence of the uncertainty of the material (ε, μ), upon the $\tilde{A}(z)$ which directly affects the α_{Gradient}.

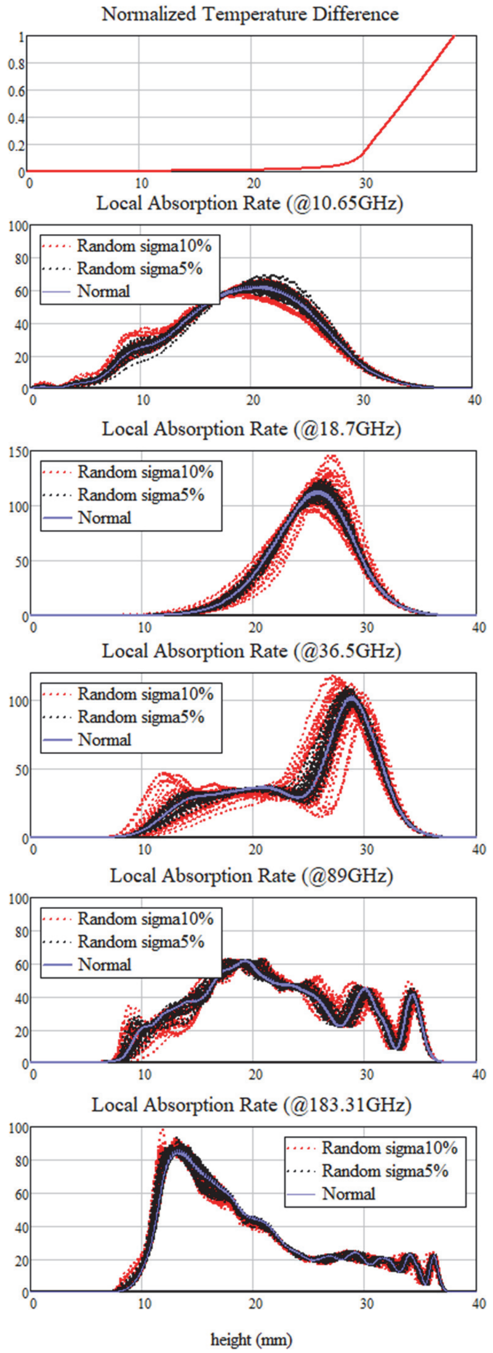

Fig. 6. Calculated local absorption distribution results in cases of different frequency, considering random samples, and referenced to the average temperature distribution in the coating layer. unit period size $p = 7.5$ mm, considering random samples with 5% std in (ε, μ) and with 10% std in (ε, μ).

In Fig. 7, the calculated α_{Gradient} and counted standard deviation σ (std for short) are plotted and compared. The data set contains the comparison between the two cases with different unit size, $p = 6.0$ mm and

$p = 7.5$ mm. In Figs. 7 (a) and (b), one can see that the calculated $\alpha_{\rm Gradient}$ in case of $p = 6.0$ mm is clearly larger than that of $p = 7.5$ mm at every frequency. When $p = 6.0$ mm, the highest $\alpha_{\rm Gradient}$ is found at 89 GHz. When $p = 7.5$ mm, the highest $\alpha_{\rm Gradient}$ is found at 36.5 GHz . Thus, the $\alpha_{\rm Gradient}$-frequency relationship is variable versus the geometry size. For std, the counted value for $\alpha_{\rm Gradient}$ when $p = 6.0$ mm is generally larger than when $p = 7.5$ mm, but not at every frequency point. When $p = 6.0$ mm and $p = 7.5$ mm, the largest counted std is found at 36.5 GHz.

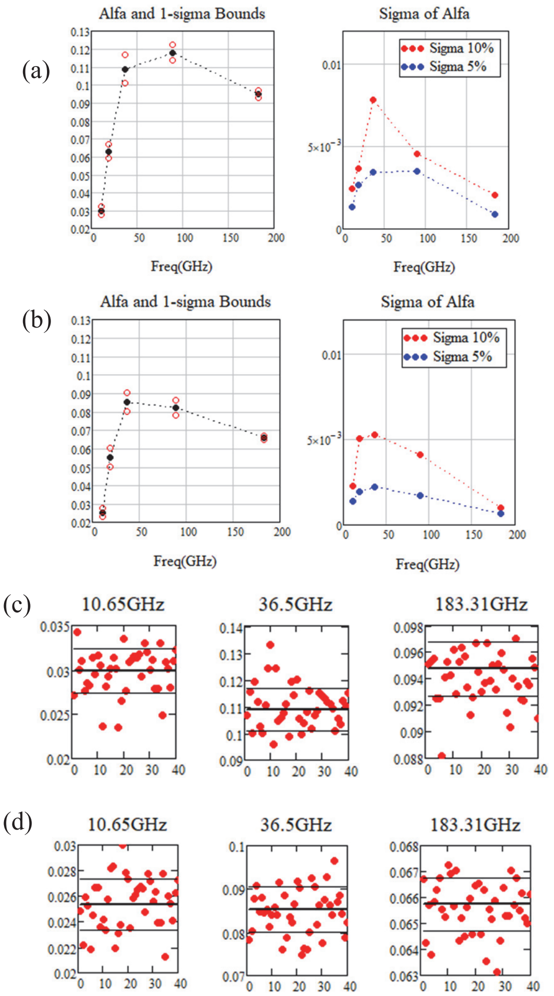

Fig. 7. Counted $\alpha_{\rm Gradient}$ values based on 40 random samples: (a) $p = 6.0$ mm, counted $\alpha_{\rm Gradient}$ at different frequencies, and counted std values in cases of (ε, μ) std at 5% and 10%; (b) $p = 7.5$ mm, counted $\alpha_{\rm Gradient}$ at different frequencies, and counted std values in cases of (ε, μ) std at 5% and 10%; (c) $p = 6.0$ mm, counted $\alpha_{\rm Gradient}$ at each random sample at 10.65 GHz, 36.5 GHz and 183.31 GHz ; (d) $p = 7.5$ mm, counted $\alpha_{\rm Gradient}$ at each random sample at 10.65 GHz, 36.5 GHz and 183.31 GHz.

In these set of results, another important fact is that a smaller (ε, μ) std leads notably smaller $\alpha_{\rm Gradient}$ std, which can be anticipated. The comparison between different (ε, μ) std level is for further investigation upon the $T_{\rm MCT}$, showing the importance of the (ε, μ) error control. For obtaining the statistical std information, 40 random samples are calculated for each frequency and each (ε, μ) sigma configuration. The calculations were implemented on one workstation with EPYC 32-core CPU and took more than 10 minutes for each sample. In running each sample, most of the computation time was consumed on performing Fourier transform at each cell for storing local fields at the specific frequency, which were then used for obtaining the local absorption distribution.

B. Uncertainty evaluation for $T_{\rm MCT}$ estimation

Based on the counted $\alpha_{\rm Gradient}$ and its std results, it is further possible to evaluate $T_{\rm MCT}$ estimation accuracy. As discussed in the previous section, there are several obstructions for accurate thermal simulation. In this case, one may not expect an accurate *BT* bias estimation based on simulated results. However, it is important that the relative temperature distribution across the pyramidal unit is fixed, and it can be inferred that the key issue of temperature measurement is to obtain the maximum value of thermal gradient, which is the bottom-tip difference $\Delta T_{\rm tip}$.

Considering the bias of the $T_{\rm MCT}$, as $\Delta T_{\rm MCT}$ described in (9), then it is possible to estimate the overall σ (std) based on Monte Carlo evaluation:

$$\Delta T_{MCT} = T_{PRT} + \alpha_{Gradient}\Delta T_{\rm tip} - T_{base}. \tag{9}$$

Specifically, the $T_{\rm base}$ is considered as the absolute value, and:

(1) $T_{\rm PRT}$ is the measurable base temperature by the PRT detector, a $\sigma_{\rm TPRT}$ at the level of 0.03 K is considered. Actually, the PRT temperature measurement has been proven to be accurate and reliable in practical MCT application.

(2) $\Delta T_{\rm tip}$ is the temperature difference between the unit tip and the bottom, measurable by the infrared camera detection. Actually, the sensitivity for temperature magnitude measurable by the infrared camera can be at the level of 0.1 K. Also, accurate infrared camera detection will rely on accurate estimation of surface emissivity, therefore, the $\sigma_{\Delta T{\rm tip}}$ shall be notably larger than 0.1 K. In this work, $\sigma_{\Delta T{\rm tip}}$ is set to be 0.5 K.

(3) $\sigma_{\alpha{\rm Gradient}}$ is the std for the calculated $\alpha_{\rm Gradient}$ because of the uncertainty of the coating material electromagnetic parameters, which is frequency dependent and calculated in the former section.

With the above factors considered, the counted T_{MCT} estimation accuracy results are presented and discussed based on Monte Carlo analysis.

In Fig. 8, a set of estimated T_{MCT} bias results are plotted at specific parameters considering ΔT tip $= 10$ K. As can be observed, T_{MCT} bias varies versus frequency with a considerable large range. The T_{MCT} bias is generally larger in magnitude around the frequency $f_0 = c_0/p$, than in high frequency range (f is notably larger than f_0). T_{MCT} bias gets smaller as frequency f gets higher. Considering the comparison of unit period, a larger unit with the same coating parameter and height to period ratio generally leads to smaller T_{MCT} bias.

Considering the above uncertainty factors, the std σ results for the estimated T_{MCT} bias are also plotted. Several sets of comparisons are plotted in Figs. 9–11.

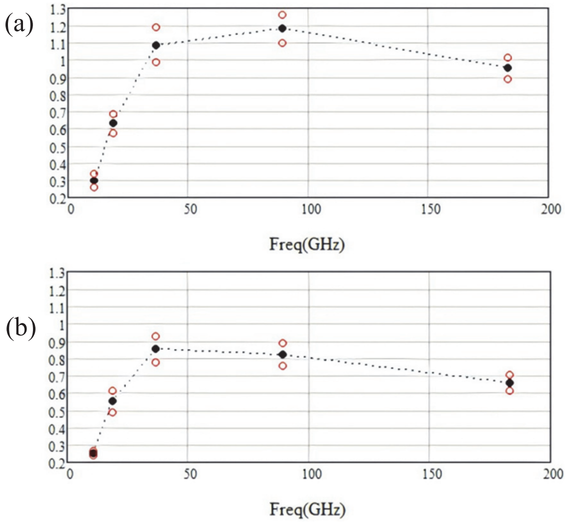

Fig. 8. Estimated T_{MCT} bias (absolute value of $T_{\mathrm{MCT}} - T_{\mathrm{base}}$) and $1 - \sigma$ std at different frequencies: (a) $p = 6.0$ mm and (b) $p = 7.5$ mm.$\sigma_\varepsilon = 0.1\varepsilon, \sigma_\mu = 0.1\mu, \Delta T_{\mathrm{tip}} = 10$ K, $\sigma_{\Delta T \mathrm{tip}} = 0.5$ K.

In Fig. 9, counted T_{MCT} bias std at different frequencies are compared. One can see the accuracy improvement contributed by achieving higher (ε, μ) determination accuracy. An interesting and important phenomenon can be observed in Fig. 9 (a). As the maximum tip temperature gradient is rising, the std of T_{MCT} estimation also gets larger, especially at center frequencies (36.5 GHz). This trend is less notable in Fig. 8 (a). This shows the importance of the coating material parameter determination accuracy, especially at central frequencies ($f_0 = c_0/p$). A sufficiently low uncertainty in the coating layer material parameter will contribute to a stably low std in the T_{MCT} estimation, even when the environmental temperature difference is quite large ($T_{\mathrm{base}} - BT_{\mathrm{b}}$).

In Fig. 10, similar std results of the T_{MCT} bias estimation are compared but considering a larger unit size $p = 7.5$ mm. Overall data trends are similar to those in Fig. 9. One can see that the std for the T_{MCT} estimation are notably smaller than that in Fig. 8. The key reason for this fact is that the $\alpha_{\mathrm{Gradient}}$ in case of a larger unit is smaller than that in case of a smaller unit, given the same coating thickness and height to period ratio. This set of comparison shows that a larger unitsize MCT design generally leads better T_{MCT} estimation accuracy.

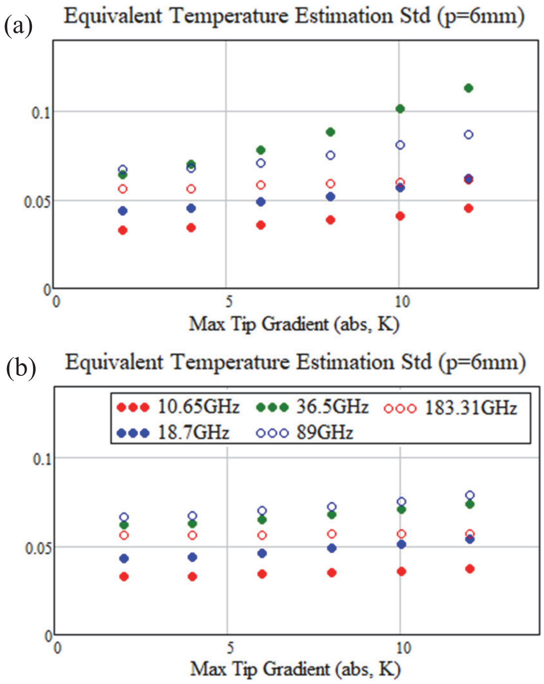

Fig. 9. Counted T_{MCT} bias std at different frequencies: (a) $\sigma_\varepsilon = 0.1\varepsilon, \sigma_\mu = 0.1\mu$ and (b) $\sigma_\varepsilon = 0.05\varepsilon$, $\sigma_\mu = 0.05\mu . p = 6.0$ mm, $\sigma \Delta T_{\mathrm{tip}} = 0.5$ K.

In Figs. 9 and 10, most of the std results are below 0.1 K, which is a considerably small value sufficient for practical BT correction. It is also important to recall the numerical analysis for the BT bias estimation in V/T test reported in [16], which gives many important insights into the BT radiation process. However, based on a full-numerical estimation approach, the counted BT bias estimation std is at the level of 0.22 K (maximum) for the MCT $p = 8.6$ mm. Considering those results, the key motivation of this work shall be concluded as: shorten the error analysis chain by considering measurable temperature values over simulated results will leads to the BT bias estimation more practical and more reliable.

Consider a higher std in the tip-bottom temperature difference measurement by infrared camera detection, which is highly possible in practical applications, specifically $\sigma \Delta T_{\mathrm{tip}} = 1$ K. The corresponding results are given

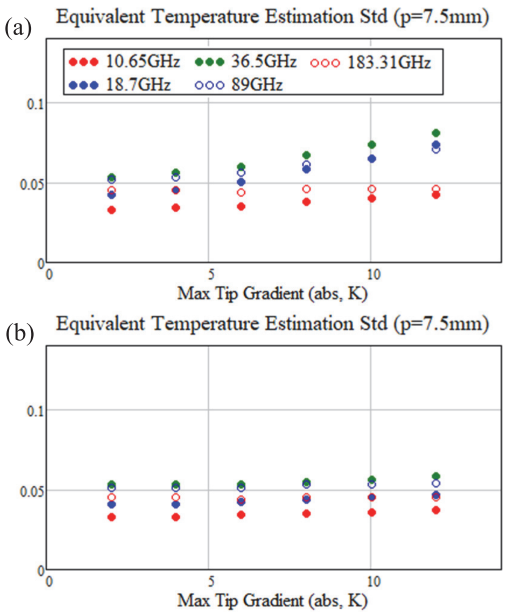

Fig. 10. Counted T_{MCT} bias std at different frequencies: (a) $\sigma_\varepsilon = 0.1\varepsilon, \sigma_\mu = 0.1\mu$ and (b) $\sigma_\varepsilon = 0.05\varepsilon, \sigma_\mu = 0.05\mu . p = 7.5$ mm, $\sigma \Delta T_{\mathrm{tip}} = 0.5$ K.

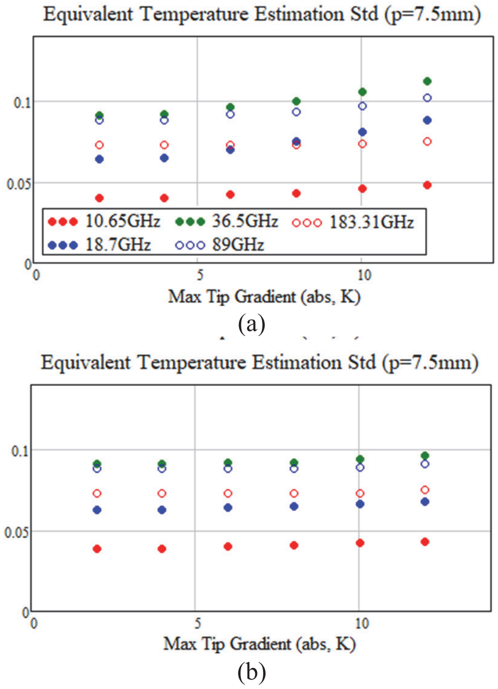

Fig. 11. Counted T_{MCT} bias std at different frequencies: (a) $\sigma_\varepsilon = 0.1\varepsilon, \sigma_\mu = 0.1\mu$ and (b) $\sigma_\varepsilon = 0.05\varepsilon, \sigma_\mu = 0.05\mu . p = 7.5$ mm, $\sigma \Delta T_{\mathrm{tip}} = 1$ K.

in Fig. 11. By achieving a sufficient (ε, μ) accuracy, $\sigma_\varepsilon = 0.05\varepsilon, \sigma_\mu = 0.05\mu$, the overall std of the T_{MCT} estimation can be below 0.1 K. This set of results indicates that T_{MCT} estimation based on PRT measurement at bottom and infrared camera detection for tip-bottom temperature difference is generally robust and can afford the relatively low accuracy for the ΔT_{tip} measurement.

IV. CONCLUSIONS

In this work, the authors investigate the equivalent physical temperature (T_{MCT}) estimation methodology for the MCT in ground-based radiometer calibration applications. It is well known that the difference between the actually T_{MCT} and the nominal temperature is the key factor for the *BT* bias. Accurate estimation of T_{MCT} is significant for practical *BT* bias correction. This work performs error analysis for T_{MCT} estimation, for a highly possible temperature measurement strategy combing PRT and infrared camera detection. It is shown in the numerical results that such a routine is possible to determine T_{MCT} at an accuracy level of $1-\sigma$ std 0.1 K, which is important for practical calibration application. This routine performs better in accuracy on the MCT with a larger unit size over that with a smaller unit size. Ensuring sufficient low uncertainty in the electromagnetic parameters of the coating layer is important to retain the overall estimation accuracy and make such a routine more tolerable to the infrared detection error. Numerical results show the possibility of the temperature measurement supported *BT* bias estimation and provide a corresponding reference for error analysis.

ACKNOWLEDGMENT

This work is supported by the National Key Research and Development Program of China, under Grant 2023YFB3905600, and the National Natural Science Foundation of China, under Grant 62371031.

REFERENCES

[1] F. Ulaby, D. Long, W. Blackwell, C. Elachi, and K. Sarabandi, *Microwave Radar and Radiometric Remote Sensing*. Ann Arbor, MI, USA: University of Michigan Press, pp. 229–278, 2024.

[2] D. W. Draper, D. A. Newell, D. A. Teusch, and P. K. Yoho, “Global precipitation measurement microwave imager prelaunch hot load calibration,” *IEEE Trans. Geosci. Remote Sensing*, vol. 51, no. 9, pp. 4731–4742, 2013.

[3] H. Yang, F. Weng, L. Lv, N. Lu, G. Liu, M. Bai, Q. Qian, J. He, and H. Xu, “The FengYun-3 microwave radiation imager on-orbit verification,” *IEEE Trans. Geosci. Remote Sensing*, vol. 49, no. 11, pp. 4552–4560, 2011.

[4] A. Schröder, A. Murk, R. Wylde, K. Jacob, K. Pike, and M. Winser, “Electromagnetic design of calibration targets for MetOp-SG microwave instruments,” *IEEE Trans. Terahertz Sci. Tech.*, vol. 7, no. 6, pp. 677–685, 2017.

[5] A. Schröder and A. Murk, “Numerical design and analysis of conical blackbody targets with advantage shape,” *IEEE Trans. Antennas Propag.*, vol. 64, no. 5, pp. 1850–1858, 2016.

[6] D. Houtz, W. Emery, D. Gu, and D. Walker, “Brightness temperature calculation and uncertainty propagation for conical microwave blackbody targets,” *IEEE Trans. Geosci. Remote Sens.*, vol. 56, no. 12, pp. 7246–7256, 2018.

[7] S. Sandeep and A. J. Gasiewski, “Electromagnetic analysis of radiometer calibration targets using dispersive 3D FDTD,” *IEEE Trans. Antennas Propag.*, vol. 60, no. 6, pp. 2821–2828, 2012.

[8] M. Bai, D. Xia, and M. Jin, “Effects of coating material properties on the wideband reflectivity performance of microwave calibration targets,” *IEEE Trans. Antenna Propag.*, vol. 65, no. 9, pp. 4909–4913, 2017.

[9] T. Zou, Z. Shang, Y. Shen, Q. Wen, G. Lu, and Z. Wu, “Research on calibration sources for a 35 – 40 GHz millimeter-wave solar radio observation system,” *IEEE Trans. Antennas Propag.*, vol. 71, no. 5, pp. 4094–4101, 2023.

[10] D. Gu, D. Houtz, J. Randa, and D. K. Walker, “Reflectivity study of microwave blackbody target,” *IEEE Trans. Geosci. Remote Sens.*, vol. 49, no. 9, pp. 3443–3451, 2011.

[11] J. Wang, Y. Yang, J. Miao, and Y. Chen, “Emissivity calculation for a finite circular array of pyramidal absorbers based on Kirchhoff’s law of thermal radiation,” *IEEE Trans. Antennas Propag.*, vol. 58, no. 4, pp. 1173–1180, 2010.

[12] M. Jin, B. Li, B. Fan, Z. Li, and M. Bai, “On the reflectivity extraction based on partial bistatic near-field scattering from microwave blackbody,” *IEEE Trans. Antennas Propag.*, vol. 69, no. 3, pp. 1692–1705, 2021.

[13] M. Jin, B. Fan, X. Li, B. Li, and M. Bai, “On the total reflectivity estimation of microwave calibration targets by backscattering measurements,” *IEEE Trans. Geosci. Remote Sens.*, vol. 60, p. 5223711, 2022.

[14] M. Jin, B. Li, and M. Bai, “On the reflectivity measurements of microwave blackbody in bistatic near-field configuration,” *IEEE Trans. Antennas Propag.*, vol. 69, no. 11, pp. 8027–8032, 2021.

[15] A. Schröder, A. Murk, R. Wylde, D. Schobert, and M. Winser, “Brightness temperature computation of microwave calibration targets,” *IEEE Trans. Geosci. Remote Sens.*, vol. 55, no. 12, pp. 7104–7112, 2017.

[16] G. Virone, G. Addamo, A. Bosisio, M. Zannoni, L. Valenziano, D. Rizzo, and P. Radaelli, “Thermal vacuum cold target for the Metop SG microwave imager,” *IEEE J. Sel. Topics Appl. Earth Observ. Remote Sens.*, vol. 14, pp. 10348–10356, 2021.

[17] M. Jin, R. Yuan, X. Li, Y. Tao, Q. Gao, and M. Bai, “Wideband microwave calibration target design for improved directional brightness temperature radiation,” *IEEE Geosci. Remote Sens. Lett.*, vol. 19, p. 7001705, 2022.

[18] R. Yuan, Y. Tao, Q. Gao, Y. Han, M. Bai, and M. Jin, “Brightness temperature analysis in the miniaturization of pyramidal calibration targets for sub-millimeter wave radiometers,” *IEEE Geosci. Remote Sens.*, vol. 19, p. 5003505, 2022.

[19] D. M. Jackson and A. J. Gasiewski, “Electromagnetic and thermal analyses of radiometer calibration target,” in *Proc. Int. Geosci. Remote Sens. Symp.*, Honolulu, HI, USA, vol. 7, pp. 2827–2829, 2000.

[20] Q. Gao, D. Li, Y. Tao, L. Yang, H. Zhang, D. Ma, M. Peng, M. Jin, Q. Guo, S. Jiang, Y. Li, C. Cheng, and X. Li, “Research on metrological calibration technology scheme of brightness temperature for the space-borne microwave radiometer calibration target,” *Journal of Infrared and Millimeter Waves*, vol. 45, no. 01, pp. 77–89, 2026 [in Chinese].

[21] I. Zivkovic and A. Murk, “Characterization of magnetically loaded microwave absorbers,” *Prog. Electromagn. Res. B*, vol. 33, pp. 277–289, 2011.

Ming Jin received the B.Sc. and Ph.D. degrees from Beihang University (BUAA), Beijing, China, in 2007 and 2013, respectively. From 2007 to 2012, he was a research assistant in the Microwave Engineering Laboratory, Beihang University. From December 2010 to March 2011, he was a Visiting Scholar at Arizona State University. In 2019, he joined the College of Information Science and Technology, Beijing University of Chemical Technology (BUCT), as an associate professor, and he became professor in 2024. His research interests include microwave radiometer calibration techniques, quasi-optical beam propagation and computational electromagnetics.

Jiacheng Qian is currently pursuing his B.Sc. degree in the College of Mathematics and Physics, majoring in Electronic Science and Technology. His research interests include numerical simulations and analysis of microwave calibration targets.

Miaomiao Peng received B.Sc. and master's degrees from Beijing University of Chemical Technology (BUCT), Beijing, China, in 2022 and 2025, respectively. She is currently pursuing her Ph.D. degree with the school of integrated circuits and electronics, Beijing Institute of Technology. Her current research interests include numerical method in electromagnetics, microwave radiometer calibration targets and brightness temperature transfer modeling in calibration links.

An Endfire Array Antenna for Simultaneous Operation in C- and X-Bands

Z. N. Jiang[1,2], **W. X. Gao**[1], **and C. Peng**[1]

[1]School of Computer Science and Information
Hefei University of Technology, Hefei, China
jiangzhaoneng@hfut.edu.cn, 2970656281@qq.com, 3061596755@qq.com

[2]Anhui Institute of Information Technology
Wuhu, China

***Abstract* –** In this paper, a broadband high-gain endfire array antenna based on spoof surface plasmon polaritons (SSPPs) is designed for simultaneous C- and X-band applications. To achieve endfire radiation, the SSPP structure is truncated to reduce its field confinement capability, while a radiating branch is loaded at the end of the transmission line to guide energy radiation. A rectangular metal ground is placed at the bottom of the antenna substrate to suppress backward radiation and optimize the contact area with the connector to ensure stable feeding. The final 1×4 endfire array antenna is formed by integrating unit antennas via a Wilkinson power divider-based feed network. A prototype was fabricated and tested, showing a 50% relative impedance bandwidth (6–10 GHz), 91% simulated radiation efficiency, 87% average measured radiation efficiency, and a maximum measured gain of 11.6 dBi at 9.7 GHz. With simple structure, low cost, and excellent performance, it is promising for C-band low-orbit satellite communication and X-band short-range radar.

***Index Terms* –** Broadband, C-band, endfire array antenna, high gain, low-orbit satellite, short-range radar, Spoof Surface Plasmon Polaritons (SSPPs), X-band.

I. INTRODUCTION

At the metal-medium interface, free electrons interact with photons to form surface plasmon polaritons (SPPs), quasiparticles that characterize photon-electron coupling behavior [1–3]. SPPs propagate along the interface but decay rapidly in the direction perpendicular to it, exhibiting unique field confinement advantages in the optical band. To extend these advantages of SPPs from the optical band to microwave/terahertz frequencies [4], Pendry and his collaborators proposed subwavelength periodic metallic structures in 2004 to simulate the low-frequency properties of SPPs [5, 6], thus enabling the emergence of spoof surface plasmon polaritons (SSPPs).

Leveraging the strong field confinement capability of SSPP structures, they have been widely employed in microwave devices, including coplanar waveguides (CPW) [7, 8], filters [9], amplifiers [10], power splitters [11], and antennas [12–16]. Among these applications, SSPP-based endfire antennas have garnered significant attention. Compared with traditional endfire antennas, they offer distinct advantages of low profile and high integration, making them well-suited for planar integration scenarios. However, existing designs still face limitations. In [17], a printed dipole fed by an SSPP structure achieves enhanced directivity but suffers from narrow bandwidth due to the dipole's resonant nature. Reference [18] adopted a substrate-integrated waveguide (SIW) structure for impedance matching; rectangular slots are cut in the SIW structure to broaden the bandwidth, yet there remains room for improvement in bandwidth enhancement. In [19], a wideband Vivaldi-shaped SSPP traveling-wave endfire antenna is proposed, yet its large transverse size hinders compact integration. Dipole-shaped odd-mode SSPPs are utilized to form a two-element array in [20], but it fails to balance high gain and high efficiency over a wide frequency band.

To address these issues, this paper proposes a novel broadband high-gain endfire array antenna based on SSPPs. It breaks the bandwidth-integration trade-off by truncating SSPP to adjust field confinement and adds a gradient groove transition section to solve microstrip-SSPP impedance mismatch. A 1×4 array with a Wilkinson power divider enhances gain while keeping compactness, a slot between the "knife" patch and feed end strengthens SSPP excitation. Experimental validation shows the antenna covers C- and X-dual bands, solves existing issues (narrow bandwidth, large size, unbalanced gain-efficiency), and provides a feasible solution

Submitted On: September 09, 2025
Accepted On: February 03, 2026

https://doi.org/10.13052/2026.ACES.J.410309

for high-performance planar endfire antennas in wireless communications.

II. ANTENNA CONFIGURATION DESIGN AND MECHANISM

A. Dispersion relationship

The emergence of SSPP has facilitated endfire antenna design with two optimization methods: periodic modulation and bandwidth expansion by truncation. Both methods break electromagnetic field confinement and are widely used in microwave antennas. This paper uses the second method, designing slotted units to weaken field confinement, thereby achieving endfire radiation. Figure 1 shows the SSPP unit, which uses F4B substrate ($\varepsilon r = 2.65$), with a thickness of $t = 0.8$ mm. The dimensions of this unit are as follows: $c = 2.5$ mm, $b = 1.5$ mm, $h = 1.2$ mm, $d = 1.2$ mm. The propagation properties of the SSPP unit were investigated using CST Microwave Studio software, aiming to provide a basis for optimizing the endfire antenna design by analyzing the influence of unit parameters on propagation characteristics.

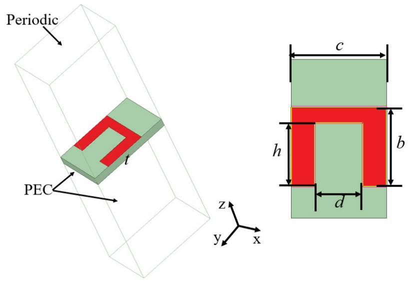

Fig. 1. SSPP unit structure diagram.

Figure 2 presents the simulated dispersion characteristics of SSPP units and transmission lines with different slot depths. Slot depth h serves as a key parameter to regulate the transmission characteristics of SSPP surface waves. From the perspective of electromagnetic field distribution, increasing h enhances the “confinement effect” of the metal slot on the electromagnetic field which causes the field distribution of surface waves to concentrate more inside the slot, thereby expanding the spatial confinement region of the electromagnetic field and further enhancing the overall field confinement capability. Besides, the strengthened field confinement extends the wavelength of SSPP surface waves and reduces the cutoff frequency. Therefore, a detailed analysis of the slot depth is crucial when extracting the unit structure’s dispersion characteristics to ultimately obtain the optimal dispersion curve and slow-wave operating mode characteristics.

As the slot depth h increases from 0.8 mm to 1.4 mm, the deviation of the SSPP dispersion curve below the light line and the transmission line becomes more pronounced, and the cut-off frequency decreases continuously from 40 GHz to 29 GHz. At the same frequency, these dispersion curves exhibit a larger wave number K and a smaller wavelength than those of electromagnetic waves in vacuum. This slow-wave effect can effectively enable antenna miniaturization, which aligns with the compact design requirement of the proposed antenna.

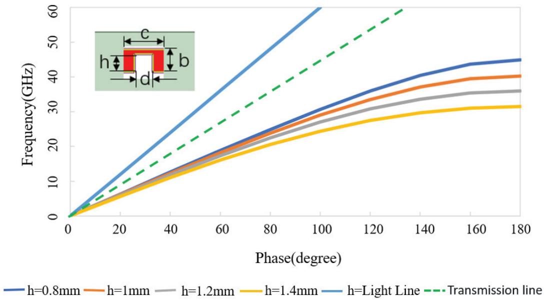

Fig. 2. Simulated dispersion characteristic curves for different slot depths.

B. Design and analysis of the unit antenna

Figure 3 shows the designed unit endfire antenna structure. The antenna is fabricated on a single-layer F4B dielectric substrate with a thickness of $t = 0.8$ mm. The antenna consists of three core parts: a knife-shaped radiator, an SMA feed connector, and an SSPP transmission line. It features symmetrically distributed radiating elements, with the SSPP structure serving as the transmission line to guide electromagnetic energy. Additionally, a rectangular metal ground is designed at the bottom of the substrate to suppress backward radiation and optimize the contact area with the feed connector for stable power feeding.

The knife-shaped radiating patch adopts a Vivaldi gradient structure, which satisfies the following exponential function relationship:

$$C_1 = \frac{y_2 - y_1}{e^{Rx_2} - e^{Rx_1}}, \tag{1}$$

$$C_2 = y_1 - C_1 e^{Rx_1}, \tag{2}$$

$$y = f(x) = C_1 e^{Rx} + C_2. \tag{3}$$

Among them, x_1, y_1, x_2, and y_2 represent the horizontal and vertical coordinates of the start point and end point of the curve, respectively. R denotes the curvature of the curve, with a value of -200.

The SSPP transmission line comprises two segments: 10 identical single-sided metal grooves (with $h = 1.2$ mm) and nine gradient grooves (with h varying from 0.04 mm to 1.2 mm), forming a two-part transition

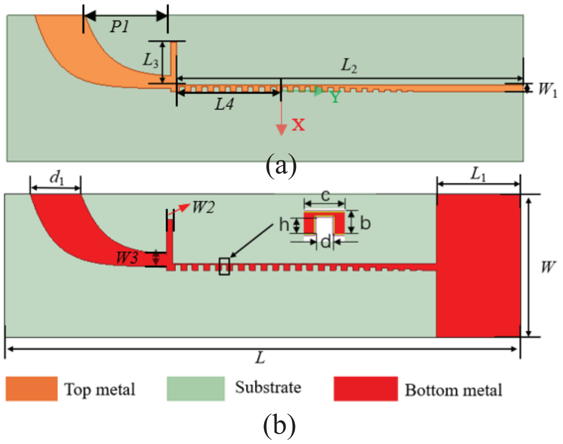

(a)

(b)

Fig. 3. Specific structure diagram of unit antenna: (a) top view and (b) bottom view. $L = 132$, $W = 32$, $W_1 = 1.5$, $W_2 = 1.2$, $W_3 = 2.75$, $L_1 = 18.5$, $L_2 = 57.5$, $L_3 = 8.5$, $L_4 = 19.5$, $P_1 = 18.8$ and $d_1 = 11$ (unit: mm).

section. This gradient periodic unit structure offers three key advantages aligned with the design goals of the antenna. First, it achieves optimal impedance matching between the microstrip line and the SSPP transmission line. Second, it moderately enhances field confinement to ensure stable SSPP mode propagation without excessive energy leakage. Third, it enables smooth conversion from the quasi-TEM mode to the SSPP mode. To further broaden the impedance bandwidth and improve the endfire directivity of the antenna, a wide knife-shaped radiating patch is cascaded with the SSPP transmission line. This patch facilitates controlled energy radiation by weakening the field confinement of the final segment of the SSPP, a process essential for realizing endfire radiation.

C. Optimization and result analysis of unit antenna

Through structural analysis of the endfire antenna, the SSPP transmission line is identified as a key component regulating the performance of the antenna. Figure 4 (a) presents the optimization analysis of the slot depth h for the SSPP transmission line unit. As shown in Fig. 4, with the increase in h (from 1.1 mm to 1.4 mm), two resonance points within the target operating band gradually shift leftward, and the reflection coefficient curve shifts upward, which indicates degraded impedance matching performance. Based on the comprehensive analysis above, the slot depth $h =$ 1.2 mm is finally selected as the parameter for the SSPP unit.

The optimization results for the slot width d of the SSPP transmission line unit are presented in Fig. 4 (b). Comparative analysis shows that as d increases (from 1.0 mm to 1.4 mm), the operating resonant frequency point of the antenna does not shift, but the reflection coefficient $S11$ shifts upward gradually. This indicates that the impedance matching performance degrades significantly as d increases. Specifically, wider slots weaken the spatial confinement of the electromagnetic field by the metal slot, thus leading to unstable propagation of the SSPP mode. After comprehensive consideration of matching performance and mode stability, the slot width $d = 1.2$ mm is selected for the SSPP unit structure.

Figure 4 (c) illustrates the effect of the stub on the S-parameters of the antenna. As the length of stub $L3$ increases from 4.5 to 8.5 mm, the impedance characteristic of the antenna is improved, and impedance matching is achieved when $L3 = 8.5$ mm.

After setting the antenna parameters to the values shown in Figure 3, the antenna model is re-simulated. Figure 5 shows the main current distribution of the antenna at 8 GHz, revealing the primary radiation area of the antenna. Figure 6 (a) shows its $S11$ curve, confirming 6–10 GHz bandwidth that covers C-band and X-band. It also includes the simulated gain curve: gain is stable but not ideal for high performance, with a maximum of 6.26 dBi at 9.5 GHz. This limitation of the single-unit structure serves as the core driver for subsequent 1×4 array integration to enhance gain. Figure 6 (b) presents the simulated radiation pattern, demonstrating that the antenna achieves directional endfire radiation with a wide main beam and low backward radiation, which verifies that the antenna simultaneously exhibits good impedance matching performance and effective endfire radiation characteristics within the operating band.

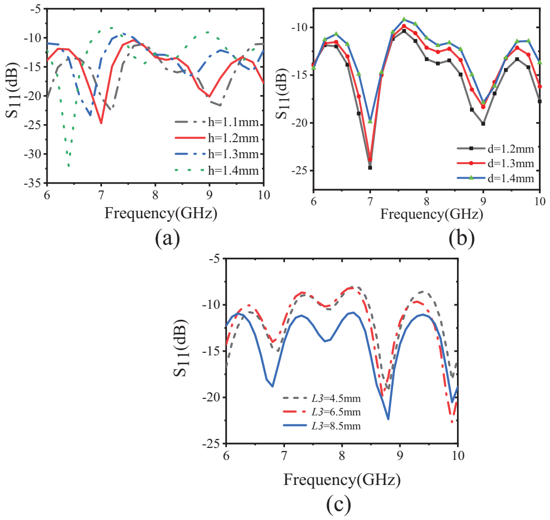

(a)

(b)

(c)

Fig. 4. Simulated S-parameters with different parameters: (a) slot depth of h, (b) slot width of d, and (c) stub length of $L3$.

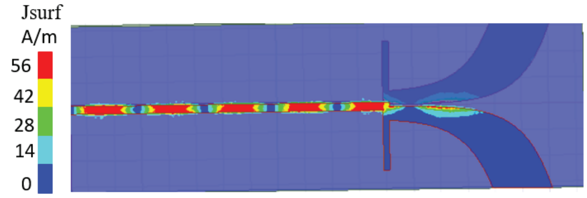

Fig. 5. Current distribution at 8 GHz.

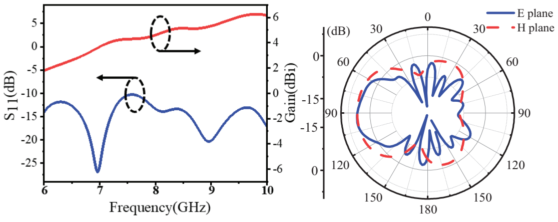

(a) (b)

Fig. 6. (a) S-parameters and gain of a single-unit endfire antenna and (b) 8 GHz direction diagram of a unit endfire antenna.

D. Design of array antennas and feed networks

To maintain the directional radiation performance of the single-unit endfire antenna and address its insufficient gain, a 1×4 array is adopted. This design enhances gain while retaining the compact planar structure for microwave system integration. A Wilkinson 1-to-4 microstrip equal-power divider serves as the feed network and is integrated with SSPP transmission lines, reducing overall size.

As shown in Fig. 7, the array has two copper layers on the F4B sheet. The top layer integrates a 1×4 SSPP feed network and the Wilkinson divider, the bottom layer has four symmetric SSPP lines and a full metallic ground. The ground suppresses backward radiation and supports the structure, while symmetrical layout ensures uniform energy distribution to avoid gain degradation.

III. ANTENNA FABRICATION AND TESTING

Figure 8 shows the physical prototype of the proposed 1×4 endfire array antenna, and tests were conducted to validate its performance. Figure 9 compares the measured and simulated S-parameters of the proposed 1×4 endfire array. The measured −10 dB impedance bandwidth covers C-band high frequencies and X-band low frequencies, matching the target design. Figure 10 shows the gain of the array and measured radiation efficiency. Within 6–10 GHz, the measured gain of the array ranges from 8.2 to 11.6 dBi. This represents a gain enhancement of 4–5.4 dBi compared to

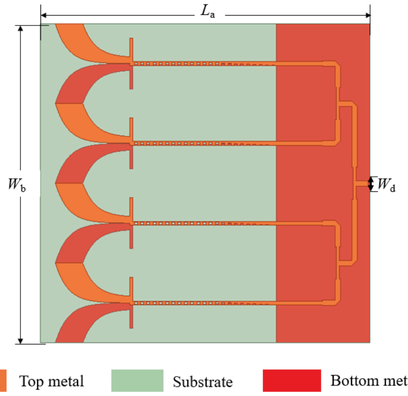

Fig. 7. Endfire array antenna: $L_a = 132$, $W_b = 128$, and $W_d = 1.5$ (unit: mm).

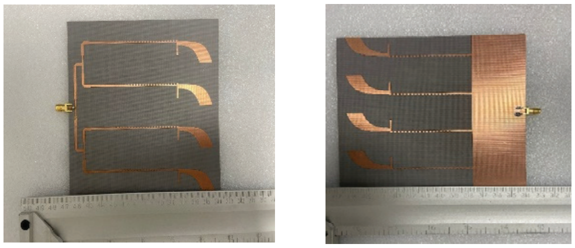

(a) (b)

Fig. 8. Photographs of the fabricated antenna: (a) top view and (b) bottom view.

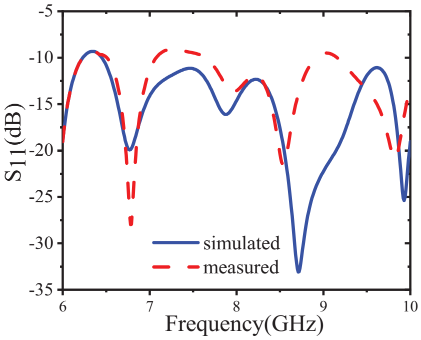

Fig. 9. Simulated and measured S-parameters of the designed array antennas.

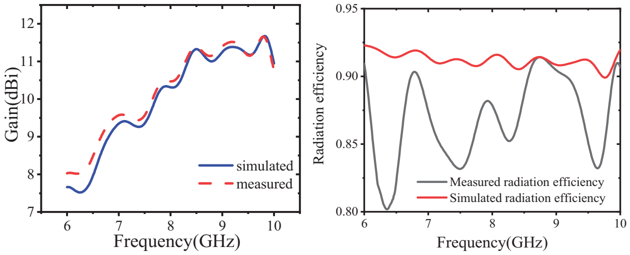

(a) (b)

Fig. 10. (a) Simulated and measured gains of the designed array antenna and (b) radiation efficiency of endfire antennas.

Table 1: Comparison with reported endfire antennas

Ref.	**f_0 (GHz)**	**Size L(λ_0) × W(λ_0)**	**Band-width (%)**	**Average Efficiency (%)**	**Max Gain (dBi)**
[14]	16.6	5.8×4.44	11	95	12.1
[16]	10	2.93×0.51	20	98	13.3
[17]	5.5	3.33×0.74	7.4	85	7.86
[18]	19.5	6.2×1.4	35	90	15.2
[19]	12.5	6.59×2.92	120	92	10.7
[20]	6	2.33×0.25	67	54	7.9
This Work	8.0	3×0.85	50	87	11.6

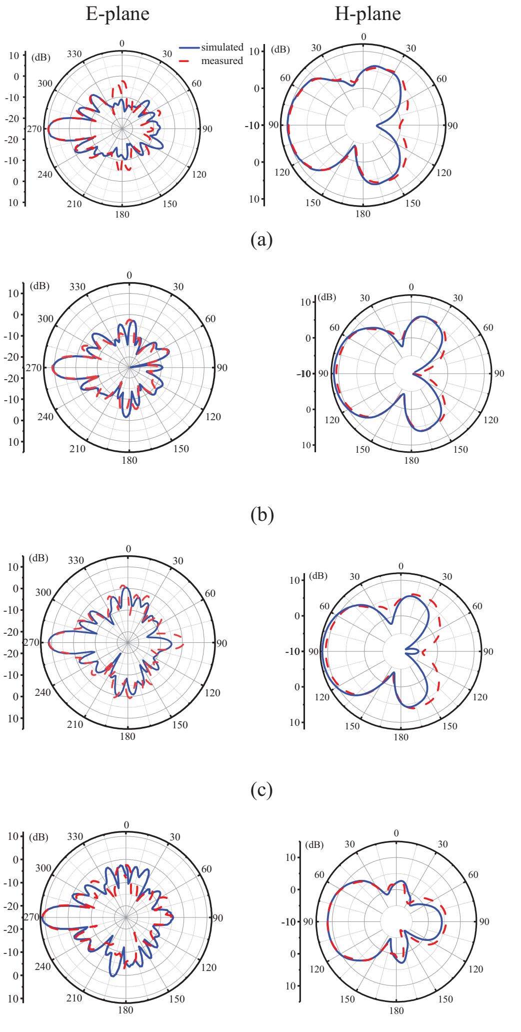

(a)

(b)

(c)

(d)

Fig. 11. Simulated and measured radiation patterns in the E-plane (*xoy*-plane) and H-plane (*yoz*-plane) at (a) 7.5 GHz, (b) 8 GHz, (c) 8.5 GHz, and (d) 9 GHz.

the maximum gain of 6.26 dBi achieved by the single-unit SSPP endfire antenna, thereby verifying the effectiveness of the 1×4 array configuration in improving antenna gain. Measured average radiation efficiency is 87%, slightly lower than the simulated 91%. Figure 11 shows the measured and simulated radiation patterns of the array in the E-plane and H-plane. The simulated and measured patterns are basically consistent, only minor back lobe differences exist. Collectively, the measured results demonstrate excellent agreement with the simulation data. The minor deviations between the measured and simulated results are primarily caused by unavoidable fabrication tolerances.

Table 1 compares the proposed antenna with recent endfire antennas, where f_0 and λ_0 are the center frequency and the wavelength at the center frequency, respectively. It has a wider bandwidth than [14, 16–18], while the antenna in [19] achieves a relatively wide bandwidth, it is too large for miniaturized integration, and the antenna in [20], though small and wideband, lacks radiation efficiency and gain. In contrast, the proposed antenna offers low profile, high integration, broadband capability, and stable radiation performance.

IV. CONCLUSION

This paper proposes a broadband high-gain endfire array antenna based on an SSPP transmission line. Endfire radiation is realized by truncating the SSPP structure to reduce field confinement. A 1×4 array is designed, with units connected via a Wilkinson power divider-based feed network. Featuring a low-profile and highly integrated structure, the antenna also possesses broadband performance and stable radiation characteristics, thus exhibiting great application potential in millimeter-wave communication, 5G/6G base stations, and satellite payloads.

ACKNOWLEDGMENT

This work was supported in part by the Teacher Research Program of Hefei University of Technology (JZ2019HGTB0093), Anhui Institute of Information Technology, the Research Fund of National

Mobile Communications Research Laboratory, Southeast University (2023D05), and the Natural Science Foundation of Anhui Province (2208085MF161, JZ2022AKZR0453).

REFERENCES

[1] S.-Y. Zhou, S.-W. Wong, J.-Y. Lin, L. Zhu, Y. He, and Z.-H. Tu, "Four-way spoof surface plasmon polaritons splitter/combiner," *IEEE Microw. Wireless Compon. Lett.*, vol. 29, no. 2, pp. 98–100, Feb. 2019.

[2] X. Shen, T. Cui, D. Martin-Cano, and F. Garcia-Vidal, "Conformal surface plasmons propagating on ultrathin and flexible films," *Proc. Nat. Acad. Sci.*, vol. 110, no. 1, pp. 40–45, 2012.

[3] L. Liu, M. Chen, J. Cai, X. Yin, and L. Zhu, "Single-beam leaky wave antenna with lateral continuous scanning functionality based on spoof surface plasmon transmission line," *IEEE Access*, vol. 7, pp. 25225–25231, 2019.

[4] W. L. Barnes, A. Dereux, and T. W. Ebbesen, "Surface plasmon sub-wavelength optics," *Nature*, vol. 424, no. 6950, pp. 824–830, 2003.

[5] J. B. Pendry, L. Martín-Moreno, and F. J. García-Vidal, "Mimicking surface plasmons with structured surfaces," *Science*, vol. 305, no. 5686, pp. 847–848, 2004.

[6] F. J. Garcia-Vidal, L. Martín-Moreno, and J. B. Pendry, "Surfaces with holes in them: New plasmonic metamaterials," *Journal of Optics and Pure and Applied Optics*, vol. 7, no. 2, p. S97, 2005.

[7] A. Kandwal, Q. Zhang, X.-L. Tang, L. W. Liu, and G. Zhang, "Low-profile spoof surface plasmon polaritons traveling-wave antenna for near-endfire radiation," *IEEE Antennas Wireless Propag. Lett.*, vol. 17, no. 2, pp. 184–187, Feb. 2018.

[8] S. Ge, Q. Zhang, A. K. Rashid, G. Zhang, C.-Y. Chiu, and R. D. Murch, "Analysis of asymmetrically corrugated Goubau-line antenna for endfire radiation," *IEEE Trans. Antennas Propag.*, vol. 67, no. 11, pp. 7133–7138, Nov. 2019.

[9] L. Li, P. Chen, P. Zhu, and K. Yang, "A compact rejection filter based on spoof surface plasmon polaritons and folded split-ring resonators with controllable rejection bandwidth," *Applied Computational Electromagnetics Society (ACES) Journal*, vol. 34, no. 09, pp. 1405–1410, Sep. 2019.

[10] H. C. Zhang, S. Liu, X. Shen, L. H. Chen, L. Li, and T. J. Cui, "Broad band amplification of spoof surface plasmon polaritons at microwave frequencies," *Laser & Photonics Reviews*, vol. 9, no. 1, pp. 83–90, 2015.

[11] X. Gao, L. Zhou, X. Yu, W. Cao, H. Li, H. F. Ma, and T. Cui, "Ultra-compact surface plasmonic Y-splitter," *Optics Express*, vol. 23, no. 18, p. 23270, 2015.

[12] J. Xu and Z. Zheng, "High-gain and wideband planar endfire antenna implemented via spoof surface plasmon polaritons and dielectric lens for x-band applications," *IEEE Antennas and Wireless Propagation Letters*, vol. 22, no. 2, pp. 382–386, Feb. 2023.

[13] Y. Shi, Z. Fan, and C. Chen, "Wideband wide-angle SSPP-fed leaky-wave antenna with low sidelobe levels," *Applied Computational Electromagnetics Society (ACES) Journal*, vol. 39, no. 10, pp. 916–926, Oct. 2024.

[14] L. Liu, M. Chen, and X. Yin, "Single-layer high gain endfire antenna based on spoof surface plasmon polaritons," *IEEE Access*, vol. 8, pp. 64139–64144, 2020.

[15] X. Du, H. Li, and Y. Yin, "Wideband fish-bone antenna utilizing odd mode spoof surface plasmon polaritons for endfire radiation," *IEEE Trans. Antennas Propag.*, vol. 67, no. 7, pp. 4848–4853, July 2019.

[16] Q. Fu, H. Ni, G. Q. Luo, L. Zhu, and L. Liu, "A high aperture efficiency endfire antenna based on spoof surface plasmon polaritons," *IEEE Transactions on Antennas and Propagation*, vol. 71, no. 1, pp. 50–57, Jan. 2023.

[17] D. Tian, R. Xu, G. Peng, J. Li, Z. Xu, and A. Zhang, "Low-profile high-efficiency bidirectional endfire antenna based on spoof surface plasmon polaritons," in *IEEE Antennas and Wireless Propagation Letters*, vol. 17, no. 5, pp. 837–840, May 2018.

[18] F. Homayoon, A.-A. Heidari, and M.-M. Pezhman, "A low-profile high-performance endfire antenna based on spoof surface plasmon polaritons," *IEEE Antennas and Wireless Propagation Letters*, vol. 22, no. 12, pp. 2891–2895, Dec. 2023.

[19] J. Y. Yin, H. C. Zhang, Y. Fan, and T. J. Cui, "Direct radiations of surface plasmon polariton waves by gradient groove depth and flaring metal structure," *IEEE Antennas and Wireless Propagation Letters*, vol. 15, pp. 865–868, 2016.

[20] Y. Jiang, L. Liu, Y. Hu, and D. Jiang, "Wideband small aperture endfire antenna based on spoof surface plasmon polaritons," *IEEE Transactions on Antennas and Propagation*, vol. 69, no. 8, pp. 5026–5031, Aug. 2021.

Zhaoneng Jiang was born in Lianyungang, Jiangsu, China. He received the Ph.D. degree from Nanjing University of Science and Technology, Nanjing, in 2012. Since 2013, he has been engaged in research on numerical methods for computational electromagnetism. He is currently a Professor at Hefei University of Technology and a Distinguished Professor at Anhui Institute of Information Technology. He has authored or co-authored more than 100 papers in prestigious international journals and conferences and has served as a Program Committee Member for several international conferences. His current research interests include antennas and microwave devices.

Weixing Gao, a native of Zhoukou, Henan Province, China, obtained his master's degree from Hefei University of Technology, in 2026. He has been engaged in the research of microwave antenna design since 2023.

Cheng Peng, a native of Yangzhou, Jiangsu Province, China, obtained his master's degree from Hefei University of Technology in 2026. He has been engaged in the research of microwave antenna design since 2023.

Enhanced Compressive Sensing Method of Moments via Physics-Aware Characteristic Modes and LSQR Solver

Yang Liu[1], Zhonggen Wang[1], Wenyan Nie[2], and Longhui Sun[1]

[1]School of Electrical and Information Engineering
Anhui University of Science and Technology, Huainan 232001, China
2023200714@aust.edu.cn, zgwang@ahu.edu.cn, 15556361695@163.com

[2]School of Mechanical and Electrical Engineering
Huainan Normal University, Huainan 232001, China
wynie5240@163.com

Abstract – To improve the computational efficiency and stability of the compressive sensing-method of moments (CS-MoM) based on characteristic mode basis functions (CMBFs) for electromagnetic scattering problems, this paper introduces an enhanced construction strategy for CMBFs. The proposed method adopts a dual strategy framework that synergistically integrates physical insight with mathematical screening, replacing the conventional approach based solely on mathematical selection. This integration significantly enhances the physical interpretability and sparsity of the resulting basis functions. In addition, the least squares QR (LSQR) iterative algorithm, which solves the problem by utilizing QR decomposition, is employed instead of the traditional LS method for the CS reconstruction problem. This replacement alleviates the detrimental effects of ill-conditioned matrices on solution stability, thereby improving the robustness and accuracy of the algorithm. Numerical results confirm that the proposed method substantially reduces computational complexity while enhancing numerical stability.

Index Terms – Characteristic mode basis functions, compressive sensing, method of moments, reconstruction algorithm.

I. INTRODUCTION

The method of moments (MoM) [1] is an effective full-wave numerical technique for solving electromagnetic scattering problems, renowned for its high accuracy and broad applicability. However, when applied to electrically large targets, the computational complexity of the resulting matrix equations increases significantly. To address this challenge, several acceleration algorithms have been proposed, including the multilevel fast multipole method [2], characteristic basis function method [3], and adaptive cross approximation [4], all aiming to reduce the matrix size or expedite the solution process. In recent years, compressive sensing (CS) [5] has been introduced into the MoM framework, offering a novel approach for the efficient solution of electromagnetic scattering problems. This integration has driven the development of CS-based MoM (CS-MoM) [6] computational models, with the core idea centered on sparsity optimization of the traditional MoM computational structure. This optimization effectively reduces the computational burden and enhances overall computational efficiency.

The CS-MoM model primarily comprises two computational frameworks. One framework targets monostatic electromagnetic scattering problems and introduces a novel excitation source construction method [7–9]. The key idea is to randomly combine incident excitations from different angles, thereby reducing the number of matrix equations that need to be solved. The other framework is designed for bistatic electromagnetic scattering [10–13], wherein CS techniques are directly integrated into the algorithmic structure of MoM. This approach transforms the full-rank matrix equations into low-dimensional underdetermined systems, significantly decreasing both the matrix filling and solution complexity.

The solution process of the second type of CS-MoM model primarily involves three key steps: constructing the sparse basis, constructing the measurement matrix, and reconstructing the current coefficients. Among these, the critical challenges lie in how to construct a sparse basis with clear physical significance and strong expressive capability, as well as how to select appropriate reconstruction algorithms to enhance computational accuracy and efficiency, both of which are central to the efficient solution of bistatic electromagnetic scattering problems using CS-MoM. Currently,

Submitted On: November 22, 2025
Accepted On: March 09, 2026

https://doi.org/10.13052/2026.ACES.J.410310

commonly used sparse bases for three-dimensional (3D) problem analysis include characteristic basis functions (CBFs) [14, 15], characteristic mode basis functions (CMBFs) [13, 16], and Krylov subspace basis functions [12, 17]. Among them, CMBFs have attracted significant attention due to their excitation-independent construction and suitability for large-scale electromagnetic scattering analysis, especially when combined with domain decomposition strategies. However, existing selection methods for CMBFs primarily rely on purely mathematical criteria [16], which may lead to redundant basis functions and reduce the efficiency of sparse representation. Moreover, many existing approaches accelerate the sparse basis construction process by eliminating basis functions associated with small-amplitude coefficients, thereby forming an overdetermined system. In such systems, ensuring the accuracy of reconstruction typically requires careful determination of the sensing matrix's column structure. Under these circumstances, classic iterative reconstruction algorithms, such as orthogonal matching pursuit (OMP) [18] or generalized OMP (gOMP) [19], often exhibit limited efficiency. To address this issue, the least squares (LS) method is adopted in conjunction with the characteristic mode-based CS-MOM (CM-CS-MoM) [13] framework to enhance the computational efficiency. Nevertheless, during the construction of the normal equations, the explicit formulation of reduced matrices may lead to ill-conditioning, adversely affecting both the stability and accuracy of the final solution.

To address the key challenges in the sparse representation and reconstruction processes described above, this study introduces improvements and optimizations from two perspectives. First, in the construction and selection of CMBFs, greater emphasis is placed on incorporating physical insights into the basis function selection process, thereby avoiding redundancy or deviation in the representation of the target's scattering field. To this end, an enhanced selection strategy that integrates physical mechanisms with mathematical criteria is proposed. By embedding the physical characteristics of current distribution into the basis selection process, the proposed method significantly improves the accuracy and sparsity of basis functions in representing electromagnetic scattering features. Second, during the reconstruction of current coefficients, the traditional LS method is replaced by the least-squares QR (LSQR) iterative algorithm. LSQR offers strong numerical stability and is well-suited to handling ill-conditioned problems, particularly in the context of high-dimensional overdetermined or underdetermined systems. It demonstrates superior reconstruction performance under such conditions. The combined effect of these two enhancements not only improves the overall computational efficiency of the CM-CS-MoM framework but also significantly enhances its robustness and adaptability.

II. THEORY

A. CM-CS-MoM framework

In the MoM, the integral equation is discretized into the following matrix equation by using the Rao-Wilton-Glisson (RWG) functions as basis functions and weighting functions:

$$\mathbf{Z}\mathbf{I} = \mathbf{V}, \tag{1}$$

where $\mathbf{Z}$ denotes a full-rank impedance matrix of dimension $N \times N$, and N represents the number of unknowns. In addition, $\mathbf{I}$ represents the induced current to be solved, and $\mathbf{V}$ represents the incident excitation of dimension $N \times 1$. At this point, by uniformly extracting M rows from $\mathbf{Z}$ and $\mathbf{V}$, the measurement matrix $\hat{\mathbf{Z}}$ and the measurement values $\hat{\mathbf{V}}$ are constructed, respectively. The equation (1) is then transformed into the following underdetermined system:

$$\hat{\mathbf{Z}}\mathbf{I} = \hat{\mathbf{V}}. \tag{2}$$

Considering that the induced current $\mathbf{I}$, discretized using RWG basis functions, is typically not sparse, a sparse transformation is therefore required:

$$\mathbf{I} = \boldsymbol{\Psi}\boldsymbol{\alpha}, \tag{3}$$

where $\boldsymbol{\alpha}$ is the weight coefficient vector, and $\boldsymbol{\Psi}$ is the sparse basis. Therefore, substituting equation (3) into equation (2) gives:

$$\hat{\mathbf{Z}}\mathbf{I} = \hat{\mathbf{Z}}\boldsymbol{\Psi}\boldsymbol{\alpha} = \boldsymbol{\Theta}\boldsymbol{\alpha} = \hat{\mathbf{V}}, \tag{4}$$

where $\boldsymbol{\Theta}$ is defined as the sensing matrix of size $M \times N$.

Since the construction of CMBFs is independent of the excitation and allows for efficient solving, they are employed as the sparse basis for current transformation [16]. Thus, $\mathbf{I}$ is expressed as equation (5), and equation (4) transforms to equation (6):

$$\mathbf{I} = \mathbf{J}^{CM}\boldsymbol{\alpha}, \tag{5}$$

$$\hat{\mathbf{Z}}\mathbf{I} = \hat{\mathbf{Z}}\mathbf{J}^{CM}\boldsymbol{\alpha} = \boldsymbol{\Theta}\boldsymbol{\alpha} = \hat{\mathbf{V}}, \tag{6}$$

where $\mathbf{J}^{\mathrm{CM}}$ has dimensions of $N \times K$, with K representing the total number of valid modes across all blocks. The sensing matrix $\boldsymbol{\Theta}$ needs to satisfy the restricted isometry property (RIP) [20] constraint. In this case, it is sufficient to solve the optimization problem under the l_1-norm:

$$\boldsymbol{\alpha} = \arg\min \|\boldsymbol{\alpha}\|_{l1} \quad s.t\ \boldsymbol{\Theta}\boldsymbol{\alpha} = \hat{\mathbf{V}}. \tag{7}$$

It is worth noting that equation (6) forms a low-dimensional overdetermined system. At this point, the

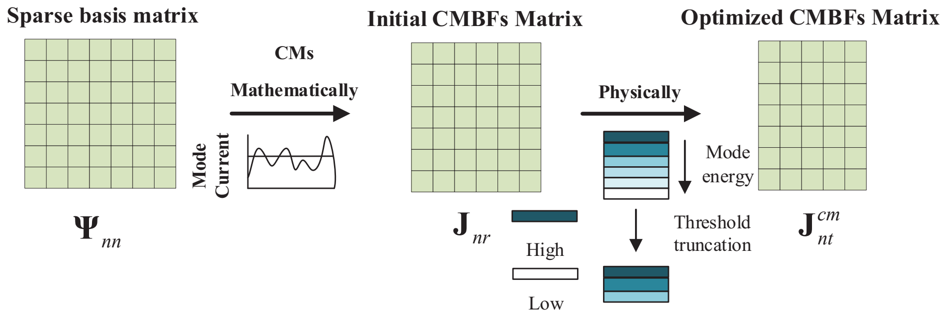

Fig. 1. Construction of CMBFs via a dual screening mechanism.

LS method can be used to replace the traditional greedy algorithm for a fast solution of the system:

$$\boldsymbol{\alpha} = (\boldsymbol{\Theta}^T \hat{\mathbf{V}})/(\boldsymbol{\Theta}^T \boldsymbol{\Theta}), \tag{8}$$

where $\boldsymbol{\Theta}^T$ is the transpose matrix of $\boldsymbol{\Theta}$.

B. Improved characteristic mode basis functions

The traditional approach for selecting CBFs primarily relies on mathematical eigenvalue decomposition. This method extracts eigenvalues from the impedance matrix through eigenvalue decomposition, and the corresponding eigenvectors are then chosen as basis functions based on these eigenvalues. From a mathematical perspective, these characteristic modes (CMs) represent inherent patterns of the scattering object. Typically, the most significant modes are selected based on the ranking of eigenvalues or mode energy. The sorting of eigenvalues is usually determined by their magnitude, with smaller eigenvalues corresponding to the characteristic modes being chosen to preserve the primary modes associated with electromagnetic scattering.

However, this method does not fully exploit the physical characteristics of the scattering object, which may result in the erroneous selection of low-energy redundant modes and the inclusion of numerical mode errors. These issues can adversely affect both the accuracy of the solution and the overall computational efficiency.

To address these limitations, a physics-informed and mathematically-guided selection strategy is proposed, which combines the electromagnetic response characteristics inherent in the physical model with the eigenvalue decomposition techniques of the mathematical model to optimize the selection of CMBFs. From a physical standpoint, modes exhibiting higher modal energy are typically associated with stronger electromagnetic responses; therefore, prioritizing modes with greater energy contributes to improved solution accuracy. By ranking characteristic modes according to their modal energies and retaining those with the highest energy, the selected basis functions are ensured to effectively represent the dominant distribution of the electromagnetic fields. As shown in Fig. 1, the process of constructing the CMBFs matrix under the dual screening of mathematical and physical principles clearly highlights the innovation of the proposed method.

From a reconstruction perspective, high-energy modes exhibit stronger physical orthogonality, leading to lower cross-correlation coefficients and enhanced sparsity concentration. From an information-theoretic viewpoint, the proposed dual-selection strategy maximizes the information entropy of the basis functions, as high-energy modes convey more scattering field information and effectively prevent the information dilution associated with low-energy modes. Modal energy directly reflects the contribution strength of the current distribution to the scattered field, thereby improving the physical interpretability of the solution. Furthermore, by reducing the number of selected modes, the proposed approach significantly enhances computational efficiency.

Specifically, from an information entropy perspective:

$$\eta(\mathbf{J}^{\mathrm{CM}}) = \sum_{i=1}^{K} P_i \log p_i \quad p_i = \frac{E_i}{\sum_{j=1}^{K} E_j}, \tag{9}$$

where $\eta(\mathbf{J}^{\mathrm{CM}})$ denotes the information entropy of the current distribution $\mathbf{J}^{\mathrm{CM}}$, which measures the uniformity of the mode energy distribution. E_i represents the energy of the ith characteristic mode, p_i denotes the proportion of the ith mode energy relative to the total energy, and K refers to the total number of modes retained.

At this stage, a physical selection mechanism is introduced to eliminate low-energy modes, effectively avoiding information redundancy and enhancing the system's information entropy, thereby achieving the goal of accelerating computational efficiency. Specifically, the modal energy is calculated as:

$$E_i = \|\mathbf{J}_i^{CM}\|^2 = \sum_{k=1}^{N_m} |\mathbf{J}_{i,k}^{CM}|, \tag{10}$$

where, $\mathbf{J}_{i,k}^{\mathrm{CM}}$ denotes the value of mode i at degree of freedom k. At this point, the index permutation mapping $\sigma : \{1,\ldots,K\} \to \{1,\ldots,K\}$ is constructed to satisfy:

$$\begin{gathered} E_{\sigma(1)} \geq E_{\sigma(1)} \geq \cdots \geq E_{\sigma(K)} \\ K = \min(|\mathbf{J}_i^e|, MaxModes). \end{gathered} \tag{11}$$

Therefore, the ordered index sequence $S = (\sigma(1), \sigma(2), \ldots, \sigma(K))$ is generated, which arranges the energy distribution in a monotonically decreasing order. In addition, *MaxModes* denotes the maximum number of modes preset for each subdomain.

Finally, the objective function for the joint physical and mathematical optimization is:

$$\Gamma = \sum_{i=1}^{N} \mathrm{II}(MS < \tau) + \beta \sum_{i=1}^{N} E_i, \tag{12}$$

where II() denotes the indicator function (which takes the value 1 when the condition is satisfied, and 0 otherwise), and β represents the weighting parameter (typically set to 1). Furthermore, the first half of the equation corresponds to numerical sparsity, while the second half represents physical significance.

C. Least square QR dissolution

In conventional CS reconstruction approaches, the LS method is frequently employed to solve for the current coefficients $\boldsymbol{\alpha}$ by minimizing the observation error, thereby enabling the recovery of the original signal.

As shown in equation (8), its analytical solution is obtained by constructing the normal equations. However, this approach suffers from numerical instability; when the columns of matrix $\boldsymbol{\Theta}$ are highly correlated, $\boldsymbol{\Theta}^T\boldsymbol{\Theta}$ may become nearly singular, resulting in an unstable solution. In addition, the requirement to store and process large-scale matrices, along with their transposes and inverses, poses significant challenges in terms of memory consumption and computational scalability, particularly for 3D electromagnetic scattering problems involving electrically large targets.

To address the aforementioned issues, this paper introduces the LSQR iterative algorithm. Rather than explicitly constructing $\boldsymbol{\Theta}^T\boldsymbol{\Theta}$, the LSQR algorithm directly performs iterations to minimize the Euclidean (L2) norm of the error:

$$\min_{\alpha} \|\boldsymbol{\Theta\alpha} - \hat{\mathbf{V}}\|_2. \tag{13}$$

In each iteration, LSQR avoids direct matrix inversion and operates without forming $\boldsymbol{\Theta}^T\boldsymbol{\Theta}$, thereby mitigating numerical instability. It achieves this by progressively approximating the solution within a Krylov subspace framework. The k-dimensional Krylov subspace is defined as:

$$\begin{aligned} &K_k(\boldsymbol{\Theta}^T\boldsymbol{\Theta}, \boldsymbol{\Theta}^T\hat{\mathbf{V}}) \\ &\quad = span\{\boldsymbol{\Theta}^T\hat{\mathbf{V}}, (\boldsymbol{\Theta}^T, \boldsymbol{\Theta})\boldsymbol{\Theta}^T\hat{\mathbf{V}}, \ldots, (\boldsymbol{\Theta}^T\boldsymbol{\Theta})^{k-1}\boldsymbol{\Theta}^T\hat{\mathbf{V}}\}, \end{aligned} \tag{14}$$

$$r_0 = \boldsymbol{\Theta\alpha} - \hat{\mathbf{V}}_0, \tag{15}$$

$$K_k(\boldsymbol{\Theta}^T\boldsymbol{\Theta}, \boldsymbol{\Theta}^T\hat{\mathbf{V}}), \tag{16}$$

where equation (15) represents the initial residual, while equation (16) denotes the sequence of Krylov subspaces. At the kth iteration, LSQR solves:

$$\boldsymbol{\alpha}_k = \arg\min_{\boldsymbol{\alpha} \in K_k} \|\boldsymbol{\Theta\alpha} - \hat{\mathbf{V}}\|_2. \tag{17}$$

This iterative process converges toward the minimum residual solution without forming or storing large-scale matrix products. The use of Golub-Kahan bidiagonalization further enhances the numerical robustness by orthogonalizing the Krylov basis and avoiding loss of orthogonality due to round-off errors.

In the context of this work, integrating LSQR into the CS-MoM framework not only enhances numerical stability in the presence of ill-conditioned systems but also provides a computationally efficient pathway for solving underdetermined or overdetermined systems arising from sparse basis pruning. This contributes directly to the robustness and scalability of the proposed method, especially in scenarios involving electrically large and geometrically complex targets.

Finally, Fig. 2 presents the computational flowchart of the LSQR algorithm. Unlike the explicit matrix construction and direct solution employed in the traditional LS method, LSQR iteratively approximates the solution through successive refinements.

D. Computational complexity analysis

In this paper, the CM-CS-MoM method and the proposed approach are employed. Their computational complexity primarily arises from three components: the construction of the sparse basis, the formation of the measurement matrix, and the recovery of the sparse coefficient vector. Since both methods share the same complexity in constructing the measurement matrix, this component is excluded from the analysis.

***Construction of sparse basis*:** In the mathematical screening method, for each subdomain, a generalized eigenvalue problem is solved based on the impedance matrix, with computational complexity $O(R \cdot N^2/(\log N)^2)$, where R is the number of subdomains and N is the number of unknowns per subdomain. The basis vectors corresponding to selected eigenvalues are

Algorithm 1 LSQR Algorithm

```
Step 0: Initialization
    $u_1 = b / \| b \|_2, v_1 = A^T u_1 / \| A^T u_1 \|_2$
    $w_1 = v_1, x_0 = 0, \varphi = \| b \|_2, \rho = \| v_1 \|_2$
    $\beta_1 = \| b \|_2, \alpha_1 = \| A^T u_1 \|_2$
for k = 1, 2, ..., max_iter:
  a) Lanczos Bidiagonalization (Krylov basis):
      $\beta_{k+1} u_{k+1} = A v_k - \alpha_k u_k$
      $\alpha_{k+1} v_{k+1} = A^T u_{k+1} - \beta_{k+1} v_k$
  b) QR Factorization (Stabilization):
      $\rho_k^{-} = \sqrt{\rho_k^2 + \beta_{k=1}^2}$
      $c_k = \rho_k / \rho_k^{-}, s_k = \beta_{k+1} / \rho_k^{-}$
      $\theta_k = s_k \alpha_{k+1}, \rho_{k+1} = c_k \alpha_{k+1}$
  c) Krylov Solution Update:
      $w_{k+1} = \left( v_{k+1} - \theta_k w_k \right) / \rho_k^{-}$
      $x_k = x_{k-1} + \left( \varphi c_k / \rho_k^{-} \right) \cdot w_{k+1}$
  d) Residual Update:
      $\varphi_{k+1} = \varphi s_k$
      if $|\varphi_{k+1}| < tol \cdot \beta_1$ : break
```

Fig. 2. Flowchart of LSQR algorithm.

assembled to construct the sparse basis matrix, with complexity $O(R \cdot N \cdot T)$, where T is the total number of selected characteristic modes.

In the physics-based and mathematical screening method, the complexity of computing the physical characteristic basis functions is the same as that in the mathematical screening method, up to a maximum of T_{bm} modes. The additional screening based on modal energy, along with eigenvalue filtering, has complexity $O(R \cdot N \cdot T_{bm})$.

Since sufficient accuracy can be achieved for bistatic scattering problems when $T_{bm} \leq 200$, the overall complexity of this hybrid method is significantly lower and more controllable than the purely mathematical screening method.

***Recovery sparse coefficient vector*:** Although both methods use the same linear algebra operations for current reconstruction, the physics-based and mathematical screening method has a significantly lower computational cost due to the enforced upper bound T_{bm} on the number of characteristic modes. In contrast, the mathematical screening method may select a much larger number of modes T, leading to higher complexity in matrix multiplications and inversions.

Therefore, under the same reconstruction framework, the computational complexity is $O(M \cdot T + M \cdot T^2 + N \cdot T)$ when using the LS algorithm with mathematical screening, whereas it is $O(M \cdot T_{bm} + k \cdot zzn(\mathbf{\Theta}) + N \cdot T_{bm})$ when employing the LSQR algorithm in combination with both mathematical and physical screening, where, k denotes the number of iterations, which is typically less than 200, and $zzn()$ represents the number of non-zero elements in the matrix. Since $T_{bm} < T$, the proposed method exhibits lower computational complexity in the reconstruction stage from an overall perspective.

III. NUMERICAL RESULTS

Different objects are simulated and analyzed to test the proposed method's effectiveness. The accuracy was evaluated using the root mean square error (RMSE) of the radar cross section (RCS), which is defined as:

$$RMSE = \sqrt{\frac{1}{N_a} \sum_{i=1}^{N_a} |RCS_{cal,i} - RCS_{ref,i}|^2}, \qquad (18)$$

where $RCS_{cal,i}$ is the calculation result of the method used, $RCS_{ref,i}$ is the calculation result using MoM, and N_a is the number of sampling points.

First, the bistatic RCS of a perfectly electrically conducting (PEC) cube with an edge length of 1 meter was calculated at an incident frequency of 1 GHz, with the scattering angle observed at position $(\theta, \varphi) = (0° - 360°, 0°)$, where θ and φ represent the azimuth and zenith angles, respectively. The surface of the cube was discretized into 21888 triangular elements. The surface electric field integral equation was discretized using RWG basis functions, resulting in 32832 unknowns. The target was partitioned into 16 blocks, each with an extension width of 0.15 times the wavelength, leading to a total of 39377 unknowns after domain expansion. In addition, during the mathematical screening process, the mode significance (MS) threshold was set to 0.001, resulting in the generation of 3196 CMs. In practice, for the CMBFM, when the extended region and the MS threshold are set to 0.1λ and 0.0001, respectively, the RMSE is 0.1 dBsm. A similar level of accuracy can also be achieved with an MS threshold of 0.002 and an extended region of 0.3λ. However, a larger extended region leads to an excessive number of unknowns on each subdomain, which significantly increases the computational time. To strike a balance between computational accuracy and efficiency, the extended region is generally set to 0.15λ, and this value is adopted consistently in all subsequent numerical examples. In the proposed method, an additional physical screening criterion was introduced, as shown in Table 1. By constraining the number of CMs generated per subdomain, the total number of CMs is effectively controlled. It can be observed that as the number of CMs increases, the

Table 1: Time and accuracy based on dual screening

	CMs count	960	1080	1200	1320	1440	1560	1680	1800	1920	2040	2160
Proposed Method	Construction time/s	33.0	33.8	35.5	37.8	40.7	43.2	44.7	46.7	48.5	50.9	53.1
	RMSE/dBsm	0.348	0.199	0.168	0.087	0.088	0.089	0.101	0.097	0.090	0.087	0.092

construction time grows accordingly, while the reconstruction error decreases. When the total number of CMs reaches 1320, the improvement in accuracy becomes marginal, indicating a saturation of the selected basis functions. Therefore, based on a trade-off between computational accuracy and efficiency, the number of CMs per subdomain was set to 110, resulting in a total of 1320 CMs. The number of CMs per subdomain is determined by the accuracy saturation behavior. When the RCS error tends to be stable, the smallest number of CMs that meets the accuracy requirement is selected. This method is objective and can be generalized to different PEC targets and mesh configurations.

To validate the advantages of the proposed method, Fig. 3 presents the solution time and reconstruction error (RMSE) under varying extraction steps for two different reconstruction approaches. The solution time includes both matrix construction and current recovery. In Fig. 3 (a), the conventional mathematical screening is employed to construct the CMBFs, while in Fig. 3 (b), the proposed dual screening strategy based on both mathematical and physical is employed.

As shown in Fig. 3 (a), when the extraction step ranges from 4 to 8, the reconstruction accuracy of the LSQR algorithm is comparable to that of the conventional LS method. However, at step size 9, the LS method begins to show noticeably higher reconstruction error compared to LSQR, and at step size 10, a sharp increase in RMSE occurs, indicating the onset of ill-conditioning. Beyond step 10, the RMSE exceeds 10, signifying complete deviation from acceptable accuracy. In contrast, the LSQR method continues to yield reliable current reconstructions, demonstrating strong numerical stability. In terms of solution time, the difference between the two methods remains within 2 seconds across all step sizes, and this difference decreases as the extraction step increases.

A closer examination of Fig. 3 (b) reveals that the overall solution time is significantly reduced due to the decreased number of constructed CMs. Owing to the higher-quality CMs obtained through the dual screening strategy, the conditioning of the LS solver is notably improved. Consequently, the RMSE values for both reconstruction methods remain nearly identical within the extraction step range of 4 to 14. Slight ill-conditioning only begins to appear when the extraction step exceeds 18 for the LS algorithm, and noticeable ill-conditioning appears only when the step size reaches 20. Overall, the reconstruction stability is further enhanced, while the difference in solution time remains negligible.

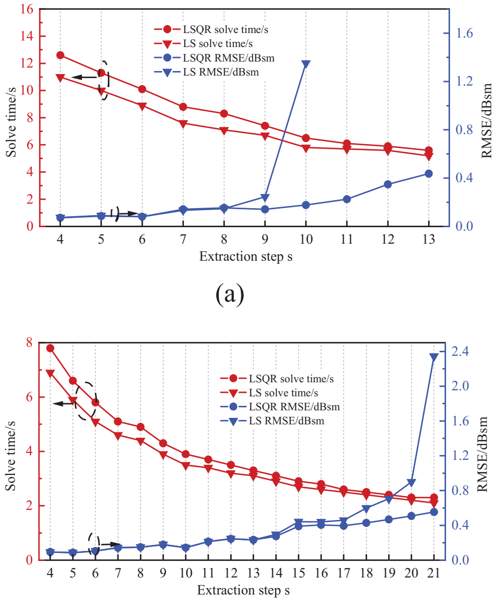

(a)

(b)

Fig. 3. Time and RMSE for different extraction steps of the cube model: (a) mathematical screening and (b) dual screening based on mathematical and physical.

Table 2 presents the correlation coefficients between the sparse basis matrix $\mathbf{J}^{CM}$ and the measurement matrix $\hat{\mathbf{Z}}$ constructed using both the CM-CS-MoM and the proposed method. It is evident that the sparse basis matrix $\mathbf{J}^{CM}$ generated by the proposed approach exhibits weak correlation with the sparse sensing matrix $\boldsymbol{\Theta}$ that satisfies the RIP [20], thereby ensuring accurate reconstruction of the current coefficients $\boldsymbol{\alpha}$.

Table 2: Correlation coefficients between measurement matrix and sparse basis matrix

Method	CM-CS-MoM	Proposed method
Coefficient	−0.0075–0.0931i	−0.0034+0.0859i

To further validate the accuracy of the proposed method, Fig. 4 presents a comparison of current distributions obtained using the proposed approach and the conventional MoM. The currents depicted correspond to common border currents uniformly sampled with a step size of 150. Figures 4 (a) and (b) illustrate the real and imaginary components of the current, respectively. As observed, the reconstructed currents from the proposed method closely align with those computed by MoM, confirming its effectiveness in current recovery. Additionally, Fig. 5 displays the RCS results obtained using both the CM-CS-MoM and the proposed method, with an extraction step size of 5. The RCS values for the horizontally polarized cube calculated using the proposed method show excellent agreement with those produced by MoM, further demonstrating the method's reliability.

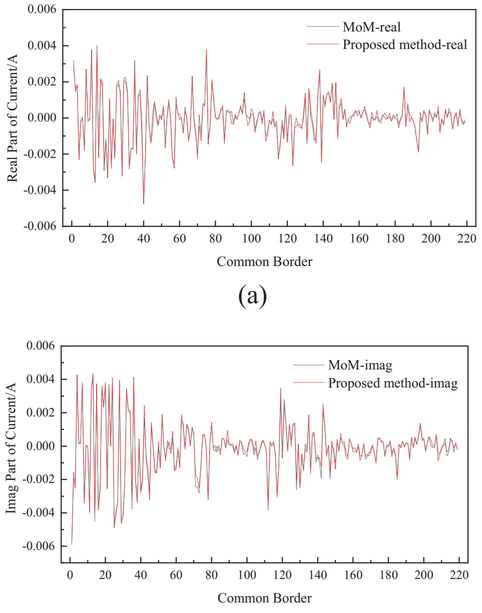

(a)

(b)

Fig. 4. Common border currents: (a) current real part and (b) current imaginary part.

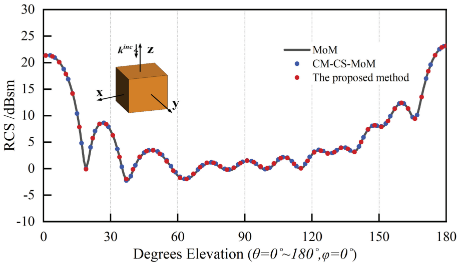

Fig. 5. Bistatic RCS of the cube in horizontal polarization.

Second, to further validate the effectiveness of the proposed method, the bistatic RCS of a 1-meter-long missile target was calculated under plane wave excitation at 4.5 GHz frequency. The incident wave direction was defined as angle $(\theta,\varphi) = (0^\circ,0^\circ)$, while the observation angle was denoted as angle $(\theta,\varphi) = (0^\circ-360^\circ,0^\circ)$. The target surface was discretized into 36510 triangles, generating 54765 unknowns through RWG basis function discretization. These unknowns were distributed across 16 computational blocks. Furthermore, with an extension width of 0.15 wavelength applied in the computation, the total number of extended unknowns reached 87729.

In this case, the mathematical filtering approach generated a total of 5115 CMs. In contrast, the proposed method incorporated an additional physical screening constraint. Considering the saturation of computational accuracy and solution efficiency, the number of CMs per subdomain is limited to 180, resulting in a total of 2880 CMs. With the extraction step set to 5, Fig. 6 presents the RCS results reconstructed using LS and LSQR for both methods. As illustrated, the results produced by the proposed method exhibit excellent agreement with those obtained from the MoM, demonstrating high computational accuracy.

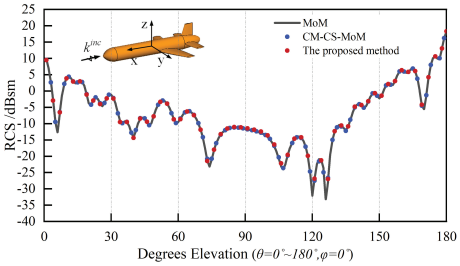

Fig. 6. Bistatic RCS of the missile in horizontal polarization.

Third, to further demonstrate the effectiveness of the proposed method in analyzing electrically large targets, an array composed of 36 PEC objects with two distinct geometries was selected for scattering simulation. The frequency of the incident plane wave was set to 800 MHz, and the scattering was observed at angle $(\theta,\varphi) = (0^\circ-360^\circ,0^\circ)$. The surface of the array was discretized using RWG basis functions, resulting in a total of 51984 triangular elements and 77976 unknowns. The entire target was partitioned into 36 blocks.

In this case, the conventional mathematical screening method generated a total of 8582 CMs. Using the dual screening strategy combining mathematical and physical constraints and considering the saturation of computational accuracy and solution efficiency, the number of CMs per subdomain is set to 120, resulting in a total of 4320 CMs. Under an extraction step of 6, simulations were performed using both methods, each with LS and LSQR reconstruction, and the results were compared with those obtained by the MoM. As shown in Fig. 7, the proposed method exhibits excellent

Table 3: Simulation time and accuracy

Model	Method	Unknown	CMs Count	Construction Time of Sparse Basis (s)	Recovery Induced Current Time (s)	Total Time (s)	RMSE (dBsm)
Cube	CM-CS-MoM	32832	3196	83.9	9.0	92.9	0.089
	Proposed method		1320	37.8	6.5	44.3	0.087
Missile	CM-CS-MoM	54765	5115	212.5	35.5	248.0	0.221
	Proposed method		2880	136.2	29.0	165.2	0.193
Array Target	CM-CS-MoM	77976	8582	184.3	105.0	289.3	0.365
	Proposed method		4320	99.8	56.6	156.4	0.379

agreement with the MoM results, confirming its high computational accuracy.

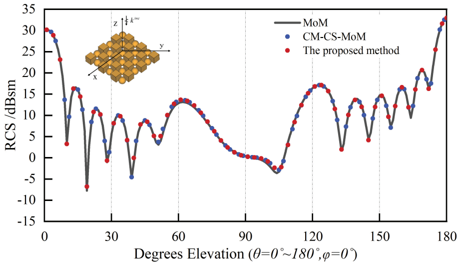

Fig. 7. Bistatic RCS of the array target in horizontal polarization.

Finally, Table 3 presents a comparative analysis of the computational time and RCS error between the CM-CS-MoM method and the proposed method across three different models. It is important to note that the current recovery time includes both the matrix equation construction and current reconstruction phases. As shown in Table 3, under the condition that the RMSE remains nearly the same, the proposed method reduces the number of basis functions by 58.7%, 43.7%, and 49.7%, respectively, compared to CM-CS-MoM. Correspondingly, the total computation time is reduced by 52.3%, 33.4%, and 45.9%, respectively.

IV. CONCLUSION

This paper proposes a dual screening mechanism incorporating physical principles for the construction of CMBFs and employs the LSQR algorithm to achieve efficient reconstruction of current coefficients. By integrating both mathematical and physical screening processes, the approach generates basis functions with higher quality and reduced redundancy, thereby significantly enhancing the efficiency of matrix construction. Meanwhile, the LSQR algorithm demonstrates strong capabilities in handling ill-conditioned matrices, contributing to improved overall computational stability. Simulation results validate that, compared to CM-CS-MoM, the proposed approach exhibits notable advantages in both computational efficiency and stability.

ACKNOWLEDGMENT

This work was supported in part the Natural Science Research Project of Anhui Educational Committee under no. 2022AH051583, in part by the Graduate Innovation Fund of Anhui University of Science and Technology under grant no. 2024cx2062.

REFERENCES

[1] R. F. Harrington, *Field Computation by Moment Methods*. New York: Macmillan, 1968.

[2] J. M. Song and W. C. Chew, “Multilevel fast-multipole algorithm for solving combined field integral equations of electromagnetic scattering,” *Microw. Opt. Technol. Lett.*, vol. 10, no. 1, pp. 14–19, Sep. 1995.

[3] E. Lucente, A. Monorchio, and R. Mittra, “An iteration free mom approach based on excitation independent characteristic basis functions for solving large multiscale electromagnetic scattering problems,” *IEEE Trans. Antennas Propag.*, vol. 56, no. 4, pp. 999–1007, Apr. 2008.

[4] K. Z. Zhao, M. N. Vouvakis, and J.-F. Lee, “The adaptive cross approximation algorithm for accelerated method of moments computations of EMC problems,” *IEEE Trans. Electromagn. Compat.*, vol. 47, no. 4, pp. 763–773, Nov. 2005.

[5] D. L. Donoho, “Compressed sensing,” *IEEE Trans. Inf. Theory.*, vol. 52. no. 4, pp. 1289–1306, Apr. 2006.

[6] M. S. Chen, F. L. Liu, H. M. Du, and X. L. Wu, “Compressive sensing for fast analysis of wide-angle monostatic scattering problems,” *IEEE Antennas Wireless Propag. Lett.*, vol. 10, pp. 1243–1246, Oct. 2011.

[7] S. R. Chai and L. X. Guo, “Compressive sensing for monostatic scattering from 3-D NURBS geometries,” *IEEE Trans. Antennas Propag.*, vol. 64, no. 8, pp. 3545–3553, 2016.

[8] M. Kong, M. S. Chen, X. Y. Cao, L. Zhang, Q. Qi, and X. L. Wu, "Fast analysis of local current distribution for electromagnetic scattering problems of electrically large objects," *IEEE Access*, vol. 8, pp. 127640–127647, July 2020.

[9] M. Kong, M. S. Chen, X. Y. Cao, J. B. Zhu, X. J. Kuang, Q. Qi, and X. L. Wu, "Fast electromagnetic scattering analysis of inhomogeneous dielectric objects over a wide incident angle," *IEEE Antennas Wireless Propag. Lett.*, vol. 20, no. 8, pp. 1527–1531, Aug. 2021.

[10] S. R. Chai and L. X. Guo, "Fast analysis of bistatic scattering problems with compressive sensing technique," *J. Electromagn. Waves Appl.*, vol. 30, no. 13, pp. 1755–1762, 2016.

[11] M. Kong, M. S. Chen, B. Wu, and X. L. Wu, "Fast and stabilized algorithm for analyzing electromagnetic scattering problems of bodies of revolution by compressive sensing," *IEEE Antennas Wireless Propag. Lett.*, vol. 16, pp. 198–201, May 2017.

[12] Z. G. Wang, H. R. Yuan, Y. F. Sun, W. Y. Nie, and P. Wang, "Block-based Krylov subspace basis functions for solving bistatic scattering problems," *IEEE Antennas Wireless Propag. Lett.*, vol. 22, no. 10, pp. 2561–2565, Oct. 2023.

[13] Y. L. Gao, M. F. Akbar, and G. N. Jawad, "Stabilized and fast method for compressive sensing-based method of moments," *IEEE Antennas Wireless Propag. Lett.*, vol. 22, no. 12, pp. 2915–2919, Dec. 2023.

[14] P. Wang, Z. G. Wang, Y. F. Sun, and W. Y. Nie, "Novel compressive sensing computing model used for analyzing electromagnetic scattering characteristics of three-dimensional electrically large objects," *Acta Phys. Sin.*, vol. 72, no. 3, pp. 54–61, Feb. 2023.

[15] Z. G. Wang, W. Y. Nie, and H. Lin, "Characteristic basis functions enhanced compressive sensing for solving the bistatic scattering problems of three-dimensional targets," *Microw. Opt. Technol. Lett.*, vol. 62, no. 10, pp. 3132–3138, May 2020.

[16] Z. G. Wang, P. Wang, Y. F. Sun, and W. Y. Nie, "Fast analysis of bistatic scattering problems for three-dimensional objects using compressive sensing and characteristic modes," *IEEE Antennas Wireless Propag. Lett.*, vol. 21, no. 9, pp. 1817–1821, Sep. 2022.

[17] X. Y. Cao, M. S. Chen, Q. Qi, M. Kong, J. H. Hu, L. Zhang, and X. L. Wu, "Solving electromagnetic scattering problems by underdetermined equations and Krylov subspace," *IEEE Microw. Wireless Compon. Lett.*, vol. 30, no. 6, pp. 541–544, June 2020.

[18] J. A. Tropp and A. C. Gilbert, "Signal recovery from random measurements via orthogonal matching pursuit," *IEEE Trans. Inf. Theory.*, vol. 53, no. 12, pp. 4655–4666, 2007.

[19] J. Wang, S. Kwon, and B. Shim, "Generalized orthogonal matching pursuit," *IEEE Trans. Signal Process.*, vol. 60, no. 12, pp. 6202–6216, Sep. 2012.

[20] E. J. Candes, "The restricted isometry property and its implications for compressed sensing," *Comptes Rendus Math.*, vol. 346, no. 9/10, pp. 589–592, 2008.

Yang Liu received the B.E. degree from Suzhou University, China, in 2023. He is currently pursuing the M.S. degree at Anhui University of Science and Technology. His current research interests include computational electromagnetics.

Zhonggen Wang received the Ph.D. degree in electromagnetic field and microwave technique from the Anhui University of China (AHU), Hefei, P. R. China, in 2014. Since 2014, he has been with the School of Electrical and Information Engineering, Anhui University of Science and Technology. His research interests include computational electromagnetics, array antennas, and reflect arrays.

Longhui Sun received the B.E. degree from Fuyang Normal University, China, in 2022. He is currently pursuing the M.S degree in Anhui University of Science and Technology. His current research interest lies in the application of Bayesian compressive sensing in electromagnetic scattering.

Wenyan Nie is a professor at Huainan Normal University, China. She received the B.S. and M.S. degrees from Anhui University of Science and Technology in 2007 and 2012, respectively. Her research interests include computational electromagnetic methods, antenna theory and design.